Self-assembly of Sulfonated Amphiphiles for Channel-like Synthetic Membranes

Von der Fakultät für Mathematik, Informatik und Naturwissenschaften der Rheinisch-Westfälischen Technischen Hochschule Aachen zur Erlangung des akademischen Grades einer Doktorin der Naturwissenschaften genehmigte Dissertation

vorgelegt von

Master of Science

Linglong Yan

aus Fuzhou, China

Berichter: Privatdozent Dr. rer. nat. Uwe Beginn

Universitätsprofessor Dr. rer. nat. Martin Möller

Tag der mündlichen Prüfung: 18.05.2006

Diese Dissertation ist auf den Internetseiten der Hochschulbibliothek online verfügbar.

Acknowledgement

I believe that my dissertation would not have been completed without the support and concern of many persons. First of all, I would like to express my extremely sincere gratitude and appreciation to my supervisor Dr. Uwe Beginn for his guidance, understanding and patience, for his encouragement and support at all levels during my Ph.D. studying. I would also like to thank Prof. Möller and Dr. Englert for reading my thesis and being my co-referee of my PhD defense.

I would like to gratefully and sincerely thank Dr. Kim-Ho Phan and Stefan Rütten for their assistance and guidance during the TEM and SEM measurements, Dr. Crisan Popescu for thermal analysis and very valuable discussion, Dr. Ahmed Mourran for helping the microscopy.

I would also like to give a special thanks to Dr. Helmut Keul for offering his extensive help, especially in my first year moving in Aachen.

A special thanks goes to Rainer Haas for numerous and efficient help in the daily working. I'm also very grateful to Martina Mennicken, Nicolas Pasquier and Cristian Vaida for the NMR measurements.

Thank also to all the members in the Beginn's research group, especially the friendship of Yvonne Noppeney. Additionally I'd like to extend my appreciation for their friendship of all the members of TexMC and DWI, to everyone who have dedicated part of their valuable time for helping me.

Finally I will never find words enough to express the gratitude that I owe to my parents and my brother, and Nicolas. Throughout the whole years, they keep their faith in me. Their love with understanding and patience always give me constant encouragement and make me believe in myself.

PUBLICATION & POSTER

Publication

L. Yan, U. Beginn, S. Chvalun, M. Möller, 'Thermotropic columnar mesophases from wedge-shaped benzene sulfonated mesogens', in preparation.

U. Beginn, L. Yan, X. Zhu, S. Chvalun, M. Möller, ″Mimicking ion channels by polymerizable supramolecular stacks of wedge-shaped tris(alkenyl-oxy)benzene sulfonates″, *Polymeric Materials: Science & Engineering*, 93, 244-245, **2005**.

Poster

Linglong Yan, Uwe Beginn and Martin Möller, ″Developments of Ion Selective Membranes from Sulfonated Mesogenic Organogelators″
Poster on *Symposium on Functional Polymer Materials*, Mol, Belgium, Oct. 7-8, **2004**.

Uwe Beginn, Xiaomin Zhu, Linglong Yan and Martin Möller, ″Self-Organized Supramolecular Sulfonic Acid Ion Channels as Nafion Mimic? ″
Poster on *Makromolekulares Kolloquium Freiburg*, Freiburg, Germany, Feb. 26-28, **2004**.

Linglong Yan, and Uwe Beginn, ″Alkoxyphenyl Sulfonic Acid and Derivatives – New Mesogenes and Gelators for the design of Ion-selective Nanostructured Supramolecular Systems. ″
Poster on *Molecular Organization for Nanosystems on Multi-Level Ordering*, Kloster Banz, Germany, Feb. 15-20**, 2003**.

献给我的父母与长兄

Dedicated to my Parents and my Brother

Contents

List of Abbreviations III

Chapter 1 Introduction 1

Chapter 2 Literature review: liquid crystals, organogels and membranes

2.1 Liquid crystals 6

A brief history of liquid crystals 6

Types of liquid crystals 7

Characterization of liquid crystal phases 15

2.2 Supramolecular organogels 27

Introduction of the gel state 27

Supramolecular organogels 30

Recent applications for new functional materials 35

2.3 Ion-selective membranes 38

Biological ion-selective membranes 38

Selective synthetic membranes mimicking biostructures 39

Proton-conducting membranes for fuel cells 42

2.4 References 47

Chapter 3 Thermotropic columnar liquid crystal phases from wedge-shaped benzene sulfonated mesogens

Introduction 55

Experimental section 57

Results and discussion 68

Synthesis of wedge-shaped benzene sulfonated amphiphiles 68

Thermal analysis of 2,3,4-substituted benzene sulfonates 71

Thermal analysis of 3,4,5-substituted benzene sulfonates · · 85
Determination of the type of mesophase by SAXS
and m*iscibility experiments* · 90
Relation between molecular structures and mesophase · · · 93
Conclusion · 97
References · 98

Chapter 4 Self-assembly of sulfonated organogelators and their morphologies
Introduction · 101
Experimental section · 102
Results and discussion · 104
Gelation capabilities of 2,3,4-substituted benzene sulfonates 105
Gelation capabilities of 3,4,5-substituted benzene sulfonates 114
Morphologies of the gels investigated by TEM · · · · · · · · 117
Conclusion · 125
References · 125

Chapter 5 Polymerized lyotropic liquid crystal assemblies for functional membranes
Introduction · 128
Experimental section · 133
Results and discussion · 136
Crosslinker · 136
Initiators · 137
*Phase diagram of **16**/HMT10* · 138
*Preparation of membranes from **16**/HMT10* · · · · · · · · · · · 142
*Phase diagram of **16**/EGDMA* · 147
*Preparation of membranes from **16**/EGDMA* · · · · · · · · · · 152
Conclusion · 155
References · 156

Summary · · · · · · · · · · · · · · · · · · ·

List of Abbreviations

ACS	American chemical society
AIBN	2,2'-azobis-*iso*-butyronitrile
t-BuAc	*tert*-butylacetate
C	concentration
$CDCl_3$	deuterated chloroform
$CHCl_3$	chloroform
Col	columnar phase
C_h	hexagonal columnar phase
C_{ho}	ordered hexagonal columnar phase
C_{hd}	disordered hexagonal columnar phase
C_L	lamello columnar phase
C_N	columnar nematic phase
C_r	rectangular columnar phase
C_{ob}	oblique columnar phase
Cmc	critical micelle concentration
Cr	crystalline phase
DMF	dimethylformamide
DMFC	direct-methanol fuel cells
DMSO	dimethylsulfoxide
DSC	differential scanning calorimetry
EA	elemental analysis
EGDMA	ethylene glycol dimethacrylate
EHMA	2-ethylhexyl methacrylate
EMA	ethylene methacrylate
e.q.	equation
EtOAc	ethyl acetate
EtOH	ethanol
Φ	mesophase
FTIR	Fourier transform infrared
H	enthalpy
HEMA	2-hydroxyethyl methacrylate

H_I	hexagonal columnar phase
H_{II}	reversed hexagonal columnar phase
HMA	*n*-hexyl methacrylate
HMT10	a mixture of 72.45 wt% ethyl methacrylate, 17.55 wt% hexyl-methacrylate and 10 wt% triethylene-glycol-dimethacrylate.
Hz	Hertz
i	isotropic phase
IR	infrared spectrum
k	crystalline phase
L_α	lamellar phase
LC	liquid crystal
M^+	metal cation
MeOH	methanol
MFSC	matrix-fixed supramolecular channels
mgc	minimum gelation temperature
m.p.	melting temperature
N	nematic phase
N_D	nematic discotic phase
NMR	nuclear magnetic resonance
δ	chemical shift
d	doublet
J	coupling constant
ppm	parts per millon
s	singlet
t	triplet
TMS	tetramethylsilane
PEEK	polyetheretherketone
PEMFC	proton exchange membrane fuel cell
Py^+	pyridinium
R_f	retention factor (TLC)

$$R_f = \frac{\text{Distance traveled by the compound}}{\text{Distance traveled by the solvent front}}$$

RP	receiving phase
RT	room temperature
Θ	half of the X-ray scatter angle
S	smectic mesophase
SAXS	small angle X-ray scattering
SEM	scanning electron microscopy
SP	source phase
t	time
T	temperature
TEGDMA	triethylene glycol dimethacrylate
TEM	transmission electron microscopy
THF	tetrahydrofuran
TGA	thermo gravimetric analysis
TLC	thin layer chromatography
T_g	glass temperature
T_{gm}	gel melting temperature
T_m	melting temperature
TMS	tetramethylsilane
TOA	thermo optical analysis
TOPM	thermo optical polarizing microscopy
UV	ultraviolet
V	volume
V-601	dimethyl 2,2'-azobis-*iso*-butyrate (Wako)
wt%	weight percent

Chapter 1

Introduction

Synthetic functional membranes, which contain well-defined and ordered nanometer-dimensioned superstructures, capable to selectively recognize and transport ions or small molecules (e.g. H_2O), represent a challenging target for preparative membrane science. Such membranes can eventually form a basis to replace some energy- or labor-intensive purification processes. Highly selective membranes can also simplify specific detection problems in the fields of biochemical, medical and even environmental analytical technology. Nowadays, the most used functional membrane is Nafion®, which is made from poly(tetrafluorethylene) containing side-chain perfluoroethyl-sulfonic acid groups [1]. The polymer bound sulfonic acid groups are located at the inner wall of a percolating, water swollen ionic "cluster phase". Within only a few nano-meters' cluster phase, ionic groups are closely packed, which enforces condensation of the mobile and the fixed charges [2]. Because Nafion® does not possess geometrically defined pores, the tortuosity of such membranes is rather high. On the other hand, presently available membranes with well-defined and ordered pores are not functionalized. Hence we attempted to *design a new class of sulfonated molecules that are able to self-assemble to spatially ordered and structurally defined ion channels, thus allowing to construct ion selective membranes with improved structural regularity and selectivity.*

Construction of synthetic membranes through the self-organized aggregation of carboxylated compounds has been investigated [3] previously in our group. However, the low ion-selectivity, low ion transport rates and the disordered superstructure remain a task for further improvements.

It has been found that wedge-shaped amphiphiles can self-assemble to form different liquid crystal phases, especially the hexagonal columnar phase [4]. V. Percec et al. reported a series of wedge-shaped amphiphiles, e.g. the alkali metal salts of 3,4,5-tris(*n*-alkan-1-yloxy)benzene acid, with the number of methylenic units in the alkyl group n = 12, 14, 16, 18 and the alkali metal being Li, Na, K, Rb, Cs [5]. Depending on the molecular structure, these molecules self-assemble to soft objects ordered in two-dimensional hexagonal columnar and three-dimensional cubic lattices.

Sulfonic acid and sulfonates are expected to be superior to carboxylate functional head groups due to their high polarity and ″superselectivity″ [6]. Polymerizable groups attached to the molecules will allow stabilizing the well-defined superstructures by polymerization permanently. First reports on the polymerization of lyotropic liquid crystalline carboxylated and sulfonates have been reported by our group [7] and D. Gin [8]. In this way thin polymer films are prepared and characterized by a superstructure with the sulfonated moieties in the center of columns, functioning as an ion transport channel (Figure 1.1).

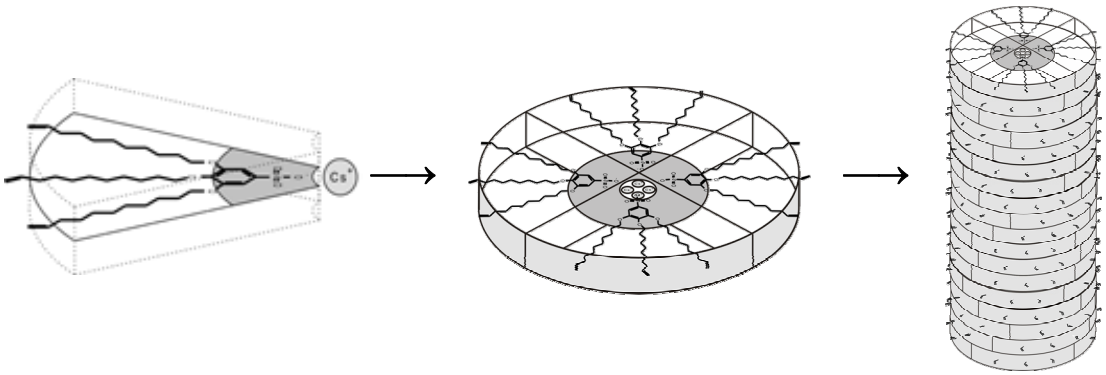

Figure 1.1 Illustration of the self-assembly of wedge-shaped amphiphiles into flat disc-like aggregates, which subsequently stack to form a column containing well-defined channel in the center.

In this thesis a series of sulfonated wedge shaped monomers is synthesized and investigated including mesophase formation and their polymerization in the lyotropic liquid crystalline state.

In *Chapter 2*, the state of the literature is summarized and evaluated regarding the objective of this thesis comprehending liquid crystals, organogelators and synthetic membranes.

Chapter 3 described the synthesis and characterization of the wedge-shaped 2,3,4-tris (dodecyloxy)benzene sulfonic acid and its derivatives, as well as the alkali metal salts of 3,4,5-tris(dodecyloxy)benzene sulfonates and cesium 3,4,5-tris(undec-10-enyloxy) benzene sulfonate. The thermal transformations and the characterization of the liquid crystal phases were reported. Furthermore, the relation between the thermal properties and molecular structures, such as molecular geometry, size of headgroup (cations) and alkyl chain, was discussed.

In *Chapter 4*, the gelation capabilities were listed for all sulfonated mesogens that were studied in chapter 3. The morphologies of the gels were investigated by transmission electron microscopy (TEM). A packing model for the self-assembly is proposed for 2,3,4-tris(dodecyloxy)benzene sulfonamide based on optimum hydrogen bonding. For the ionic compounds the effect of a systematic variation of the molecular structure was presented regarding the self-assembly driven by the Coulomb interaction.

Chapter 5 reported the synthesis, characterization and the thermal properties of cesium 3,4,5-tris(undec-10-enyloxy)benzene sulfonate (**16**). The phase diagrams of two binary system **16** / EGDMA (ethylene glycol dimethacrylate) and **16** / HMT10 were presented, supported with polarized micrographs. The preparation of functional membranes based on the polymerization of the columnar aggregates in the lyotropic mesophase was described. Preliminary ion transport experiments through the prepared membranes were reported as well.

References

[1] C. W. Martin, P. J. Nanapurkar, S. S. Katti, "*Ionomeric Membranes, Perfluorinated*", in "*Encyclopedia of Polymeric Material*", CRC Press, Boca Raton, **1996**, Vol.5, p. 3427.

[2] L. Streyer, "*Biochemistry*", 4ed., Freeman, New York, **1995**.

[3] (a) U. Beginn, G. Zipp, M. Möller, *Adv. Mater.*, **2000**, 12, 510; (b) U. Beginn, G. Zipp, A. Mourran, P. Walther, M. Möller, *Adv. Mater*, **2000**, 12, 513.

[4] V. Percec, G. Johansson, J. Heck, G. Ungar, S. V. Batty, *J. Chem. Soc. Perkin Trans. I*, **1993**, 1411.

[5] G. Ungar, V. Percec, M. N. Holerca, G. Johansson, J. A. Heck, *Chem. Eur. J.*, **2000**, 6, 1258-1266.

[6] H. Reiss, I. C. Bassignana, *J.Membr. Sci.*, **1982**, 11, 219.

[7] U. Beginn, G. Zipp, M. Möller, *J. Polym. Sci., Part A*: *Polym. Chem*., **2000**, 38, 631-640.

[8] D. L. Gin, W. Gu, B. A. Pindzola, W-J. Zhou, *Acc. Chem. Res.*, **2001**, 34(12), 973-980.

Chapter 2

Literature Review:

Liquid Crystals, Organogels and Membranes

2.1 Liquid crystals

Liquid crystals are liquid substances that exhibit anisotropic physical properties like a solid crystal, because the molecules of the liquid crystal are oriented along a preference direction (the director) and additionally may possess a one or a two dimensional long range positional order. Since their physical properties, as well as their existence temperature region, are located between the crystalline and liquid state, this state was denoted "mesophase", which came from Greek "mesos" (μεσοζ) means "middle", or "liquid crystal"(LC). Hence, over the existence region of the liquid crystal phase mesomorphic materials are fluid and, at the same time, exhibit anisotropic physical properties, such as the birefringence, as well as anisotropic elasticity, viscosity and conductivity.

A brief history of liquid crystals

The discovery of liquid crystals is commonly attributed to the Austrian botanist F. Reinitzer [1] in 1888. He observed a "double melting" behaviour of cholesterol benzoate. The crystals of this material melted at 145.5 °C into a cloudy fluid, which became clear upon further heating to 178.5 °C. This discovery represented the first recorded documentation of the LC phase. Further investigations by the German physicist O. Lehmann [2] observed and proved this phenomenon by using a polarized optical microscope designed by himself. He described the observation as "crystals [which] can exist with a softness [...] that one could call them nearly liquid". In 1922 the French scientist G. Friedel [3] produced the first classification scheme of LCs, dividing them into three different types of mesogens (materials able to sustain mesophases), based upon the level of order that the molecules possessed in the bulk material:

1. nematic (from the Greek word nematos (νηματοζ) meaning 'thread') [4],
2. smectic (from the Greek word smectos (σμηκτκοζ) meaning 'soap') [4], and
3. cholesteric (better defined as 'chiral nematic').

Following these first observations and discoveries, the scientific research turned attention towards a growing number of compounds, which displayed liquid crystalline properties. In order to establish a relationship between the molecular structure and the

exhibition of liquid crystalline properties, a series of systematic modifications of the structures of mesogens was undertaken, leading in 1973 [5], to the discovery of the most technologically and commercially important class of liquid crystals to date: the 4-alkyl-4'-cyanobiphenyl (CB) of which an example, 4-pentyl-4'-cyanobiphenyl (5CB) is illustrated in Figure 2.1.

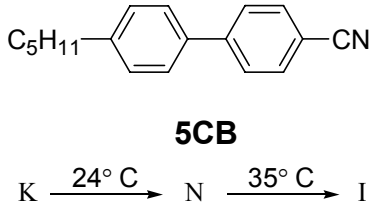

Figure 2.1 Molecular structure of 4-pentyl-4'-cyanobiphenyl (5CB) (K = crystalline phase, N = nematic phase, I = isotropic melt).

These are the types of the materials, which still constitute the simple common displays found in calculators or mobile phones. However, the numerous and increasingly sophisticated applications, relying on the use of liquid crystalline materials, require such a complexity of superior properties to achieve improved devices performance, that the quest for ever new liquid crystals has grown enormously over the last three decades. Nowadays, liquid crystals play a dominant role in a large part of the display technology.

Types of liquid crystals

Generally, the two major categories of liquid crystals are:

1. *thermotropic liquid crystals*, whose mesophase formation is temperature dependent, and
2. *lyotropic liquid crystals*, whose mesophase formation is concentration and solvent dependent.

"Amphotropic" substances form both type of mesophases [6, 7, 8].

Thermotropic liquid crystals

The essential requirement for a molecule to be a thermotropic mesogen was assumed to contain a structure consisting of a central rigid core (often aromatic) and flexible

peripheral moiety (generally aliphatic groups). This structural requirement leads to two general classes of liquid crystals:

1. *calamitic* liquid crystals, and
2. *discotic* liquid crystals.

Calamitic liquid crystals consist of rod-like molecules and have order in the direction of the longer axes of the molecules. It is important that the molecule are fairly rigid for at least some portion of its length, since it must maintain an elongated shape in order to produce interactions that favour alignment. Calamitic liquid crystals can be divided into two general types of mesophases:

1. *nematic* mesophase, and
2. *smectic*.

The least ordered mesophase (the closest to the isotropic liquid state) is the *nematic* (N) phase, where the molecules have only an orientational order. The molecules' centers of gravity are distributed in space without mutual long range order. As shown in Figure 2.2, the molecular long axis points on average in one favoured direction referred to as the director (ñ).

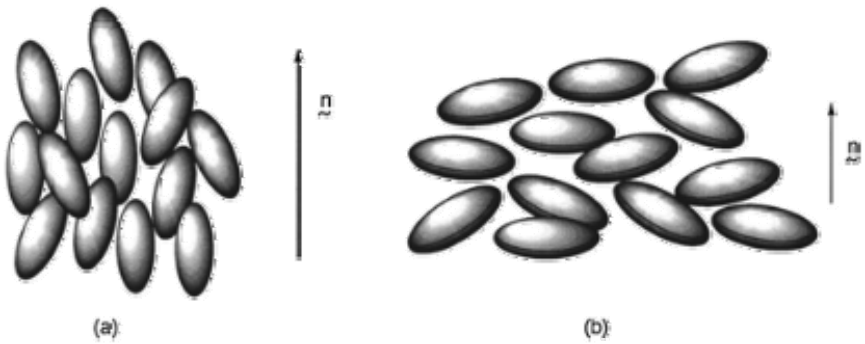

Figure 2.2 Scheme of a nematic liquid crystal phase of (a) rodlike; (b) disklike molecules. The calamitic molecules are oriented, on average, in the same direction referred to as the director (ñ), with no positional ordering with respect to each other, while disclike molecules are oriented perpendicular to the mesophases director(b).

The next level of organization is classified as *smectic* (S), where in addition to the orientational order the molecules possess positional order, such that the molecules' centers of gravity organize in layered structures. The smectic phase characterized by the lowest order is the orthogonal S_A phase, where the layers are perpendicular to the

director (Figure 2.3a). Otherwise when the director is tilted against the plane normal vector of the layers (z), the result is the S_C phase (Figure 2.3b). In both cases no long range order is found within the layers.

Other smectic phases exhibit different degree of order within the layers. Their symbols are S_B, S_D, S_E S_F, S_G, S_H, S_I, S_J, S_K. Note that the indices follow the historical order of discovery, hence no indication on the degree of molecular order can be derived from the sequence S_A – S_K.

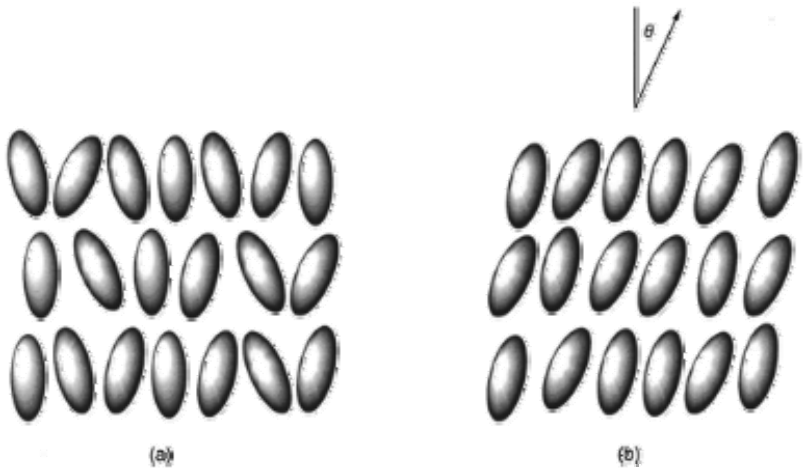

Figure 2.3 Scheme of (a) a smectic A (S_A) phase; (b) a smectic C (S_C) phase.

In 1977, the second type of mesophases, based on a disc-shaped molecular structure that consisted of one central benzene ring surrounded by six alkyl chains was discovered by the Indian scientist Sivaramakrishna Chandrasekhar [9]. Since then, a large number of discoid mesogenic compounds have been discovered in which triphenylene-, porphyrine-, phthalocyanine-, coronene-, and other aromatic molecules are involved [10]. The discotic liquid crystals possess a general structure comprising a planar (usually aromatic) central rigid core surrounded by a flexible periphery, represented mostly by pendant chains, as illustrated in Figure 2.4. As it can be seen, the molecular diameter (d) is much greater than the disc thickness (t), imparting the anisotropy to the molecular structure.

The typical discotic liquid crystalline molecules have a π-electron-rich aromatic core grafted by flexible alkyl chains. Such structure has attracted particular attention for molecular electronics in which the aromatic units transport electrons or holes and alkyl

chains act as insulating parts. The advantages of liquid crystalline conductors are their anisotropy, processability and self-healing characteristics for structural defect.

Similar to calamitic molecules, discotic molecules can show several types of mesophases, with varying degree of organization. The two principle mesophases are:

1. *nematic discotic*, and
2. *columnar*.

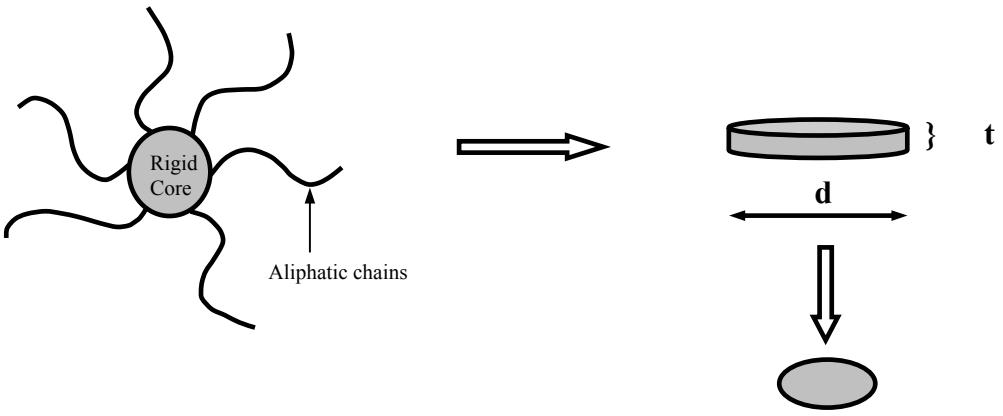

Figure 2.4 Scheme of the general shape of discotic liquid crystals, where **d** >> **t**.

Nematic discotic (N_D) is the least ordered mesophase, where the molecules have only orientational order being aligned on average with the director. There is no positional order.

Columnar (Col) phases are more ordered. The disc-shaped cores have a tendency to stack one on the top of each other, forming columns. Generally, the mesogens form cylinders of macroscopic (infinite) length and regularly arrange in one or two dimensions. Hence, columnar phases are regarded as two- or one-dimensional liquids. Arrangement of columns into different lattice structures gives rise to a number of columnar mesophases. The most structural simple columnar phase is obtained when the columns only exhibit an orientational order without positional lone range order. That is called as ″columnar nematic″ phase (C_N), which was reviewed elsewhere [11]. If the parallel oriented columns are ordered in layers, the ″lamello columnar″ phase (C_L) is yielded [12]. The C_L phase is described by one orientational order parameter, regarding the parallel arrangement of the columns, and one lattice parameter describing the layer

thickness *d*. Figure 2.5 [12] depicts projections of two dimensionally ordered columnar phases parallel to their column axis. According to Levelut, columnar phases are classified with respect to the symmetry of the spatial arrangements of the columns, described by two-dimensional planar space groups [13]. So far, phases of two-dimensional hexagonal (C_h), rectangular (C_r), and oblique (C_o) symmetry have been distinguished (Figure 2.5).

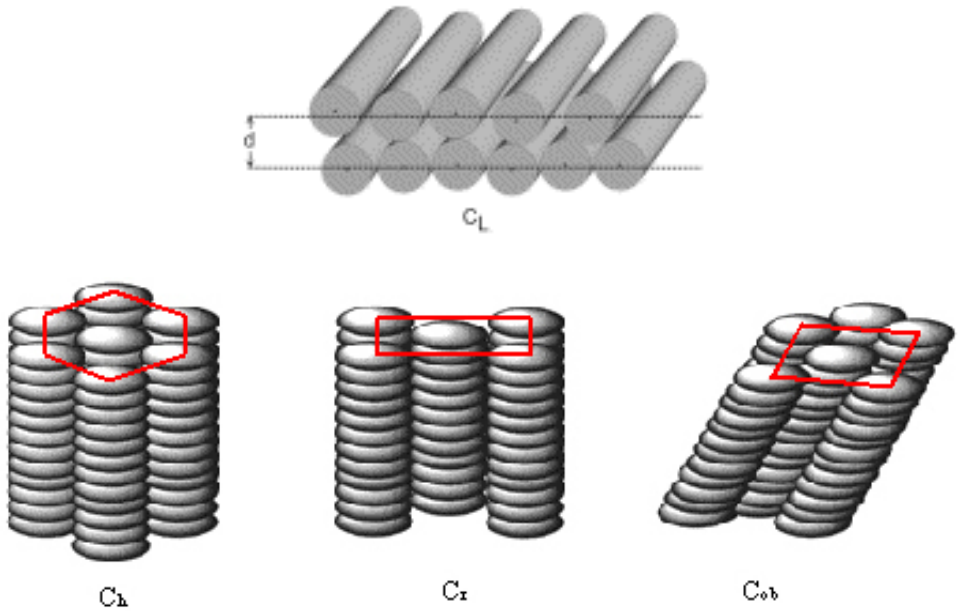

Figure 2.5 Scheme of structures of columnar mesophases according to Ref. [12]. One-dimensional lattice symmetry: lamello columnar phase (C_L); two-dimensional lattice symmetries: hexagonal columnar phase (C_h), rectangular columnar phases (C_r), oblique columnar phase (C_{ob}).

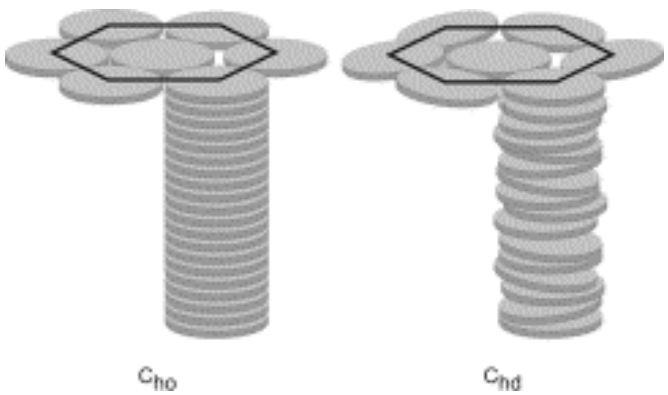

Figure 2.6 Degree of order along the column axis with the example of the hexagonal columnar phase: ordered (C_{ho}), and disordered (C_{hd}).

Any columnar structure may occur in two different versions, depending on the order within each single column. As long as the distance of the mesogenes (centers of gravity) parallel to the column axis are not regularly arranged, the phase is denoted as a *disordered* phase, and the phase symbol is completed by addition of an indexed 'd'. Otherwise the phase is considered as *ordered* phase (symbol C_{xo}) [14]. Figure 2.6 depicts an example with the hexagonal columnar phase that can be found as hexagonal columnar ordered (C_{ho}), or as hexagonal columnar disordered (C_{hd}) phase.

Besides the above classification, liquid crystal phases can be also classified based on different thermal behaviours as:

1. *enantiotropic* mesophases, and
2. *monotropic* mesophases.

An *enantiotropic* mesophase is a thermodynamic stable phase that appears above the melting temperature and is therefore seen on melting the sample from crystals (or a lower temperature mesophase) and always reappears on cooling.

A *monotropic* phase is a thermodynamic metastable phase that appears only on cooling from a higher temperature phase. Monotropic phases can only be observed in case that the thermodynamic stable phase that exist in the respective temperature range can be supercooled below the existence temperature of the monotropic phase. In addition, the supercooling of fluids makes it possible to observe monotropic phases.

The phenomenon of supercooled transitions can be used as indication for the presence of mesophases. Isotropic liquids usually supercool before they crystallize under non-equilibrium conditions. This is also the truth with mesophases. This means that the crystallization temperature will usually be lower than the melting temperature. For some compounds, this supercooling will be small (< 10 °C) and therefore appears to be non-existent, but in most compounds it is large enough to be easily detected. It tends to be larger in branched chain mesogens than in linear chain ones. Since supercooling represents an unstable condition, it also means that the crystallization temperature is dependent on such things as cooling rate, vibration and previous history of the sample. Transitions between mesophases usually exhibit small supercooling.

Lyotropic liquid crystals

A lyotropic liquid crystal consists of two or more components that exhibits liquid-crystalline properties in certain concentration and temperature ranges. In lyotropic phases, solvent molecules fill the space around the compounds to provide fluidity to the system. In contrast to thermotropic liquid crystals, these lyotropics have the additional degree of freedom to vary the concentration of the mesogen to induce a variety of different phases. Furthermore the lyotropic liquid crystals structure depend also on the type of solvents.

Many amphiphilic molecules show lyotropic liquid crystal phases and the types of mesophases depend on the volume balances between the hydrophilic part and hydrophobic part [15]. These structures are formed through the micro-phase segregation of two incompatible components on a nanometer scale. Soap is an everyday example of a lyotropic liquid crystal.

The content of water or other solvent molecules changes the self-assembled structures. At very low amphiphile concentration, the molecules will be dispersed randomly without any ordering. At slightly higher (but still low) concentration, amphiphilic molecules will spontaneously assemble into micelles or vesicles. This is done so as to 'hide' the hydrophobic tail of the amphiphile inside the micelle core, exposing a hydrophilic (water-soluble) surface to aqueous solution. However, these spherical objects stay randomly in solution without any order. The usually well defined transition concentration separating the micellar region from the molecular disperse region is called 'critical micelle concentration' (cmc). At higher concentration, the assemblies start to become ordered. A typical phase is a hexagonal columnar phase, where the amphiphiles form long cylinders (again with a hydrophilic surface) that arrange themselves into a roughly hexagonal lattice. This is called the middle soap phase. At even higher concentration, a lamellar phase (neat soap phase) may form, wherein extended sheets of amphiphiles are separated by thin layers of water. For some systems, a cubic (also called viscous isotropic) phase may exist between the hexagonal and lamellar phases, wherein either spheres are formed that create a dense cubic lattice, or a bicontinuous network makes up the cubic phase.

The assemblies created by amphiphiles can be spherical (as in the case of micelles), disc-like (bicelles), rod-like, or biaxial (all three micelle axes are distinct). These anisotropic self-assembled nano-structures can arrange themselves orderly in much the similar way as liquid crystals do, forming large-scale versions of all the thermotropic phases (such as a nematic phase of rod-shaped micelles).

For some systems, at high concentration, inverse phases are observed where the water is confined inside the associates. That is, one may generate an inverse hexagonal columnar phase (columns of water encapsulated by amphiphiles) or an inverse micellar phase (a bulk liquid crystal sample with spherical water cavities).

A generic progression of phases, going from low to high amphiphile concentration, is:

Discontinuous cubic phase (micellar phase)
Hexagonal columnar phase (middle phase)
Bicontinuous cubic phase
Lamellar phase
Bicontinuous cubic phase
Reverse hexagonal columnar phase
Inverse cubic phase (Inverse micellar phase)

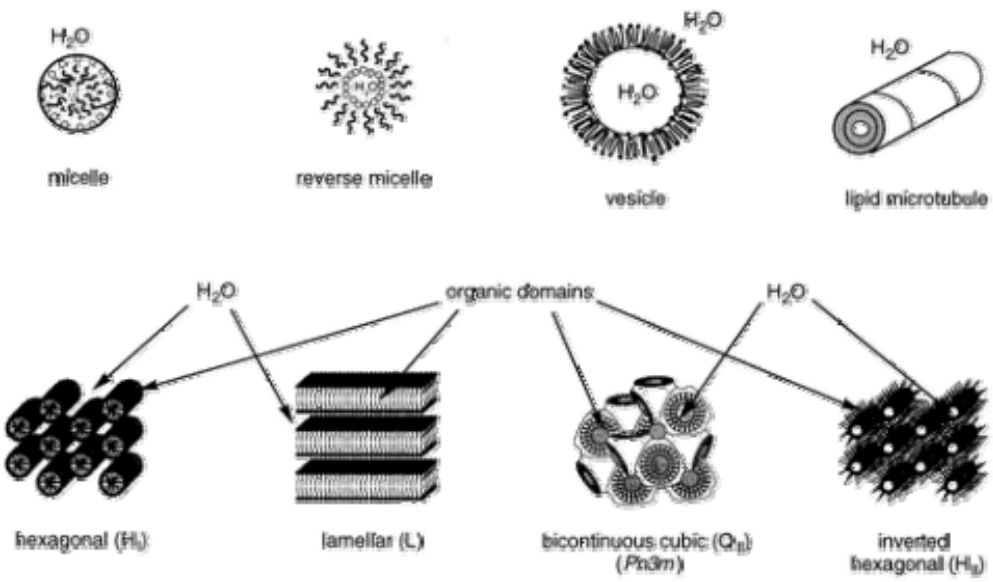

Figure 2.7 Common aggregate structures (top row) and LLC phases (bottom row) of amphiphiles in water.

Figure 2.7 illustrates the common aggregate structures and lyotropic liquid crystal phase of amphiphiles in water [16, 17]. They differ in the long-range symmetry of the surfactant aggregates and in the curvature of the micelle surface. Except for the phases with flat aggregate surfaces, each class can occur with either the polar regions or the nonpolar regions as the continuous medium, the former being referred to as *normal*, while the latter are *reversed*.

Even within one mesophase, the self-assembled structures are tunable by the concentration: for example, in lamellar phases, the layer distances increase with the solvent volume. It is more difficult to analyze their structures and properties than those of thermotropic liquid crystals. The analytical problems arise from low concentration of the mesogen, low contrast between mesogens and solvents and the low degree of order. On the other hand, lyotropic liquid crystals have immediate relevance in biology because of the prevalence of organized lipid structures in living systems. In addition, they also have many virtues that make them ideal for constructing of nano-structured functional materials [18,].

Characterization of liquid crystal phases

Liquid crystal phases are usually characterized by using a combination of three techniques: optical polarization microscopy (OPM), differential scanning calorimetry (DSC) and X-ray diffraction. DSC can be used to determine transition temperatures, therefore to distinguish phases. But one cannot identify the phases itself by this method. Polarizing microscope is the most widely used method in identifying different phases. One can look at a thin layer of liquid crystal substances placed in between two glass cover plates. Depending on the boundary condition and the type of phase, different kinds of optical patterns called textures are observed. Usually the textures change while going from one phase to the other. Polarizing microscopy is a powerful tool when used in combination with miscibility of binary mixtures, which are possible to distinguish the type of mesophase according to the reference mesogens with known type of mesophase in the case that two mesogens are miscible. More precise techniques in identifying phase and arrangements of molecules are X-ray and neutron scattering technique, since liquid crystal phases are periodic on the scale of angstroms. These

techniques provide direct information of positional and orientational characteristics of liquid crystals, especially if performed on a macroscopically aligned sample.

Optical polarization microscopy (OPM)

Optical polarization microscope is the most frequent applied method in the field of liquid crystal science since it unambiguously allows proving the presence of a mesomorphic state, to measure the transition temperatures with high accuracy and to get first hints on the kind of the mesophase. In some, but with supramolecular columnar phases not too frequent cases, it is possible to determine the mesophase type from optical textures.

The origin of optical patterns is the birefringence phenomenon. Anisotropic (liquid) crystals have crystallographically distinct axes and interact with light in a manner that is dependent upon the orientation of the crystalline lattice with respect to the incident light. When light enters a crystal parallel to its optical axis of anisotropic (liquid) crystals, it acts in a manner similar to interaction with isotropic crystals and passes through at a single velocity. However, when light enters a non-equivalent axis, it is refracted into two polarized rays with their polarization directions oriented perpendicular to each another, and travelling at different velocities. This phenomenon is termed *double* or *birefraction* and is seen to a greater or lesser degree in all anisotropic crystals [19]. One of the beams that travel with the same velocity in every direction through the crystal is termed the ″ordinary beam″. The second beam travels with a velocity that is dependent on the propagation direction within the (liquid) crystal. This light beam is termed the ″extraordinary beam″. The retardation between the ordinary and extraordinary beam increases with increasing (liquid) crystal thickness. The two independent refractive indices of anisotropic (liquid) crystals are quantified in terms of their birefringence, a measure of the difference in refractive index, as illustrated in Figure 2.8. Thus, the *birefringence* (**B**) of a (liquid) crystal is defined as:

$$\mathbf{B} = \left| \mathbf{n}_{\text{high}} - \mathbf{n}_{\text{low}} \right| \qquad \textbf{e.q. 2.1}$$

where $\mathbf{n}_{\text{high}}$ is the largest refractive index and $\mathbf{n}_{\text{low}}$ is the smallest. This expression holds true for any part or fragment of an anisotropic (liquid) crystal with the exception of light waves propagated along the optical axis of the crystals.

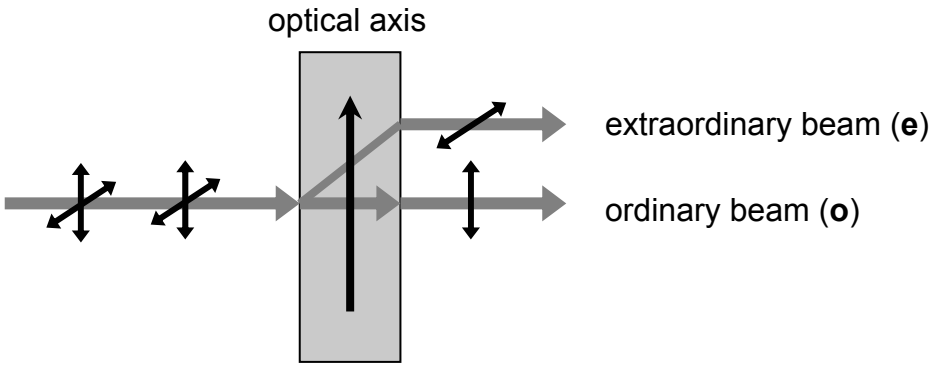

Figure 2.8 Illustration of birefringence: ordinary and extraordinary beams are orthogonally polarized.

If light enters a birefringent material, it splits into two separate fractions, one vibrating parallel to the projection of the crystallographic axes to the samples plane and the second oscillating perpendicular to this direction. The two waves are polarized perpendicular to each other and travel through the substance with different speeds, according to individual refractive indices. When the light leaves the birefringent layer the two waves own a path difference Γ (Retardation) depending on the passed layer thickness d, and the difference in refractive index Δn:

$$\Gamma = \mathrm{d} \cdot \Delta n \qquad \textbf{e.q. 2.2}$$

A schematic illustration of microscopic configuration for crossed polarized illumination [20] is presented in Figure 2.9(a) and Figure 2.9(b) shows the image of one of polarizing microscope. A polarizer place beneath the substage condenser is oriented plane. Polarized light enters the anisotropic crystal where it is refracted and divided into two separate components vibrating parallel to the crystallographic axes and perpendicular to each other. The polarized light waves then pass through the specimen and objective before reaching a second polarizer (usually termed as 'analyzer') that is oriented to pass a polarized vibration direction perpendicular to that of the substage polarizer. Therefore, the analyzer passes only those components of the light waves that are parallel to the polarization direction of the analyzer. When the ordinary and extraordinary rays emerge from the birefringent crystal, they are still vibrating at right angles with respect to each other. However, the component vectors of these waves that pass through the analyzer are vibrating in the same plane. Because one wave is retarded with respect to the other, interference (either constructive or destructive) occurs between the waves as they pass through the analyzer. Since the polarization directions

of polarizer and analyser are oriented perpendicular to each other, the relative amount of transmitted light is obtained from Eq. 2.3:

$$I / I_0 = \tfrac{1}{2} \operatorname{Sin}^2(2\varphi) \operatorname{Sin}^2(\pi\Gamma / \lambda) \qquad \textbf{e.q. 2.3}$$

I = transmitted intensity, I_0 = initial intensity, φ = angle between polarization direction of the polarizer and the in-plane projection of the materials optical axis, λ = wavelength of applied light.

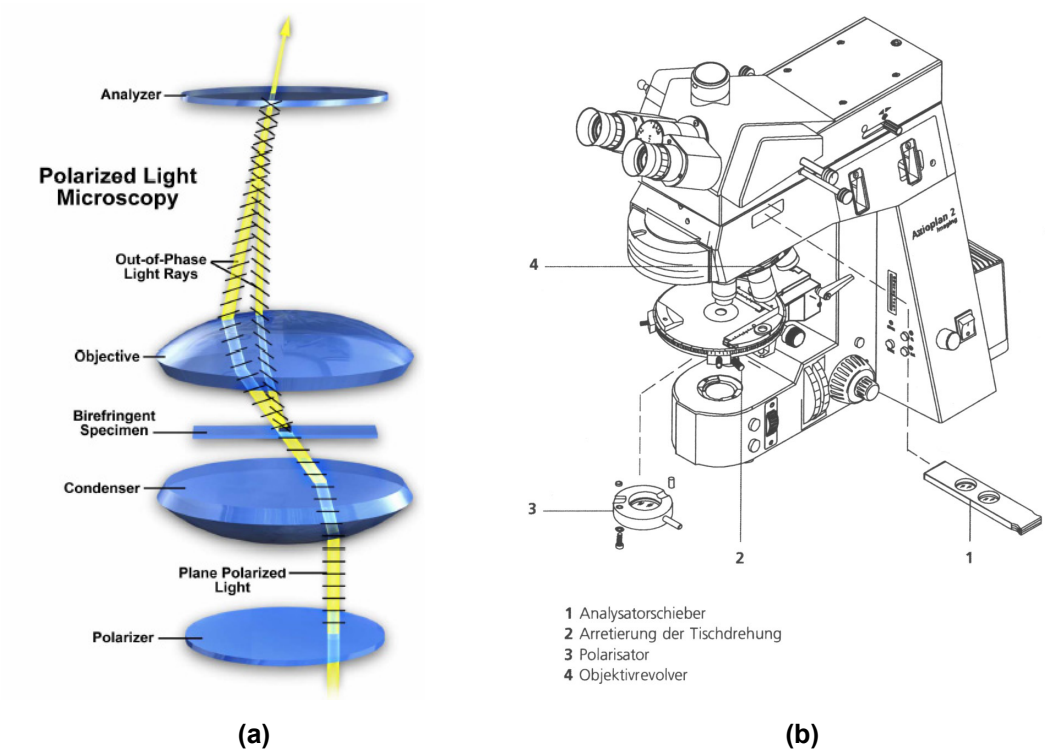

Figure 2.9 (a) Schematic microscope configuration for observing birefringent specimens under crossed polarized illumination [20]. White light passing through the polarizer is plane polarized and concentrated onto the birefringent specimen by the condenser. Light rays emerging from the specimen interfere when they are recombined in the analyzer, subtracting some of the wavelengths of white light, thus producing a myriad of tones and colours; (b) Image of the polarization microscope.

If the director of a sample with homogeneous orientation is oriented perpendicular to the plane of the sample or its projection to this plane is parallel to analyser or polarizer (φ = 0 or 90°), the sample will appear completely dark. Darkness is also experienced if the path difference Γ is a discrete multiple of the lights wavelength. Since the sample is usually illuminated with white light, there is always at least one wavelength that

becomes extinguished and the remaining light is intensively coloured. The net result is that some birefringent samples (normally observation is with white light) acquire a spectrum of colour when observed through crossed polarizers.

All (liquid) crystals – except from cubic structures – show birefringence. Though the layer thickness of microscopy specimen is much to small to cause doubling of pictures, birefringence is recognized by the occurrence of colourful interference phenomenon. Analogous to the crystallization, in the phase transition from isotropic to mesophase, the growth of the mesophase starts from nuclei, and results in many structural defects. Consequently, the director has different orientations in (nearly) every point of the sample, giving raise to multi-coloured complicated patterns, which is called ″texture″.

Textures can be a valuable tool to mesophase identification since a given mesophase can exhibit only certain fixed textures. Some samples of typical textures are depicted in Figure 2.10 to 2.15. Schlieren textures are often observed for nematic liquid crystals (Figure 2.10). Figure 2.11 shows the so-called oily-streaks texture, which is the most commonly observed appearance of cholesteric phases, obtained for planar boundary conditions.

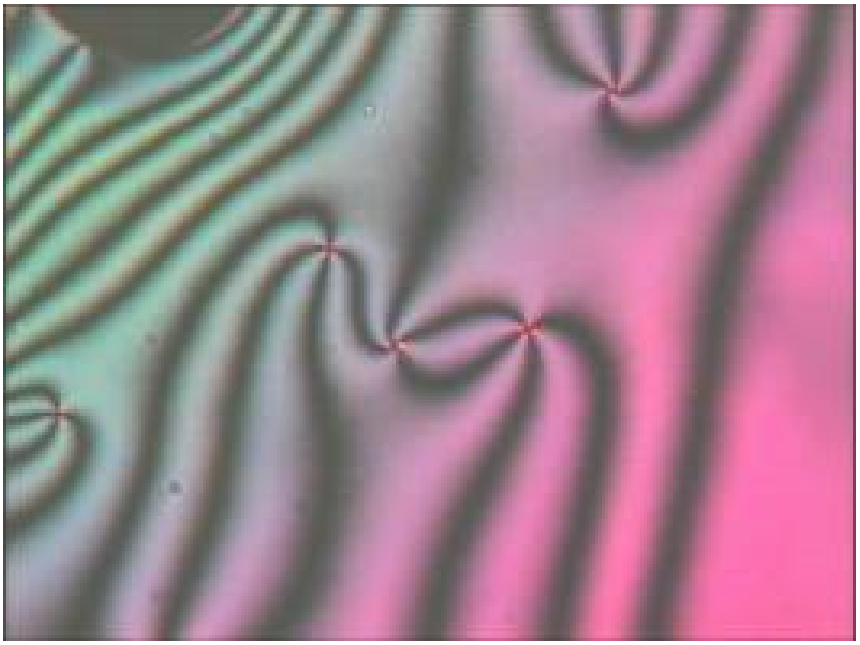

Figure 2.10 Polarized micrograph of a Schlieren texture of a nematic mesophase.

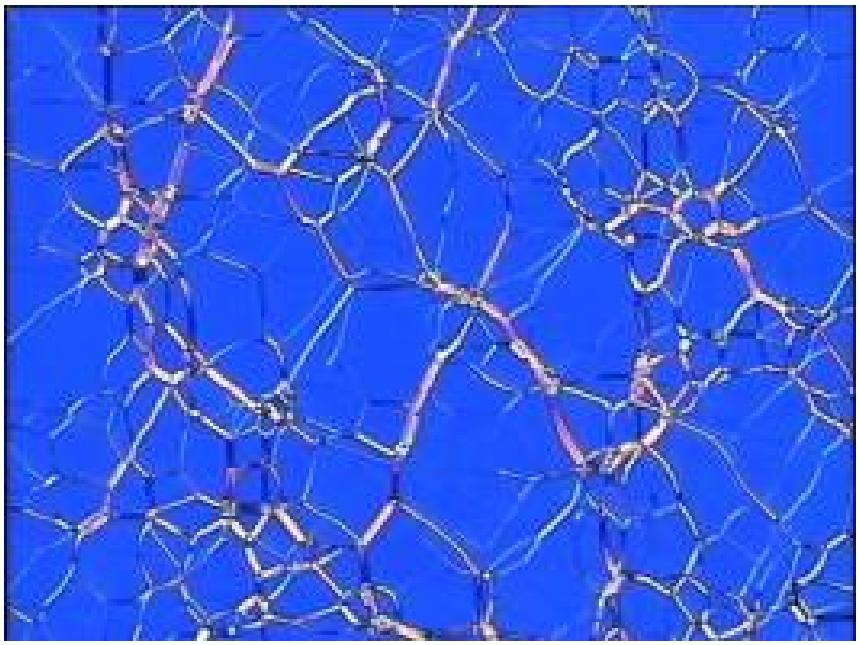

Figure 2.11 Polarized micrograph of a oil-streaks texture of a cholesteric mesophase.

One of the most commonly observed appearances of the least ordered of the fluid smectic phases is the fan-shaped texture, as shown in Figure 2.12. Another most often observed texture is the focal-conic texture, which is found for relatively thin sample preparations. The smectic layers are arranged in so-called Dupin cyclides, which contain a pair of focal conics (Figure 2.13).

Figure 2.12 Polarized micrograph of a fan-shaped texture of a smectic mesophase.

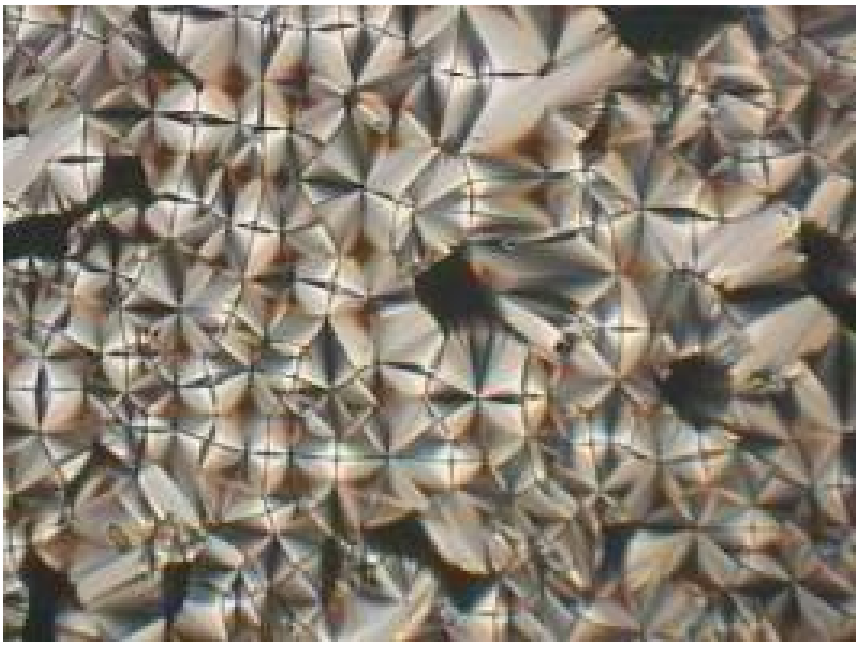

Figure 2.13 Polarized micrograph of a fan-shaped texture of a smectic mesophase.

In columnar mesophases, the most common texture is the fan-shaped texture as well (Figure 2.14). The spherulitic texture is also observed sometimes in columnar mesophases (Figure 2.15). The relation between microscopic structural defects, the apparent topology of the director, and the macroscopically observable textures has been tabled by Demus [21] for calamitic mesophase, by Chandrasekhar [22] and Destrade [23] for discotic phases.

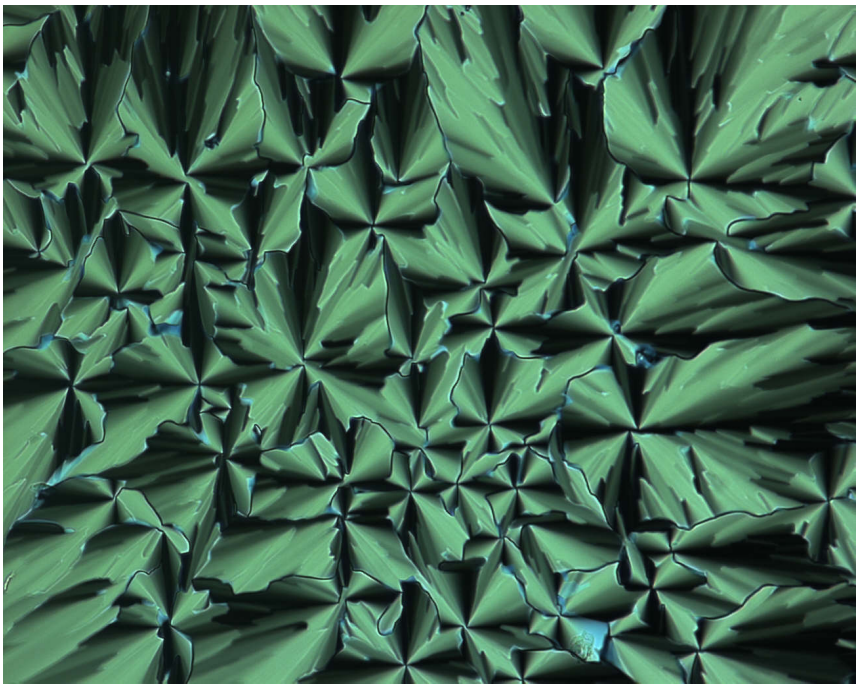

Figure 2.14 Polarized micrograph of a fan-shaped texture of a hexagonal columnar mesophase.

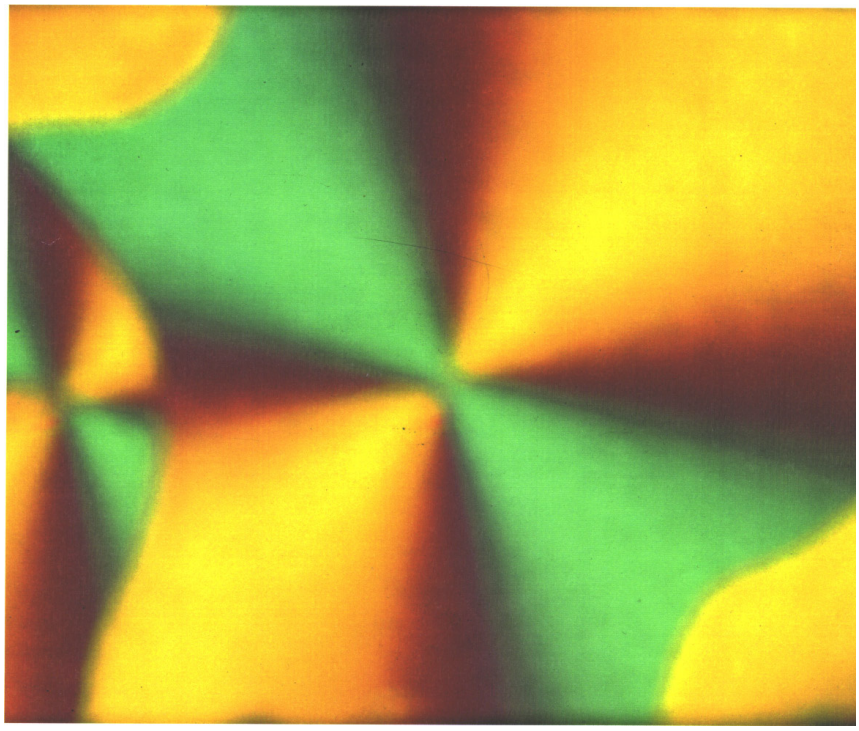

Figure 2.15 Polarized micrograph of a spherulitic texture of a hexagonal columnar mesophase.

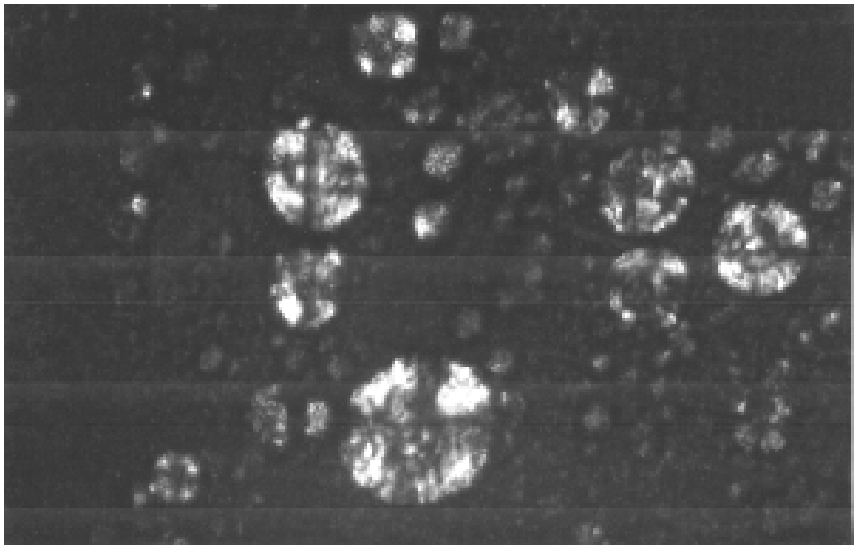

Figure 2.16 Polarized micrograph of the Maltese crosses for a lamellar phase.

As with thermotropic mesophases, the most important technique to identify the lyotropic mesophase type is polarizing microscopy as well. The birefringent phases usually have typical textures, while cubic phases have none, but they are very viscous[].

By far the most common surfactant mesophase is the lamellar phase (L_α), also known as the neat phase from its occurrence during soap manufacture. In this phase, the amphiphile molecules are arranged in bilayers frequently extending over large

distances, which are separated by water layers. Usually the lamellar phase is readily identified from its characteristic optical textures. Typical optical textures of a lamellar phase are mosaic oily streaks and Maltese crosses (Figure 2.16).

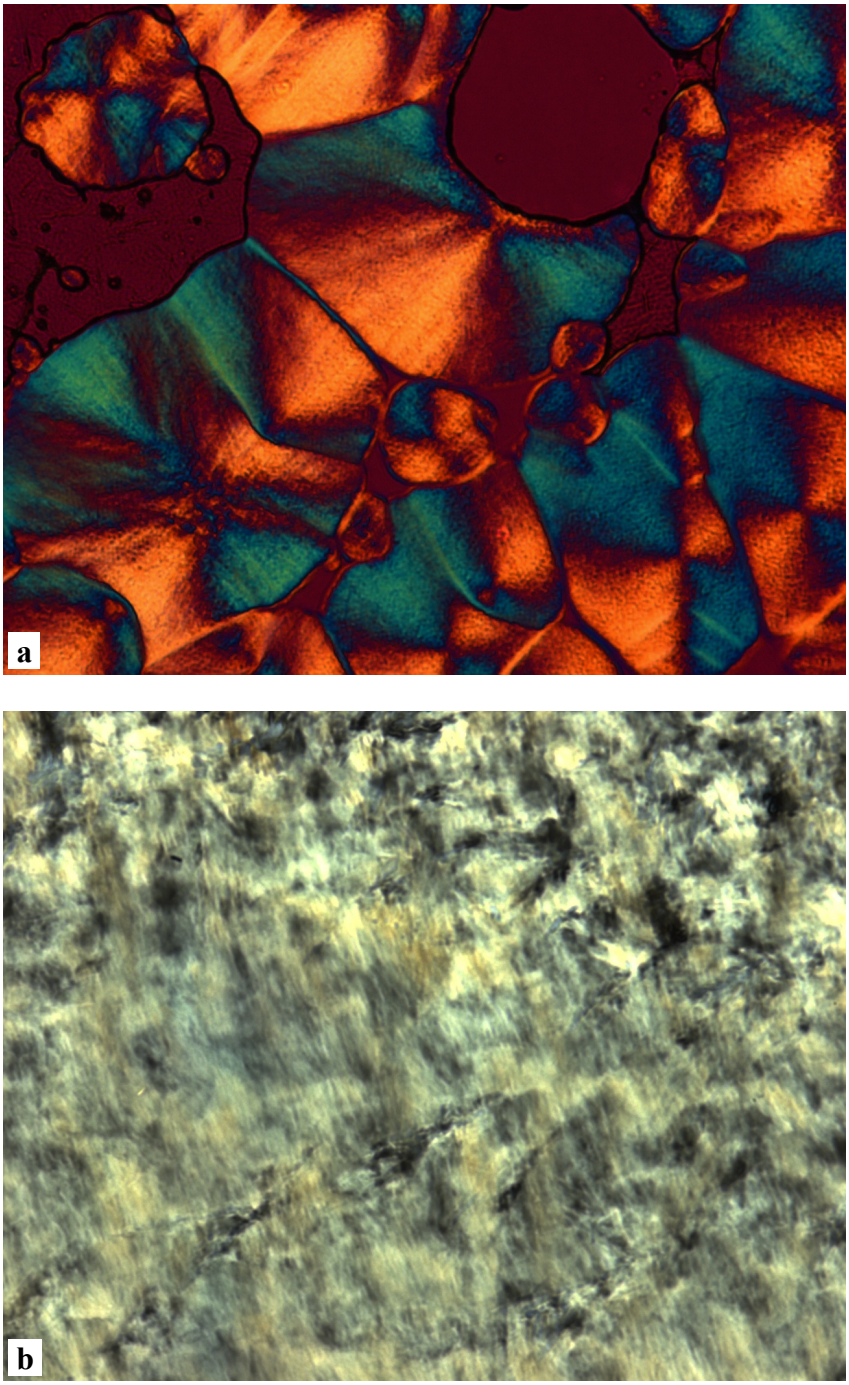

Figure 2.17 Polarized micrograph (a) of a fan-shaped texture of a lyotropic hexagonal phase; (b) of a non-geometric of a lyotropic hexagonal phase.

The next most common lyotropic mesophase type is the hexagonal phase. Both ″normal hexagonal″ and ″reversed hexagonal″ phases are rather viscous, much more than the

lamellar phase. The optical textures (fan-shaped and non-geometric) are similar for both types and shown in Figure 2.17.

Differential scanning calorimetry (DSC)

The principle of DSC is to simultaneously heat or cool the sample, and a reference compound that does not show any phase transition in the temperature range of interest, in two well-isolated compartments at constant rate. The temperature of the samples is compared. Whenever a phase transition in the sample occurs, its temperature will deviate from that of the reference due to the release or gain of transition enthalpy. This temperature difference becomes compensated by heating of the more cold oven, and the required electrical power is a measure of the enthalpy changes with temperature, dH / dT. The primary output of DSC scan is a plot of dH / dT versus the sample temperature T, characterized by peaks at the occurrence of first-order transitions, and distinct steps at glass transitions.

The main advantage of DSC is to obtain simultaneously the transition temperatures and the transition enthalpies of mesogens, allowing an improved judgement of the thermal stability of the phase under observation. The highly precise temperature ramps offer the opportunity to investigate the kinetics of the phase transition depending on the rate of heating / cooling. Additionally DSC is applied to build detailed phase diagrams of mesogenic mixture.

Miscibility studies

The basis of miscibility studies is the Arnold-Sackmann rule [24]:

> *All liquid crystalline phases of compounds that are connected via a continuous region of miscibility in a binary phase diagram can be labelled with a common structure symbol without contradiction. Free of contradiction means that phases that are connected by such a miscibility relation do not form continuous miscibility with phases of a different structure type* [24a].

If two mesogens are not miscible, no statement on the phase type can be given since naturally two compounds can be immiscible, though they possess identical phase types. On the other hand, a complete miscibility series between a mesogen of known phase type, and an unknown mesophase allows determination of the phase type.

The usual procedure is as followed. The two compounds are brought in contact under an optical microscope, heated above their melting temperature, and allowed to inter-diffuse. It is highly recommended not to work with strongly curved contact lines, and to avoid any flow of the compounds during this annealing step. Otherwise artefacts, e.g. apparent doubling of the phase diagram, enclosed isles, or partial coverage of a mixed region may occur. In the generated contact zone, all possible concentration ratios are spatially arranged, and at constant temperature one obtains the isothermal cross-section of the binary phase diagram. On heating / cooling all thermal transitions in the phase diagram are recognized, and it is possible to determine the respective transition temperatures. Though it is impossible to relate transition temperatures and mixture compositions, the type of phase diagram becomes visible. In particular the miscibility question can be decided.

X-ray diffraction

Like DSC, X-ray diffraction technique is wide spread and of common knowledge. The large variety of available experimental techniques, and methods are intensively referenced [25, 26] and need not be discussed here. For liquid crystal investigation, the experimental set-up must allow control of the sample temperature with some accuracy (at least ± 0.5 °C) roughly between ambient temperature and 300 °C.

X-ray diffraction experiments directly demonstrate the combination of liquid and crystalline properties of a mesophase. The diffractograms exhibit sharp reflections at smaller scattering angles ($2\Theta \approx 10 - 20°$) proving the existence of spatial wide range order. One- and two dimensionally ordered phases, e.g. N, S_A, S_C, C_N, C_{hd}, or C_{rd}, possess a distinct halo at larger scattering angles ($2\Theta > 20°$), caused by the fluid like properties of the molten alkyl chains of the mesogens.

If a sufficient number of reflections is available, the phase type can be determined unambiguously. From the reflection positions the lattice constants of two- or three-dimensional columnar phases can be calculated. The two-dimensional quadratic forms stated in Equation 2.4 (D_{hd}) and 2.5 (D_{rd}) are used to index the measured reflections of disordered columnar phases.

$$d_{hk} = \frac{a}{\sqrt{\frac{4}{3}(h^2 + h \cdot k + k^2)}} \qquad \textbf{e.q. 2.4}$$

$$d_{hk} = \frac{a}{\sqrt{h^2 + k^2 \cdot (a/b)^2}} \qquad \textbf{e.q. 2.5}$$

d_{hk} is scattering length, is defined as $\lambda_{X\text{-ray}}$ / [2·Sin(2Θ)], a, b are lattice constants and h, k are Miller indices of reflecting lattice planes.

In combination with density measurements of the mesophase, the number of mesogens per average unit can be obtained (Eq. 2.6 (C_h), Eq. 2.7 (C_r)).

$$N = \frac{3\sqrt{3} \cdot N_A \cdot \rho \cdot a^2 \cdot < h >}{2M} \qquad \textbf{e.q. 2.6}$$

$$N = \frac{N_A \cdot \rho \cdot a \cdot b \cdot < h >}{M} \qquad \textbf{e.q. 2.7}$$

N is number of mesogens per average elementary cell, N_A is Avogadros constant, ρ is density of the mesophase, a, b are lattice constants, $<h>$ is average height of the two-dimensional elementary cell and M is molecular weight of the mesogen.

2.2. Supramolecular Organogels

Introduction of the Gel State

Everyone knows what a gel is, but from a scientific point of view, the term "gel" encompasses chemically very diverse systems. Already in 1926, Jordon Lloyd wrote, "A gel is easier to recognize then to define," [27] however, an exact definition of a gel is still a problem. Perhaps the most general definition is given by Flory, who described gels as dilute mixtures of at least two components, in which both components form a separate continuous phase throughout the system [28]. This definition includes not only gels composed of a solid phase and a gas phase (so-called aerogels, in which the solid phase often consists of silicates) [29] but also gels consisting of a solid-like phase and a fluid phase. In most gels, the solid-like phase is the minor component that forms a network structure in the fluid phase. Because of the coexistence of a network structure with a liquid phase, a gel behaves like an elastic solid at low stress values, but above a finite yield stress, they turn into a viscous liquid. This was described by Tanaka as follows: "the solid network structure prevents the fluid from flowing, whereas the fluid prevents the solid from collapsing." [30].

According to the rheological properties, gels can be classified into transient and persistent gels. Transient gels do not exhibit yield stress, i.e. transient gels become irreversibly deformed on every value of applied stresses. To discriminate a transient gel from a viscous fluid one has to consider the frequency dependence of the viscoelastic flow. If the stress is applied at high frequencies the gels acts like an elastic body, while at low frequencies viscous flow is observed. It goes without saying that this frequency dependence can make the distinction between a viscous liquid and a transient gel rather difficult.

Typical transient gels arise from solutions of entangled macromolecules. Over short periods of time the entanglements physically connect different polymer molecules. The system is solid, since the interconnected macromolecules percolate the sample. If the time the stress acts to the system exceeds a polymer specific 'disengagement time', the macromolecules disentangle and slip against one another, resulting in viscous deformation. Examples from every day's life are polymer melts and solutions. The

transient gels are also found for surfactant-based systems like hair shampoos, hair gels or cosmetic gels.

The latter examples demonstrate that the gel formation is not restricted to networks of macromolecules. The literature describes solutions of low molecular weight surfactants that self assemble into long, fluid cylindrical micelles. The micelles interact to form a network, creating so-called 'elastic liquids'[31]. Because of the rapid exchange of individual surfactant molecules between the associated and the dissolved state, the cylinder micelles represent highly dynamic structures. Consequently the stress resistance of this solution is low, and it may not be simple to recognize them as 'gels'.

In contrast to transient gels, the persistent – or permanent – gels need a minimum stress to show flow or creep behavior. A simple, but sometimes time-consuming experiment to distinguish transient and persistent gels is to disperse little air bubbles into the gel samples. In a transient gel the bubbles will raise and finally leave the gel, though this process can last for years. In a permanent gel the bubbles will remain trapped forever, since below the yield stress a permanent gel is an elastic solid. Note that many persistent gels posses large yield stresses, where 'flow' requires the irreversible damage of the materials structure.

Classical permanent gels consist of solvent swollen, chemically cross-linked macro-molecules. The solidification of monomer solutions on cross-linking polymerisation has been so common to polymer chemists, that the terms 'gelation' and 'cross-linking' are still used as synonyms.

Chemical gelation through covalent cross-linking of dilute solutions of polymers or inorganic oxides is thermally irreversible[29]. Chemical gels can, nevertheless, have many interesting properties and applications. Smart gels, for example, are hydrogels from cross-linked polymers that can reversibly swell and shrink in response to a physical or chemical stimulus (Figure 2.18a), and are of great interest for novel drug delivery systems or artificial muscles[30]. Opposite to the chemical gels are the physical gels[32]. In physical gels, the network structure is built up from smaller subunits, which are held together by non-covalent interactions. Many gels, which are formed by polymers, proteins, surfactants, small organic molecules, and even mineral clays, belong to this class. Despite the different natures of their constituents, they mostly

exhibit a characteristic thermally reversible gel–sol phase transition at moderate temperatures, because the strengths of the non-covalent interactions are comparable to the thermal energy (Figure 2.18b).

The connection between the macromolecules can be made up from all kinds of physical interactions, like van-der-Waals forces, hydrogen bonds, ionic interactions, or donor – acceptor complexes [33, 34].

Gel systems forms by, for instance, dilute solutions of polymers, proteins and inorganic substances like silica or clays in water and organic solvents have been well studied and are widely used in, for example, photographic, cosmetics, food and petroleum industries [35]. A prominent example of a reversible gel is the gelatine gels. Gelatine is a mixture of proteins, obtained by hydrolytical extraction of collagen from the white connective tissue and bones of animals [36]. The protein molecules possess structures that allow for the complexation together with two other chains to form a triple helix. The thermoreversible gelation of aqueous gelatine solutions is well known and has intensively been used for the preparation of gelled foods, from puddings, aspic to cream cakes. Since the formation of the triple helix linkages is a time consuming step, the most stable puddings are formed by slow cooling of the gelatine solutions [33].

Stereo regular macromolecules like it-PMMA or it-PS have also been described to form persistent physical gels by building small crystallites that join together different polymer chains. Physically linked persistent gels can be obtained by microdomain formation, i.e. by a microscopically heterogeneous distribution of the macromolecular units over the gel. Examples comprise the poly(ethylene) gels, where the macromolecules form networks consisting of long fibrils of 10 – 100 nm diameter. This type of gel has been utilized for the preparation of high modulus fibers, e.g. for ropes, fishery networks and protective fabrics [33].

Also, certain types of low-molecular-weight organic molecules ($M_w \approx$ 300–1000) are capable of forming physical gels [37]. Gelation of a solvent by low-molecular-weight organic molecules is the result of self-assembly of the compound into elongated fibers, which then form an entangled network within the solvent (Figure 2.18b). In these networks, the fibers consist of almost infinite arrays of small molecules that are solely held together by non-covalent interactions. The focus of this thesis will be on gelation

phenomena by low-molecular-weight organic molecules, because this is a striking macroscopic manifestation of self-assembly and supramolecular structure formation.

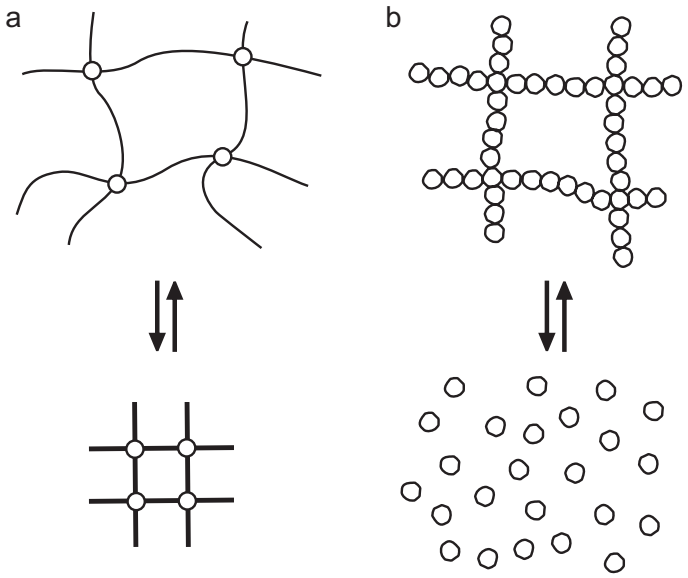

Figure 2.18 (a) A change of the environment can cause the reversible shrinking or swelling of a chemical gel, but the network structure remains intact; (b) a physical gel can undergo a reversible gel–sol phase transition [37].

Supramolecular Organogels

Supramolecular organogels are persistent gels arising from relatively low molecular weight organic molecules (namely, gelators). They can be defined as thermally reversible viscoelastic liquid like or solid like materials comprised of an organic liquid and low concentration (typically < 5wt%) of gelators [38]. Due to their applications in templated materials synthesis [39], drug delivery [40], separations [41] and biomimetic [42], organogels have been the topic of several extensive reviews [43; 44, 45]. In recent years there has been a rapidly growing interest in low molecular weight gelling agents, which is motivated not only by the manifold potential applications of gels, but also by the fact that these systems exhibit striking properties with respect to self-assembly phenomena [38].

The self-assembly of gelators of fiber-like structures, which entangle to form a three-dimensional (3D) network, is solely driven by physical interactions, including hydrogen bonding, π-π stacking and hydrophobic (solvophobic) effects. The nature of

interaction responsible for self-assembly can be used to classify the structurally diverse organogelators. The majority of gelators are covered by classification into hydrogen-bond-based gelators and non-hydrogen-bond-based gelators. Typical examples of the former group are aliphatic amide derivatives and of the latter group, cholesterol derivatives. In particular, modified cholesterol-based gelators have been widely used: crown-ether [46, 47] and amino [48] cholesterol derivatives have been developed for further research on the gelation phenomenon. Gelators with large conjugated systems, such as anthraquinones [49] or porphyrins [50] aggregate through π-π stacking. Gelation can also be driven by the coordination of metal-containing gelators [51]. The self-assembly of the hydrogen-bond-based gelators is based on the formation of highly directional hydrogen bonds and is, therefore best understood. Gelators that assemble by means of hydrogen bonds usually possess hydroxyl groups, amide groups [52] or urea groups [53] and they are also often based on amino acids or sugars [54]. Some of the examples are presented in Figure 2.19.

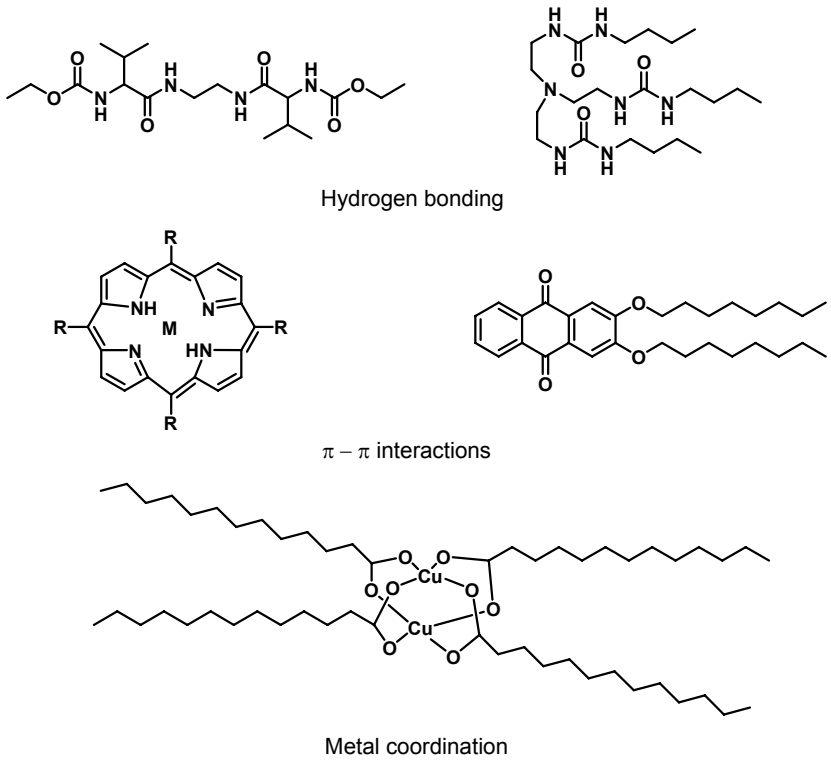

Figure 2.19 Examples of some organogelators [51, 55].

Actually, many gelations occur by means of the combination of more than two interactions. The large number of different organogelators is expanded with new

discoveries regularly, often by chance, but recently there is a tendency to actively design new organogelators [50, 56, 57]. Since Gelation is a process that occurs at the borderline of solubility, a moderate solubility could be regarded as a requirement. A poorly soluble compound, that also has difficulty with crystallization, will have a tendency to form a gel. This is the reason why most organogels are formed upon heating and subsequently cooling of a solution of organogelators in an appropriate solvent. Only a small amount of gelator is necessary to form a network and to gel a large amount of solvent: concentration of about 1wt% of organogelators are usually sufficient. Besides the variation in which organogelators aggregate inside the fibers, there is also variation in the interaction between the fibers in the 3D network [58]. Figure 2.20 shows examples of loose, transient interactions and crystalline micro-domains at the positions where the fibers meet. The structure of the network has influence on the macroscopic properties of organogels, such as viscosity.

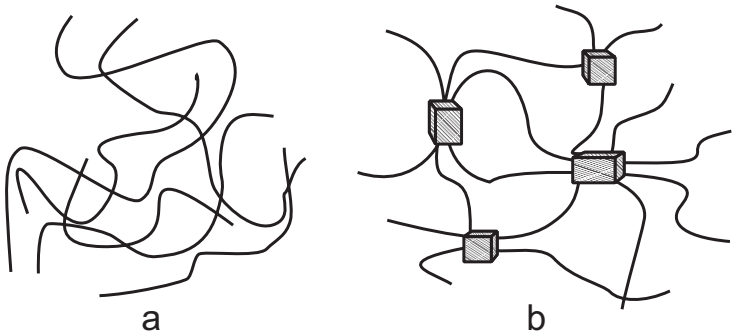

Figure 2.20 Schematic representation of possible organogel networks: transient interactions (a) and microcrystalline knots (b) at positions where the fibers meet.

An organogel is usually prepared by warming a gelator in an organic liquid until the solid dissolves and then cooling the solution (or solvent) to below the gelation transition temperature (i.e., the temperature below which flow no longer is discernible over long periods). The formal description and classification is based upon rheological properties.

The gel is usually characterized by several methods. An efficient methodology to elucidate the nature of an organogel is to begin with a thermal characterization, which determines the solution-to-gel phase transition temperature. As the gel formation corresponds to formation of micro-domains' segregation and ordering, a phase diagram can be constructed by differential scanning calorimetry (DSC) and optical polarizing

microscopy. Electron microscopy techniques (scanning electron microscopy (SEM) and transmission electron microscopy (TEM) are frequently used to give information of the morphologies of the gel (for example, fibrous or spherical)[59]. Electron transmission micrographs are informative and provide structural information in direct ways. In the case of SEM, the freeze-dried gel (xerogel) is in general observed, rather than the 'wet' gel. Other characterization methods, such as NMR, IR, UV, circular dichroism (CD) spectroscopy, as well as rheological studies are often used to study gel systems.

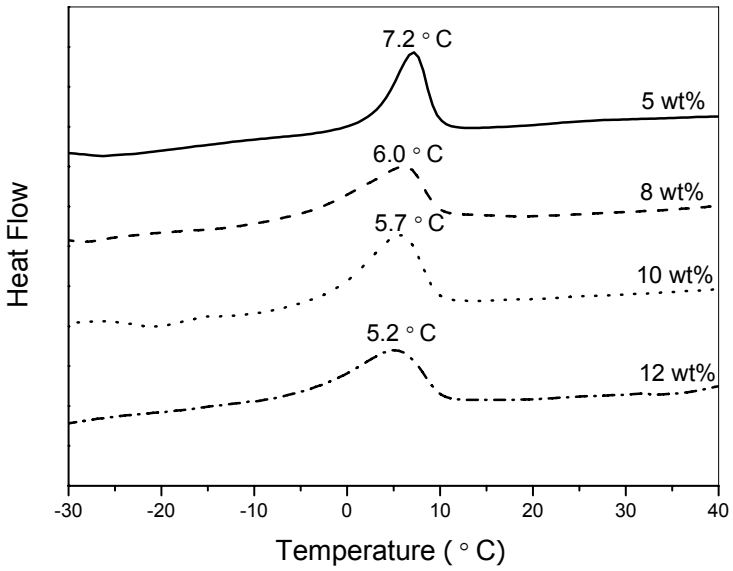

Figure 2.21 DSC thermograms of the gels from sodium 2,3,4-tris(dodecyloxy)benzene sulfonate in EHMA (2-ethylhexyl methacrylate).

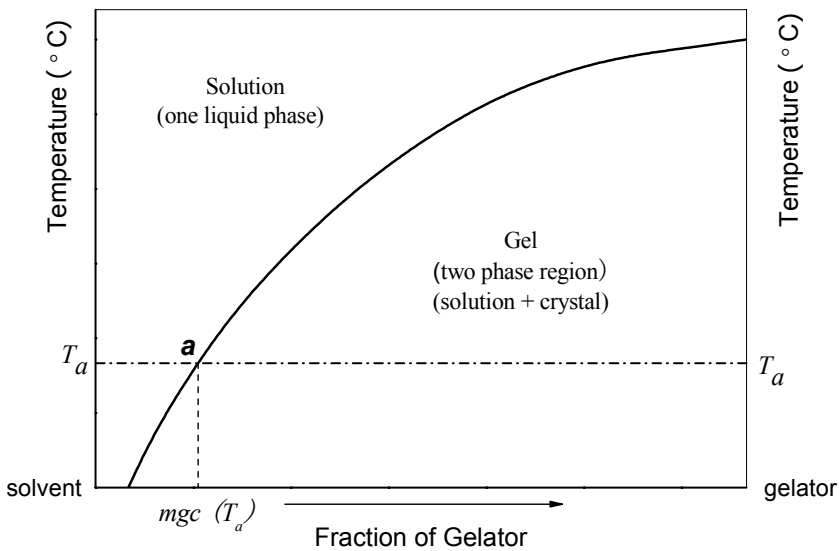

Figure 2.22 A schematic phase diagram of gels formed from crystalline microdomains.

Figure 2.21 shows an example of organogel that was characterized by DSC. The endothermic peak temperatures were recorded as the gel melting temperatures. According to those gel melting temperatures together with corresponding composition of gelator and solvent, a binary phase diagram can be plotted. Figure 2.22 depicts a schematic phase diagram, where the gel melting temperatures increase with increasing concentration of the gelator. At a certain temperature (T_a), the state point ***a*** on the phase transition line yields the minimum gelation concentration (*mgc*) at the respective temperature. At this concentration the microdomains loose connectivity and the gel falls apart.

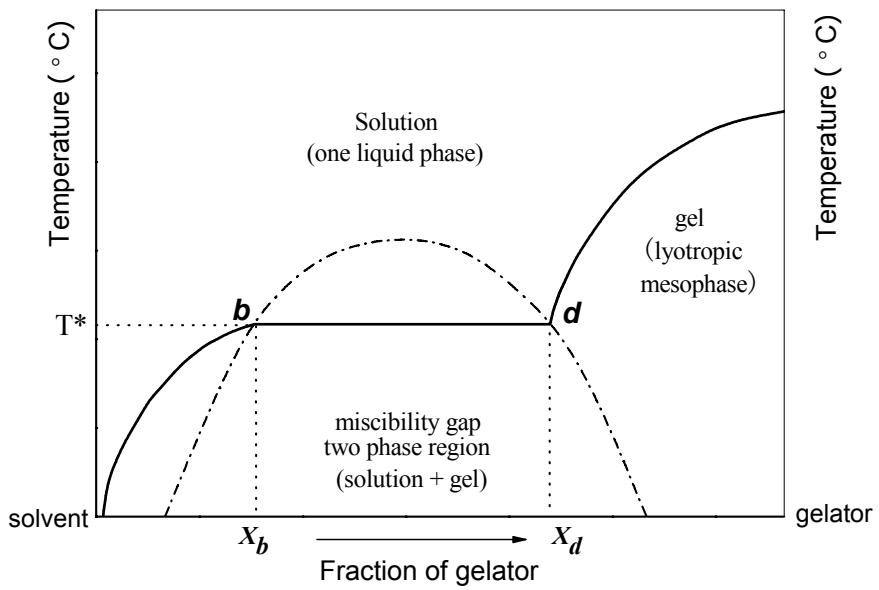

Figure 2.23 A phase diagram of gels with miscibility gap.

Sometimes, the gel melting temperatures remain constant over a certain range of gel composition. This indicates the presence of a miscibility gap in the gel system. A schematic phase diagram with miscibility gap is shown in Figure 2.23. At the certain temperature (T^*), a mixture of gelator and solvent, which lays between the fraction X_b and X_d will be separated into two phases of composition ***b*** and ***d***. Actually, the same two phase (***b*** and ***d***) would exist for any mixture at T^* in the two-phase region (between X_b and X_d). Hence, the gel melting temperatures of all the gels with a composition between X_b and X_d must remain constant, because the composition of the gel phase d is not altered. Only the amount of the gel phase *d* will change on variation of the gelator concentration. In such cases dynamic measurement methods like DSC may produce a

virtual concentration dependency of the gel melting temperature, since a smaller quantity of gel phase will melt rapidly than a large one. Furthermore the mechanical properties of the gel will vary also in the miscibility gap region.

Recent applications for new functional materials

Within a very short period organogels have developed from a chemical and physical curiosity to a highly promising new area of research. Their well-defined structure, the coexistence of highly ordered fibers with a liquid phase, the large interfacial area, and the possibility to entrap solutes within the network pores make organogels very attractive materials for membrane, separation technology, catalysis, or drug delivery.

Table 2.1 lists some properties of organogels that have potential to be exploited for industrial applications. The preparation of reversible (= ″smart″) thickeners has been applied. One nice application is thickeners for wall paints, preventing the inconvenient formation of drops during the painting and subsequent to the spreading process [60]. The advantage of organogels is that they can be ″self-repairing″. In the case macromolecules are broken by strong shear forces the thickening properties will deteriorate, while shear-broken supramolecular fibers in organogels reassemble.

Table 2.1 Potential applications of supramolecular organogels and possible future directions.

Property	**Application**	**Examples**	
		Industry	Academia
Thermoreversibility *Thixotropy /* *Shear thinning*	‘smart’ thickeners	Lubricants, Greases, Napalm, Inks, Wall Paints	Solid Electrolytes [61], Solar Cells
Structural definition *Functionality*	Supramolecular Chemistry, Adaptive Materials, Switchable Materials	----	Templates, Tectons, New Polymers, Functional Membranes

The ordered arrangement of organogelators has also been exploited as a framework for the spatial organization of covalently attached functional groups, for example the conjugated moieties. It has been shown that this strategy can be very successful for improving collective properties like electron conductivity [62]. Another attractive feature of supramolecular gels is the development of 'smart' or 'responsive' gel systems [63]. Tanaka 's group developed a novel gel system, which can bind guest molecules by multiple-point noncovalent interactions [64].

Obviously such filaments offer the opportunity for signal transmittance along the fiber axis over macroscopic distances. Suitable functional groups my guide ions, electrons or even photons. First approaches towards such supramolecular transport channels are described in the literature: Alkali metal ions can pass through stacks from crown ether moieties [65], and a ‘molecular cable’ has been designed to transport electrons with linear phthalocyanine-arrays [66]. High charge carrier mobilities were found in supra-molecular organogels from bis-urea modified dithiophene units [67]. Moreover, micrometer wide filaments of self-organised perylene based fluorescence dyes have been demonstrated to act as optical wave guides [68].

The high structural definition of elementary fibers in the gels makes them suitable as templates for the preparation of porous materials [69]. Recently helical fibers of a cholesterol-type gelator were used to form silica hollow fibers with helically shaped bores [70]. Also porous polymer films have been prepared containing uniformly shaped cylindrical voids that have been proposed for application as porous membranes [71, 72].

Although the formation of organogels from small organic molecules is an excellent example of a supramolecular self-assembly process, most organogelators have been found by serendipity rather than design, and many aspects of organogels still need to be well understood. In recent 10 years, the control of gelation and the design of new gelling agents have been challenging and a number of successes have been achieved. An exciting development is the use of organogelators as template for the preparation of nanostructured materials. First Möller [73] and later also Weiss [74] and Nolte [75] prepared membranes with nanosized pores by the gel-template-leaching process. In this process, gels of various gelling agents are prepared in polymerizable solvents like methacrylates or styrene in the presence of a cross-linking agent. After polymerization of the matrix, the organic gelling agent is removed again by extraction with a proper solvent

(Fig. 2.24). In this way, the organogel fiber network is 'imprinted' in the cross-linked polymer matrix, resulting in porous membranes with channels of nanometer dimensions. However, by this way the preservation of the original fiber morphology in the polymer network is often poor, which is most likely due to the flexible nature of the cross-linked polymer used. Shinkai 's group managed to use gels formed by chiral organogelators as a template to control the morphology of silica formed by a concurrent inorganic sol-gel process [76].

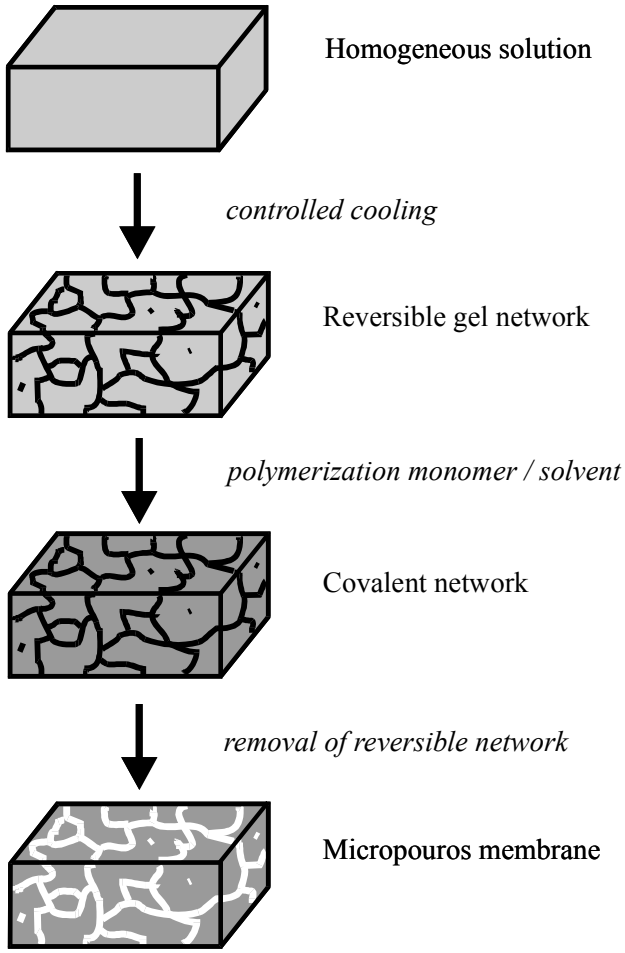

Figure 2.24 Schematic representation of the “Gel Template Leaching” approach: preparation of organic gels and microporous membranes from organogels.

2.3 Ion-Selective Membranes

An ideal membrane is a selective barrier, which separates two phases of different composition, and only allows the permeation of a particular type of species[77]. Numerous types of membranes have been developed, which can be used for the separation of both liquid and gaseous mixtures. Meanwhile, due to the high level of interest in fuel cells during the last century, there have been numerous scientists and efforts focused on the proton-conducting membranes, which is the key component of a fuel cell system. Below, both will be described in some details.

Biological ion-selective membranes

Biological cell membranes are the most functional membranes that we can find in this world. The enormous selectivity of biological cells can be seen from the examples of bacteria. Without vital need the simple cells accept only one type of carbohydrate as food, and in a mixture of more than 30 sugars they first selectively consume their favourite one. After the most liked food has been used up, the cells now selectively harvest a second type of carbohydrate, and so on. Each type of bacteria shows its own sequence of preferred carbohydrates, for which they never deviate. It is known that bacterial cell membranes at least distinguish 30 different carbohydrates. In comparison, there is no synthetic membrane available that selectively recognises even one carbohydrate.

The fluid mosaic model of the cell membrane[78] consists of a lipid bilayer containing active elements constructed from proteins. In its ordered state, this lipid bilayer represents an excellent barrier to the passage of polar molecules and therefore has the ability to partition discrete metabolic aqueous compartments. The impermeability of the lipid bilayer to polar or charged molecules allows the solute concentration on each of its sides to differ dramatically. The second function of the lipid bilayer is to accommodate proteins with various tertiary structures that are able to provide the transfer of energy and materials and also act as catalysts.

Simultaneously, the cell membrane has the ability to respond to changing external conditions that demand that certain molecules and ions pass through the lipid bilayer (Fig. 2.25). Partly this is achieved by active transport mechanisms involving

membranes proteins, i.e. proteins bound to the membrane mostly by hydrophobic interactions. Partly this is achieved by perfusion or endocytosis.

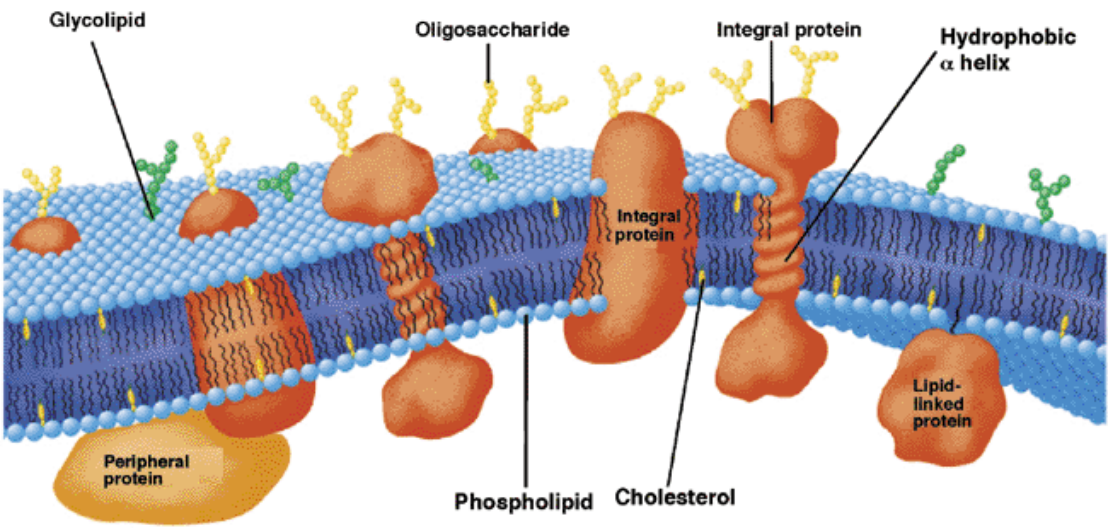

Figure 2.25 Schematic representation of the bilayer fluid mosaic model of the cell membrane. Integral proteins are embedded in the bilayer composed of phospholipids and cholesterol. Reproduced from reference 1b with permission of John Wiley & Sons, Inc. Copyright 1999, John Wiley & Sons, Inc.

Ion-selective transport takes places either by means of carrier-mediated diffusion, or by flow or site-to-site hopping through transmembrane channels [79, 80]. The difference between ion transport via channels and ion transport via carriers is described as followed: a channel provides a membrane spanning molecular structure that enables ion translocation along or through the transporter [81]; in contrast, a carrier forms a complex with the transported ion which diffuses across the membrane. The transport through channels is approximately 1000 times faster than the carrier mediated transport, but it cannot be coupled to an energy source: Channel mediated transport can never be active [82, 83]. In return, channels can reversibly be opened, and closed [84]. According to the stimuli that trigger the activity of the channel voltage-gated, mechanically-gated, ligand-gated, ion-gated, or transmitter-gated channels are distinguished.

Selective synthetic membranes mimicing biostructures

A similar synthetic supramolecular system capable to be externally regulated could have immense technological implications for areas such as selective membranes, ionic,

protonic, and electronic conductors, enzymatic-like catalysis, energy transfer and conversion, particularly if all these functions could be incorporated into the same unit.

The largest problem of membrane technology concerns the selectivity of the employed membranes. Today's technically available membranes can separate molecules according to their sizes, their polarity, electrical charges or their solubility. The separation will only work effectively if the feed objects greatly differ in these physical properties. Separation principles based on differences in the molecular geometry, polarisability or due to chemical reactivity are in its infancy. Separations of similar sized molecules with identical charges and polarity usually fail. The chemical industry e.g. even cannot separate aromatic- from aliphatic, or linear and branched hydrocarbons with membrane plants. The other main important separation problems that still cannot be solved with the present-day membranes are the production of pure oxygen from air, the removal of hydrogen sulfide from natural gas, splitting of racemates into optically pure enantiomers, or the separation of alkali metals and so on. In addition, proton conducting membranes that are impermeable to H_2O or methanol also represent great challenges to membrane science. Obviously the solution of these problems requires 'functional' membranes, which selectively recognize and transport individual ions or molecules.

Since the thickness of technical membranes (20 – 100 μm) far exceeds that of lipid-bilayer (15 nm), biological membranes cannot be simply copied. But a bioinspired synthetic system can use its principles as models to create a non-natural system that is adaptable to the current technological concepts [85]. Therefore, the lipid bilayer barrier may be replaced with an alternative barrier material that has the required combination of order and fluidity at least during certain stages of its self-assembly and self-organization. Simultaneously, the membrane proteins may be replaced with currently available ion-selective or ion-active elements such as crown ethers or polypodants that are equipped with the ability to spontaneously self-assemble into channels that are incorporated in the barrier part of the material. By analogy with a protein-based ionic channel, this material should be able to flux energy and materials among various compartments. New synthetic mechanisms to externally regulate the on and off states of the channel should be discovered and/or designed. Therefore, bioinspired design and synthesis are not always expected to duplicate concepts from Nature but also can be

used to design new concepts that may be suitable for related or different applications. Some of the research has been reviewed [86].

Ion transport takes place in living cell either by means of carrier-mediated diffusion or through channels. Different carrier-mediated ion transporting membranes have been developed and will not be discussed in this thesis. Here we focus on the ion channel transport.

Basically, two different approaches for the construction of ion-channels can be distinguished. The first possibility involves the self-assembly of low molecular weight compounds into channel-like structures. In the second approach a polymeric backbone is used to induce stacking of covalently attached receptor-moieties into a regular channel-like array. Pioneering work on low molecular weight compounds, which are able to self-organize into channel-like structures has been reported by V. Percec [86] and is schematically summarized in Figure 2.26 [85].

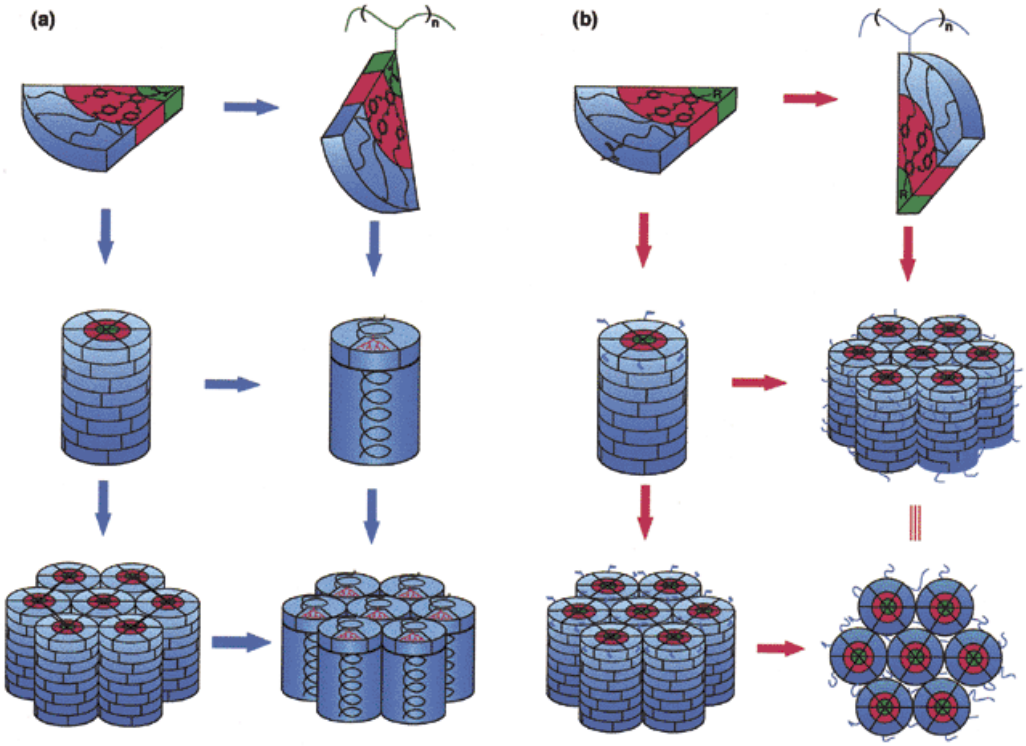

Figure 2.26 Self-assembly and self-organization followed by polymerization or polymerization followed by self-assembly and self-organization of tapered monodendrons containing a polymerizable group at the apex (a) or on the periphery of the taper (b). The R group in (b) represents the ionic, electronic, or protonic active element.

This concept is based on tapered minidendritic units containing crown ethers or oligo (ethylene oxide) units in their core (Fig. 2.26) [86]. Based on this approach our group employed self-assembling tapered molecules containing crown ethers were employed in a new concept for the design of functional nanoporous membranes known as gel template leaching [87]. The mono- [88] and multi-functionalization [89] of the periphery of these building blocks with polymerizable groups has been employed for the design of self-organized soluble and insoluble nanostructured ion-selective membranes. Self-assembling tapered groups containing active element(s) in their core and one or more polymerizable groups on their periphery (Fig. 2.26) can be developed to generate a multifunctional membrane that has many features available in the fluid mosaic model of the cell membrane.

The strategy of the preparation of functional membranes by means of supramolecular organogels has been reported as ″matrix-fixed supramolecular channels″ (MFSC) [89]. The detail has been introduced in the section of ″Organogel″ in this chapter. The other approach was applied by means of polymerizable lyotropic liquid crystal assemblies to create the nanostructural functional material [18].

Proton-conducting membranes for fuel cells

A fuel cell is an electrochemical conversion device that has a continuous supply of fuel such as hydrogen, natural gas or methanol and an oxidant such as oxygen, air or hydrogen peroxide. It can have auxiliary parts to feed the device with reactants as well as a battery to supply energy for start-up [90]. Fuel cell technology is expected to become one of the key technology of the 21st century both for stationary applications like block power stations and instationary applications like mobile electronic (laptops, cell phones), personal vehicles, trucks, buses and so on.

There are several different types of fuel cells, each using a different chemistry. Fuel cells are usually classified by the type of electrolyte they use: proton exchange membrane fuel cell (PEMFC), solid-oxide fuel cells (SOFC), molten-carbonate fuel cells (MCFC), phosphoric-acid fuel cell (PAFC) and alkaline fuel cells (AFC). Some types of fuel cells work well for use in stationary power generation plants. Others may be useful for small portable applications or for powering cars.

Alkaline fuel cells (AFC) are one of the oldest designs. They have been used in the U.S. space program since the 1960s. The AFC is very susceptible to contamination, so they require pure hydrogen and oxygen. It is also very expensive, so this type of fuel cell is unlikely to be commercialized.

Phosphoric-acid fuel cells (PAFC) are a type of fuel cell that uses a sponge soaked in phosphoric acid as an electrolyte. They are not affected by carbon monoxide impurities in the hydrogen stream. They require platinum catalysts, which drives up the price. Unfortunately, the phosphoric acid solidifies below 40 ºC, making startup very difficult. Phosphoric acid fuel cells have been used for stationary applications with an efficiency of about 40%, and many believe they do not offer much potential for further development.

Solid-oxide fuel cells (SOFC) are best suited for large-scale stationary power generators that could provide electricity for factories or towns. This type of fuel cell operates at very high temperatures (around 1000 °C). This high temperature makes reliability a problem, but it also has an advantage: The steam produced by the fuel cell can be channeled into turbines to generate more electricity. This improves the overall efficiency of the system.

Molten-carbonate fuel cells (MCFC) are also best suited for large stationary power generators. They operate at 600 °C, so they also generate steam that can be used to generate more power. They have a lower operating temperature than the SOFC, which means they don't need such exotic materials. This makes the design less expensive.

The *proton exchange membrane fuel cell* (PEMFC) is one of the most promising technologies. This is the type of fuel cell that will probably end up powering cars, buses and maybe even your house.

A single PEMFC is made of a *membrane electrode assembly* (MEA), which is placed between two flow field plates. The MEA consists of two electrodes, the anode and the cathode, which are each coated on one side with a thin layer of platinum-based catalyst, and separated by a proton exchange membrane which, when fed with a fuel, reacts electrochemically to create electricity. The working principle is illustrated in Figure 2.27. The flow field plates direct hydrogen to the anode and oxygen (from air) to the cathode. The catalyst splits the hydrogen molecule into protons and electrons. The

protons can pass through the membrane to the cathode, where they combine with absorbed oxygen forming water. Meanwhile, the electrons cannot pass through the membrane and have to pass through an external circuit, which create electricity. The chemical reactions occur as followed:

Anode:	$2\ H_2$	$\longrightarrow$	$4\ H^+ + 4\ e^-$
Cathode:	$4\ e^- + 4\ H^+ + O_2$	$\longrightarrow$	$2\ H_2O$
Overall:	$2\ H_2 + O_2$	$\longrightarrow$	$2\ H_2O$

By stacking together single cell, a fuel cell *stack* is made to produce the required amount of power. Increasing the number of cells in a stack increases the voltage, while increasing the surface area of the cells increases the current.

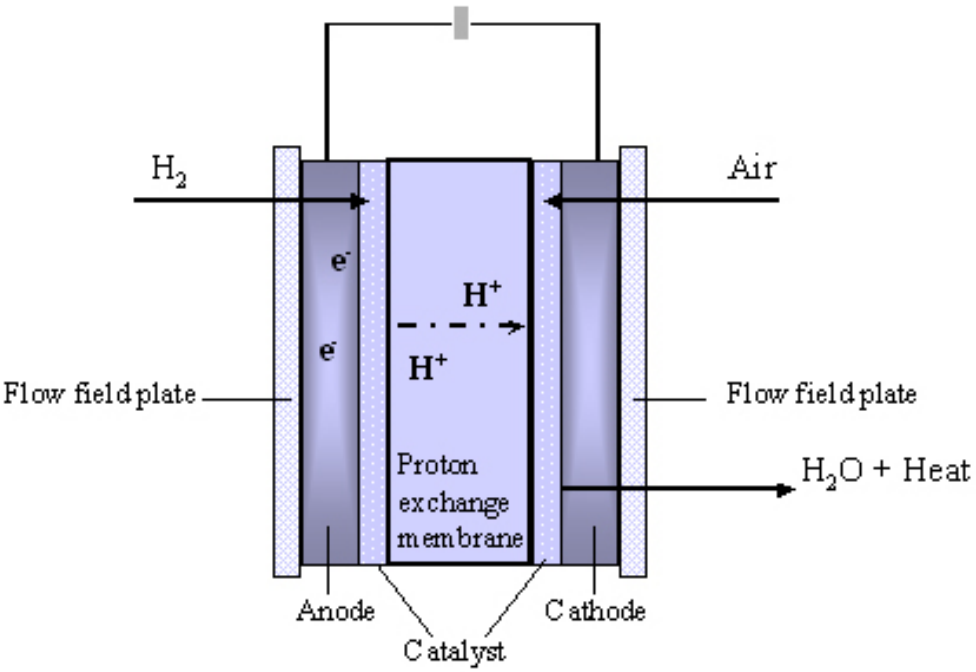

Figure 2.27. Scheme of basic elements and the working principle of PEMFC.

To make fuel cells economically competitive, there are many practical problems to be overcome as well. Water management remains a key problem in PEMFC, where generated water will need to be disposed of. Too much water will flood the membrane, while too little will dry it; in both cases, power output will drop. Furthermore, the platinum catalyst on the membrane is poisoned by carbon monoxide at temperatures below 120 °C and the membrane is sensitive to metal ions (which can be introduced by corrosion of metallic bipolar plates).

PEM systems using reformed methanol were proposed. Reforming methanol (producing hydrogen) is however a very complicated process, which requires also purification from the carbon monoxide produced in the reaction. A platinum-ruthenium catalyst is necessary since some carbon monoxide will unavoidably reach the membrane. The level should not exceed 10 parts per million. Furthermore, the start-up times of such a reformer reactor are of about half an hour. Efficiencies of PEMs are in the range of 40-50%.

Direct-methanol fuel cells (DMFC) are presented as well, where the fuel (methanol) is not reformed, but fed directly to the fuel cell. Because methanol is fed directly into the fuel cell, complicated catalytic reforming is not needed, and storage of methanol is much easier than that of hydrogen because it does not need to be done at high pressures, as methanol is a liquid. The energy density of methanol (the amount of hydrogen in a given volume) is orders of magnitude greater than even highly compressed hydrogen. However, efficiency is low due to the high permeation of methanol through the membrane and the dynamic behaviour is sluggish. Additionally methanol is poisonous. Nowadays, one of the smallest commercially available fuel cell is held by Toshiba [91], at 22 × 56 × 4.5 millimeters. This device outputs 100 milliwatts at 10 hours per milliter of fuel, and takes advantage of new technology allowing the use of undiluted (99.5 %) methanol.

The core of PEMFC is a polymer membrane that is electronically insulating but conducts protons and separates the fuel from the oxidant. The material used historically and most frequently in PEM fuel systems is the DuPont product Nafion® [92], a perfluorocarbon-based polymer carrying sulfonic acid residues, and the Dow product Dow® membrane [93]. The difference between these two ionomer types is that the side chain of the Dow® membrane is shorter than the side chain of Nafion®. Nafion® is a commercial material and has received the most extensive study (Figure 2.28). Mauritz and Moore gave a review of the current understanding of this membrane system [94]. Nafion® membranes are quite expensive, minimum 800 $/m^2 [95], and the production process includes strongly toxic and environment-unfriendly intermediates. Another shortcoming of the perfluorinated ionomers especially related to their application in direct methanol fuel cells (DMFC) is their high methanol permeability, which drastically reduces the DMFC performance [96, 97]. Therefore, other polymer systems

that would have been better performance than Nafion® (or Dow®) and / or lower costs are being sought by researchers around the world.

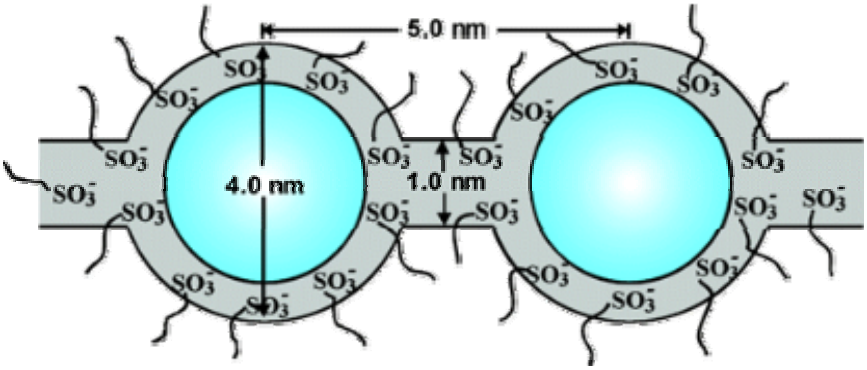

Figure 2.28 Cluster-network model for the morphology of hydrated Nafion® [98].

Performing as PEMFC membranes requires high proton selectivity and conductivity, impermeability of electrons hydrogen, air, water and methanol, high stability and durability (e.g. against acidity, temperature, oxidation, voltage, current and so on). Generally, there are five kinds of ionomer membranes for fuel cell applications [99], 100:

Perfluorinated ionomers and its composites: homogeneous like Nafion®, Dow®, micro-reinforced perfluorinated ionomer composite [101];

Partially fluorinated ionomers: such as grafted ionomer membranes [102] and copolymer;

Nonfluorinated ionomers: such as sulfonated vinyl polymer [103, 104], phosphazene-based cation-exchange membranes [105, 106, 107], partially sulfonated arylene main-chain polymers (e.g. PEEK), cross-linked arylene ionomers and ionomer blends [108];

Polymer / low-molecular composite membranes: such as polybenzimidazole in which was deposited phosphoric acid (or sulfonic acid) as proton-conducting electrolyte [109];

Organic / inorganic composite membranes: such as the Nafion® incorporated with highly porous SiO_2 'Aerosil' particles (Degussa product) [110]; or organic–inorganic hybrid polymers, for example, poly(benzylsulfonic acid siloxane) [111]; or ionomer / inorganic oxide 'nanocomposites' via sol-gel techniques [112];

2.4 References

[1] F. Reinitzer, *Liq. Cryst.*, **1989**, 5, 7-18.

[2] O. Lehmann, *Z. Phys. Chem.*, **1889**, 8, 8, 462-472.

[3] G. Friedel, *Ann. Physique*, **1922**, 18, 273.

[4] H. Sackmann, *Liq. Cryst.*, **1989**, 5, 43-45.

[5] G. W. Gray, K. J. Harrison, J. A. Nash, *Electronics Lett.*, **1973**, 9, 130-131.

[6] FD. Saeva, *Liquid crystals - the fourth state of matter*, New York: Marcel Dekker, **1979**.

[7] H. Kelker, R. Hatz, *Handbook of liquid crystals*, Weinheim, Verlag Chemie, **1980**, p.512.

[8] C. Tschierske, *Prog. Polym. Sci.*, **1996**, 21, 775-882.

[9] S. Chandrasekhar, B. K. Sadashiva and K. A. Suresh, *Pranama*, **1977**, 9, 471-480.

[10] N. Andrew, In: D. Demus, J. Goodby, G.W. Gray, H.W. Spiess and V. Vill, Editors, *Handbook of liquid crystals* **vol. 2b**, Wiley–VCH, Weinheim, **1998**, pp. 693-749.

[11] S. Chandrasekhar, In: D. Demus, J. Goodby, G.W. Gray, H.W. Spiess and V. Vill, Editors, *Handbook of liquid crystals* **vol. 2b**, Wiley–VCH, Weinheim, **1998**, pp. 757–758.

[12] J. Malthete, A.-M. Levelut, L. Liebert, *Adv Mater*, **1992**, 4, 37–41.

[13] A.M. Levelut, *J Chim Phys, Phys Chim Biol*, **1983**, 80, 149–161.

[14] S. Chandrasekhar, G. S. Ranganath, *Rep Prog Phys*, **1990**, 53, 57–84.

[15] G. Burducea, *Romanian Reports in Physics*, **2004**, 56, 66-86.

[16] P. J. Collins, In *Liquid Crystals: Nature's Delicate State of Matter*, Princeton University Press: Princeton, NJ, **1990**.

[17] G. J. T. Tiddy, *Phys. Rep.*, **1980**, 57, 1-46.

[18] D. L. Gin, W. Gu, B. A. Pindzola, W-J. Zhou, *Acc. Chem. Res.*, **2001**, 34(12), 973-980.

[19] E. A. Wood, *Crystals and Light: An Introduction to Optical Crystallography. 2e*, Dover Publications, Inc., New York, **1977**, 156 pp.

[20] M. W. Davidson, M. Abramowitz, *Optical Microscopy*, Molecular Expressions, online review.

[21] D. Demus, L. Richter, *Textures of Liquid Crystals*, Weinheim: Verlag Chemie, **1978**.

[22] S. Chandrasekhar, GS Ranganath, *Rep. Prog. Phys.*, **1990**, 53, 57-84.

[23] C. Destrade, P. Foucher, H. Gasparoux, N. Huu Tinh, A-M. Levelut, J. Malthete, *Mol. Cryst. Liq. Cryst.*, **1984**, 106, 121-146.

[24] (a) H. Sackmann, D. Demus, *Z. Phys. Chem.*, **1963**, 222, 127-142; (b) H. Sackmann, D. Demus, *Z. Phys. Chem.*, **1963**, 222, 143-160.

[25] Ladd MFC, R. A. Palmer, *Structure determination by X-ray crystallography*, New York: Plenum Press, **1994**.

[26] C. E. Williams, R. P. May, A. Guinier, *A Small-angle Scattering of X-rays and Neutrons. In: E. Lifshin, Editor, X-ray Characterisation of Materials*, Weinheim: Wiley-WCH, **1999**, p. 211-254.

[27] Jordon Lloyd D., *Colloid Chemistry,* Alexander J. The Chemical Catalog Co., New York, **1926**.

[28] J. P. Flory, Gels and gelling processes, *Faraday Discuss. Chem. Soc.,* **1974**, 57, 7–18.

[29] H. D. Gesser, P. C. Goswami, Aerogels and related porous materials, *Chem. Rev.*, **1989**, 89, 765–788.

[30] T. Tanaka, Gels, *Sci. Am.,* **1981**, 244, 110–123.

[31] H. Hoffmann, G. Ebert, *Angew. Chem.*, **1988**, 100, 933.

[32] J. P. Guenet, *Thermoreversible Gelation of Polymers and Biopolymers,* Acad. Press Ltd., London, **1992**.

[33] W. Burchard, S. B. Ross-Murphy (Eds.), *'Physical Networks – Polymers and Gels'*, Elsevier Applied Science, London / New York **1990**.

[34] K. te Nijenhuis, *Adv. Polym. Sci.*, **1997**, 130, 1.

[35] a). R. J. P. Corriu, D. Leclercq, *Angew. Chem. Int. Ed.*, **1996**, 35, 1420-1436; b). M. T. Reetz, *Adv. Mater.*, **1997,** 9, 943-954.

[36] E. W. Hellendoorn, R. de Boer, *Conserva*, **1965**, 14, 100 – 121.

[37] Jan H. Van Esch, Ben L. Feringa, *Encyclopedia of Supramolecular Chemistry*, **2004**, 586-596.

[38] P. Terech and R. G. Weiss, *Chem. Rev.*, **1997**, 97, 3133-3159.

[39] G. D. Rees, B. H. Robinson, *Adv. Mater.*, **1993**, 5, 608-619.

[40] G. Haering, P. L. Luisi, *J. Phys. Chem.*, **1986**, 90, 5892-5895.

[41] R. J. Phillips, W. M. Deen, F. J. Brady, *J. Colloid Interface Sci.*, **1990**, 139, 363-373.

[42] R. J. H. Hafkamp, P. A. Kokke, I. M. Danke et al., *J. Chem. Soc. Chem. Commun.*, **1997**, 6, 545-546.

[43] D. J. Abdallah, R. G. Weiss, *Adv. Mater.*, **2000**, 12, No. 17, 1237-1247.

[44] O. Gronwald, S. Shinkai, *Chem. Eur. J.*, **2001**, 7, 4328-4334.

[45] O. Gronwald, E. Snip, S. Shinkai, *Current Opinion in Colloid & Interface Science*, **2002**, 7, 148-156

[46] V. Percec, J. Heck, M. Lee, G. Ungar, A. Alvarez-Castillo, *J. Mater. Chem.*, **1992**, 2, 1033.

[47] V. Percec, G. Johansson, J. Heck, G. Ungar, S. V. Batty, *J. Chem. Soc. Perkin Trans. I*, **1993**, 1411.

[48] V. Percec, M. N. Holerca, S. Uchida, W. Cho, G. Ungar, Y. Lee, J. P. Yeardley, *Chem. Eur. J.*, **2002**, 8, 1106-1117.

[49] G. M. Clavier, J. F. Brugger, H. Bouas-Laurent, J. L. Pozzo, *J. Chem. Soc., Perkin Trans. 2*, **1998**, 2527-2534.

[50] S. Tamaru, M. Nakamura, M. Takeuchi, S. Shinkai, *Org. Lett.*, **2001**, 3, 3631-3634.

[51] a). P. Terech, V. Schaffhauser, P. Maldavi, J. M. Guenet, *Europhys. Lett.*, **1992**, 17, 515-521; b). R. J. H. Hafkamp, B. P. A. Kokke, et al., *Chem. Commun.*, **1997**, 545-546.

[52] U. Beginn, B. Tartsch, *Chem. Commun.*, **2001**, 19, 1924-1925.

[53] Jan H. van Esch, F. Schoonbeek, M. de Loos, H. Kooijman, A. L. Spek, R. M. Kellogg, and Ben L. Feringa, *Chem. Eur. J.*, **1999**, 5, 937-950.

[54] K. Yoza, N. Amanokura, et al., *Chem. Eur. J.*, **1999**, 5, 2722-2729.

[55] Kjeld J. C. van Bommel, A. Friggeri, S. Shinkai, *Angew. Chem. Int. Ed.*, **2003**, 42, 980-999.

[56] Jan H. van Esch, Ben L. Feringa, *Angew. Chem. Int. Ed.*, **2000**, 39, 2263-2266.

[57] G. Mieden-Gundert, L. Klein, M. Fischer, F. Vögtle, et al., *Angew. Chem. Int. Ed.*, **2001**, 40, 3164-3166.

[58] P. Terech, *Progr. Colloid Polym. Sci.*, **1996**, 102, 64-70.

[59] K. Koumoto, T. Yamashita, T. Kimura, R. Luboradzki, S. Shinkai, *Nanotechnology*, **2001**, 12, 25-31.

[60] BYK Gulden, private communication.

[61] K. Hanabusa, K. Hiratsu, M. Kimura, H. Shirai, *Chem. Mater.*, **1999,** 11, 649.

[62] (a) A. M. Cassell, C. L. Asplund, J. M. Tour, *Angew. Chem. Int. Ed.*, **1999**, 111, 2403-2405; (b) K. Oishi, T. Ishi-i, M. Sano, S. Shinkai, Chem. Lett., 1999, 1089-1090.

[63] Y. Osada, J. -P. Gong, *Adv. Mater.*, **1998**, 10,827-837.

[64] T. Oya, T. Enoki, A. U. Grosberg, S. Masamune, T. Sakiyama, Y. Takeoka, K. Tanaka, G. Wang, Y. Yilmaz, M. S. Feld, R. Dasari, T. Tanaka, *Science*, **1999**, 286, 1543-1545.

[65] U. Beginn, G. Zipp, M. Möller, *Adv. Mater.*, **2000**, 12(7), 510-516.

[66] C. F. Van Nostrum, *Adv. Mat.*, **1996**, 8, 1027-1030.

[67] F. S. Schoonbeek, J. H. van Esch, B. Wegewijs, D. A. B. Rep, M. P. de Haas, T. M. Klapwijk, R. M. Kellogg, B. L. Feringa, Angew. Chem. **111**, 1486 – 1491 (1999).

[68] F. Würthner, C. Thalacker, A. Sautter, *Adv. Mater.*, **1999**, 11, 754-758.

[69] U. Beginn, *Adv. Mat.*, **1998**, 10, 1391-1394.

[70] Y. Ono, Y. Kanekiyo, K. Inoue, J. Hojo, S. Shinkai, *Chem. Lett.*, **1999**, 23.

[71] H. Gankema, M. A. Hempenius, M. Möller, G. Johansson, V. Percec, *Macromol. Symp.*, **1996**, 102, 381.

[72] W. Gu, L. Lu, G. B. Chapman, R. G. Weiss, *Chem. Commun.*, **1997**, 543.

[73] (a) H. Gankema, Ph.D. Thesis, University of Twente, The Netherlands, 1995; (b) U. Beginn, S. Keinath, M. Möller, *Macromol. Chem. Phys.*, **1998**, 199, 2379-2384.

[74] W. Gu, L. Lu, G. B. Chapman, R. G. Weiss, *Chem. Commun.*, **1997**, 543-544.

[75] R. J. Hafkamp, B. P. A. Kokke, I. M. Danke, H. P. M. Geurts, A. E. Rowan, M. C. Feiters, R. J. M. Nolte, *Chem. Commun.*, **1997**, 545-546.

[76] Y. Ono, K. Nakashima, M. Sano, J. Hojo, S. Shinkai, *Chem. Lett.*, **1999**, 1119-1120.

[77] M. Mulder, *Basic Principles of Membrane Technology*, **1992**, Kluwer (Dordrecht).

[78] (a) S. J. Singer, G. L. Nicolson, *Science*, **1972**, 175, 720; (b) D. Voet, J. G. Voet, C. W. Pratt, *Fundamentals of Biochemistry*, J. Wiley: New York, **1999**, p 239.

[79] J. -M. Lehn, *Supramolecular Chemistry*, **1995**, VCH (Weinheim).

[80] H. C. Visser, D. N. Reinhoudt, F. de Jong, *Chem. Soc. Rev.*, **1994**, 23, 75.

[81] P. Läuger, *Science*, **1978**, 172, 24.

[82] B. Alberts, D. Bray, J. Lewis, M. Raff, K. Roberts, J. D. Watson, 'Molecular Biology of the Cell', 3th ed., Garland Publishing Inc., New York, 1994.

[83] W. D. Stein, 'Channels, Carriers and Pumps: an Introduction to Membrane Transport', Academic Press, San Diego CD **1990**.

[84] M. Schleyer, W. Neupert, Cell **43**, 339 – 350 (1985).

[85] V. Percec, T. K. Bera, *Biomacromolecules*, **2002**, 3, 167-181.

[86] (a) V. Percec, G. Johansson, J. Heck, G. Ungar, S. V. Batty, *J. Chem. Soc., Perkin Trans. 1*, **1993**, 1411; (b) D. Tomazos, R. Out, J. A. Heck, G. Johansson, V. Percec, M. Möller, *Liq. Cryst.* **1994**, 16, 509; (c) V. Percec, G. Johansson, G. Ungar, J. Zhou, *J. Am. Chem. Soc.*, **1996**, 118, 9855; (d) S. D. Hudson, H.-T. Jung, V. Percec, W.-D. Cho, G. Johansson, G. Ungar, V. S. K. Balagurusamy, *Science*, **1997**, 278, 449.

[87] H. Gankema, M. A. Hampenius, M. Möller, G. Johansson, V. Percec, *Macromol. Symp.*, **1996**, 102, 381.

[88] (a) V. Percec, G. Zipp, G. Johansson, U. Beginn, M. Möller, *Macromol. Chem. Phys.*, **1997**, 198, 265; (b) U. Beginn, G. Zipp, M. Möller, G. Johansson, V. Percec, *Macromol. Chem. Phys.*, **1997**, 198, 2839.

[89] a) U. Beginn, G. Zipp, M. Möller, *J. Polym. Sci., Part A*: *Polym. Chem.*, **2000**, 38, 631-640; (b) U. Beginn, G. Zipp, M. Möller, *Chem.-Eur. J.*, **2000**, 6, 2016; (c) U. Beginn, G. Zipp, A. Mourran, P. Walther, M. Möller, *Adv. Mater*, **2000**, 12, 513; (d) U. Beginn, G. Zipp, M. Möller, *Adv. Mater.*, **2000**, 12, 510.

[90] M. Winter, R: J. Brodd, *Chem. Rev.*, **2004**, 104, 4245-4269.

[91] From Website: *Wikipedia, the free encyclopedia, Fuel cell*, **2005**.

[92] W. G. Grot, *Macromol. Symposia*, **1994**, 82, 161-172.

[93] A. Steck, in: *Proceedings of the 1st International symposium on New Materials for Fuel Cell Systems, Membrane Materials in Fuel Cells*, Montreal, Canada, **1995**, 74-94.

[94] K. A. Mauritz, R. B. Moore, *Chem. Rev.*, **2004**, 104, 4535-4585

[95] F. Babir, T. Gomez, *Int. J. Hydrogen Energy*, **1996**, 21, 891.

[96] S. Surampudi, S. R. Narayanan, E. Vamos, H. Frank, G. Halpert, A. LaConti, J. Kosek, G. K. Surya Prakash, G. A. Olah, *J. Power Sources*, **1994**, 47, 377-385.

[97] H. Sun, G. Sun, S. Wang, J. Liu, X. Zhao, G. Wang, H. Xu, S. Hou, Q. Xin, *J. Membr. Sci.*, **2005**, 259, 27-33.

[98] W. Y. Hsu, T. D. Gierke, *J. Membr. Sci.*, **1983**, 13, 307–326.

[99] J. A. Kerres, *J. Membr. Sci.*, **2001**, 185, 3-27.

[100] M. A. Hickner, H. Ghassemi, Y. S. Kim, B. R. Einsla, J. E. McGrath, *Chem. Rev.*, **2004**, 104, 4587-4612.

[101] B. Bahar, A. R. Hobson, J. A. Kolde, D. Zuckerbrod, *US Patent*, **1996**, 5, 547-551.

[102] G. G. Scherer, *Ber. Bunsenges. Phys. Chem.*, **1990**, 94, 1008-1014.

[103] G. Hübner, E. Roduner, *J. Mater. Chem.*, **1999**, 9, 409-418.

[104] J. Qiao, T. Hamaya, T. Okada, *Chem. Mater.*, **2005**, 17, 2413-2421.

[105] Q. Guo, P. N. Pintauro, H. Tang, S. O'Connor, *J. Membr. Sci.*, **1999**, 154, 175.

[106] H. Tang, P. N. Pintauro, Q. Guo, S. O'Connor, J. *Appl. Polym. Sci.*, **1999**, 71, 387.

[107] C. W. Lin, R. Thangamuthu, C. J. Yang, *J. Membr. Sci.*, **2005**, 253, 23-31.

[108] J. Kerres, W. Cui, M. Junginger, *J. Membr. Sci.*, **1998**, 139, 227-241.

[109] J. S. Wainright, J.-T. Wang, D. Weng, R. F. Savinell, M. H. Litt., *J. Electrochem. Soc.*, **1995**, 142, L121-L123.

[110] A. S. Arico, P. Creti, P. L. Antonucci, V. Antonucci, E*lectrochem. Solid-State Lett.*, **1998**, 1(2), 66-68.

[111] J. Ganthier-Luneau, A. Denoyelle, J. Y. Sanchez, C. Poinsignon, *Electrochim. Acta*, **1992**, 37, 1615.

[112] K. A. Maurizz, *Mater. Sci. Eng.*, **1998**, C6, 121-133.

Chapter 3

Thermotropic Columnar Liquid Crystal phases from Wedge-shaped Benzene Sulfonated Mesogens

Introduction

Functional materials with well-defined nanostructures are of great interest in material sciences. Liquid crystals, which self-assemble into different superstructures, e.g. lamellar, columnar and (micellar or bicontinuous) cubic mesophases, provide a facile strategy to construct structural defined functional materials. Various amphiphilic molecules self-assemble into liquid crystalline phases, depending on the strength of intra- and interactions and the relative fractions of different groups within the molecules, as well as the architecture or geometrical shape of the molecules [1,2,3,4,5]. During the last 20 years a high interest has risen up in investigating the microstructure and properties of columnar mesophase because of their potential applications as selective membranes [6] and as electrooptic materials [7].

It is well known that disk-like molecules form columnar liquid crystals, in which the discs stack up and create infinite columns. The columns in turn pack laterally in a two-dimensional, mostly hexagonal lattice [8]. Columnar liquid crystals can also evolve through self-assembly of taper-shaped molecules where the bulky side is usually made up of two or three flexible aliphatic chains [9,10]. Self-assembly of such tapered wedge-shaped molecules into columns can be visualized as packing of slices to form a disc-like aggregate and stacking of discs on the top of one another to create columns (cf. Figure 3.1). The concept to design tapered molecules as a building unit for self-assembling cylinders was inspired by the Tabacco Mosaic Virus [11]. Then 3,4,5-tris(alkyl-1-oxy) benzoates (cf. Figure 3.2) were demonstrated forming the supra-molecular cylindrical columnar packs in the thermotropic columnar hexagonal mesophase [12].

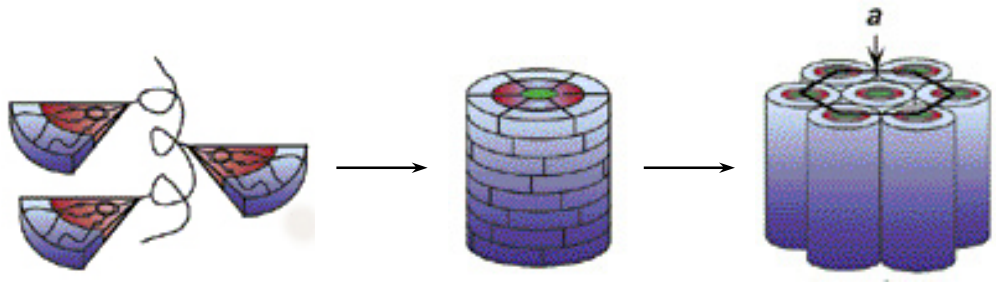

Figure 3.1 Scheme of self-assembly of wedge-shaped molecules into a hexagonal columnar mesophase.

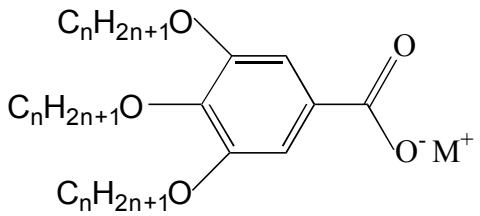

$M^+ = N(CH_3)_4^+, Li^+, Na^+, K^+, Rb^+, Cs^+$
$n = 8, 10, 12, 14, 16$

Figure **3.2** Structural formular of the alkali metal and tetramethyl ammonium 3,4,5-tris(alkyl-1-oxy) benzoates.

The carboxylate group connected with benzene (e.g. benzoate) is a polar planar sp^2-center, which has been investigated systematically. However, the highly polar sp^3-centers have not been investigated so far. Among polar sp^3-centers, the sulfonate group $–SO_3^{\Theta}$ is an accessible functional group, highly polar and non-planar that has sparsely been used so far to construct liquid crystal molecules. Additionally the attachment of a sulfonate group to alkoxy benzoyl moiety brings the functions of ion or small molecules transporting, which is great potential to be developed to high performance nonfluorinated hydrocarbon membrane materials.

Hence, in this chapter, the synthesis of wedge-shaped amphiphiles with sulfonated moiety will be demonstrated. The phase behaviors will be reported and the types of mesophase will be detected by small angel x-ray scattering and miscibility experiments. Furthermore, the relation between the self-organization and the molecular structures, e.g. molecular geometries, cations, alkyl-chains will be presented.

Experimental Section

Materials

DMF was dried over calcium hydride (CaH_2) for 12h and distilled under vacuum. 1,2,3-Trihydroxy-benzene (99+%, Aldrich), 1-bromododecane (99+%, Aldrich), potassium carbonate (97%, Aldrich), sulphuric acid (95~97%, Merck), thionyl chloride (99%, Merk), ammonia gas (Merck), methyllithium (Aldrich), sodium methanolate (ACS reagent), potassium methanolate (ACS reagent), caesium hydroxide (97%, Aldrich), pyridine (97%, Aldrich), tetramethylammonium hydroxide (0.1M in methanol, Aldrich), tetraethylammonium hydroxide (0.1M in methanol, Aldrich), tetrabutyl-ammonium hydroxide (0.1M in methanol, Aldrich), sodium sulfite (ACS reagent, Merck), sodium hydroxide (ACS reagent), hydrochloric acid (0.1 M, ACS reagent), barium acetate (99%, Fluka), Amberlite IR120 (Fluka), lithium carbonate (99+%, Aldrich), sodium carbonate (ACS reagent), potassium carbonate (ACS reagent), caesium carbonate (99+%, Aldrich) and 11-bromo-1-undecene (95%, Aldrich) were used as received. Ethanol, methanol, acetone, diethylether, *n*-hexane, toluene, ethyl acetate, tetrahydrofurane, dichloromethane, isopropylether were all ACS reagents and used as received. All the deuterated solvents for NMR were received from Chemotrade (Leipzig).

Techniques

^{1}H NMR (300MHz) and ^{13}C NMR (75MHz) were recorded on a Bruker DPX-300 spectrometer with tetramethylsilane (TMS) internal standard in the deuterated solvents (e.g. chloroform-d_3, DMSO-d_6, DMF-d_7, D_2O) at 20 °C.

FT-IR spectra were performed using a Bruker IFS 113V spectrometer. KBr pellets were used as substrates for the measurement recorded in transmission.

DSC (Differential Scanning Calorimetry) measurements were made with samples of about 5mg to 10mg. Thermal transitions were determined on a Netzsch DSC 204 'Phoenix' differential scanning calorimeter. In all cases, the heating and cooling rates were 10°C/min. First-order transitions were reported as the maxima or minima of the endothermic and exothermic peaks during the second heating and the first cooling scans. Indium and cyclohexane were used as calibration standards.

For **Thermo Optical Polarizing Microscopy** a Zeiss AXIOPLAN 2 polarizing microscope, equipped with a METTLER FP 90 hot stage was used. Pictures were taken from a digital Zeiss AxioCam MRC4 camera with a resolution of 4 Megapixels in combination to the Zeiss AxioVision software.

Small Angle X-ray Scattering data were recorded using a Kratky block camera and Ni-filtered CuK_α radiation. The diverging and receiving slits were 60 and 100 mm wide, respectively, providing high resolution: the half-width of the primary beam was approximately 1.4' (angular minutes), i.e. 2.5×10^{-4} $Å^{-1}$. The oriented fiber specimen was positioned with the draw direction (fiber axis) parallel to the slits in order to record the equatorial scattering. The scattered intensity was measured at angular increments of 0.5' in the region of the narrow, intense 100 reflections, and at 1' increments over the rest of measured region.

1,2,3-Tris(dodecyloxy)benzene (1): 1,2,3-trihydroxy-benzene (10.1 g, 0.08 mol) and K_2CO_3 (55.5 g, 0.4 mol) were mixed with 125 ml freshly dried DMF in a 250 ml three-necked flask with a magnetic stirrer under a nitrogen atmosphere. At 60 °C, 1-bromododecane (55.2 ml, 0.23 mol) was added dropwise. The reaction mixture was stirred for 5 hours at 60 °C. After reaction, the mixture was slowly poured into 600 ml ice water. The precipitate was isolated by filtration and dried *in vacuo*. The crude product was recrystallized from 300 ml acetone for three times to yield a white powder (yield: 38.3 g ≅ 76% of theory).
m.p. 39–40 °C (ref.[8] 39.5–40.5 °C); TLC (*n*-hexane : EtOAc = 20 : 1): $R_f = 0.68$; ^{1}H NMR (300MHz, $CDCl_3$, 20 °C, TMS, δ, ppm): 0.88 (t, 9H, CH_3, $J = 6.6$ Hz), 1.26 (overlapped peaks, 48H, $CH_3(CH_2)_8$), 1.47 (m, 6H, $O(CH_2)_2CH_2$), 1.78 (m, 6H, OCH_2CH_2), 3.90 (overlapped t, 6H, OCH_2, $J = 6.3$ Hz), 6.55 (d, 2H, 4,6-benzene-*H*, $J = 8.1$ Hz), 6.90 (t, 1H, 5-benzene-*H*, $J = 8.4$ Hz); ^{13}C NMR (75 MHz, $CDCl_3$, 20 °C, TMS, δ, ppm): 14.1 (CH_3), 22.7 (CH_3CH_2), 26.1 ($OCH_2CH_2CH_2$), 29.4 ($CH_3CH_2CH_2CH_2$), 29.5 ($CH_3CH_2CH_2CH_2(CH_2)_5$), 29.9 (1,3-OCH_2CH_2), 30.3 (2-OCH_2CH_2), 31.9 ($CH_3CH_2CH_2$), 69.0 (1,3-OCH_2), 73.3 (2-OCH_2O), 106.7 (4,6-benzene-*C*), 123.1 (5-benzene-*C*), 138.4 (2-benzene-*C*), 153.4 (1,3-benzene-C).

2,3,4-Tris(dodecyloxy)benzene sulfonic acid (2): Under a nitrogen atmosphere, 1.27 g **1** (2.0 mmol) was added in 10 ml concentrated sulfuric acid (95-97%) at 0 °C.

The reaction suspension was stirred for 2 hours while the temperature of the water bath was gradually increased until 20 °C. The suspension was poured slowly into 50 ml ice water. The resulting light-yellow suspension was kept at 4 °C for 1 hour and the precipitate was isolated by filtration and pre-dried *in vacuo*. The crude product was recrystallized from 30 ml acetone at 4 °C for three times and dried *in vacuo* to yield a white powder (yield: 1.24 g ≅ 87.2% of theory).

m.p. 65.0–65.5 °C; ^{1}H NMR (300MHz, $CDCl_3$, 20 °C, TMS, δ, ppm): 0.88 (t, 9H, CH_3, J = 6.7 Hz), 1.27 (overlapped peaks, 48H, $CH_3(CH_2)_8$), 1.45 (m, 6H, $O(CH_2)_2CH_2$), 1.83 (m, 6H, OCH_2CH_2), 4.00 (overlapped t, 4H, 3- and 4-OCH_2), 4.29 (t, 2H, 2-OCH_2, J = 6.98 Hz), 6.69 (d, 1H, 5-benzene-H, J = 9.06 Hz), 7.54 (d, 1H, 6-benzene-H, J = 8.85 Hz); ^{13}C NMR (75MHz, $CDCl_3$, 20 °C, TMS, δ, ppm): 14.13, 22.70, 25.77, 26.10, 29.11, 29.39, 29.72, 30.00, 30.29, 31.94, 73.96, 75.77, 107.40, 123.20, 124.78, 141.89, 149.73, 157.79; IR (KBr, cm^{-1}): 3435.11 (s, broad), 2956.86 (m), 2917.63 (vs), 2851.29 (s), 1732.56 (w), 1631.30 (w), 1582.85 (w), 1486.22 (w), 1466.57 (m), 1441.26 (w), 1380.14 (w), 1304.58 (w), 1281.34 (w), 1226.56 (m), 1162.99 (w), 1087.42 (s), 1041.04 (w), 885.31 (w), 802.42 (w), 787.36 (w), 719.54 (w), 709.03 (w), 691.90 (w), 634.69 (w), 606.35 (w), 578.87 (w), 531.66 (w); elemental analysis calculated (%): C 71.04, H 10.93; found: C 69.13, H 11.32.

2,3,4-Tris(dodecyloxy)benzene sulfonyl chloride (3): In a two-necked round-bottom flask with a Teflon-coated magnetic stirrer, 1.0 g **2** (1.4 mmol) was dissolved in 150 ml fleshed dried dichloromethane under nitrogen protection and catalytic amount (0.5 ml) of DMF was added. And 0.12 ml thionyl chloride (1.65 mmol) was added dropwise into the reaction solution at 0 °C. The reaction mixture was stirred at room temperature for 1 hour. The solvent was removed and the resulting compound was dried under vacuum. The product was continued to be used without further purification.

^{1}H NMR (300MHz, $CDCl_3$, 20 °C, TMS, δ, ppm): 0.88 (overlapped t, 9H, CH_3, J = 6.60 Hz), 1.26 (overlapped peaks, 54H, $CH_3(CH_2)_9$), 1.83 (m, 6H, OCH_2CH_2), 3.96 (tetra, 4H, 3- and 4-OCH_2, J = 6.06 Hz), 4.19 (t, 2H, 2-OCH_2, J = 6.98 Hz), 6.59 (d, 1H, 5-benzene-H, J = 8.67 Hz), 7.55 (d, 1H, 6-benzene-H, J = 8.67 Hz); ^{13}C NMR (75MHz, $CDCl_3$, 20 °C, TMS, δ, ppm): 14.12, 22.70, 25.89, 26.10, 29.22, 29.40, 29.65, 29.70, 29.76, 31.94, 73.74, 74.81, 106.63, 123.74, 142.23, 151.18, 156.71, 165.07.

2,3,4-Tris(dodecyloxy)benzene sulfonamide (4): In a two-necked round-bottom flask with a Teflon-coated magnetic stirrer, 1.0 g **3** (1.4 mmol) was dissolved in 50 ml fleshed saturated ammonia THF solution under nitrogen protection. The reaction mixture was stirred at room temperature for 7 days. The solvent was removed under vacuum and the resulting compound was freeze-dried to yield **4** (overall yield: 0.7 g ≅ 70.1% of theory).

m.p. 55.5 °C; TLC (EtOAc : MeOH = 6 : 1): $R_f = 0.23$; ^{1}H NMR (300MHz, $CDCl_3$, 20 °C, TMS, δ, ppm): 0.88 (overlapped t, 9H, C*H*$_3$), 1.26 (overlapped peaks, 54H, $CH_3(CH_2)_9$), 1.69 (m, 6H, OCH_2CH_2), 3.82 (broad, 4H, 3- and 4-OC*H*$_2$), 4.05 (broad, 2H, 2-OCH_2), 6.28 (broad, 1H, 5-benzene-*H*), 7.34 (broad, 1H, 6-benzene-*H*); ^{13}C NMR (75MHz, $CDCl_3$, 20 °C, TMS, δ, ppm): 14.12, 22.71, 26.27, 29.44, 29.62, 29.80, 31.96, 31.96, 73.42, 106.7, 139.52, 140.03, 152.99; elemental analysis calculated (%): C 71.03, H 11.21, N 1.97; found (%): C 68.81, H 11.93, N 1.72.

Lithium 2,3,4-tris(dodecyloxy)benzene sulfonate (5): Under a nitrogen atmosphere, 0.2 ml (0.32 mmol) ether solution of methyl lithium (1.6 mol/L) was added in 5 ml freshly dried ether solution of compound **2** (227.6 mg, 0.32 mmol) at room temperature. The reaction mixture was stirred for 2h, subsequently all solvent was removed by a membrane pump. The obtained solid was dried at 40 °C under an oil-pump vacuum to yield white powder **5** (yield: 0.2 g ≅ 87% of theory).

m.p. –11.1 °C (by DSC); TLC (EtOAc : MeOH = 6 : 1): $R_f = 0.45$; ^{1}H NMR (300MHz, $CDCl_3$, 20 °C, TMS, δ, ppm): 0.88 (t, 9H, C*H*$_3$, $J = 6.23$ Hz), 1.26 (overlapped peaks, 54H, $CH_3(CH_2)_9$), 1.77 (m, 6H, OCH_2CH_2), 3.84 (broad, 4H, 3- and 4-OC*H*$_2$), 4.08 (broad, 2H, 2-OC*H*$_2$), 6.34 (broad, 1H, 5-benzene-*H*), 7.34 (d, 1H, 6-benzene-*H*, $J = 8.28$ Hz); ^{13}C NMR (75MHz, $CDCl_3$, 20 °C, TMS, δ, ppm): 14.12, 22.72, 25.75, 26.33, 29.44, 29.55, 29.81, 30.53, 31.99, 32.04, 68,62, 73.67, 106.85, 123.74, 128.96, 141.82, 150.02, 155.73; elemental analysis calculated (%): C 70.35, H 10.82; found (%): C 68.28, H 10.97.

Sodium 2,3,4-tris(dodecyloxy)benzene sulfonate (6): Under a nitrogen atmosphere, 19.0 mg sodium methoxide (0.35 mmol) was dissolved in 5 ml freshly dried methanol. Subsequently, compound **2** (250 mg, 0.35 mmol) was added and the reaction mixture was stirred vigorous for 2h at room temperature. Afterward, all solvent was removed by

membrane pump. The obtained solid was freeze-dried from benzene *in vacuo* to yield white powder **6** (yield: 0.21 g ≅ 82% of theory).
m.p. 7.7 °C (by DSC); TLC (EtOAc : MeOH = 6 : 1): $R_f = 0.34$; ^{1}H NMR (300MHz, $CDCl_3$, 20 °C, TMS, δ, ppm): 0.88 (overlapped t, 9H, C*H*$_3$), 1.26 (overlapped peaks, 54H, $CH_3(CH_2)_9$), 1.67 (broad, 6H, $O(CH_2)_2CH_2$), 3.79 (broad, 4H, 2,4-OC*H*$_2$), 4.03 (broad, 2H, 3-OC*H*$_2$), 6.18 (broad, 1H, 5-benzene-*H*), 7.28 (broad, 1H, 6-benzene-*H*); ^{13}C NMR (75MHz, $CDCl_3$, 20 °C, TMS, δ, ppm): 14.12, 22.74, 25.74, 26.42, 29.51, 29.60, 29.70, 29.95, 30.63, 32.01, 68,54, 73.47, 75.42, 106.61, 123.85, 128.90, 141.77, 150.20, 155.30; elemental analysis calculated (%): C 68.61, H 10.59; found (%): C 67.32, H 11.16.

Potassium 2,3,4-tris(dodecyloxy)benzene sulfonate (7): Under a nitrogen atmosphere, 61.6 mg potassium methoxide (0.88 mmol) was dissolved in 10 ml freshly dried methanol. Subsequently, compound **2** (625.4 mg, 0.88 mmol) was added and the reaction mixture was stirred vigorous for 2h at room temperature. Afterward, all solvent was removed by membrane pump. The obtained solid was freezing dried from benzene *in vacuo* to yield white powder **7** (yield: 0.62 g ≅ 94% of theory).
m.p. 17.8 °C (by DSC); TLC (EtOAc : MeOH = 6 : 1): $R_f = 0.16$; ^{1}H NMR (300MHz, $CDCl_3$, 20 °C, TMS, δ, ppm): 0.88 (overlapped t, 9H, C*H*$_3$), 1.26 (overlapped peaks, 54H, $CH_3(CH_2)_9$), 1.75 (m, 6H, OCH_2CH_2), 3.84 (broad, 4H, 3- and 4-OC*H*$_2$), 4.07 (broad, 2H, 2-OC*H*$_2$), 6.29 (d, 1H, 5-benzene-*H*, $J = 8.28$ Hz), 7.35 (d, 1H, 6-benzene-*H*, $J = 8.70$ Hz); ^{13}C NMR (75MHz, $CDCl_3$, 20 °C, TMS, δ, ppm): 14.12, 22.73, 25.83, 26.39, 29.49, 29.58, 29.92, 30.62, 32.03, 68.56, 73.55, 74.96, 106.79, 123.63, 130.71, 142.00, 150.34, 155.23; elemental analysis calculated (%): C 67.33, H 10.36; found (%): C 66.36, H 10.49.

Caesium 2,3,4-tris(dodecyloxy)benzene sulfonate (8): In a 100 ml two-necked flask with a magnetic stirrer under a nitrogen atmosphere, 0.71 g of **2** (1.0 mmol) was dissolved in 50 ml ethanol at 60 °C. Subsequently, the 0.34 g alkali caesium hydroxide monohydrate (2.0 mmol) was added. The reaction mixture was refluxed for 30 minutes, and was filtered hot. The filtrate was cooled to room temperature and the precipitate was isolated by filtration and washed with water until the washing water became

neutral. After pre-dried *in vacuo*, the crude product was twice crystallized from *n*-hexane to obtain a white powder of **8** (yield: 0.8 g > 98% of theory).
m.p. 50.3 °C (by DSC); TLC ($CHCl_3$: MeOH = 6 : 1): $R_f = 0.44$; ^{1}H NMR (300MHz, $CDCl_3$, 20 °C, TMS, δ, ppm): 0.88 (t, 9H, C*H*$_3$, *J* = 6.6 Hz), 1.26 (overlapped peaks, 48H, $CH_3(CH_2)_8$), 1.47 (broad, 6H, $O(CH_2)_2CH_2$), 1.72 (m, 6H, OCH_2CH_2), 3.90 (overlapped peaks, 6H, OCH_2, *J* = 6.6 Hz), 7.03 (s, 2H, 2,6 position); ^{13}C NMR (75MHz, $CDCl_3$, 20 °C, TMS, δ, ppm): 14.12, 22.71, 26.27, 29.44, 29.62, 29.80, 31.96, 31.96, 73.42, 106.7, 139.52, 140.03, 152.99; elemental analysis calculated (%): C 59.84, H 9.21; found (%): C 59.71, H 9.23.

Pyridinium 2,3,4-tris(dodecyloxy)benzene sulfonate (9): In a three-necked round-bottom flask, 0.50 g **2** (0.7 mmol) was dissolved in 10 ml pyridine under a nitrogen atmosphere. The solution was stirred at room temperature for 24 hours. Afterward pyridine was removed completely by a rotary evaporator. The residue was recrystallized twice from methanol and subsequently dried *in vacuo* at 40 °C to give white crystals (yield: 0.5 g > 98% of theory).
m.p. 79.4 °C; TLC ($CHCl_3$: MeOH = 6 : 1): $R_f = 0.65$; ^{1}H NMR (300MHz, $CDCl_3$, 20 °C, TMS, δ, ppm): 0.88 (t, 9H, C*H*$_3$, *J* = 6.6 Hz), 1.27 (overlapped peaks, 48H, $CH_3(CH_2)_8$), 1.46 (overlapped peaks, 6H, $O(CH_2)_2CH_2$), 1.73 (m, 6H, OCH_2CH_2), 3.97 (overlapped t, 4H, 3- and 4-OCH_2), 4.18 (t, 2H, 2-OCH_2, *J* = 6.98 Hz), 6.60 (d, 1H, 5-benzene-*H*, *J* = 8.67 Hz), 7.70 (d, 1H, 6-benzene-*H*, *J* = 8.67 Hz), 7.97 (t, 2H, 2,4 position in pyridium ring, *J* = 6.99 Hz), 8.42 (t, 1H, 3 position in pyridium ring, *J* = 7.73 Hz), 9.07 (d, 2H, 1,5 position in pyridium ring, *J* = 5.31 Hz); ^{13}C NMR (75MHz, $CDCl_3$, 20 °C, TMS, δ, ppm): 14.12, 22.69, 25.90, 26.11, 26.19, 29.27, 29.39, 29.70, 30.42, 31.94, 68.68, 73.66, 74.68, 106.61, 123.66, 126.96, 130.88, 142.26, 142.44, 145.27, 151.18, 155.54; elemental analysis calculated (%): C 70.27, H 11.67, N 1.78; found: C 69.77, H 11.59, N 1.66.

Tetramethyl ammonium 2,3,4-tris(dodecyloxy)benzene sulfonate (**10a**): In a three-necked round-bottom flask, 0.71 g **2** (1mmol) was dissolved in 50 ml ethanol under a nitrogen atmosphere. At 60 °C, 0.8 ml (2.0 mmol) tetramethyl ammonium hydroxide (25wt% in methanol) was added. The mixture was refluxed at 60 °C for 30 minutes and filtered hot. The filtrate was stored at 4 °C overnight. The precipitate was isolated by

filtration and washed with water twice. The crude product was recrystallized twice from *n*-hexane and subsequently dried *in vacuo* at 60 °C to give white needle crystals (yield: 0.7 g > 98% of theory).

m.p. 47.0 °C; TLC ($CHCl_3$: MeOH = 6 : 1): $R_f = 0.12$; ^{1}H NMR (300MHz, $CDCl_3$, 20 °C, TMS, δ, ppm): 0.88 (t, 9H, CH_3, $J = 6.6$ Hz), 1.27 (overlapped peaks, 48H, $CH_3(CH_2)_8$), 1.45 (m, 6H, $O(CH_2)_2CH_2$), 1.79 (m, 6H, OCH_2CH_2), 3.42 (s, 12H, $^+N(CH_3)_4$), 3.94 (t, 4H, 3- and 4-OCH_2, $J = 6.6$ Hz), 4.16 (t, 2H, 2-OCH_2, $J = 7.17$ Hz), 6.57 (d, 1H, 5-benzene-*H*, $J = 9.06$ Hz), 7.57 (d, 1H, 6-benzene-*H*, $J = 9.06$ Hz); ^{13}C NMR (75MHz, $CDCl_3$, 20 °C, TMS, δ, ppm): 14.12, 22.69, 26.03, 26.14, 26.21, 29.40, 29.46, 29.66, 29.71, 29.77, 29.86, 31.94, 55.59, 68.63, 73.59, 74.50, 106.49, 123.21, 132.96, 142.34, 151.13, 154.86; IR (KBr, cm^{-1}): 3435.83 (s, broad), 2956.35 (m), 2920.78 (vs), 2875.95 (m), 2850.81 (s), 1630.32 (m, broad), 1583.60 (w), 1468.10 (m), 1436.11 (w), 1379.47 (w), 1300.63 (w), 1276.34 (w), 1216.62 (s), 1195.41 (m), 1156.99 (w), 1087.84 (s), 1063.19 (w), 1039.60 (w), 885.73 (w), 811.16 (w), 738.43 (w), 721.39 (w), 686.57 (w), 667.28 (w), 633.80 (w), 607.99 (w), 580.02 (w), 535.26 (w); elemental analysis calculated (%): C 70.27, H 11.67, N 1.78; found: C 69.77, H 11.59, N 1.66.

Tetraethyl ammonium 2,3,4-tris(dodecyloxy)benzene sulfonate (**10b**): In a three-necked round-bottom flask, 1.1 g **2** (1.5 mmol) was dissolved in 50 ml ethanol under a nitrogen atmosphere. At 60 °C, 0.8 ml (2 mmol) tetraethyl ammonium hydroxide (25wt% in methanol) was added. The mixture was stirred at 60 °C for 30 minutes and filtered hot. The filtrate was stored at 4 °C overnight. The precipitate was isolated by filtration and washed with water twicw. The crude product was recrystallized twice from *n*-hexane and subsequently dried *in vacuo* at 60 °C to give white crystals (yield: 1.2 g > 98% of theory).

m.p. 124.7 °C; TLC ($CHCl_3$: MeOH = 6 : 1): $R_f = 0.20$; ^{1}H NMR (300MHz, $CDCl_3$, 20 °C, TMS, δ, ppm): 0.90 (t, 9H, CH_3, $J = 6.71$ Hz), 1.27 (overlapped peaks, 60H, $CH_3(CH_2)_8$ and $^+N(CH_2CH_3)_4$), 1.45 (m, 6H, $O(CH_2)_2CH_2$), 1.77 (m, 6H, OCH_2CH_2), 3.38 (tetra, 8H, $^+N(CH_2CH_3)_4$, $J = 7.17$ Hz), 3.94 (tetra, 4H, 3- and 4-OCH_2, $J = 6.42$ Hz), 4.17 (t, 2H, 2-OCH_2, $J = 7.16$ Hz), 6.53 (d, 1H, 5-benzene-*H*, $J = 8.85$ Hz), 7.61 (d, 1H, 6-benzene-*H*, $J = 8.67$ Hz); ^{13}C NMR (75MHz, $CDCl_3$, 20 °C, TMS, δ, ppm): 7.73, 14.14, 22.71, 26.09, 26.15, 26.22, 29.41, 29.72, 29.78,

30.46, 31.96, 52.60, 133.81, 142.30, 144.93, 145.27, 151.31, 154.46; IR (KBr, cm^{-1}): 3440.32 (s, broad), 2919.37 (vs), 2851.42 (vs), 1631.43 (w), 1583.89 (w), 1487.08 (m), 1468.70 (m), 1438.27 (m), 1379.08 (w), 1301.87 (w), 1277.64 (w), 1220.43 (m), 1194.21 (m), 1161.39 (w), 1129.02 (w), 1087.92 (m), 1064.11 (w), 1046.01 (w), 956.37 (w), 948.50 (w), 800.55 (w), 721.65 (w), 692.38 (w), 634.40 (w), 611.10 (w), 581.82 (w), 537.59 (w); elemental analysis calculated (%): C 71.46, H 11.63, N 1.67; found: C 71.55, H 11.28, N 1.64.

Tetrabutyl ammonium 2,3,4-tris(dodecyloxy)benzene sulfonate (**10c**): In a three-necked round-bottom flask, 1.1 g **2** (1.5 mmol) was dissolved in 50 ml ethanol under a nitrogen atmosphere. At 60 °C, 0.8 ml (2.0 mmol) tetrabutyl ammonium hydroxide (25wt% in methanol) was added. The mixture was refluxed at 60 °C for 30 minutes and filtered hot. The filtrate was stored at 4 °C overnight. The precipitate was filtered and washed with water twice. The crude product was recrystallized twice from *n*-hexane and subsequently dried *in vacuo* at 60 °C to give white crystals (yield: 1.4 g > 98% of theory).

m.p. 81.4 °C; TLC ($CHCl_3$: MeOH = 6 : 1): $R_f = 0.46$; ^{1}H NMR (300MHz, $CDCl_3$, 20 °C, TMS, δ, ppm): 0.88 (m, 9H, CH_3), 0.96 (t, 12H, $(CH_3C_3H_6)_4N^+$, $J = 7.37$ Hz), 1.27 (overlapped peaks, 48H, $CH_3(CH_2)_8$), 1.40 (m, 14H, $O(CH_2)_2CH_2$ and $(CH_3CH_2C_2H_4)_4N^+$), 1.63 (m, 8H, $(CH_3CH_2CH_2CH_2)_4N^+$), 1.83 (m, 6H, OCH_2CH_2), 3.31 (t, 8H, $^+N(CH_2C_2H_4CH_3)_4$, $J = 8.12$ Hz), 3.94 (overlapped t, 4H, 3- and 4-OCH_2), 4.18 (t, 2H, 2-OCH_2, $J = 7.16$ Hz), 6.51 (d, 1H, 5-benzene-*H*, $J = 8.67$ Hz), 7.63 (d, 1H, 6-benzene-*H*, $J = 8.67$ Hz); ^{13}C NMR (75MHz, $CDCl_3$, 20 °C, TMS, δ, ppm): 13.70, 14.12, 19.70, 22.69, 24.09, 26.08, 26.12, 26.21, 29.39, 29.46, 29.65, 29.69, 29.76, 30.44, 30.53, 31.94, 58.71, 68.56, 74.48, 106.19, 134.17, 142.29, 151.41, 154.29; IR (KBr, cm-1): 3437.84 (s, broad), 2918.15 (vs), 2582.00 (s), 1633.53 (m), 1583.19 (m), 1467.97 (m), 1438.32 (m), 1375.90 (w), 1303.52 (w), 1276.11 (w), 1211.57 (s), 1156.19 (w), 1085.04 (m), 1041.41 (w), 801.63 (w), 721.46 (w), 684.15 (w), 610.77 (w), 578.15 (w), 536.00 (w); elemental analysis calculated (%): C 73.13, H 11.96, N 1.47; found: C 72.40, H 11.05, N 1.40.

3,4,5-Trihydroxy-benzene sulfonic acid (11): Air was bubbled for five hours through 100 ml of an aqueous solution of pyrogallol (10 g, 0.08 mol), Na_2SO_3 (24.1 g, 0.19 mol)

and NaOH (3.34 g, 0.08 mol). The reaction solution was then acidified with 40 ml HCl (16%) and became continuously extracted with diethylether for 48 hours in a liquid-liquid extraction apparatus. Barium acetate aqueous solution (48.84 g, 0.191 mol) was added until no further precipitate was formed and the filtrate was run subsequently over a pre-acidified ion-exchanger column (Amberlite IR120) to remove all metal ions. After decoloration of the eluate by boiling (15 min) with two spoon of activated carbon, the water was removed by a rotary evaporator to yield white crystals. The product was dried over P_4O_{10} *in vacuo* for 24 hours to produce 9.98 g of compound **11** (yield: 9.98 g ≅ 61% of theory).

^{1}H NMR (300 MHz, D_2O, 20 °C, δ, ppm): 6.95 (s, 2H, aromatic *H*); ^{13}C NMR (75 MHz, D_2O, 20 °C, δ, ppm): 105.89 (2-benzene-*C*), 133.91 (4-benzene-*C*), 135.42 (1-benzene-*C*), 144.80 (3-benzene-*C*).

Lithium 2,3,4-tris(dodecyloxy)benzene sulfonate (12): 3,4,5-trihydroxy-benzene sulfonic acid (1.4 g, 6.75 mmol) and Li_2CO_3 (10,75 g, 0.15 mol) were mixed with 50 ml dried DMF in a 100 ml three-necked flask with a magnetic stirrer under a nitrogen atmosphere. At 100 °C, 1-bromododecane (6.3 ml, 0.026 mol) was added dropwise. The reaction mixture was stirred for 48 hours at 100 °C. After reaction, the mixture was poured into 50 ml ice water slowly and was extracted by chloroform three times. The chloroform was removed and large amount of acetone was added to obtain the precipitation. The precipitate was isolated by filtration and was recrystallized in 100 ml methanol twice to give a crude light yellow powder. The further purification was done by chromatography on silica gel with mixed methanol and $CHCl_3$ (1 / 6) to yield about 50 mg white solid (yield: 50 mg ≅ 10% of theory).

m .p. 51.7 °C (by DSC); TLC ($CHCl_3$: MeOH = 6 : 1): R_f = 0.31; ^{1}H NMR (300MHz, DMSO-d_6, 20 °C, TMS, δ, ppm): 0.86 (t, 9H, CH_3, J = 6.8 Hz), 1.25 (overlapped peaks, 54H, $CH_3(CH_2)_9$), 1.62 (m, 6H, OCH_2CH_2), 3.20 (m, 4H, 3- and 5-OCH_2), 3.83 (t, 2H, 4-OCH_2, J = 6.8 Hz), 6.59 (s, 2H, 2,6-benzene-*H*); ^{13}C NMR (75MHz, DMSO-d_6, 20 °C, TMS, δ, ppm): 13.86, 21.53, 22.02, 29.36, 29.01, 29.38, 31.22, 71.56, 105.08, 134.30, 143.27, 149.70.

Sodium 3,4,5-tris(dodecyloxy)benzene sulfonate (13): 3,4,5-trihydroxy-benzene sulfonic acid (**11**) (0.45 g, 2.2 mmol) and Na_2CO_3 (6.76 g, 4.9 mmol) were mixed with

25 ml dried DMF in a 100 ml three-necked flask with a magnetic stirrer under a nitrogen atmosphere. At 60 °C, 1-bromododecane (3.5 ml, 14.6 mmol) was added dropwise. The reaction mixture was stirred for 24 hours at 80 °C. After reaction, the mixture was poured into 50 ml ice water slowly and was extracted by chloroform three times. The chloroform was removed and large amount of acetone was added to obtain the precipitation. The precipitate was isolated by filtration and was recrystallized in 100 ml methanol at 4 °C twice to give a crude light yellow powder. The further purification was done by chromatography on silica gel with mixed methanol and $CHCl_3$ (1 / 6) to yield about 450 mg white solid. (yield: 0.45 g ≅ 28% of theory).
m.p. -7.1 °C (by DSC); TLC ($CHCl_3$: MeOH = 6 : 1): $R_f = 0.59$; ^{1}H NMR (300MHz, $CDCl_3$, 20 °C, TMS, δ, ppm): 0.88 (t, 9H, C*H*$_3$, *J* = 6.6 Hz), 1.26 (overlapped peaks, 48H, (C*H*$_2$)$_8$), 1.47 (broad, 6H, O(CH$_2$)$_2$C*H*$_2$), 1.72 (m, 6H, OCH$_2$C*H*$_2$), 3.90 (overlapped peaks, 6H, OC*H*$_2$, *J* = 6.6 Hz), 7.03 (s, 2H, 2,6-benzene-*H*); ^{13}C NMR (75MHz, $CDCl_3$, 20 °C, TMS, δ, ppm): 14.12, 22.71, 26.27, 29.44, 29.62, 29.80, 31.96, 31.96, 73.42, 106.7, 139.52, 140.03, 152.99.

Potassium 3,4,5-tris(dodecyloxy)benzene sulfonate (14): 3,4,5-trihydroxy-benzene sulfonic acid (**11**) (0.45 g, 2.2 mmol) and K_2CO_3 (6.76 g, 49 mmol) were mixed with 25 ml dried DMF in a 100 ml three-necked flask with a magnetic stirrer under a nitrogen atmosphere. At 60 °C, 1-bromododecane (3.5 ml, 14.6 mmol) was added dropwise. The reaction mixture was stirred for 24 hours at 80 °C. After reaction, the mixture was poured into 50 ml ice water slowly and was extracted by chloroform three times. The chloroform was removed and large amount of acetone was added to obtain the precipitation. The precipitate was isolated by filtration and was recrystallized in 100 ml methanol twice to give a crude light yellow powder. The further purification was done by chromatography on silica gel with mixed methanol and ethyl acetate (1 / 6) to yield about 50 mg white solid (yield: 0.5 g ≅ 30% of theory).
m.p. -9.1 °C; TLC (EtOAc : MeOH = 6 : 1): $R_f = 0.15$; ^{1}H NMR (300MHz, $CDCl_3$, 20 °C, TMS, δ, ppm): 0.88 (t, 9H, C*H*$_3$, *J* = 6.6 Hz), 1.26 (overlapped peaks, 48H, (C*H*$_2$)$_8$), 1.47 (broad, 6H, O(CH$_2$)$_2$C*H*$_2$), 1.72 (m, 6H, OCH$_2$C*H*$_2$), 3.90 (overlapped peaks, 6H, OCH$_2$, *J* = 6.6 Hz), 7.03 (s, 2H, 2,6-benzene-*H*); ^{13}C NMR (75MHz, $CDCl_3$, 20 °C, TMS, δ, ppm): 14.12, 22.71, 26.27, 29.44, 29.62, 29.80, 31.96, 31.96, 73.42, 106.7, 139.52, 140.03, 152.99.

Caesium 2,3,4-tris(dodecyloxy)benzene sulfonate (15): 3,4,5-trihydroxy-benzene sulfonic acid (**11**) (2.25 g, 6.3 mmol) and Cs_2CO_3 (23.8 g) were mixed with 60 mL dried DMF in a 100 ml three-necked flask with a magnetic stirrer under a nitrogen atmosphere. At 60 °C, 1-bromododecane (10 ml, 41.6 mmol) was added dropwise. The reaction mixture was stirred for 24 hours at 60 °C. After reaction, the mixture was poured into 100 ml ice water slowly. The precipitate was isolated by filtration and dried *in vacuo*. The crude product was recrystallized from 100 ml methanol twice to give a white powder (yield: 1.8 g ≅ 34% of theory).
m.p. 80.6 °C (by DSC); TLC ($CHCl_3$: MeOH = 6 : 1): R_f = 0.46; ^{1}H NMR (300MHz, $CDCl_3$, 20 °C, TMS, δ, ppm): 0.88 (t, 9H, C*H*$_3$, *J* = 6.6 Hz), 1.26 (overlapped peaks, 48H, $CH_3(CH_2)_8$), 1.43 (broad, 6H, $OCH_2(CH_2)_2$), 1.72 (m, 6H, OCH_2CH_2), 3.90 (m, 6H, OCH_2, *J* = 6.6 Hz), 7.03 (s, 2H, 2,6-benzene-*H*); ^{13}C NMR (75MHz, $CDCl_3$, 20 °C, TMS, δ, ppm): 14.12, 22.71, 26.27, 29.44, 29.62, 29.80, 31.96, 31.96, 73.42, 106.7, 139.52, 140.03, 152.99; elemental analysis calculated (%): C 59.84, H 9.21; found (%): C 59.06, H 9.30.

Caesium 3,4,5-tris(undec-10-enyloxy)benzene sulfonate (16): 3,4,5-trihydroxy-benzene sulfonic acid (**11**) (2.25 g, 6.3 mmol) and Cs_2CO_3 (23.8 g) were mixed with 60 ml dried DMF in a 100 ml three-necked flask with a magnetic stirrer under a nitrogen atmosphere. At 60 °C, 9.5 ml 1-bromo-undecene (41.6 mmol) was added dropwise. The reaction mixture was stirred for 24 hours at 60 °C. After reaction, the mixture was poured into 100 ml ice water slowly. The precipitate was isolated by filtration and dried *in vacuo*. The crude product was recrystallized from 100 ml methanol twice to give a white powder (yield: 1.9 g ≅ 38% of theory).
m.p. 111.5 °C (by DSC); TLC ($CHCl_3$: MeOH = 6 : 1): R_f = 0.51; ^{1}H NMR (300MHz, $CDCl_3$, 20 °C, TMS, δ, ppm): 0.88 (t, 9H, C*H*$_3$, *J* = 6.6 Hz), 1.26 (overlapped peaks, 48H, $CH_3(CH_2)_8$), 1.47 (m, 6H, $O(CH_2)_2CH_2$), 1.78 (m, 6H, OCH_2CH_2), 3.90 (overlapped t, 6H, OCH_2, *J* = 6.3 Hz), 6.55 (d, 2H, 4,6-benzene-*H*, *J* = 8.1 Hz), 6.90 (t, 1H, 5-benzene-*H*, *J* = 8.4 Hz); ^{13}C NMR (75MHz, $CDCl_3$, 20 °C, TMS, δ, ppm): 14.1, 22.7, 26.1, 29.4, 29.5, 29.9, 30.3, 31.9, 69.0, 73.3, 106.7, 123.1, 138.4, 153.4; elemental analysis calculated (%): C 58.93, H 8.24; found (%): C 57.68, H 8.00.

Results and Discussion

Synthesis of wedge-shaped benzene sulfonated amphiphiles

2,3,4-Tris(alkoxy)benzene sulfonates are readily accessible by sulfonation of 2,3,4-tris(alkoxy)benzenes that have been prepared by alkylation of pyrogallol (1,2,3-trihydroxybenzene) as depicted in Scheme 3.1. 1,2,3-Trihydroxybenzene was alkylated with 1-bromo-dodecane in DMF to produce 1,2,3-tris(dodecyloxy)benzene (**1**) in 76% yield after recrystallization from acetone [13].

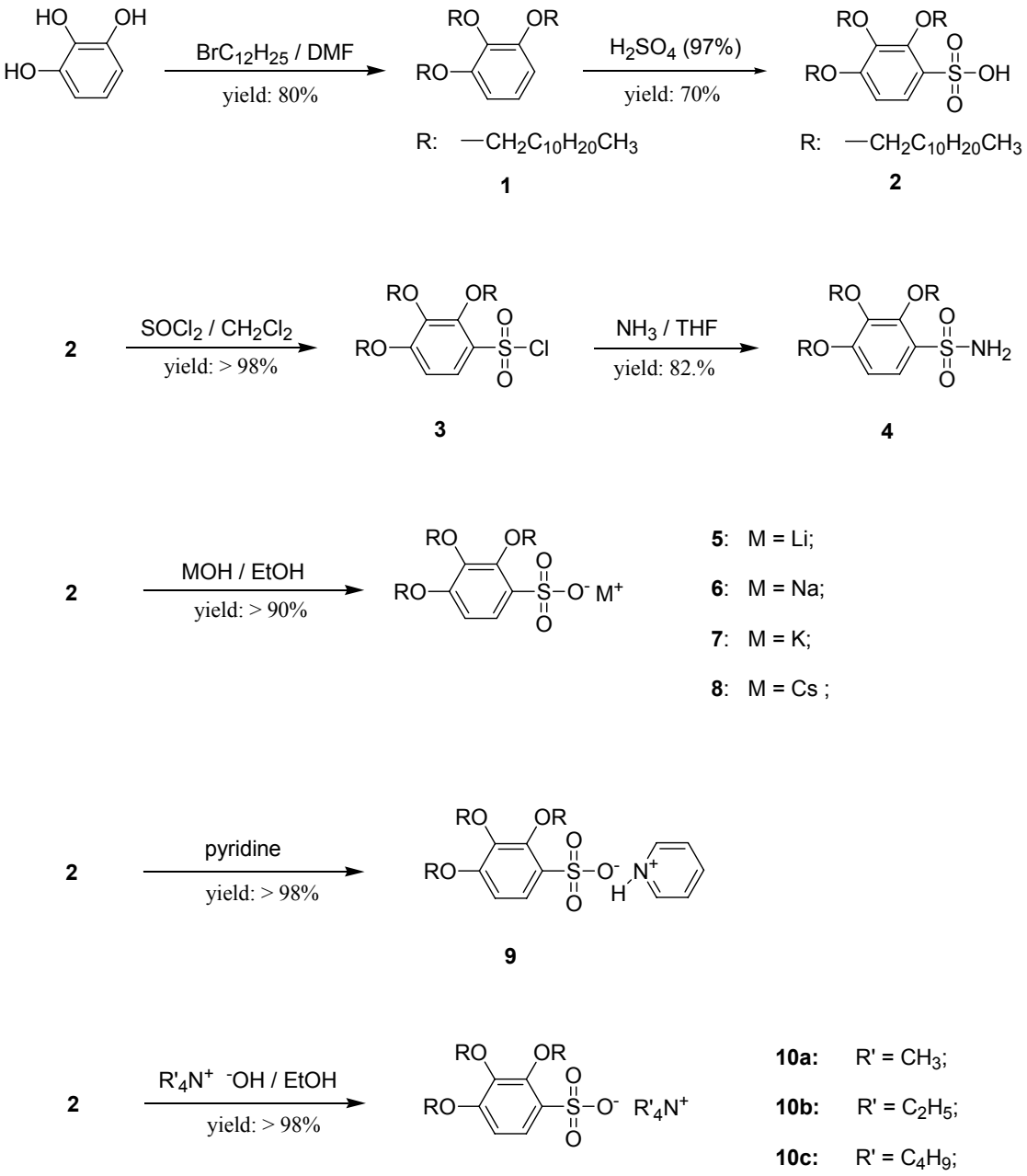

Scheme 3.1 Synthesis of 2,3,4-tris(dodecyloxy)benzene sulfonic acid and its derivatives.

Sulfonation of the 1,2,3-tris(dodecyloxy)benzene was carried out with concentrated sulfuric acid at 20 °C for 2 hours to produce 2,3,4-tris(dodecyloxy)benzene sulfonic acid (**2**) in 87.2% yield after recrystallization from *n*-hexane. Lithium (**5**), sodium (**6**), potassium (**7**) and caesium sulfonates (**8**) were synthesized by neutralizing the sulfonic acid **2** with methyl lithium, sodium methoxide, potassium methoxide and caesium hydroxide respectively at room temperature. The pyridinium sulfonate (**9**) and the alkyl ammonium sulfonates (**10a-c**) were produced analogously by converting **2** with the corresponding organic nitrogen bases at room temperature to obtain the products in nearly quantitative yield. Reacting the sulfonic acid **2** with thionylchloride yielded sulfonchloride **3** that could be transformed into 2,3,4-tris(dodecyloxy)benzene sulfonamide **4** by dissolving compound **3** in ammonia gas saturated THF solution and stirring the mixture for one week at 30 °C.

Attempts were made to produce 2,3,4-tris(alkoxy)benzene sulfonic acids with short alkoxy chains (Scheme 3.2). The reactions yielded oily products that could not be purified by crystallization because of their low melting temperatures. Column chromatography on silica gel was unsuccessful too, since the highly polar molecules permanently adhered to the stationary phase. The description of their preparation and purification via suitable salts will be the matter of the subsequent experiments.

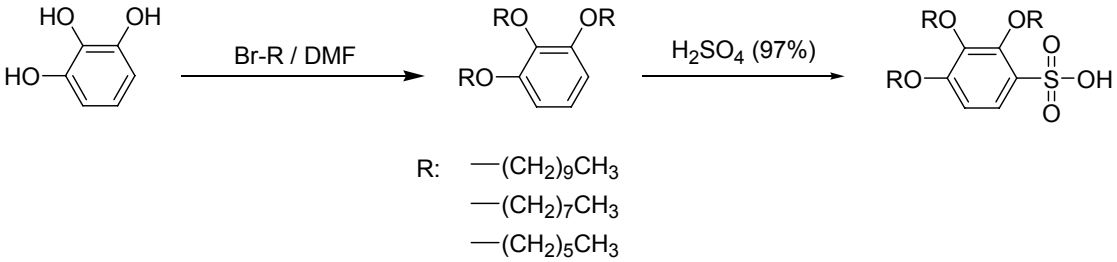

Scheme 3.2 Scheme of the synthesis strategy of 2,3,4-tris(alky1oxy)benzene sulfonic acid.

Based on the mechanism of electrophilic substitution, the sulfonation of 1,2,3-alkoxy benzenes will always occur in position 4 or 6 of the benzene ring. Hence, the symmetrically substituted 3,4,5– derivatives cannot be prepared by this method. It is known that nitration in 5-position of the 1,2,3-alkoxy benzene ring can be achieved on reacting the aromate with silica adsorbed nitric acid [14]. However, the analogous reaction with silica adsorbed sulphuric acid failed to yield the symmetrically substituted product.

The synthesis of the desired symmetric products was performed via the 3,4,5-trihydroxy-benzene sulfonic acid. The preparation of this compound has been described previously by sulfonation of pyrogallol with concentrated sulphuric acid [15]. However, since mixtures of isomers were obtained, it was decided to generate the sulfonic acid under oxidative sulfonation conditions as depicted in Scheme 3.3. Pyrogallol was oxidized in an alkaline solution of sodium sulfite in the presence of air. Since phenols rapidly form black oxidation products in the presence of bases and oxygen, the obtained crude 3,4,5-trihydroxy-benzene sulfonic acid need to be purified in three steps. First, the organic impurities were washed off by continuous extraction of the reaction mixture with diethyl ether. Subsequently all sulfite ions were removed by precipitation with barium acetate. And finally the organic acid was liberated by cation exchange. After adsorption of remaining yellow-brownish colorants on activated charcoal, the acid was isolated from the aqueous solution and dried over phosphorus pentoxide *in vacuo* to yield 61% of pure acid **11**.

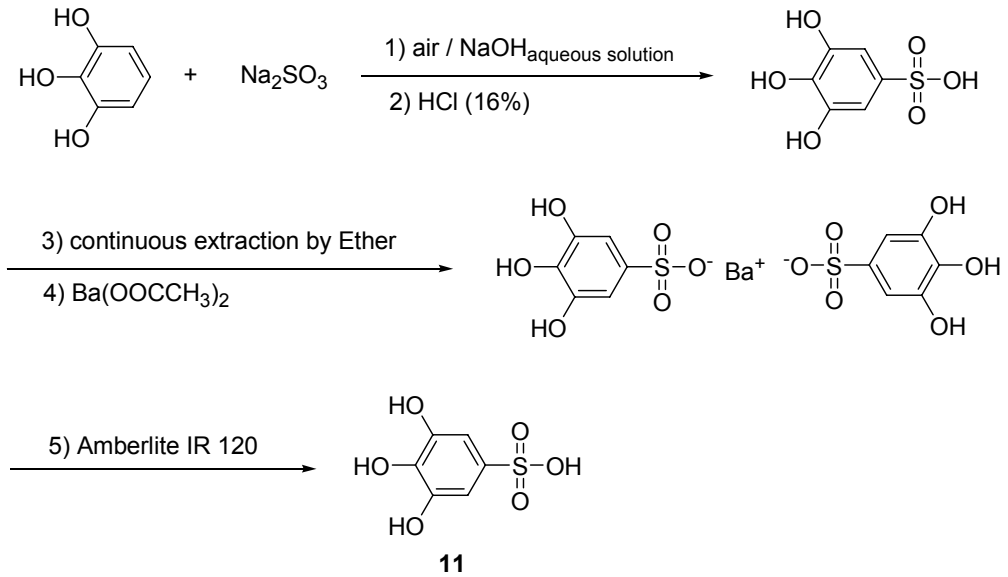

Scheme 3.3 Synthesis of 3,4,5-trihydroxybenzenesulfonic acid (**11**).

The symmetrically substituted compounds **12 – 15** were synthesized from **11** by alkylation with 1-bromododecane in dried DMF using the corresponding alkali metal carbonates (M_2CO_3: M = Li, Na, K, Cs) as base (cf. Scheme 3.4). The purification of **12 – 14** (Li, Na, K) was achieved by column chromatography over silica on elution with mixtures from methanol and chloroform. The caesium sulfonate **15** could simply

be purified by recrystallization from hot methanol and subsequent freeze-drying from benzene. In an analogous method caesium 3,4,5-tris(undec-10-enyloxy)benzene sulfonate (**16**) was obtained as well (cf. Scheme 3.4).

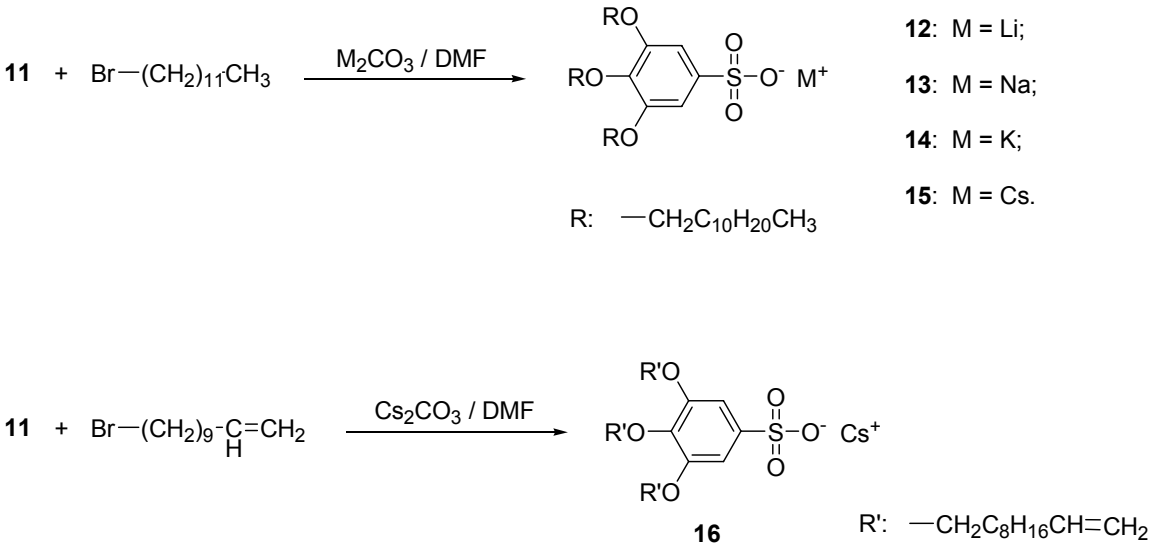

Scheme 3.4 Synthesis of 3,4,5-tris(dodecyloxy)benzene sulfonate of alkali metal (Li^+, Na^+, K^+, Cs^+) and caesium 3,4,5-tris(undec-10-enyloxy)benzene sulfonate.

The purity of the synthesized materials was checked by thin layer chromatography (TLC) and elemental analysis to exceed 99% in all cases. The salts were freeze-dried and stored under nitrogen prior to use.

Thermal analysis of 2,3,4-substituted benzene sulfonates

The thermal characterization was carried out by a combination of differential scanning calorimetry (DSC) and hot-stage thermal optical polarized microscopy (TOPM). Transition temperatures were determined by means of DSC at a heating / cooling rate of 10 °C min^{-1} throughout. The DSC measurement program usually was composed of at least two heating runs and one cooling run. During the first heating run many compounds exhibit phase transitions that do not appear in the second and further heating runs, and that hence are called 'Virgin phase'. The occurrence of virgin phases is connected to the specific condition of isolation or recrystallization of the pure material during synthesis. Virgin phases hence belong to a class of memory effects that depend on the (thermal) history of a compound.

Table 3.1 Thermal characterization of 2,3,4-tris(dodecyloxy)benzene sulfonate compounds **2–10** obtained from DSC measurements (second heating run, dT/dt = 10 °C/min)

	Functional group	Phase transition (°C) and corresponding enthalpy change (kJ/mol)	
		First heating	Cooling
2	**-OH**	k 70.7 (100.7) i	i 14.0 (-38.83) k
4	**-NH$_2$**	k 57.3 (59.87) Φ 119.0 (4.20) i	i 93.5 (-2.80) Φ 46.4 (35.06) k
5	**Li$^+$**	k 93.2 (4.71) Φ 117.6 (48.07) i	i –17.0 (-12.63) k
6	**Na$^+$**	k 49.7 (108.87) Φ 145.0 (1.80) i	i ? Φ 4.8 (-51.32) k
7	**K$^+$**	k 4.1 (8.91) Φ_1 46.9 (5.75) Φ_2 122.0 (4.57) Φ_3 170.5 (3.15) i	i 162.2 (-3.16) Φ_3 117.5 (-5.26) Φ_2 37.3 (1.03) Φ_1 10.8 (-21.09) k
8	**Cs$^+$**	k 51.3 (25.05) C_{hd} 205.9 (4.20) i	i 198.7 (-1.38) C_{hd} 37.3 (-20.52) k
9	**Py$^+$**	k 85.7 (96.4) C_{hd} 131.7 (1.4) i	i 114.3 (-0.93) C_{hd} 17.0 (-35.77) k_1
10a	**Me$_4$N$^+$**	k 89.8 (97.1) Φ_1 132.0 (6.6) Φ_2 159.7 (10.6) C_{hd} 231.5 (1.6) i	i 226.8(-1.3) C_{hd} 148.4 (-8.2) Φ_2 115.1 (-5.7) Φ_1 41.9 (-21.0) i
10b	**Et$_4$N$^+$**	k 125.6 (79.3) i	i 107.3 (-0.3) Φ_{mono} 98.5 (-74.6) k
10c	**Bu$_4$N$^+$**	k 85.1 (82.8) i	i 67.8 (-76.4) k
		Second heating	
2	**-OH**	k 55.7 (32.55) i	
4	**-NH$_2$**	k 55.0 (37.43) Φ 117.9 (3.89) i	
5	**Li$^+$**	k –11.1 (6.67) Φ 160.9 (0.27) i	
6	**Na$^+$**	k_1 7.7 (19.95) k_2 21.2 (33.19) Φ 145.0 i	
7	**K$^+$**	k 17.8 (21.53) Φ_1 46.9 (1.38) Φ_2 123.4 (5.94) Φ_3 170.8 (3.06) i	
8	**Cs$^+$**	k 50.3 (23.51) C_{hd} 193.3 (2.24) i	
9	**Py$^+$**	k_1 29.9 (-25.06) k_2 52.7 (-5.11) k_3 79.4 (71.49) C_{hd} 122.0 (1.08) i	
10a	**Me$_4$N$^+$**	k 47.0 (20.5) Φ_1 129.7 (5.9) Φ_2 153.9 (9.2) C_{hd} 230.6(1.3) i	
10b	**Et$_4$N$^+$**	k 124.7 (77.0) i	
10c	**Bu$_4$N$^+$**	k 81.4 (74.5) i	

k = crystalline phase, cub = cubic mesophase, C_{hd} = hexagonal disordered columnar mesophase, Φ = mesophase – phase type not determined, {Φ_{mono}} = monotropic mesophase, i = isotropic phase, dec = decomposition.

In case of crystallization from solvents, the occurrence of a virgin phase can be caused by the cooperative interactions between the solvent used for crystallization and the

compound. When the compound is purified by recrystallization, solvent molecules may be incorporated in the matrix of the crystal. After drying under vacuum all solvent molecules volatilize and the remaining crystal lattice may differ from the thermodynamically stable, melt crystallized structure. When such a crystal is heated for the first time, the measured transition temperatures and the enthalpies can considerably differ from the 'true' i.e. thermodynamically defined melting transition. One of the crystal structure formed from the isotropic melt is the thermodynamically defined reference state of the pure compounds solid phase. Therefore the melting temperature and the enthalpy measured during the second heating is often different from that measured in the first heating scan. In this chapter, the discussion below will be based on the transitions that were observed during the second and further heating runs, as compiled in Table 3.1 and Table 3.2. Table 3.1 summarizes the measured transition temperatures as well as the corresponding enthalpy changes of compounds **2**–**10**, while Table 3.2 contains the respective thermal analysis data on the symmetrically substituted sulfonates **12**–**16**. The assignment of the type of thermal transition was supported by microscopic observations.

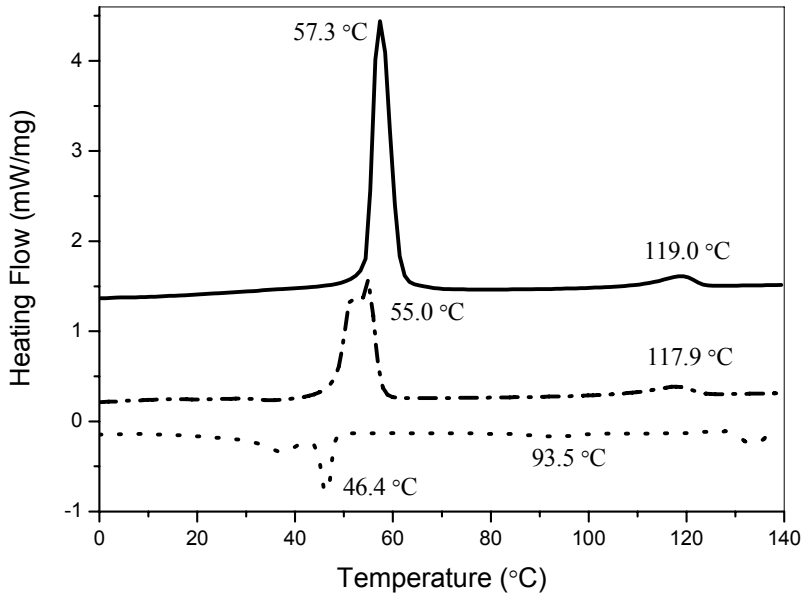

Figure 3.3 DSC thermogram of sulfonamide **4** (— = first heating scan, ·—·—·— = second heating scan, ····· = cooling scan).

The prepared amphiphilic sulfonate derivatives can be divided into hydrogen bond- and ionic compounds. Only two representatives of the first class, namely acid **2** and sulfon-

amide **4** have been prepared. While the sulfonic acid is a crystalline material, melting at 57 °C to an isotropic phase, the sulfonamide **4** exhibits a columnar mesophase between 55 and 118 °C (cf. Figure 3.3). The texture between crossed polartizers is shown in Figure 3.4. This is a first important difference to the analogous 2,3,4-tris(dodecyloxy) benzamides that do not form mesophases because the presence of an alkoxy chain in 2-position of a carbonic acid amide impedes the formation of a hydrogen bond network due to steric hindrance [16,17].

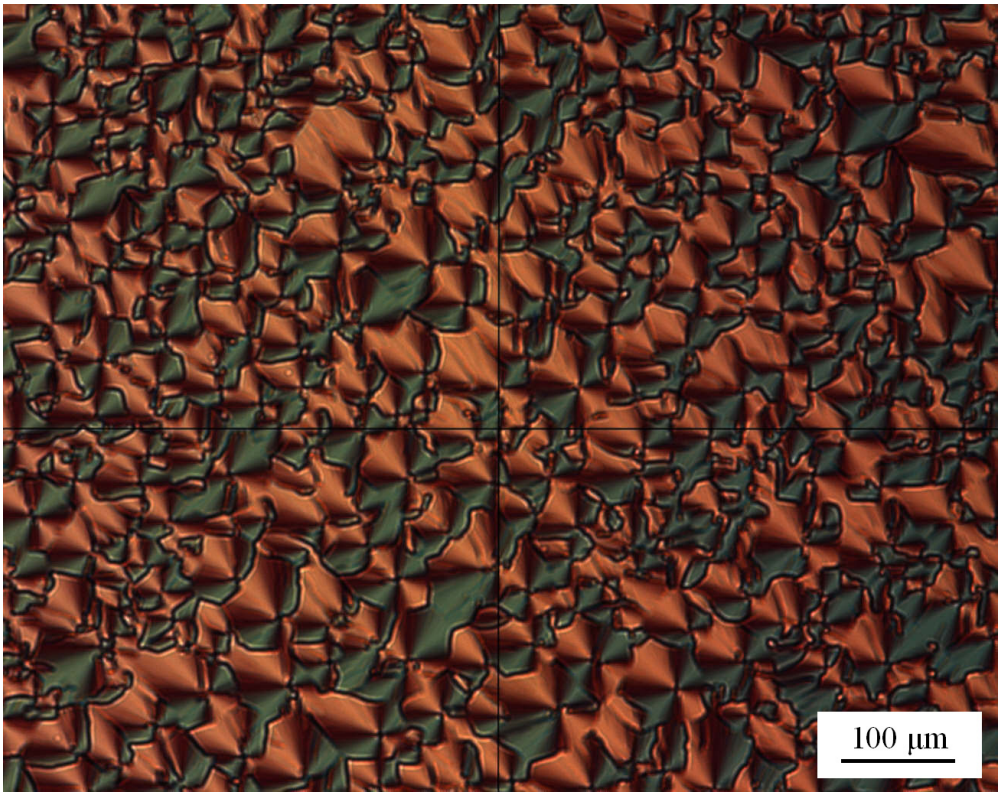

Figure 3.4 Texture of sulfonamide **4** between crossed polarizers at 80 °C

Figure 3.5 depicts a DSC thermogram of the asymmetrically substituted lithium salt **5** that is also representative for the sodium salt **6** (cf. Figure 3.7), showing two endothermic signals upon heating. Both salts form highly viscous, but optically isotropic liquids above the respective DSC melting endotherm (cf. Figure 3.6 and 3.8). The melt viscosity of both the compounds reduces abruptly on increasing the temperature above the second endotherm (**5**: T = 161 °C, **6**: T = 103 °C). Since the high viscous phase did not show shear-induced birefringence, the presence of a cubic mesophase was deduced for both salts. It has been reported [18,19] as well that the smallest alkali metal salts produce the most perfect spheres directly from the cylinders.

That also confirms from the other side that lithium (**5**) and sodium sulfonate (**6**) prefer to form the cubic phase than columnar phase.

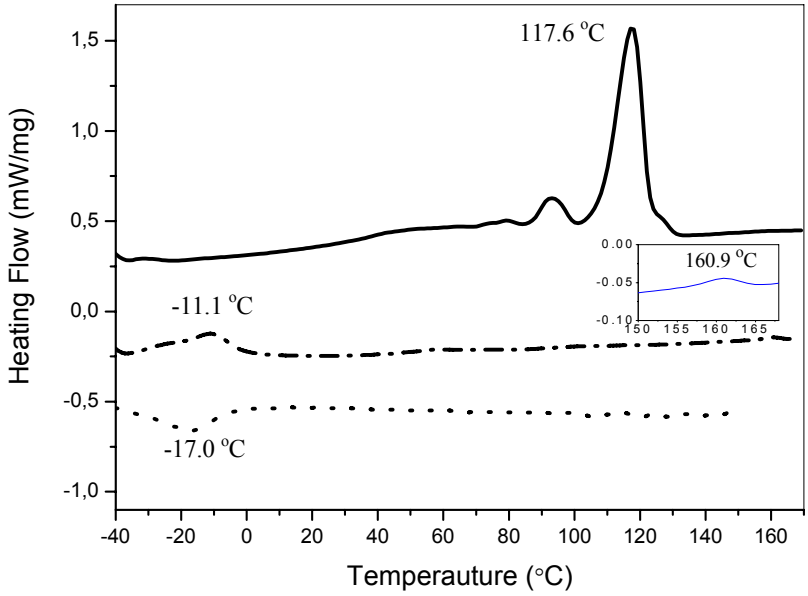

Figure 3.5 DSC thermogram of lithium salt **5** (— = first heating scan, –·–·– = second heating scan, ····· = cooling scan).

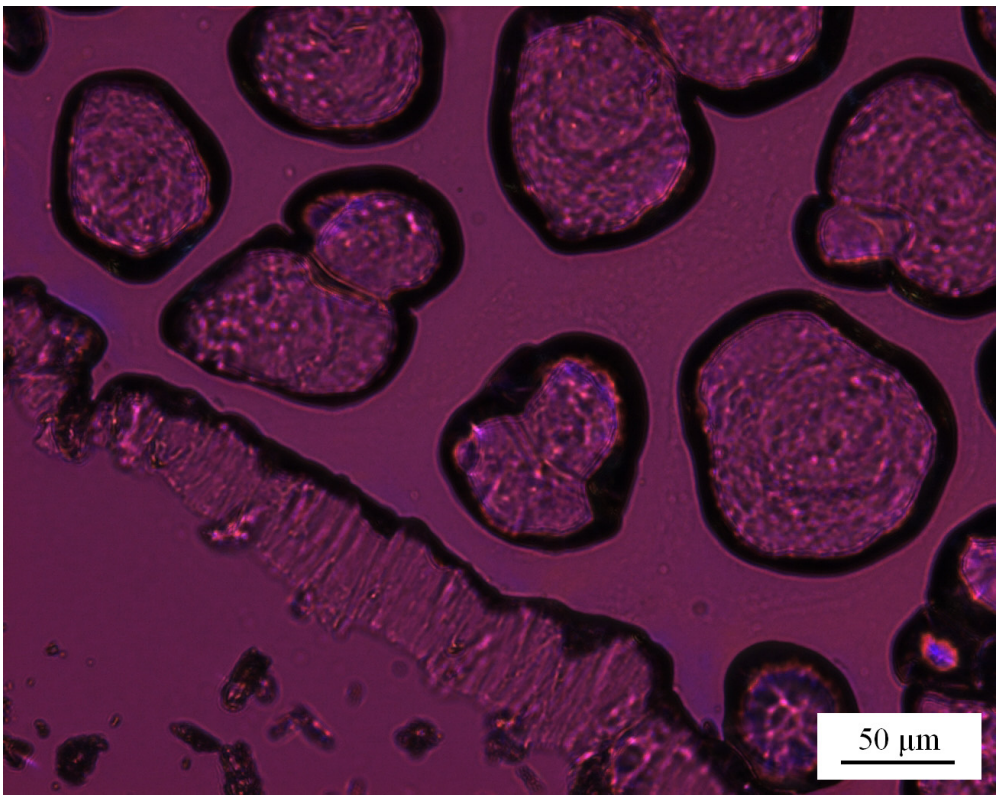

Figure 3.6 Texture of lithium salt **5** between crossed polarizers at 30°C.

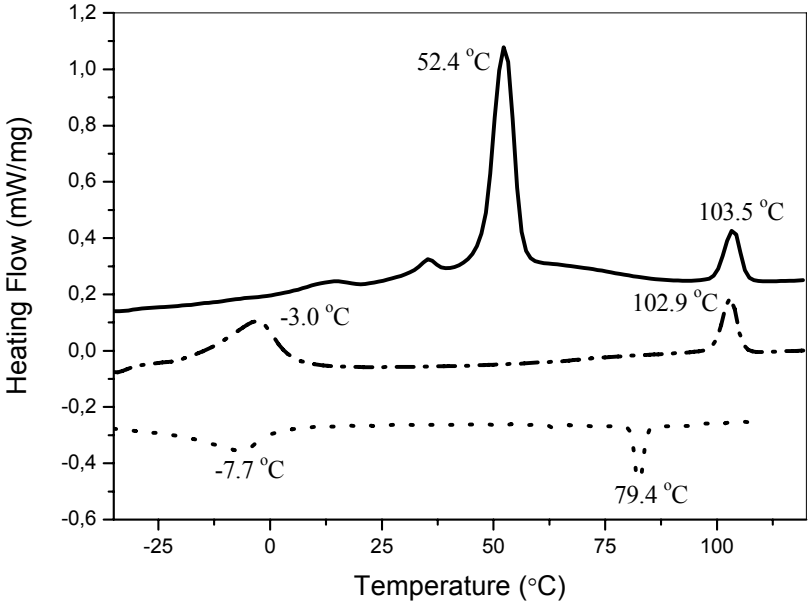

Figure 3.7 DSC thermogram of sodium salt **6** (— = first heating scan, –·–·– = second heating scan, ····· = cooling scan).

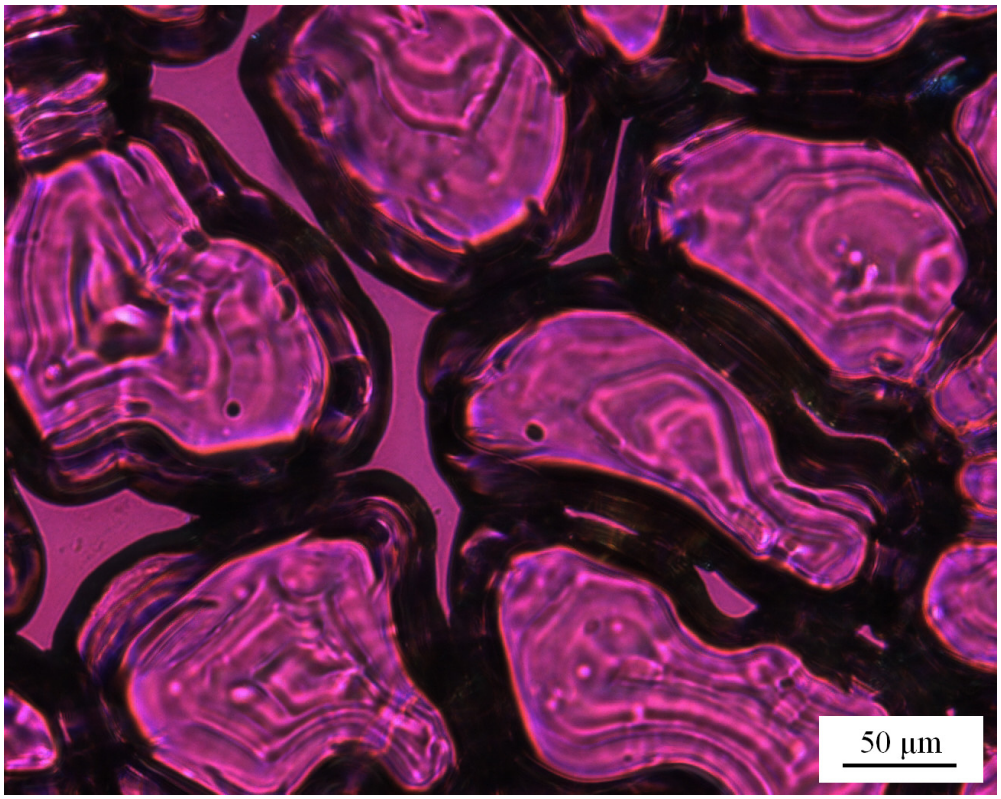

Figure 3.8 Texture of sodium salt **6** between crossed polarizers at 50°C.

The potassium salt **7** showed a complex phase sequence involving three subsequent liquid crystalline phases (cf. Figure 3.9). Although the differential calorimetry clearly detected four phase transitions between -30°C and 180 °C, only one single type of optical texture was observed under polarized light. The fan-like texture (cf. Figure 3.10) formed on cooling below the clearing temperature of 171 °C and did not significantly change on cooling to ambient temperature. However, without supporting x-ray structure determination it should not be speculated on a possible structural similarity of these three phases.

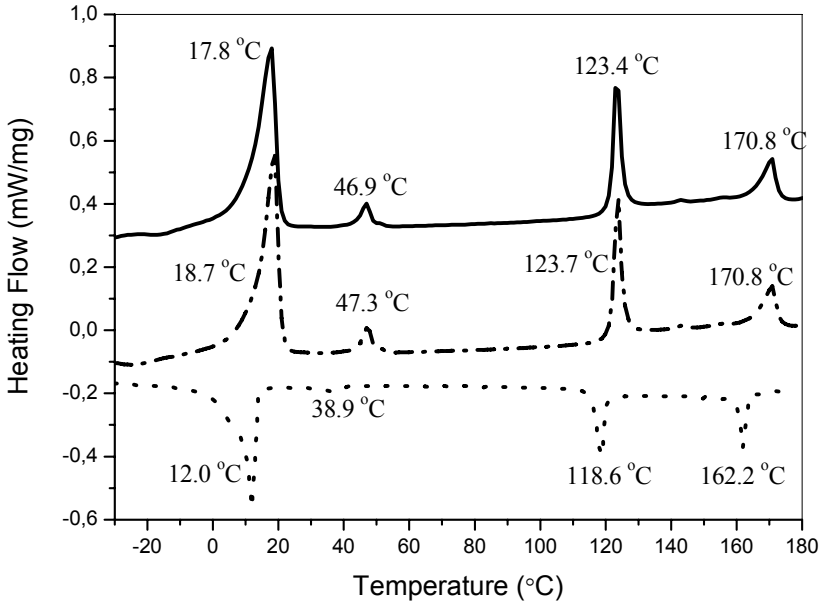

Figure 3.9 DSC thermogram of potassium salt **7** (— = first heating scan, –·–·– = second heating scan, ····· = cooling scan).

The caesium **8** and pyridinium sulfonate **9** both exhibited one mesophase, which showed optical textures characteristic for columnar mesophases (cf. Figure 3.11 and 3.12a). While the caesium salt **8** was stable at elevated temperatures (T > 240 °C) for several minutes, the pyridinium salt lost its optical anisotropy even after a short heating to 150 °C, accompanied by the evolution of gaseous decomposition products. On cooling compound **9** from the mesophase to 35 °C, a rapid phase transition that corresponded to the mesophase / crystalline transition was observed and the amorphous texture took the place of the fan-shaped texture (cf. Figure 3.12b).

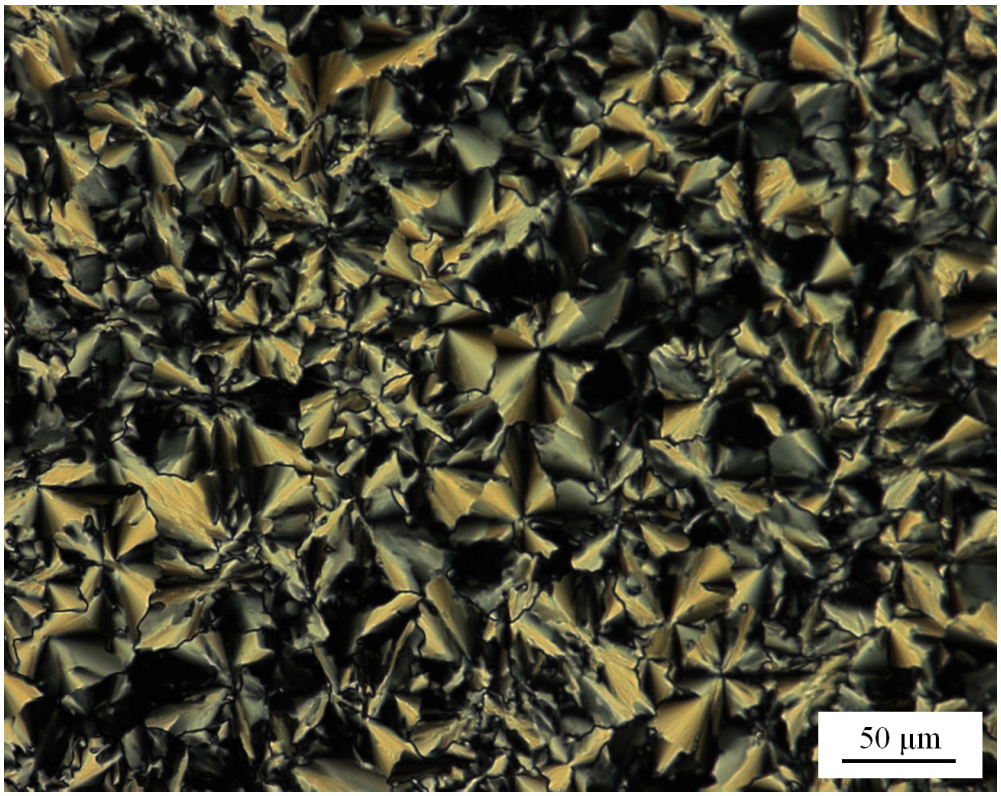

Figure 3.10 Texture of potassium salt **7** between crossed polarizers at 120°C.

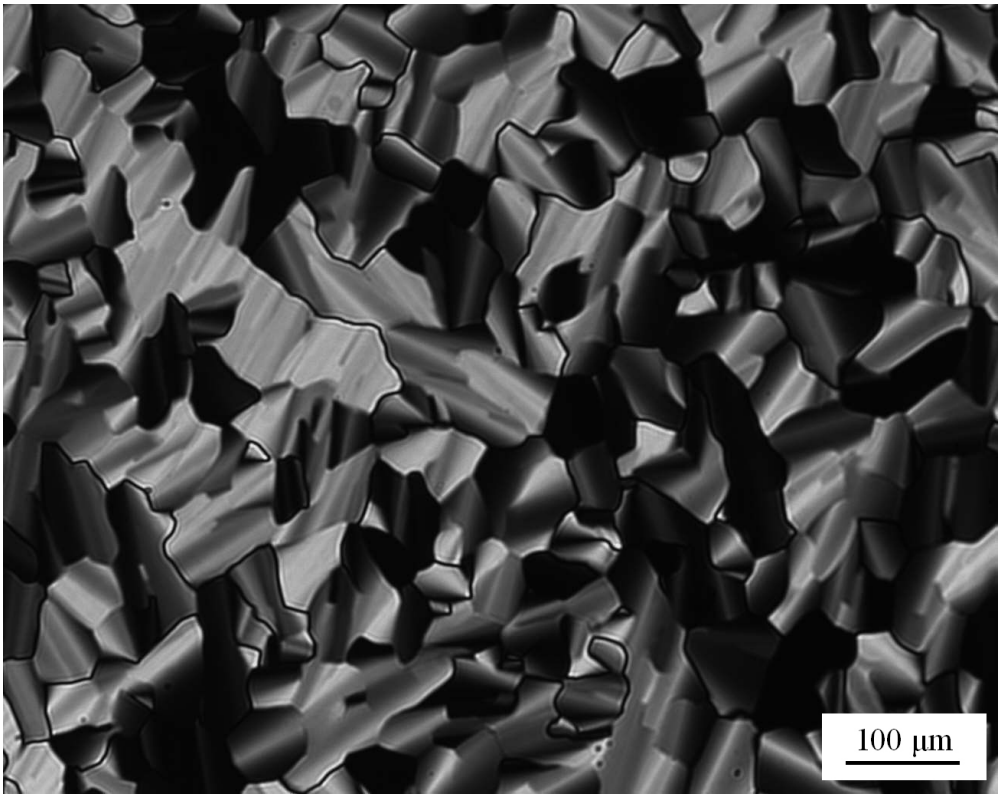

Figure 3.11 Texture of caesium salt **8** between crossed polarizers at 120°C.

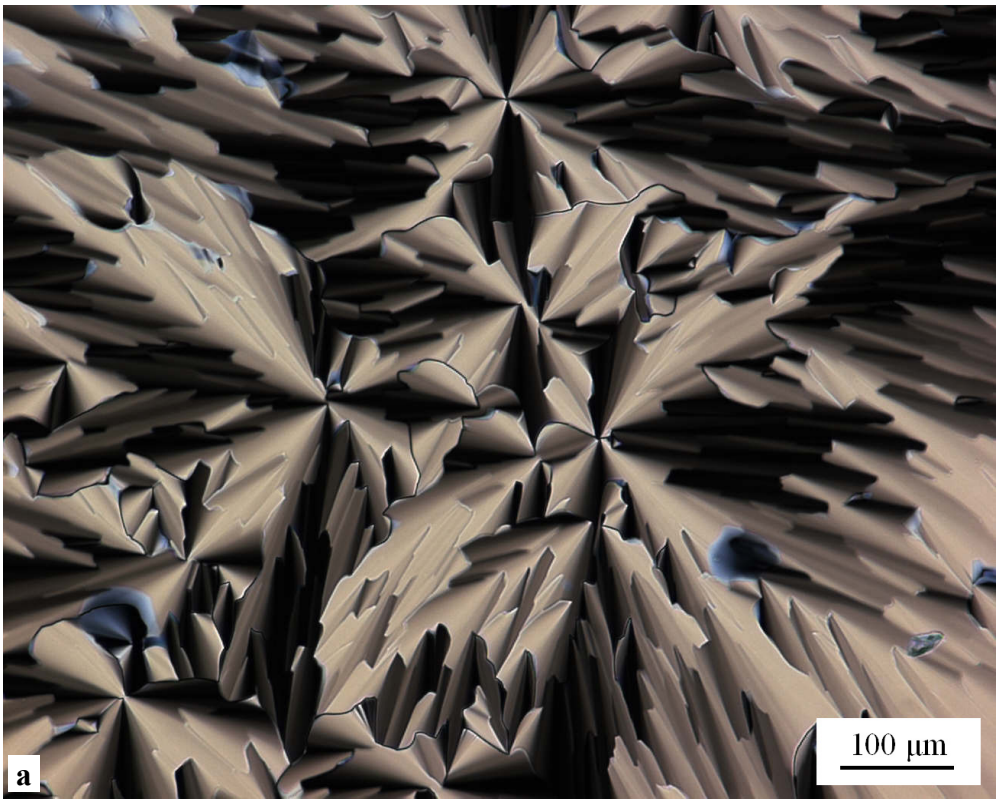

Figure 3.12 (a) Texture of pyridinium sulfonate **9** between crossed polarizers at 100°C.

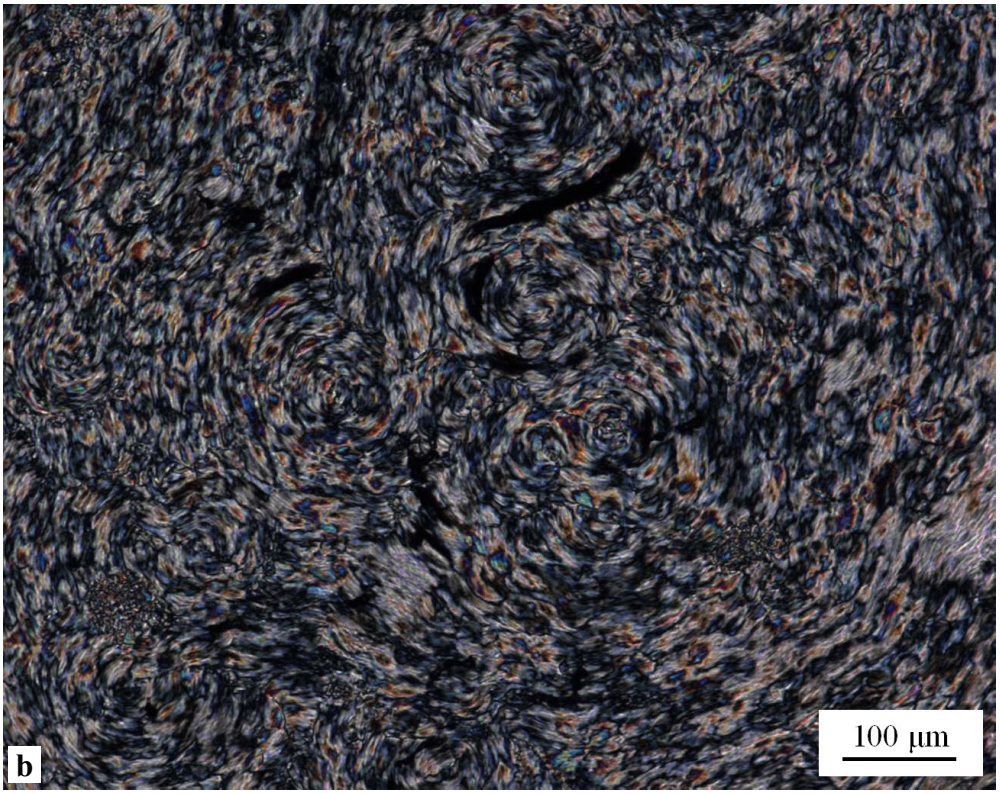

Figure 3.12 (b) Texture of pyridinium sulfonate **9** between crossed polarizers at 30 °C.

The polarized optical textures in the liquid crystal phase and the specific type of defects formed by the mesophase can manifest its intrinsic structure [20]. Although a valid phase type determination should never be based on textures alone, first hints of the phase type can be obtained. In the high temperature phase of the potassium salt **7** and in the single mesophase of the caesium sulfonate **8**, similar kinds of spherolithic textures were observed. Spherolithes can be formed in smectic as well as in columnar hexagonal phases. In Figure 3.10 and Figure 3.11 two different types of defects can be detected. First, the ends of all four cones of a spherolithic domain point towards its centre. In the columnar phase, molecular columns inside the flowerlike domains lie parallel to the glass substrate and bend into circles around the brush centres or emerge radially from the central defect [21].

The second type of defect, which can be a signature of a columnar phase is the so called "developable domain" [22], expressing that the two pairs of cones do not contact at the central point of a shperolite (cf. centre of Figure 3.10). Developable domains result from the specific topology of hexagonal columnar phases and are highly indicative for this type of phase [23,24]. Since neither conic focal domains nor oily streaks have been found that origin from topological defects observed in some smectic mesophases [25], the texture observations make the presence of columnar mesophases probable. Furthermore it was known from previous studies that wedge-shaped (tapered) amphiphiles frequently prefer to self-assemble into columnar mesophases [26].

A series of tetraalkyl ammonium 2,3,4-tris(dodecyloxy)benzene sulfonates has been prepared to generate amphiphiles with large polar head groups. The tetramethyl ammonium salt **10a** showed three subsequent mesophases (cf. Figure 3.13), similar to the DSC thermogram resembled by potassium salt **7**. On cooling from the isotropic melt compound **10a** showed a spherolithic – type texture that is frequently found with columnar mesophases (cf. Figure 3.14a). On further cooling below 160 °C the texture changed by developing a pattern of concentric black arcs around the center of each shperolithe as depicted in Figure 3.14b. Such changes are known to be characteristic for the transition from one columnar mesophase into another columnar mesophase of higher degree of structural order, e.g. disordered / ordered ($C_d \rightarrow C_o$) or hexagonal / rectangular ($C_h \rightarrow C_r$) [27]. The phase transition around 130 °C did not alter the texture;

only on crystallization at 40 °C the boundaries between the spherolithes became crumbled.

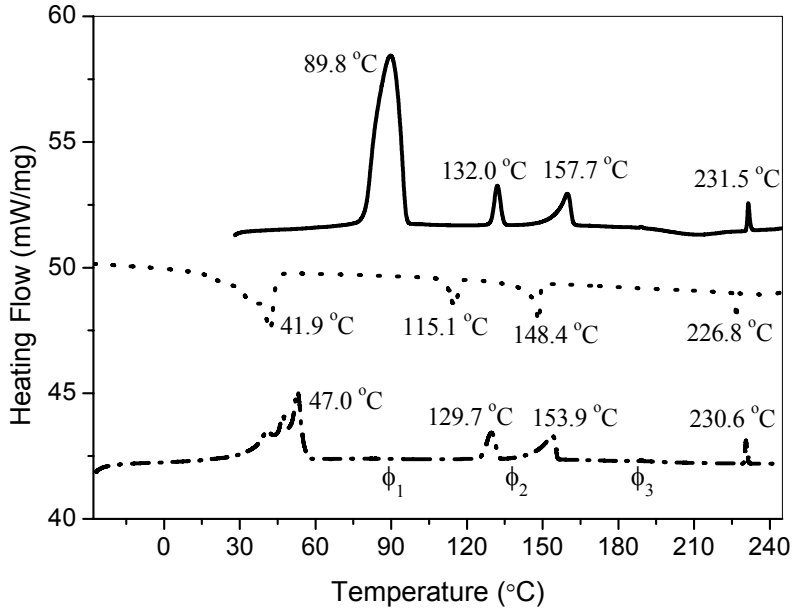

Figure 3.13 DSC thermogram of tetramethyl ammonium sulfonate **10a** (— = first heating scan, –·–·– = second heating scan, ····· = cooling scan), Φ_1, Φ_2 and Φ_3 present three mesophases.

The tetraethyl ammonium salt **10b** melted at 126 °C into the isotropic phase, but exhibited a monotropic mesophase that appeared at 98 °C upon cooling from the isotropic melt. The clearing temperature could not be measured because of rapid crystallization from the mesophase. The observed texture resembled a broken fan-shaped texture (cf. Figure 3.16a) and the transition enthalpy of the mesophase formation I → Φ was rather small (0.3 kJ/mol) (cf. Figure 3.15). From these indications alone the mesophase type cannot even be estimated. Since monotropic mesophases are metastable states with respect to crystallization, small perturbations can induce the formation of the crystalline state. Once a nucleus of the ordered solid phase was formed, it rapidly grew until the material was completely transformed to crystalline phase. Figure 3.16b depicts the growth front of the stable crystalline phase on proceeding in the liquid crystalline phase of **10b**. Compound **10c,** a tetrabutyl ammonium salt, was a purely crystalline material with a melting temperature of 81.4 °C.

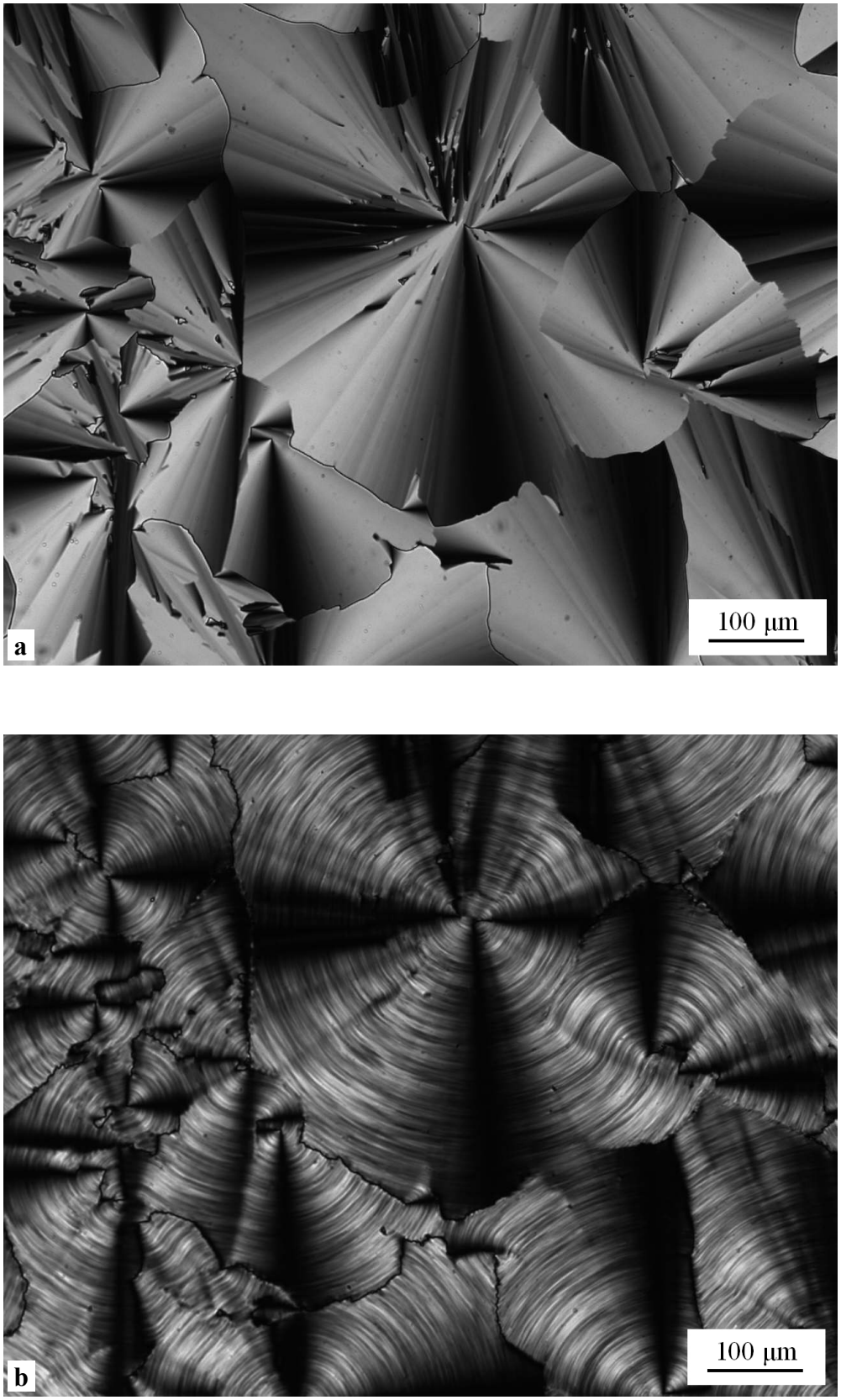

Figure 3.14 Texture of tetramethyl ammonium sulfonate **10a** between crossed polarizers, (a) Φ_3 at 180°C; (b) Φ_1 at 100°C.

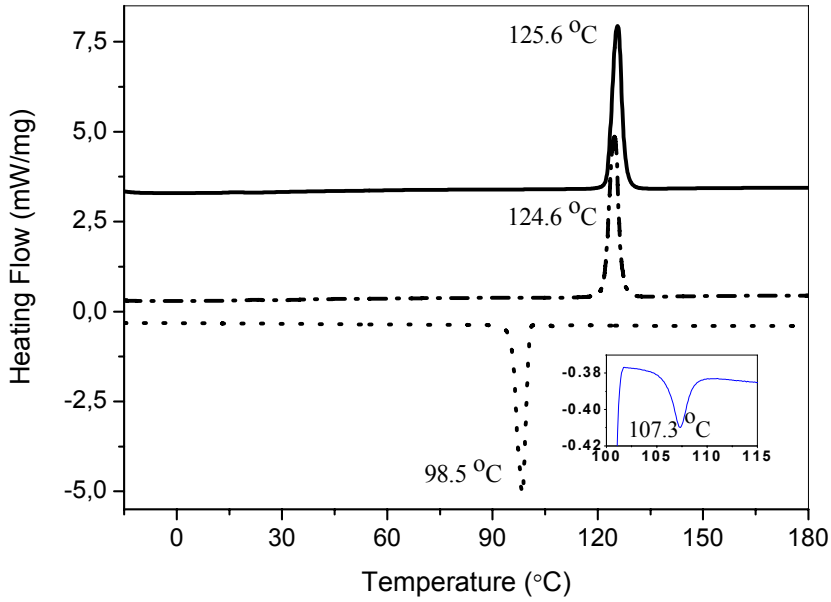

Figure 3.15 DSC thermogram of tetraethyl ammonium sulfonate **10b** (— = first heating scan, –·–·– = second heating scan, ····· = cooling scan).

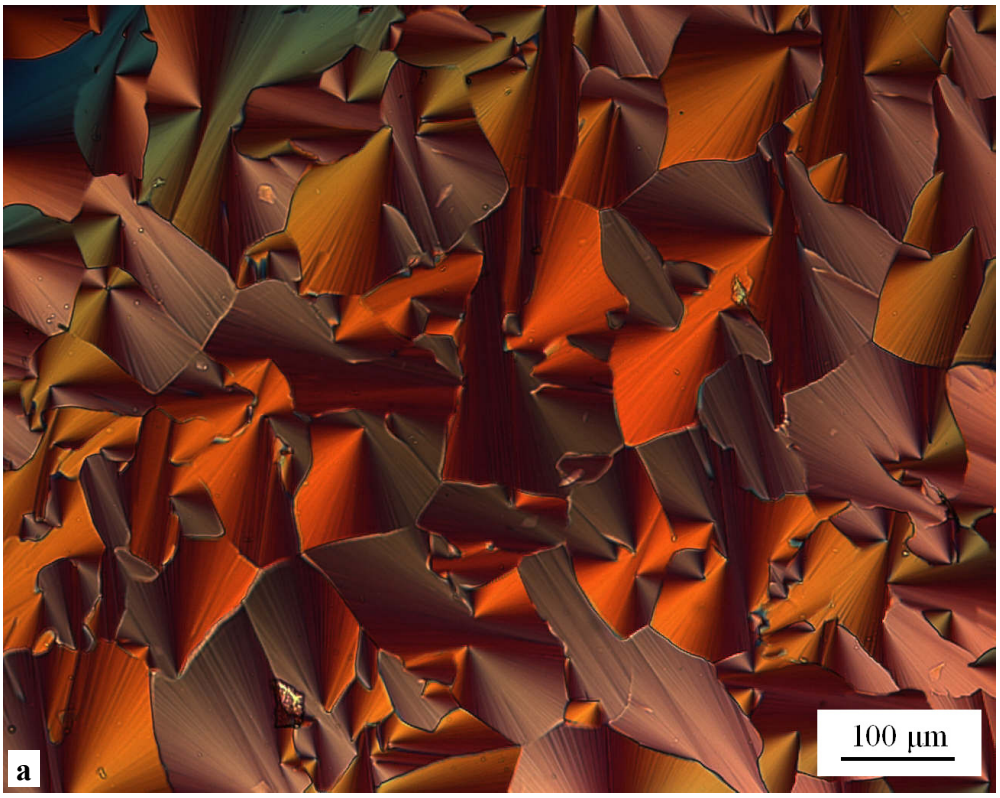

Figure 3.16 (a) Texture of tetraethyl ammonium sulfonate **10b** between crossed polarizers at 110°C.

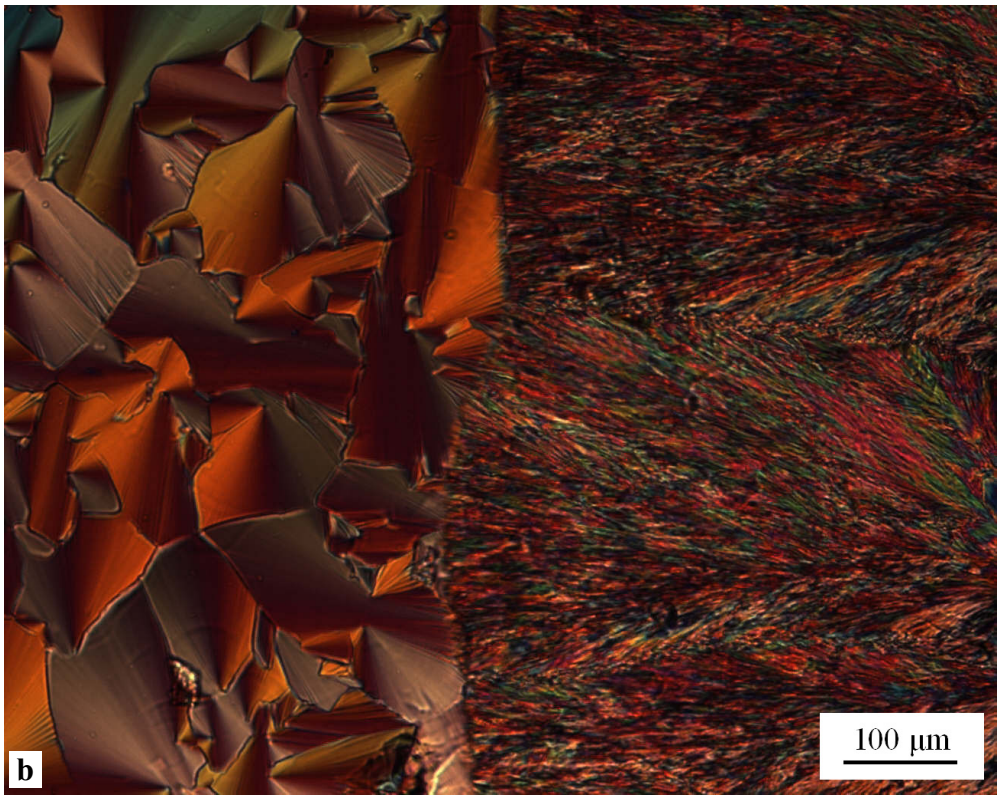

Figure 3.16 (b) Texture of tetraethyl ammonium sulfonate **10b** between crossed polarizers, a growth front of the stable crystalline phase proceeds from the right to the left in the liquid crystalline phase.

Thermal analysis of 3,4,5-substituted benzene sulfonates

Four alkali metal salts have been prepared from the symmetrically substituted 3,4,5-tris(dodecyloxy)benzene sulfonic acid, namely the lithium- (**12**), the sodium- (**13**), the potassium (**14**) and the caesium salt (**15**). In a view of the spatial structure 3,4,5-tris(dodecyloxy)benzene sulfonates show higher symmetric than 2,3,4-tris(dodecyloxy) benzene sulfonates (cf. Figure 3.17). Principally the symmetric molecules are expected favourable of the self-assembly into the ordered superstructure, e.g. 2-dimensional columnar lattices.

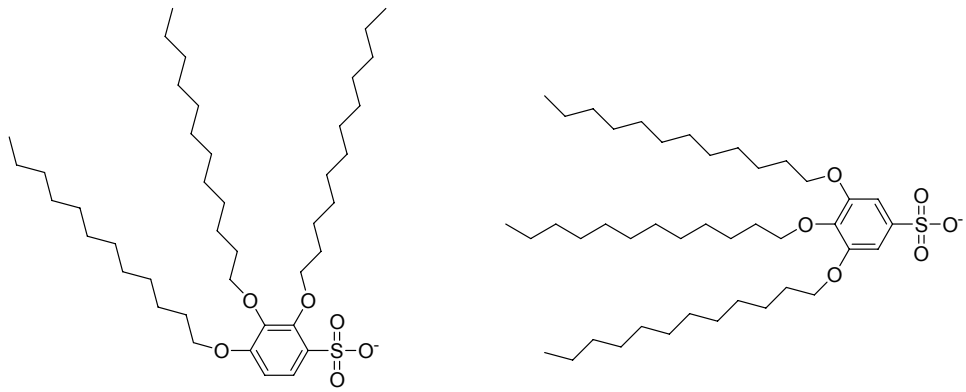

Figure 3.17 Chemical structures of 2,3,4- and 3,4,5-tris(dodecyloxy)benzene sulfonates.

Table 3.2 summarizes the transition temperatures and the corresponding enthalpy changes of the symmetric compounds **12**–**16**. According to the DSC thermograms the lithium, sodium and potassium salts exhibited two subsequent mesophases, while the caesium sulfonate showed only one mesophase (cf. Figure 3.18). The clearing transitions of sodium **13** and potassium salts **14** were broad. However the caesium salt **15** showed sharp transition to the isotropic phase at 234.4 °C. With increasing cation size the melting and the isotropization temperature increased as well.

The lithium, sodium and potassium salts decomposed above 250 °C prior to isotropization, hence it was not possible to generate textures by cooling from the isotropic melt. However, characteristic textures of the high temperature phases have been obtained from compound **12** and **13** on annealing at 180 ~ 200 °C. From the optical appearance of the textures of **12** and **13** that contain elements of fan-shaped focal conic textures, as well as the band-like textures of **15**, the formation of columnar mesophases became probable (cf. Figure 3.19-21). The texture of potassium sulfonate

14 exhibited a mosaic-like pattern that still contained features from the low temperature phases (cf. Figure 3.22) and hence could not be consulted for the determination of the mesophase type of compound **14**.

Table 3.2 Thermal characterization of 3,4,5-tris(dodecyloxy)benzene sulfonates **12**–**16** obtained from DSC measurements (second heating run, *dT*/*dt* = 10 °C/min)

	Functional group	Phase transition (°C) and corresponding enthalpy change (KJ/mol)	
		First heating	Cooling
12	**Li^+**	k_2 51.0 (8.04) k_2 59.0 (29.41) Φ_1 200.8 (1.69) Φ_2 dec	Φ_2 133.2 (–0.16) Φ_1 44.0 (-7.18) k
13	**Na^+**	k_1 89.2 (2.82) k_2 110.4 (13.06) Φ dec	Φ -3.5 (-7.02) k
14	**K^+**	k_1 56.3 (27.72) k_2 66.7 (38.17) Φ_1 182.0 (4.94) Φ_2 dec	Φ_1 -13.1 (-17.58) k
15	**Cs^+**	k 118.8 (23.87) C_{hd} 236.5 (3.43) i	i 230.1 (-2.71) C_{hd} -6.9 (-18.07) k
16	**Cs^+**(vinyl)	k 73.7 (39.22) k_2 116.2 (39.36) C_{hd} 233.9 (2.82) i	i 217.2 (-1.73) C_{hd} 71.2 (-24.71) k
		Second heating	
12	**Li^+**	k 51.7 (7.76) Φ_1 188.4 (6.62) Φ_2 dec	
13	**Na^+**	k -7.1 (6.77) Φ_1 145.1 (?)Φ_2 dec	
14	**K^+**	k -9.1 (12.59) Φ_1 172.9 (2.27) Φ_2 dec	
15	**Cs^+**	k 80.6 (8.60) C_{hd} 234.4 (3.16) i	
16	**Cs^+**(vinyl)	k 111.5 (25.87) C_{hd} 233.7 (2.45) i	

k = crystalline phase, C_{hd} = hexagonal disordered columnar mesophase, Φ = mesophase – phase type not determined, i = isotropic phase, dec = decomposition.

Introducing terminal vinyl groups at the end of the alkyl chains did not considerably alter the phase sequence of the symmetrically substituted caesium salt. Caesium 3,4,5-tris(10-undecenyl-1-oxy)benzene sulfonate **16** showed an isotropization temperature that was less than 1 °C below that of the saturated dodecyl derivative **15** (cf. Table 3.2) and its optical texture was similar to the one depicted in Figure 3.21.

Figure 3.23 showed the polarizing micrograph of **16** (Cs^+) at 200 °C. In this picture we observed that some large areas between the fan-domain showed completely black that seemed like an isotropic phase. However, if the sample was sheared, all areas showed the birefringence. This phenomenon is called ‘homeotropically orientated mesophases’.

In a homeotropic mesophase, the alignment of the columns is perpendicular to the surface of the substrate. Consequently the optical axis of the structure is parallel oriented to the observation direction and no birefringence phenomenon can be observed.

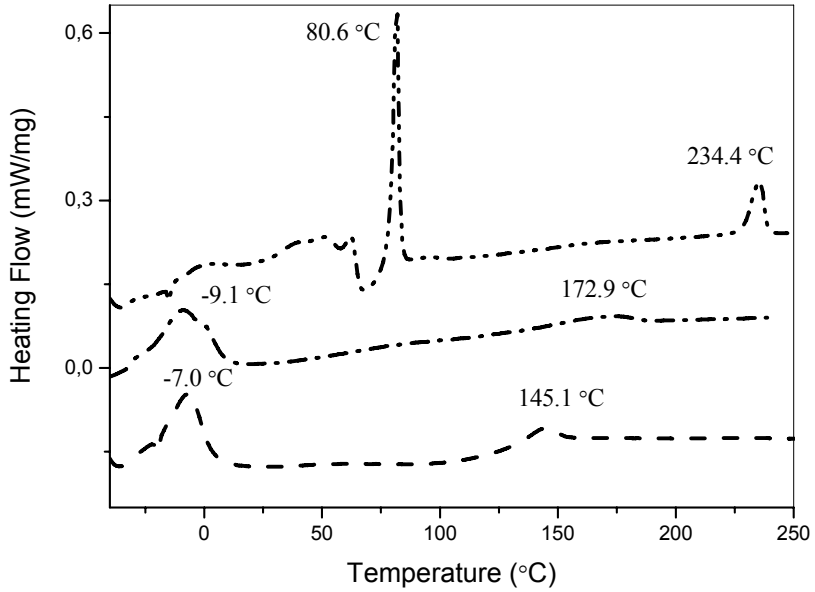

Figure 3.18 DSC thermogramms (second heating run) of the 3,4,5-tris(dodecyloxy)benzene sulfonates **12** (Li: —), **13** (Na: -----), **14** (K: – – –) and **15** (Cs: –··–).

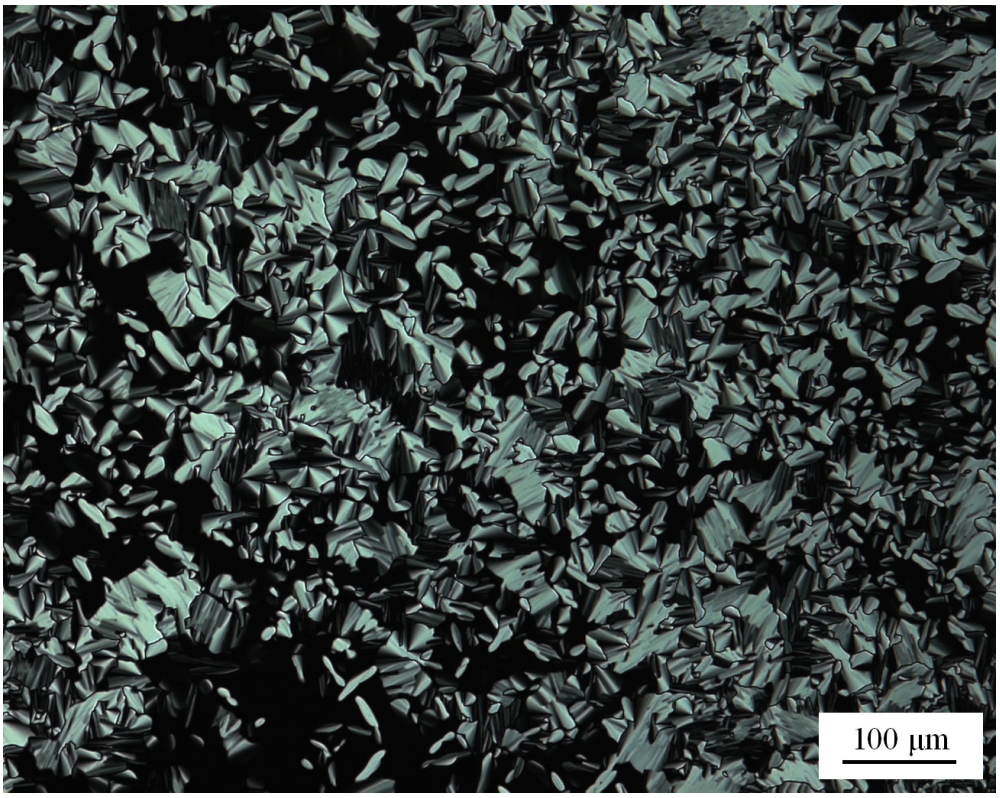

Figure 3.19 Texture of 3,4,5-substituted lithium salts **12** between crossed polarizers at 200°C.

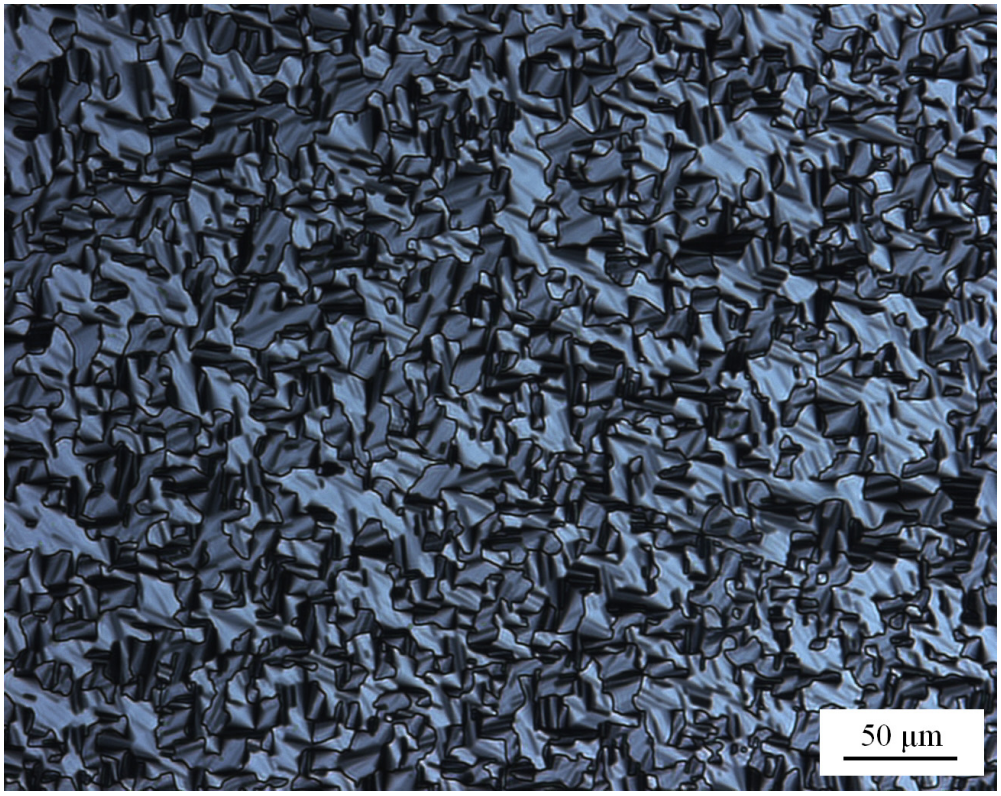

Figure 3.20 Texture of 3,4,5-substituted sodium salts **13** between crossed polarizers at 180°C.

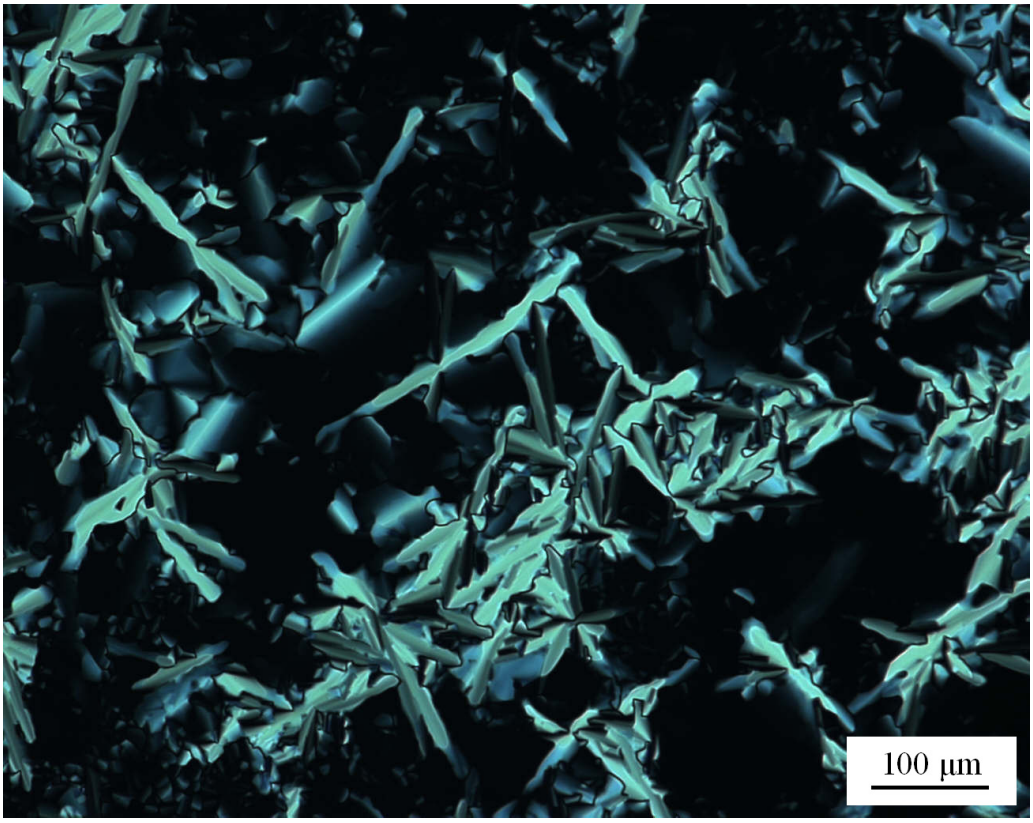

Figure 3.21 Texture of 3,4,5-substituted caesium salts **15** between crossed polarizers at 180°C.

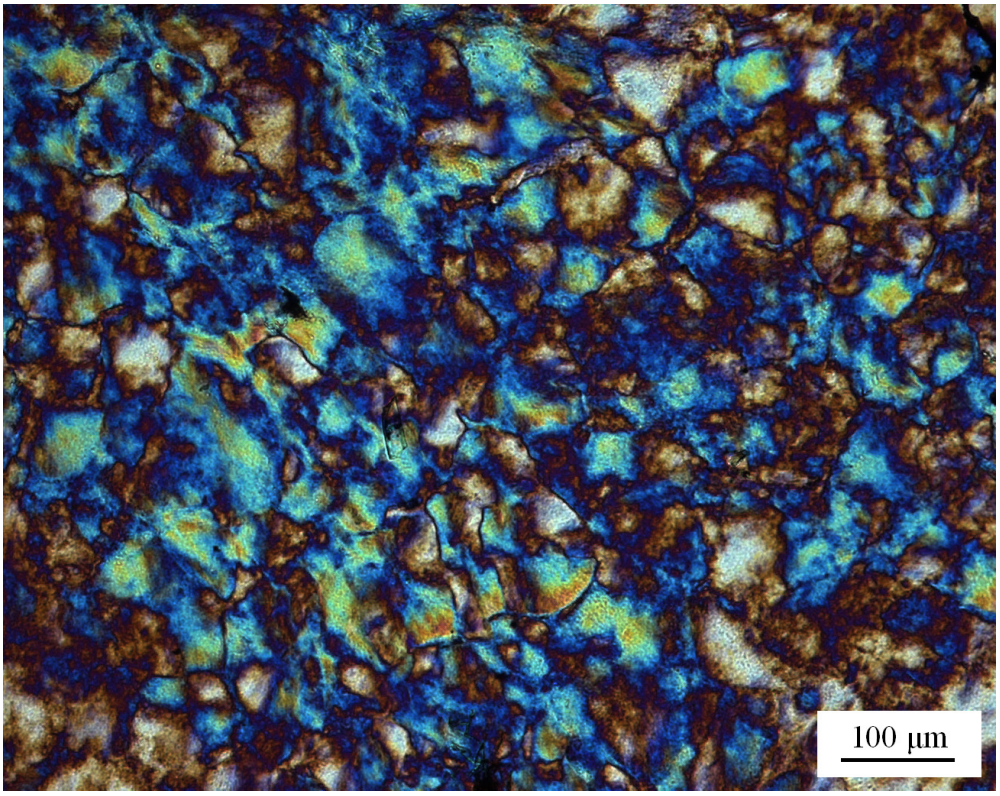

Figure 3.22 Texture of 3,4,5-substituted potassium salts **14** between crossed polarizers at 60°C.

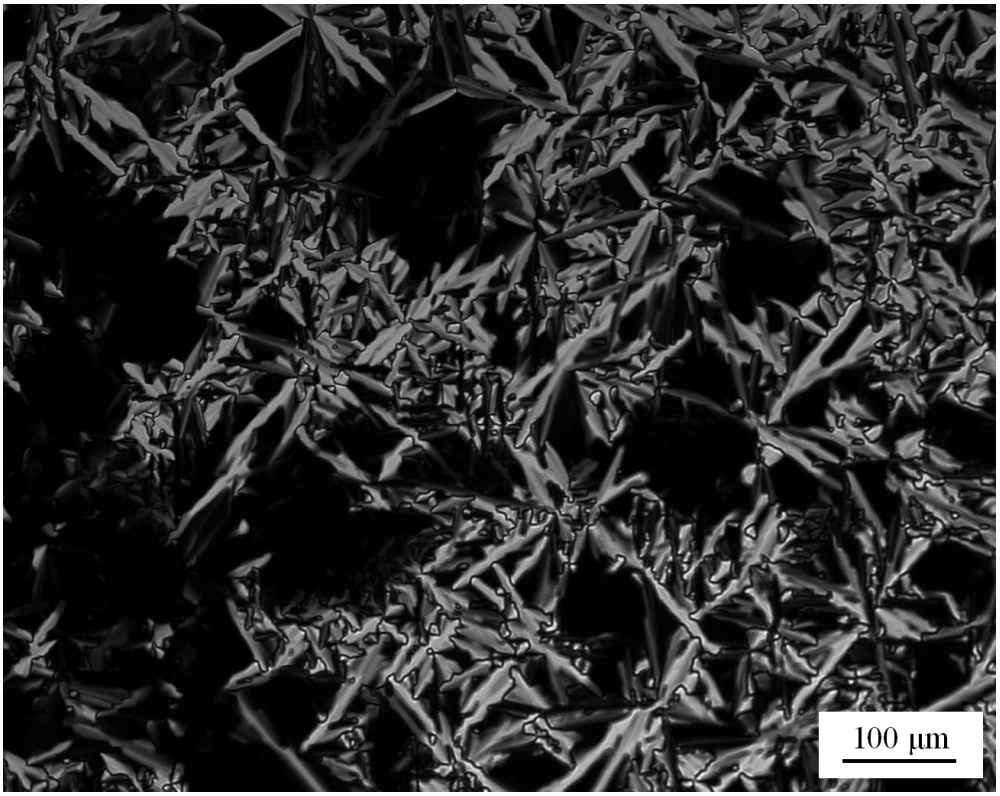

Figure 3.23 Texture of 3,4,5-substituted caesium salts with vinyl groups **16** between crossed polarizers at 200°C.

Determination of the type of mesophase by SAXS and miscibility experiments

The determination of the mesophase type was performed by a combination of small angle x-ray scattering techniques and thermo optical investigations of phase diagrams by means of the contact preparation methode [16,28].

Figure 3.24 depicts the small angle x-ray scattering (SAXS) diffractograms of 2,3,4-tris(dodecyloxy)benzene sulfonate **8** at temperatures below and above the melting temperature. In the anisotropic melt three reflections at Θ = 161.3, 282.5 and 327.0 min have been measured, the inverse sine values form the ratios $1/\sin(\Theta_1) : 1/\sin(\Theta_2) : 1/\sin(\Theta_3) = 1 : 1.75 : 2.03$, and $1/\sin(\Theta_2) : 1/\sin(\Theta_3) = 1 : 1.16$, that are close to the theoretical values of a two hexagonal lattice (1 : 1.732 : 2 and 1 : 1.155 respectively) [29]. The mesophase of compound **8** is hence a hexagonal columnar phase with a lattice constant of 3.76 nm at 60 °C. On increasing the temperature to 150 °C the lattice constant decreased for 6% to 3.52 nm (cf. Figure 3.25). The measured changes in the lattice parameter changed reversibly with the temperature. Note that the lattice constants can be calculated from the reflection position (d), as shown in e.q. 3.1.

$$d_{hk} = \frac{a}{\sqrt{\frac{4}{3}(h^2 + h \cdot k + k^2)}} \qquad \textbf{e.q. 3.1}$$

d_{hk} is scattering length, a are lattice constant and h, k are Miller indices of reflecting lattice planes.

From the lattice constant (3.52 nm at 150 °C), the molecular weight of the compound **8** (M = 842.45 g/mol), its density (ρ = 1.05 ± 0.1 g/cm^3) and the average vertical distance of the mesogenic units along the column as estimated from molecular modelling calculations (h = 0.55 nm) the number of mesogenic units per column cross section, N_{col} was calculated according to e.q. 3.2 to yield N_{col} = 4.5 ± 1.

$$N_{col} = \frac{\sqrt{3}}{2} \cdot N_A \frac{\rho \cdot a_{hex}^2 \cdot h}{M} \qquad \textbf{e.q. 3.2}\ [30]$$

N_A = Avogadros number (6.022×10^{23}), ρ = density of the mesogen, M = molecular weight of the mesogen, h = average vertical distance of the mesogenic units along the column, a_{hex} = column diameter in the hexagonal columnar phase.

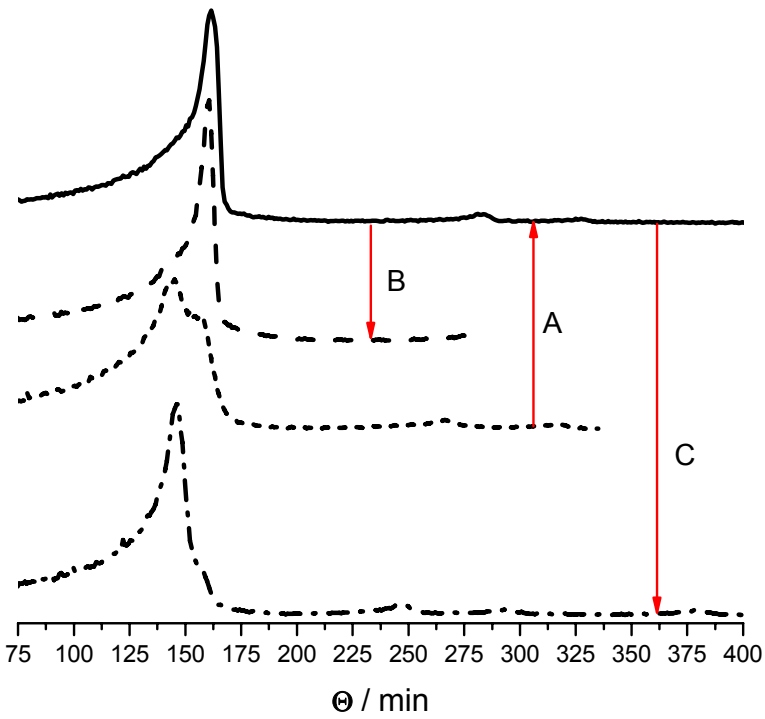

Figure 3.24 SAXS diagrams of caesium 2,3,4-tris(dodecyloxy)benzene sulfonate **8** at different temperatures (----- = 20 °C, ——— = 60 °C, ———— = fast cooling to 20 °C, –·–·–·– = slow cooling to 20 °C), **A** referred to the process of the first heating from 20 °C to 60 °C, **B** referred to the fast cooling from 60 °C to 20 °C, **C** referred to the slow cooling from 60 °C to 20 °C.

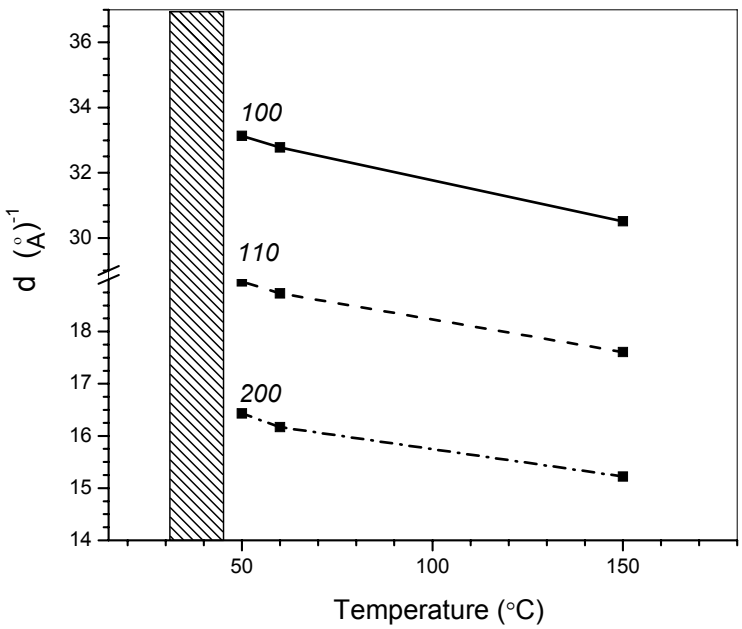

Figure 3.25 Temperature dependence of the scattering length (d) for compound **8**.

When the compound **8** was cooled rapidly down to 20 °C, the crystalline phase also exhibits a hexagonal symmetry (cf. Figure 3.24, Θ = 161 min), with a column diameter of 4.09 nm at 20 °C, however in the small angle scattering region no information on the *c*-axis of the system could be obtained. On the other hand, by slowly cooling down anisotropic melted **8** to 20 °C, the monoclinic crystalline phase was obtained (cf. Figure 3.24, Θ = 145 min), which is the same as the ″virgin″ state of the crystalline phase before heating.

Miscibility experiments have been performed within the sulfonate series to determine the mesophase type of other mesogens. According to the Arnold-Sackmann miscibility rule, two mesogens exhibit identical mesophases if the bordering regions of the two phases are connected by a continuous series of (liquid) mixed crystals [31]. The binary phase diagrams of **8** / **7**, **8** / **9**, **8** / **10a**, **8 / 15** and **8 / 16** were investigated by means of Kofler's contact preparation technique [28]. Small drops of the molten compounds were brought in contact and were observed between crossed polarizers. In the contact zone, the two components diffused into one another, creating a region in which all possible compositions of the binary mixtures were realized. At a given temperature the interdiffusion area represents a complete isothermal section of the phase diagram.

Figure 3.26 depicts a series of polarized micrographs of the mixtures of compound **8** and compound **10a** together with qualitative phase diagram that was constructed from these pictures. In this phase diagram both pure compounds exhibit high isotropization temperatures (**8:** T_C = 195 °C, **10a**: T_C = 231 °C, maximum in mixture series (**15**): T_C^{max} = 238 °C), hence the presence of caesium ions stabilised the mesophase of the tetramethyl ammonium salt, and *vice versa*. As can be seen from Figure 3.26, above 170 °C a continuous connection of mixed mesophases existed between the mesogens, hence the high temperature mesophase of compound **10a** is of hexagonal columnar type. The immiscibility between the low temperature phases Φ_1 and Φ_2 of **10a** and the C_h phase of **8** is indicated by the fact that the changes in the morphologies of **10a** due to its phase transitions did not protrude in the second half of the contact zone.

Similar investigations of contact preparations demonstrated the miscibility of **8** / **7**, **8** / **9**, **8** / **15** and **8 / 16** in their mesophases, hence the mesophase of the pyridinium salt **9** and the high temperature phase of the potassium salt **7** are hexagonal columnar phases as

well as the mesophases of the symmetrically substituted caesium salts **15** and **16**. Note that on preparing the interdiffusion zone between **8** and **9** care must be taken not to overheat the pyridinium salt. Best results were obtained on annealing the preparation below 135 °C, i.e. having in contacts the mesophase of **8** and the isotropic phase of **9.**

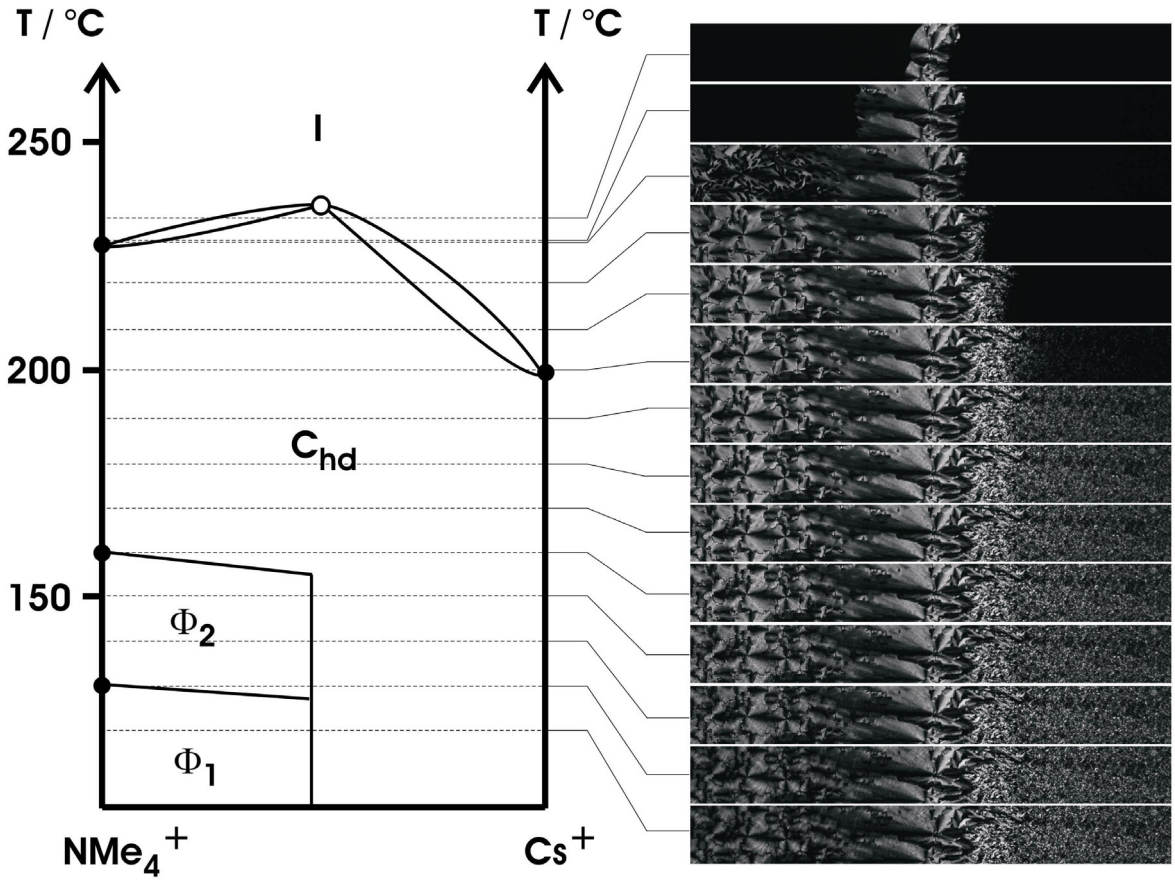

Figure 3.26 Schematic binary phase diagram of the mesogens **10a** and **8** together with polarized micrographs of the inter-diffusion zone in a contact preparation of compound **10a** and compound **8**.

Relation between molecular structures and mesophase

The occurrence of mesophases depends on the geometric shape of the mesogenic unit and the distribution of polar groups along the molecular skeleton. In particular with supramolecular mesogens the tendency of microphase segregation [32] and hence the amphiphilicity of the constituents of the supramolecular mesogenic unit are decisive if and what type of mesophase can exist [16]. For these reasons the relation between the

mesophases of the sulfonate amphiphiles and their molecular architecture is important to be understood.

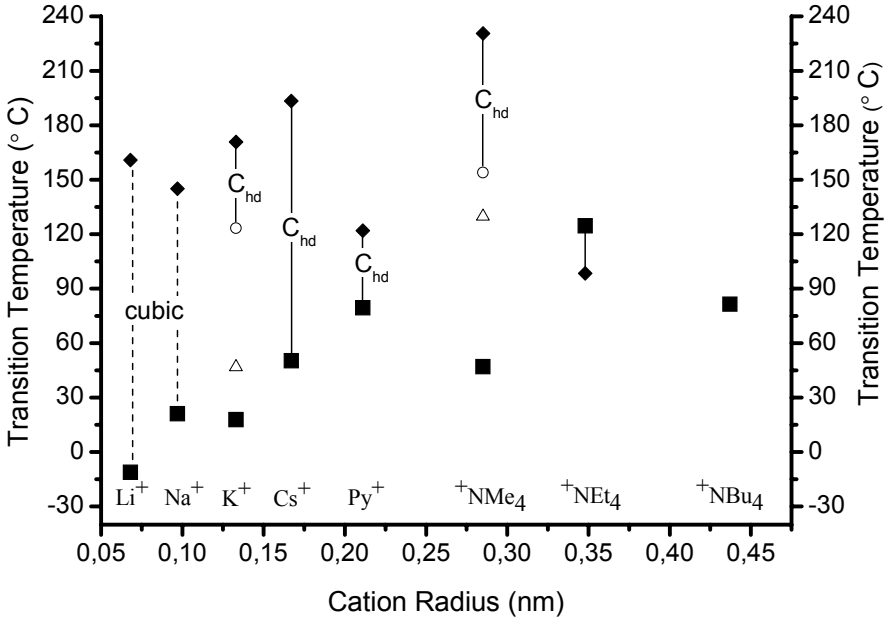

Figure 3.27 Plot of the transition temperatures of 2,3,4-tris(dodecyloxy)benzene sulfonates versus the radius of the cation (■ = melting temperature, ◆ = isotropization temperature, O and △ = mesophase / mesophase transition temperatures; C_{hd} = hexagonal disordered columnar mesophase).

At a given substitution pattern of the aromatic core the phase type and the transition temperatures are controlled by the size of the cations. In Figure 3.27 the transition temperatures of the asymmetrically substituted sulfonates **5–10c** are plotted versus the radius of the respective cations. Figure 3.28 depicts the analogous relation for the symmetrically substituted compounds **12–15**. With 2,3,4-substituted mesogens the graph is clearly separated in three domains: At cation radii below 0.12 nm only cubic phases are observed, while for intermediate cation sizes (0.15 nm < r_{cation} < 0.27 nm) the hexagonal columnar mesophase dominates and with large cations (r_{cation} > 0.35 nm) only crystalline phases exist. The compounds that represent the border between these domains (**7**: cubic ←→ C_{hd}, **10a**: C_{hd} ←→ crystalline) exhibit a complex phase sequence of three subsequent enantiotropic mesophases, with the hexagonal columnar phase being the last phase before isotropization. Note that similar relations have been observed with other mesogenic homologues that show polymorphism if the phase type depends on variation of the molecular structure [32,33]. The overall tendency of the

isotropization temperatures is an increase with growing cation radius until $r_{cation} \approx$ 0.3 nm, above this value the clearing point falls short of the melting temperature, i.e. the mesophase becomes monotropic (**10b**). The pyridinium salt **9** does not perfectly fit in this scheme, most probably because the pyridinium ion is not a spherical but a flat ion.

From a pure geometric point of view small polar head groups should cause a cone-like shape of the molecules that preferably assembles to spherical aggregates and arranges in lattices of cubic symmetry. Larger head groups generate molecules of truncated cone shape that prefers to organize into cylindrical superstructures and columnar phases. With very large cations, in particular the long chain tetra-alkyl ammonium ions that consist of a charged centre and an electro-neutral alkyl shell, it can be doubted that the general scheme of arranging the head group in the centre of a supramolecular aggregate can hold true. Hence, at cation radii larger than 0.4 nm mesophases do not occur.

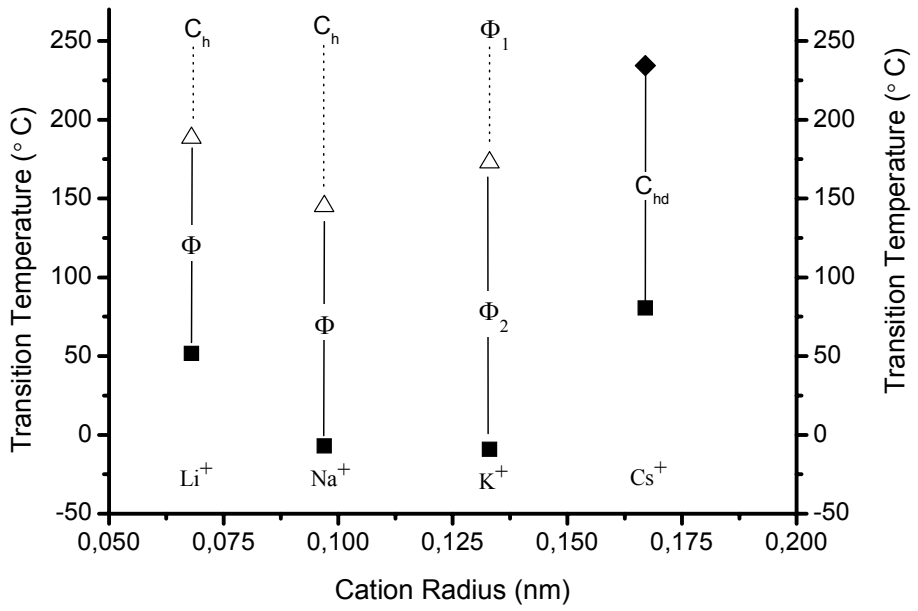

Figure 3.28 Plot of the transition temperatures of 3,4,5-tris(dodecyloxy)benzene sulfonates versus the radius of the cation (■ = melting temperature, ◆ = isotropization temperature, △ = mesophase / mesophase transition temperatures; C_{hd} = hexagonal disordered columnar mesophase, Φ = undetermined mesophase).

The transition temperatures of the symmetrically substituted sulfonates are depicted in Figure 3.28. Both, the melting temperatures as well as the isotropization temperatures

show a minimum-behaviour when plotted against the cation radius. Oppositely to the asymmetrical sulfonates the temperatures decrease form the lithium to the potassium salt that represents the minimum of the series. The subsequent caesium salt **15** exhibits considerably higher transition temperatures than its predecessor.

Meanwhile, the dependence of the transition enthalpies on the cation radius of compounds **5**–**10** supports the distinction of the three domains, in particular since the melting enthalpies of the two crystalline compounds **10b** and **10c** are about 3-4 times larger than the values of the mesogens **5**–**9** (cf. Figure 3.29a). For the symmetric series, the melting enthalpies continuously rise from the sodium (**12**) to the caesium salt (**15**) (cf. Figure 3.29b), while the values of the isotropization enthalpy seem to exhibit a maximum with the potassium compound (**14**).

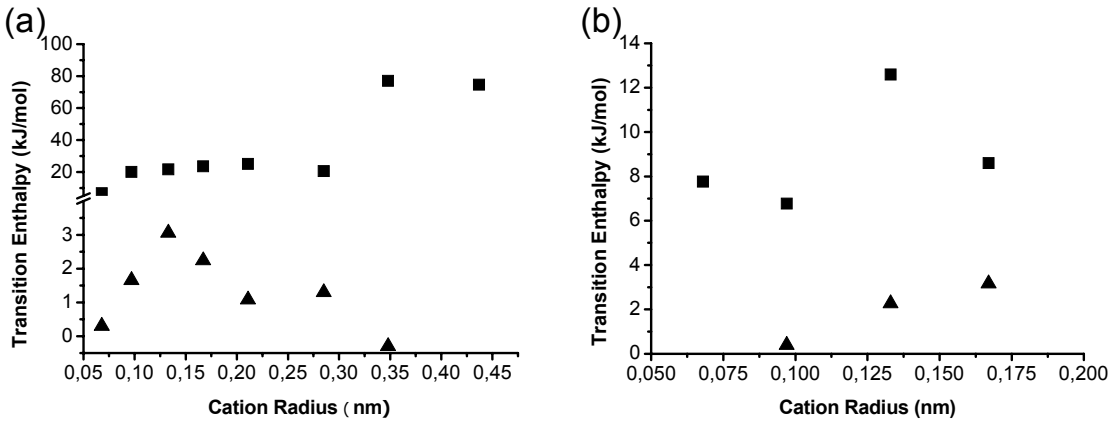

Figure 3.29 Plot of the melting- and isotropization enthalpies of (a) 2,34- and (b) 3,4,5-tris(dodecyloxy) benzene sulfonates (■ = melting enthalpies, ◆ = isotropization enthalpies).

It is instructive to compare the mesophases of the alkali sulfonates to that of the analogous carboxylate mesogens. While no literature is available for the alkali 2,3,4-tris(alkoxy)benzoates, the isomeric alkali 3,4,5-tris(alkoxy)benzoates have been investigated earlier in great detail [18]. The thermal transitions of the dodecyloxy derivatives are depicted in Figure 3.30 to show that the carboxylates melt into columnar mesophases that transfer on heating into cubic phases. All five compounds do not reach the isotropic melt but decompose at elevated temperatures from their cubic mesophase of Im$\underline{3}$m symmetry. The melting temperatures do not strongly depend on the cation size, but it seems that the columnar–cubic transition temperature tends to increase with growing cation diameter.

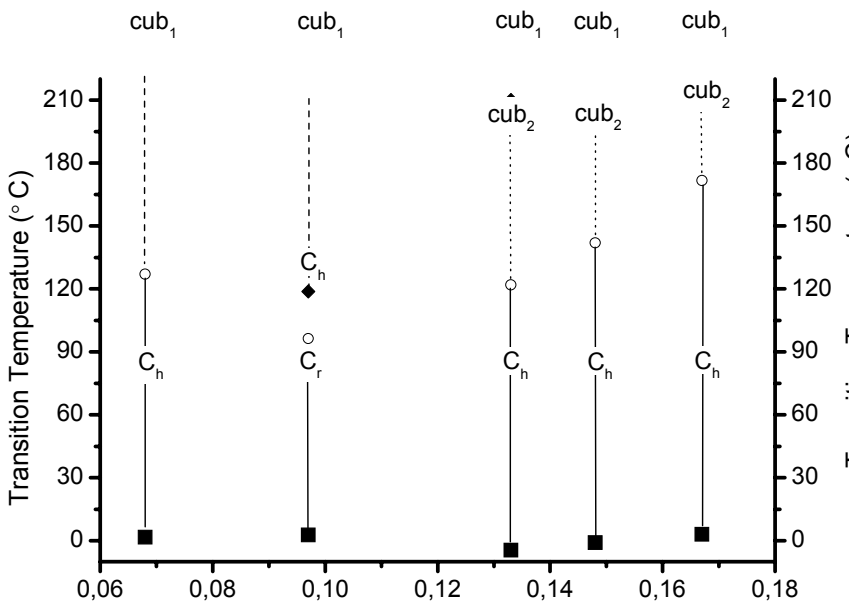

Figure 3.30 Plot of the transition temperatures of alkali metal 3,4,5-tris(dodecyloxy)benzoates versus the radius of the cation (■ = melting temperature, ◆ and ○ = mesophase / mesophase transition temperatures, C_h = hexagonal columnar, C_r = c2mm rectangular columnar, cub_1 = Im3m cubic lattice, cub_2 = Pm3n cubic lattice). Data taken from Table 2 of reference [18].

Conclusion

Two series of wedge-shaped tris(dodecyloxy)benzene sulfonate amphiphiles have been synthesized and characterized with respect to their mesophases. From the dependences of transition temperatures and enthalpies on the cation radius it is conclusive that the occurrence of mesophases with these compounds is more ruled by the geometric shape of the mesogen than by the ionic interactions between cations and sulfonate anion.

Depending on the radius of the cation the asymmetrically substituted compounds **5–10a** exhibit cubic and columnar mesophases; the cubic symmetries are limited to the cations of small size. Compounds with larger radius exhibit columnar mesophases as long as the cation radius is below 0.35 nm, on exceeding this value only crystalline materials are obtained. The symmetrical substituted alkali metal sulfonates all exhibit columnar mesophase on melting from the crystalline phase.

References

[1] V. Percec, J. Heck, G. Johansson, D. Tomazos, G. Ungar, *Macromol. Symp.*, **1994**, 77, 237.

[2] J. S. Moore, *Curr. Opin. Colloid Interface Sci.*, **1999**, 4, 108.

[3] A. Klug, Angew. *Chem., Int. Ed. Engl.*, **1983**, 22, 565.

[4] H.-T. Jung, B. Coldren, J. A. Zasadzinski, D. J. Iampietro, E. W. Kaler, *Proc. Natl. acad. Sci. U.S.A.*, **2001**, 98, 1353.

[5] S. D. Hudson, H.-T. Jung, P. Kewsuwan, V. Percec, W.-D. Cho, *Liq. Cryst.*, **1999**, 26, 1493.

[6] T. Kato, *Science*, **2002**, 295, 2414.

[7] I. Shiyanovskaya, K. D. Singer, V. Percec, T. K. Bera, Y. Miura, M. Glodde, *Physical Review B*, **2003**, 67, 035204.

[8] S. Chandrasekhar in *Handbook of Liquid Crystals, Vol. 2B* (Eds.: D. Demus, J. Goodny, G. W. Gray, H.-W. Spiess, V. Vill), Wiley-VCH, Weinheim, **1998**, 749.

[9] a) J. Malthete, A. Collet, A. M. Levelut, *Liq. Cryst.*, **1989**, 5, 123; b) J. Malthete, P. Davidson, *Bull. Soc. Chim. Fr.*, **1994**, 131, 812.

[10] G. Ungar, V. Percec, M. N. Holerca, G. Johansson, J. A. Heck, *Chem. Eur. J.*, **2000**, 6, 1258-1266.

[11] (a) A. Klug, *Angew. Chem., Int. Ed. Engl.*, **1983**, 22, 565; (b) J. S. Lindsey, *New J. Chem.*, **1991**, 153; (c) G. M. Whitesides, J. P. Mathias, C. T. Seto, *Science*, **1991**, 254, 1312.

[12] (a) V. Percec, G. Johansson, J. Heck, G. Ungar, S. V. Batty, *J. Chem. Soc. Perkin Trans. I*, **1993**, 1411; (b) S. Weinmann, *Dissertation*, University of Ulm, **2000**.

[13] V. Percec, C-H. Ahn, T. K. Bera, G. Ungar, D. J. P. Yeardley, *Chem. Eur. J.*, **1999**, 5, 1070-1083.

[14] R. Tapia, G. Torres, J. A. Valderrama, *Syn. Commun.*, **1986**, *16*, 681-687.

[15] D. S. Veselinovic, M. V. Obradovic, S. S. Mitic, S. B. Djordjevic, J. S. Zakrzewska, *Zhurnal Prikladnoi Spektroskopii*, **1995**, 62(6), 71-75.

[16] U. Beginn, *Prog. Polym. Sci.*, **2003**, 28, 1049–1105.

[17] U. Beginn, G. Lattermann, *Mol. Cryst. Liq. Cryst.*, **1994**, 241, 215-219.

[18] V. Percec, M. N. Holerca, S. Uchida, W. Cho, G. Ungar, Y. Lee, J. P. Yeardley, *Chem. Eur. J.*, **2002**, 8, 1106-1117.

[19] G. Ungar, V. Percec, M. N. Holerca, G. Johansson, J. A. Heck, *Chem. Eur. J.*, **2000**, 6, 1258.

[20] I. Shiyanovskaya, K. D. Singer, *Physical Review B*, **2003**, 67, 035204.

[21] F. C. Frank, S. Chandrasekahar, *J. Phys.*, **1980**, 41, 1285.

[22] M. Klemann, *Rep. Prog. Phys.*, **1989**, 52, 555.

[23] P. Oswald, *J. Phys. Lett.*, **1981**, 42, L171.

[24] Y. Bouligand, *J. Phys.*, **1980**, 41, 1297.

[25] V. Percec, M. Glodde, T. K. Bera, Y. Miura, I. Shiyanovskaya, K. D. Singer, V. S. K. Balagurusamy, P. A. Heiney, I. Schnell, A. Rapp, H.-W. Spiess, S. D. Hudson, H. Duan, *Nature*, **2002**, 419, 384.

[26] P. Boltenhagen, O. D. Lavrentovich, M. Kleman, *J. Phys. II*, **1991**, 10, 1233.

[27] (a) S. Chandrasekhar in *Handbook of Liquid Crystals, Vol. 2B* (Eds.: D. Demus, J. Goodny, G. W. Gray, H.-W. Spiess, V. Vill), Wiley-VCH, Weinheim, **1998**, p. 749; (b) C. Destrade, P. Foucher, H. Gasparoux, N. Huu Tin, A. M. Levelut, J. Malthete, *Mol. Cryst. Liq. Cryst.* **1984**, *106*, 121-146.

[28] L. Kofler, A. Kofler, M. Brandstätter, ”Thermo-Mikromethoden”, p. 151ff, Verlag Chemie GmbH, Weinheim, Bergstrasse **1954**.

[29] P. S. Pershan, *Structure of Liquid Crystal Phases*; World Scientific: Singapore, **1988**.

[30] V. Percec, G. Johansson, J. Heck, G. Ungar, S. Batty, *J. Chem. Soc., Perkin Trans. 1*, **1993**, 1411.

[31] (a) H. Sackmann, D. Demus, *Z. Phys. Chem.*, **1963**, 222, 127-142; (b) H. Sackmann, D. Demus, *Z. Phys. Chem.*, **1963**, 222, 143-160.

[32] Pegenau A, Hegmann T, Tschierske C, Diele S. *Chem Eur J.*, **1999,** *5*, 1643–1659.

[33] G. Staufer, M. Schellhorn, G. Lattermann, *Liquid Crystals* **1995**, *18*, 519-527.

Chapter 4

Self-Assembly of Sulfonated Organo-gelators and their Morphologies

Introduction

Self-assembly is a powerful tool to prepare functional materials [1]. One typical example is the formation of fibrous assemblies in organic solvents, which leads to the formation of physical organogels [2,3]. In these materials non-covalent physical interactions such as hydrogen bonding, π—π stacking, solvophobic effects or donor-acceptor interaction drive the two- or three-dimensional assembly of organogelators [4,5]. Despite numerous of achievements of supramoleuclar chemistry in the controlled self-assembly of small molecules [6,7], most of the low molecular weight gelators so far have been found by serendipity rather than design.

In recent years, the interest in the design and synthesis of supramolecular structures has grown rapidly [8,9]. For example, one can design a new gelator for organic solvents, starting from criteria derived from some common features of known gelators [10,11]. Carbohydrate amphiphiles are known to exhibit numerous forms of self-organization [12] and in particular several N-alkylgluconamide derivatives [13] have been shown to give supramolecular aggregates in aqueous solutions [14,15].

Our approach is the attachment of sulfonic acid derivatives as functional group to alkoxy benzoyl moieties, which has high polarity and has great potential to be developed into high performance nonfluorinated hydrocarbon membrane materials [16]. In Chapter 3 the synthesis of 2,3,4-tris(dodecyloxy)benzene sulfonic acid and its derivatives (**2**–**10**), 3,4,5-tris(dodecyloxy)benzene sulfonates with alkali metal cations (**12**–**15**) and caesium 3,4,5-tris(undec-10-enyloxy)benzene sulfonate (**16**) has been described. Because of their wedge-shaped molecular geometry and the highly polar sulfonate head group at the tip of the wedge, the amphiphilic molecules form hexagonal columnar mesophases, which demonstrates self-organizing to columnar supramolecular units (Figure 4.1).

In this chapter, gelling capability and morphologies of these sulfonated amphiphiles in organic solvents will be reported. Furthermore, the structural effect, such as the size of cations and the geometrical symmetry of the amphiphiles on the gelling capabilities and morphologies will be discussed.

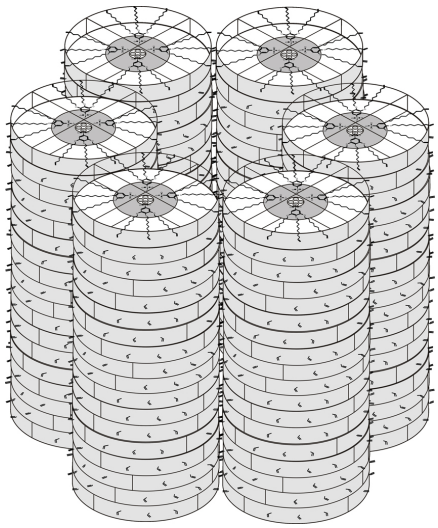

Figure 4.1 Scheme of the self-organization of hexagonal columnar supramolecular unit.

Experimental Section

Materials

tert-Butyl acetate (≥99.0%, Fluka), 2-hydroxyethyl methacrylate (HEMA) (≥99%, Fluka), triethylene glycol dimethacrylate (TEGDMA) (≥95%, Fluka), ethylene glycol dimethacrylate (EGDMA) (≥97%, Fluka), 2- ethylhexyl methacrylate (EHMA) (≥98%, Fluka), n-hexyl methacrylate (HMA) (≥97%, Lancaster), styrene (≥99.5%, Fluka), acetone, n-hexane, toluene, ethanol, methanol, ethyl acetate (A.C.S. Reagents).

Techniques

^{1}H NMR (300MHz) and ^{13}C NMR (75MHz) were recorded on a Bruker DPX-300 spectrometer with tetramethylsilane (TMS) as internal standard.

DSC (Differential Scanning Calorimetry) measurements were made with samples of about 5mg to 10mg. Thermal transitions were determined on a Netzsch DSC 204 'Phoenix' differential scanning calorimeter. In all cases, the heating and cooling rates were 10 °C/min. First-order transitions were reported as the maxima or minima of the endothermic and exothermic peaks during the second heating and cooling scans. Indium and cyclohexane were used as calibration standards.

Thermal Optical Polarizing Microscope (Zeiss AXIOPLAN polarizing microscope) equipped with a METTLER FP 90 hot stage and the digital AxioCam MRc4 Zeiss camera with a resolution of 4 Megapixels was used to verify thermal transitions and to characterize the anisotropic textures.

Transmission Electron Microscope (Zeiss EM 109, 80kV and Philip CM 10, 100KV) was used to analysis the morphologies of dried gels. Preparation of TEM samples is as follows: a dried gel, prepared by evaporation of solvent from gel, was picked up on carbon-coated cupper grids. Then the grids covered by gel were stained in the gas phase with ruthenium tetroxide freshly developed from the ruthenium trichloride hydrate in a 10wt% sodium hypochloride solution [17]. For a favourable contrast the sections were stained for 10-20 minutes before the investigation by TEM.

Preparation of Gel

A typical procedure for gelation testing is as follows: a weighed gelator was mixed with an organic solvent in a test tube with a screw cap, and the mixture was heated until the solid was dissolved. The resulting solution was cooled in the air at the determining temperature and left for 2 h at this temperature, and then turned upside down to be checked visually. When the gelator formed a clear or slightly opaque (translucent) or opaque gel by immobilizing the solvent at this stage, it was judged as ‘successful gelation’ and was denoted by 'G' mark in the following tables. Meanwhile, the ″Quenched Gelation″ procedure was applied to study gelation as well. In ″Quench Gelation″, the mixture of gelator and solvent was heated until a clear solution was obtained and subsequently was rapidly frozen by liquid nitrogen to yield a clear glass. The resulting solid was gradually thawed to the determining temperature and left for 2 h at this temperature. The gelling ability was evaluated qualitatively by determining the gelling at three different temperatures: 25 °C, 4 °C and -20 °C depended on the different gelling temperature. Normally, three different kinds of gels were distinguished: clear gel, translucent gels (opaque, semi-transparent gels) and white gels (non-transparent). The gel-solution transition temperatures were measured by means of DSC with the responding solvent as the reference. The temperature was increased (decreased) at a rate of 10 °C/min. And the gel melting temperature (T_{gm}) was defined as the temperature at which the gel turned into the sol phase.

Results and Discussion

In Chapter 3, the thermal transitions and phases (especially the liquid crystal phases) of wedge-shaped sulfonated amphiphiles in bulk have been discussed. Besides their self-assemblies into mesophases, most of this series of amphiphiles showed potential gelation abilities as well. Figure 4.2 depicts the corresponding chemical structures of compounds **2**–**16**. Their syntheses have been reported in Chapter 3.

2:

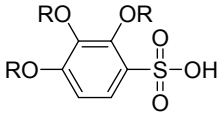

4:

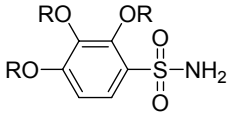

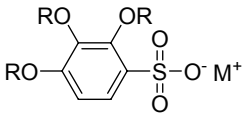

5: M = Li;

6: M = Na;

7: M = K;

8: M = Cs ;

9:

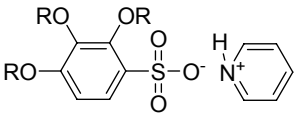

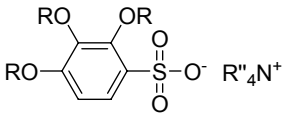

10a: R'' = CH_3;

10b: R'' = C_2H_5;

10c: R'' = C_4H_9;

11:

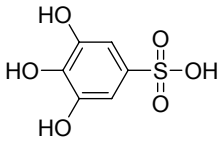

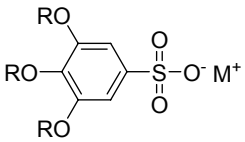

12: M = Li;

13: M = Na;

14: M = K;

15: M = Cs ;

16:

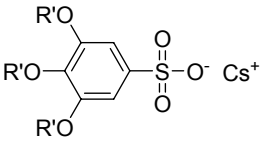

R: $—C_{12}H_{25}$

R': $—CH_2C_8H_{16}CH{=}CH_2$

Figure 4.2 Chemical structures of **2**–**16**.

Gelation capabilities of 2,3,4-substituted benzene sulfonates

Thermoreversible gelation of solutions was studied as a first indication of the self-ordering to columnar superstructures. Table 4.1 and 4.2 summarize the gelation behaviour of 2,3,4-tris(dodecyloxy)benzene sulfonate derivatives (**2**–**10c**) in various polar and non-polar organic solvents, including some monomer liquids (5 kinds of methacrylates). The gelation experiments were performed with two different experimental conditions. For the comparison of gelation abilities, the concentrations of gelators were fixed to 5wt%. Three kinds of gels were distinguished: clear-transparent gel, translucent / semi-transparent gels and white / non-transparent gels.

In the first series of experiments the sulfonate / solvent mixtures were heated until clear solutions were obtained and subsequently allowed to cool down to ambient temperature (20 °C), to -4 °C and to -20 °C respectively. Usually, the compounds are sparingly soluble in most of the gelling solvents, but upon heating at about 100 ~ 150 °C they gradually dissolve. The cooling rates were between 10 °C/min and 20 °C/min. In Table 4.1 the highest temperature is indicated where gel formation was observed. Upon heating all gels melted into the clear solution and re-gelled on cooling. This process can be repeated many times indicating that the gelation is fully thermoreversible. The sulfonamide (**4**) turned out to be the gelator with the broadest gelation spectrum, gelling acetone, *t*-butyl-acetate, HEMA, EGDMA and TEGDMA at 20 °C as well as EHMA, HMA, styrene, toluene and hexane at 4°C. Of lower but mutually comparable gelation power were the sodium salt (**6**) and the ammonium salts **10a** and **10b**. Ethanol could not be gelled by any 2,3,4-sulfonate and only three gelators (**5**, **6** and **8**) were found forming gels for DMF. Most of the compounds gelled the semi-low polar solvents, namely all the tested methacrylates (e.g. EHMA). Aromatic solvents were gelled only by a minority of the sulfonates (styrene: **2**, **4**; toluene: **4**, **7**, **8**, **9**), while five compounds were able to gel *n*-hexane (**4**–**7**, **10a**).

Clearly, transparent gels were found only with low temperature gels (-20 °C: toluene/**7**, toluene/**8**, *n*-hexane/**7**) and translucent gels were also preferably formed below ambient temperature with exception of the sulfonamide gels. At ambient temperature white gels were formed in the majority of cases. However, since the class of 2,3,4-tris(dodecyloxy)benzene sulfonates results in gelation with 56% of all experiments, it seems to be justified to describe them as versatile organogelators.

Table 4.1 Spontaneous gelation of **2–10c** in various organic liquids (5wt%).

	2	**4**	**5**	**6**	**7**	**8**	**9**	**10a**	**10b**	**10c**
	-OH	$-NH_2$	Li^+	Na^+	K^+	Cs^+	^+Py	$^+NMe_4$	$^+NEt_4$	$^+NBu_4$
Ethanol	×	×	×	×	×	×	×	×	×	×
DMF	×	×	CG[b]	*WG*[c]	×	*WG*[c]	×	×	×	×
Acetone	×	*WG*[a]	×	*WG*[c]	×	×	×	×	×	*WG*[c]
***t*-butylacetate**	×	*WG*[a]	*WG*[a]	*WG*[c]	*WG*[b]	*WG*[b]	×	*WG*[a]	×	*WG*[b]
HEMA	*TG*[c]	*TG*[a]	*TG*[b]	*TG*[a]	*TG*[c]	*TG*[c]	×	*WG*[c]	*WG*[c]	×
TEGDMA	*WG*[b]	*TG*[a]	*TG*[a]	*WG*[a]	*WG*[c]	*TG*[c]	×	*TG*[b]	*WG*[a]	*TG*[b]
EGDMA	×	*TG*[a]	*TG*[b]	*WG*[a]	*TG*[c]	*TG*[c]	×	*WG*[a]	*WG*[a]	*WG*[c]
EHMA	*TG*[c]	*TG*[b]	*TG*[a]	*TG*[b]	*TG*[c]	*TG*[b]	×	*WG*[a]	*WG*[c]	*TG*[b]
HMA	*WG*[c]	*TG*[b]	*TG*[b]	*TG*[c]	*TG*[c]	*TG*[b]	×	*WG*[b]	×	*TG*[a]
Styrene	*TG*[b]	*TG*[b]	×	×	×	*TG*[c]	×	×	×	*TG*[c]
Toluene	×	*TG*[b]	×	×	*CG*[c]	*CG*[c]	*TG*[a]	×	×	×
n-Hexane	×	*TG*[b]	*TG*[b]	*WG*[c]	*CG*[c]	×	×	*TG*[a]	×	×

×: no formation of Gel; CG: Clear Gel ; TG: Translucent Gel; WG: White Gel;
a: Gel was formed at 25°C; ***b***: Gel was formed at 4°C; ***c***: Gel was formed at -20°C;
HEMA: 2-hydroxyethyl methacrylate; TEGDMA: triethylene glycol dimethacrylate;
EGDMA: ethylene glycol dimethacrylate; EHMA: 2- ethylhexyl methacrylate; HMA: n-hexyl methacrylate.

In the second series of screening experiments the hot homogeneous solutions were rapidly quenched with liquid nitrogen to -196 °C and subsequently allowed to warm up to -20 °C, 4 °C and 20 °C respectively. The solution vitrified during the quench process without formation of crystalline precipitates. Table 4.2 summarizes the observation after 5 hours of annealing at the indicated temperature. Like in Table 4.1 only the results of highest temperature that allowed for gel formation are shown. Quenching / thawing gave gels in 62% off all the experiments, a value that is not significantly different from the first treatment (slow cooling). In fact the overall pattern of gels' occurrence looks very similar to that of Table 4.1. Note that this is the first time that a series of gelators give similar results with such different gelation condition. The most frequently described ″spontaneous″ gelations reported in literatures tend to loose

their gelation abilities on increased cooling rates [18], while typical "quench gelation" do not gel on slow cooling [19].

Table 4.2 Quench gelation of **2**–**10c** in various organic liquids (5wt%).

	2	**4**	**5**	**6**	**7**	**8**	**9**	**10a**	**10b**	**10c**
	-OH	$-NH_2$	Li^+	Na^+	K^+	Cs^+	^+Py	$^+NMe_4$	$^+NEt_4$	$^+NBu_4$
Ethanol	×	×	*WG* [c]	×	×	×	×	*WG* [c]	×	×
DMF	*WG* [b]	*WG* [b]	CG [b]	*WG* [c]	×	*WG* [a]	*WG* [a]	*WG* [b]	×	×
Acetone	*WG* [b]	*WG* [b]	×	*WG* [c]	×	×	×	×	×	×
t-butylacetate	*WG* [b]	*WG* [a]	*WG* [a]	*WG* [c]	*WG* [b]	*WG* [a]	×	*WG* [b]	*WG* [c]	×
HEMA	×	*TG* [a]	*WG* [a]	*TG* [a]	*WG* [a]	*TG* [b]	*WG* [a]	*WG* [a]	*WG* [c]	×
TEGDMA	*TG* [a]	*CG* [a]	*TG* [a]	*WG* [a]	*TG* [a]	*TG* [c]	*WG* [a]	*TG* [a]	*TG* [c]	*TG* [c]
EGDMA	*WG* [a]	*CG* [a]	*WG* [a]	*WG* [a]	*TG* [a]	×	*WG* [a]	*WG* [a]	×	*WG* [a]
EHMA	*WG* [a]	*TG* [a]	*TG* [a]	×	*TG* [b]	*TG* [b]	*WG* [a]	*WG* [a]	×	*TG* [c]
HMA	*WG* [c]	*TG* [a]	*TG* [a]	*TG* [c]	*TG* [b]	*TG* [b]	*WG* [a]	*WG* [a]	×	×
Styrene	*TG* [a]	*TG* [b]	*TG* [b]	×	×	*TG* [c]	*TG* [b]	*TG* [a]	*TG* [c]	×
Toluene	*TG* [b]	*CG* [b]	*CG* [c]	×	×	×	*TG* [b]	*WG* [a]	×	×
n-Hexane	×	×	*TG* [b]	*WG* [c]	*CG* [c]	*WG* [c]	×	×	×	×

×: no formation of Gel; CG: Clear Gel ; TG: Translucent Gel; WG: White Gel;
a: Gel was formed at 25°C; ***b***: Gel was formed at 4°C; ***c***: Gel was formed at -20°C;
HEMA: 2-hydroxyethyl methacrylate; TEGDMA: triethylene glycol dimethacrylate;
EGDMA: ethylene glycol dimethacrylate; EHMA: 2- ethylhexyl methacrylate; HMA: n-hexyl methacrylate.

Sulfonamide **4** is a very potent gelator for most of organic solvents, except ethanol and DMF, which strongly compete for hydrogen-bond formation [20,21]. The gelling results from Table 4.1 and 4.2 also showed that all gelling temperatures of **4** were higher than 4 °C, which indicates the relative high thermal stability of the sulfonamide gels. The minimum gelling concentration of **4** in TEGDMA (triethylene glycol dimethacrylate) at –20 °C is around 0.1wt%. The high gelling capability of sulfonamide (**4**) can be explained by the formation of intermolecular hydrogen bonds. The highly directed H-bond acts as a strong driving force to induce the self-organization of molecules forming gels.

Besides sulfonamide (**4**), the other sulfonates (**5**–**10c**) have no possibility to form hydrogen bonds. In this cases Coulomb interaction between cations and sulfonate anions is the main driving force in gels formation. There are two series of sulfonates shown here. One is the alkali cations (Li^+, Na^+, K^+, Cs^+) sulfonates. The second series consists of tetra-alkyl-ammonium sulfonate, where the alkyl chains are methyl, ethyl and butyl respectively. However, in terms of the gelation spectrum hydrogen bonds seem to be superior over Coulomb interaction within the investigated examples.

As summarized in Table 4.1 and 4.2, all sulfonates gelled various solvents, especially the monomer solvents (methacrylates). Compounds **5**–**8** formed the thermoreversible gels in *t*-butylacetate, *n*-hexane and all the tested methacrylate solvents. In addition, **5** (Li^+) and **8** (Cs^+) formed gels also in DMF, styrene and toluene. Therefore, both the smallest cation (**5**) and the largest cation (**8**) sulfonate were observed as the best gelators in this series, which is able to form gels with a wider range of solvents.

Pyridinium sulfonate (**9**) did not gel any organic solvent by the spontaneous gelation process. However, by means of quench gelation it gelled DMF, styrene, toluene and all methacrylates.

Within the second series of gelators (**10a**–**c**), we found that tetramethyl ammonium sulfonate (**10a**) exhibited the best gelation capability, since it gelled almost all the solvents except from acetone at room temperature. When the ammonium cation became larger, the gelation capability decreased dramatically. It's worth to mention that the liquid crystal phases also disappear in the case of the larger ammonium cation (**10b** and **10c**) due to the large size of the headgroup. Most probably the longer alkyl chains at the nitrogen atom that reduce the polarity of the tetra-alkyl ammonium ions also diminish the amphiphilicity of the sulfonate salts and hence reduce the driving force for self assembly. Moreover, the large cations do not fit in the center of spherical or cylindrical superstructures and effectively impede their formation.

In upcoming work the sulfonate amphiphiles will be investigated for the preparation of functional materials by permanent embedding of the gel structures in crosslinked polymethacrylates. For this reason EHMA and the crosslinker EGDMA were selected for detailed investigations of the gel melting temperatures.

The concentration dependence of the gel melting temperatures was investigated on the alkali metal sulfonates (**5**–**8**) with 2-ethylhexyl methacrylates (EHMA) as solvent by means of DSC measurements. Figure 4.3 depicts typical DSC thermograms of the sodium salt **6**/EHMA mixtures. A broad endothermic transition was observed at about 5 °C, which corresponded to the gel-sol phase transition. However, potassium sulfonate (**7**) with EHMA showed a different thermal behavior. As shown in Figure 4.4, two broad endothermic transitions were found in the DSC heating curves. First a large endothermic transition was observed at 5 ~ 8 °C. Then around 21 ~ 23 °C a much smaller endothermic transition occurred. The similar phenomenon was observed for tetrabutyl-ammonium sulfonate (**10c**) in EHMA. Figure 4.5 showed the DSC heating curves of a gel of **10c** in EHMA. At about 51 °C a strong endothermic transition was observed which occurred over a narrow temperature range, indicating a highly cooperative phase transition. At about 80 °C, another endothermic transition occurred. Both the position of transition at 51 °C and at 80 °C shifted to lower temperature with decreasing concentration of the gels.

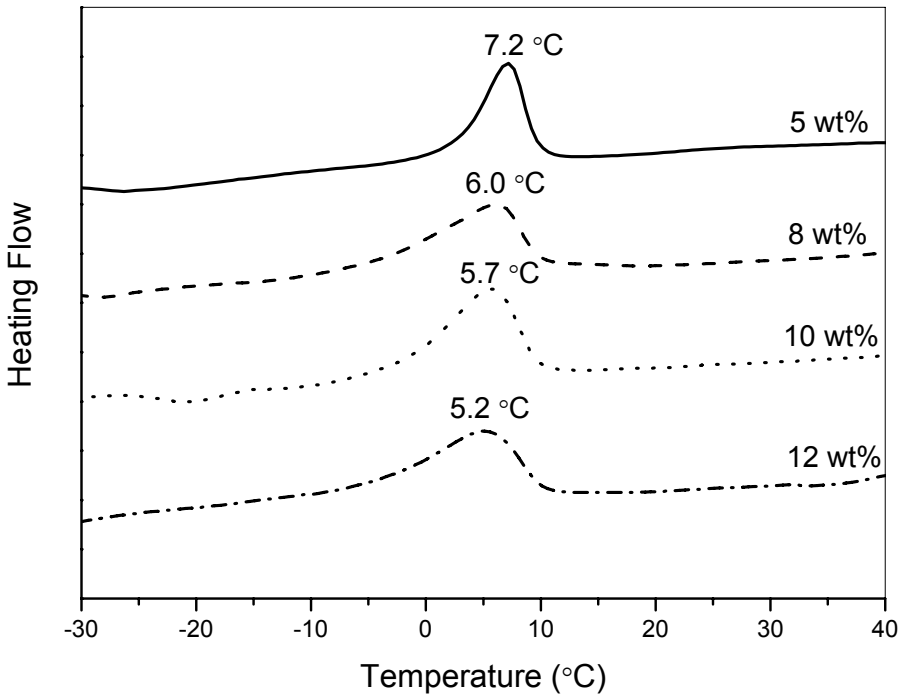

Figure 4.3 DSC thermogram of the sodium salt **6**/EHMA at different concentration.

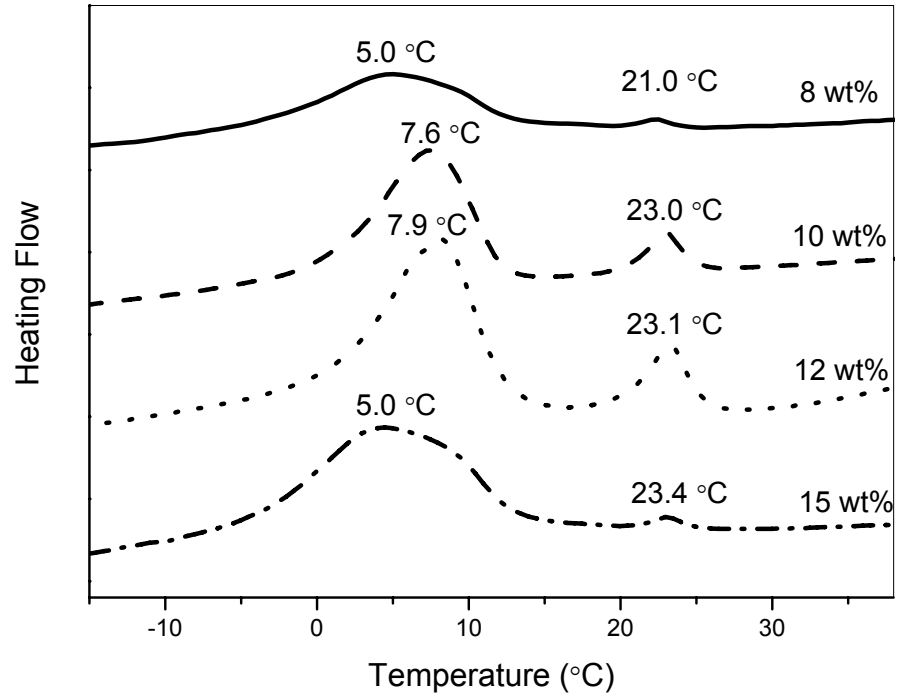

Figure 4.4 DSC thermogram of the potassium salt **7**/EHMA at different concentration.

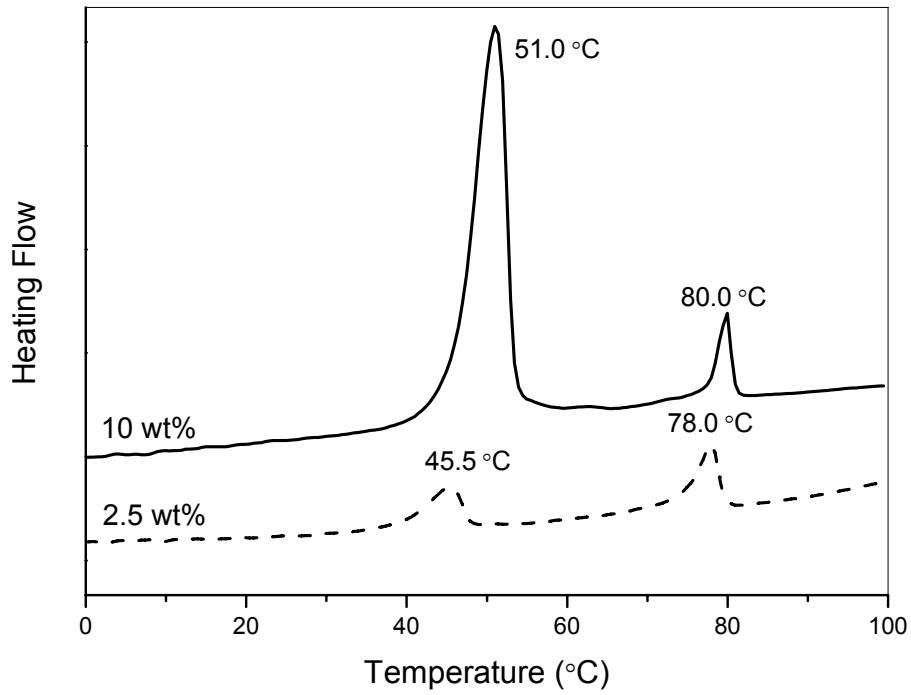

Figure 4.5 DSC thermogram of the tetrabutyl ammonium **10c**/EHMA at different concentration.

Thermal optical measurements revealed that the gel melting process occurred over a broad temperature range, which corresponded to the high temperature transition in the DSC thermograph. During the transition at 51 °C, no texture change was observed by

polarizing microscopy. Hence the high temperature DSC transition was attributed to the gel-sol phase transition. The lower temperature transitions observed by DSC either could be the onset of gel melting, or may correspond to structural changes of the gels indicating a thermotropic polymorphism of the **10c**/EHMA gel system. Similar observations were made also for some other systems, like caesium salt (**8**) in EHMA. The structural polymorphism in gel systems has been described by J. van Esch [22].

Figure 4.6 shows the concentration dependence of the gel melting temperatures. It was observed that compound **5** (Li^+) exhibited the highest gel melting temperature (45 ~ 50 °C), followed by the caesium salt (**8**) (25 ~ 35 °C) and the potassium salt (**7**) (22 ~ 25 °C), while the gels of the sodium salt (**6**) melted between 5 ~ 8 °C. Note that the concentration dependence of the measured gel melting temperature is comparably small indicating that a miscibility gap is present in the gelation region.

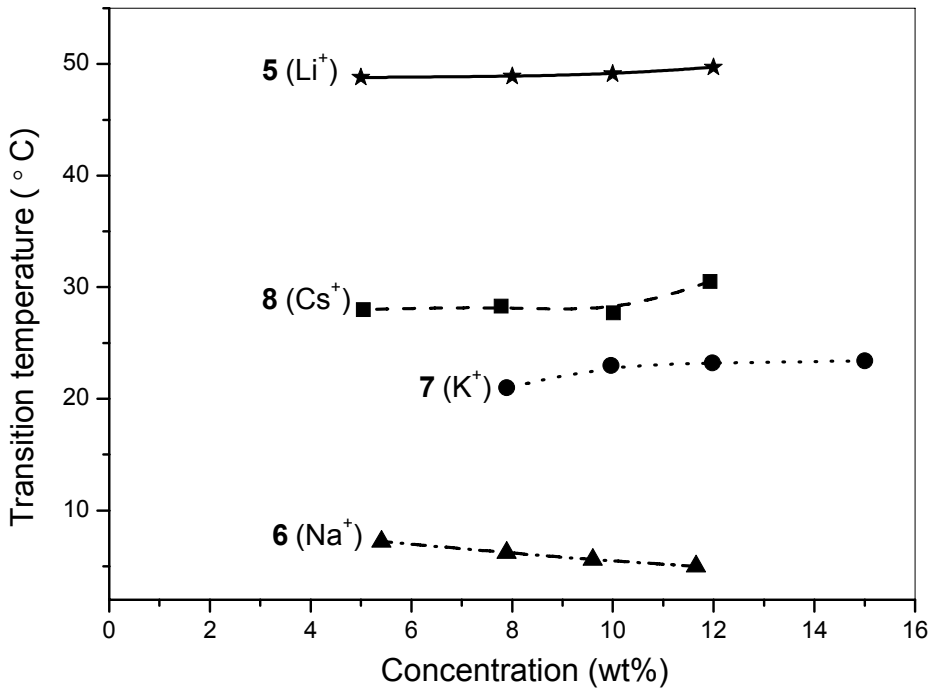

Figure 4.6 Concentration dependence of the gels melting temperature of **5**–**8** in EHMA.

Figure 4.7 shows the concentration dependence of the gel melting temperatures of pyridinium (**9**) and tetra-alkyl ammonium sulfonates (**10a**–**10b**) in EGDMA as the solvent. Compound **10b** ($^+NEt_4$) exhibited the highest gel melting temperature (73 ~ 85 °C), followed by **10a** ($^+NMe_4$), its gels melted at around 65 ~ 70 °C. Compound **10c** ($^+NBu_4$) showed relatively low gel melting temperature (35 ~ 43 °C).

The gels of the pyridinium sulfonate (**9**) melted between 60 ~ 65 °C. Clearly, the alkyl chain length connected to the ammonium cations has large effects on the gel formation. Since the alkyl chains usually have disordered arrangement, longer alkyl chains lead to larger cations that are more difficult to arrange in an ordered network. Thus tetra-butyl ammonium sulfonate (**10c**) exhibited the lowest gels melting temperature. On the other hand, different concentration dependence of the gels melting temperatures for **10b** ($^{+}NEt_4$) and **10c** ($^{+}NBu_4$) in EGDMA has been found. The gel melting temperatures of **10b** and **10c** obviously increased with increasing concentration, while **10a** ($^{+}NMe_4$) and **9** (Py^{+}) showed only small change with concentration. This observation indicates that the miscibility of **10b** (or **10c**) with EGDMA is higher than that of **10a** (or **9**) with EGDMA. The explanation can be that the longer alkyl chains of ammonium cation result in lower polarity of amphiphiles, which is in favour of good miscibility with semi-low polar solvent (EGDMA). For more polar compounds, such as pyridinium (**9**) and tetra-methyl-ammonium sulfonate (**10a**), a miscibility gap may occur in the gelation region.

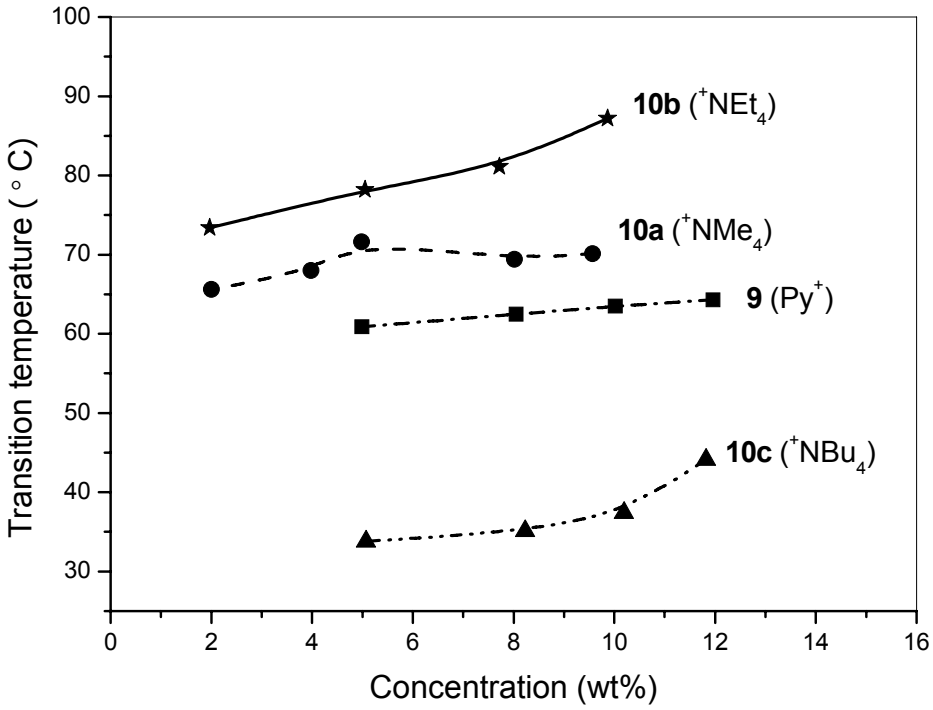

Figure 4.7 Concentration dependence of the gels melting temperature of **9** and **10a–c** in EGDMA.

Mixtures composed of sulfonic acid (**2**) or sulfonamide (**4**) and EHMA were also investigated by means of DSC measurements (cf. Figure 4.8). The gel of sulfonamide

(**4**) in EHMA melted around 45 ~ 50 °C, while sulfonic acid (**2**) exhibited gel melting temperature between 25 ~ 30 °C. Both systems showed small concentration dependence of gel melting temperatures, which indicates a miscibility gap existing in the gelation region.

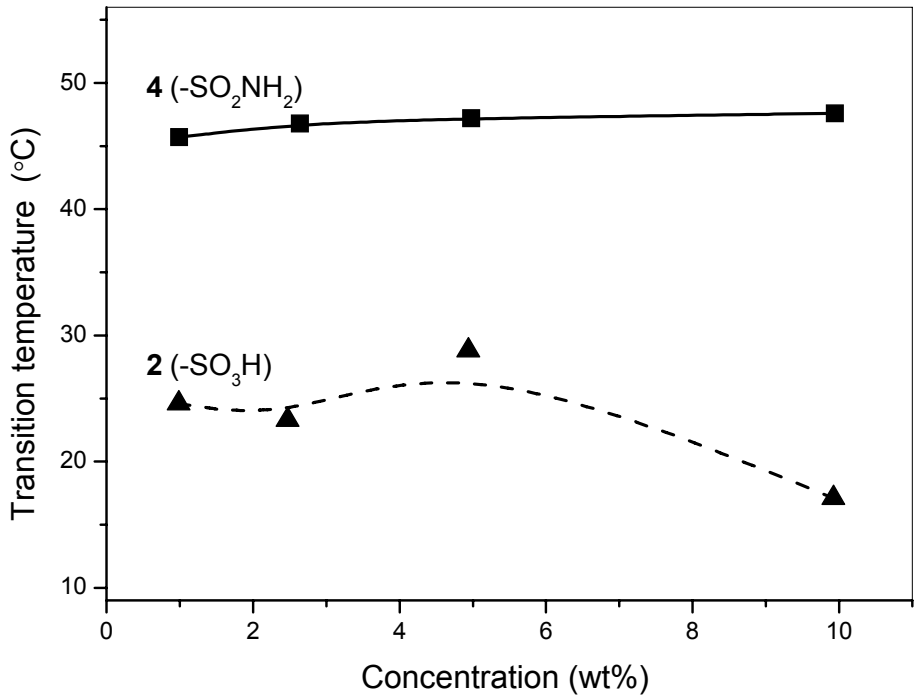

Figure 4.8 Concentration dependence of the gel melting temperatures of **2** and **4** in EHMA.

The series of 2,3,4-tris(dodecyloxy)benzene sulfonates were demonstrated to be versatile organogelators. Independent of the gelling conditions (slowing cooling or quenching) most of the compounds exhibited strong gelling behavior, which is the first time to be observed. Meanwhile, only **10b** ($^{+}NEt_4$) and **10c** ($^{+}NBu_4$) that are less polar molecules due to the long alkyl chain ammonium cations, showed an increasing dependence of the gel melting temperatures on concentration, which indicates a good miscibility between gelators and solvents. The others exhibited quite small dependence on concentration, which indicates the presence of a miscibility gap in the temperature / concentration phase diagrams of gelators and solvents.

Gelation capabilities of 3,4,5-substituted benzene sulfonates

Table 4.3 summarizes the gelation behaviours of 3,4,5-tris(dodecyloxy)benzene sulfonate derivatives (**12**–**16**) in various polar and non-polar organic solvents, including some monomer liquids. As previous described the hot solutions were subjected to slow cooling to 20 °C, 4 °C and -20 °C as well as quenching to -196 °C and slow warming up to the respective temperature.

Table 4.3 Spontaneous and Quench Gelation of **12**–**16** in various organic liquids (5wt%).

	12	**13**	**14**	**15**	**16**	**12**	**13**	**14**	**15**	**16**
	Li^+	Na^+	K^+	Cs^+	Cs^+	Li^+	Na^+	K^+	Cs^+	Cs^+
	Spontaneous Gelation					Quench Gelation				
Ethanol	×	×	×	×	*TG*[c]	×	×	×	*TG*[b]	*WG*[c]
DMF	×	*WG*[a]	×	×	×	×	*WG*[a]	×	×	×
***t*-butylacetate**	×	×	*WG*[b]	*OG*[a]	*WG*[a]	×	×	×	×	×
HEMA	*CG*[a]	*WG*[a]	*TG*[c]	*TG*[b]	*TG*[c]	*WG*[a]	*WG*[a]	*OG*[a]	*TG*[a]	*TG*[a]
TEGDMA	*TG*[a]	*TG*[a]	*WG*[c]	*TG*[a]	*TG*[b]	*TG*[a]	*WG*[c]	*OG*[a]	*TG*[a]	*TG*[a]
EGDMA	*TG*[a]	*TG*[a]	*TG*[c]	*TG*[a]	*TG*[a]	*WG*[b]	*WG*[a]	×	*TG*[a]	*TG*[a]
EHMA	*TG*[a]	×	*TG*[c]	*TG*[a]	*TG*[a]	*WG*[a]	×	×	×	×
HMA	*TG*[a]	×	*TG*[c]	*TG*[a]	*TG*[a]	×	×	×	×	×
Styrene	×	×	×	*TG*[a]	*CG*[a]	×	*TG*[a]	*TG*[a]	×	×
Toluene	×	×	*CG*[c]	*CG*[a]	*CG*[a]	×	×	*CG*[a]	×	×
n-Hexane	×	×	*CG*[c]	×	×	×	×	×	×	×

×: no formation of Gel; CG: Clear Gel ; TG: Translucent Gel; WG: White Gel;
a: Gel was formed at 25°C; ***b***: Gel was formed at 4°C; ***c***: Gel was formed at -20°C;
HEMA: 2-hydroxyethyl methacrylate; TEGDMA: triethylene glycol dimethacrylate;
EGDMA: ethylene glycol dimethacrylate; EHMA: 2- ethylhexyl methacrylate; HMA: n-hexyl methacrylate.

From Table 4.3 it is obvious to realize that alkali sulfonates with symmetric structure are powerful gelling agent. Compound **15** (Cs^+) gelled almost all the solvents at room temperature except from DMF and *n*-hexane. Most of the gels formed from **15** are

either of the clear or translucent gel type, which indicates that the superstructures of the networks formed in the gels, is in the scale of nanometer dimension.

Comparing the number of gelled samples (34 out of 55 by slow cooling vs. 21 out of 55 after quenching) it reveals that the symmetrically substituted materials react more sensitive to quenching than the asymmetric ones. Furthermore it seems that the asymmetric sulfonates tend to gel more solvents. In opposition the caesium compounds **15** and **16** formed the most stable gels, while with the 2,3,4-substituted materials, the lithium salt (**5**) was the best gelator within the asymmetric alkali salts.

Figure 4.9 illustrates the structural difference between three caesium sulfonates **8**, **15**, and **16**. Compound **8** corresponds to the 2,3,4-dodecyl-oxy substituted benzene sulfonates, and it is an asymmetric molecule. **15** and **16** are denoted to 3,4,5-substituted benzene sulfonates, which are geometrically symmetric from the structural point of view. The difference between **15** and **16** is that compound **16** is the undecenyl-oxy substituted instead of dodecyl-oxy substituted for **15**. That means that the native of **16** molecules are a little bit less hydrophobic but more flexible than **15** molecules.

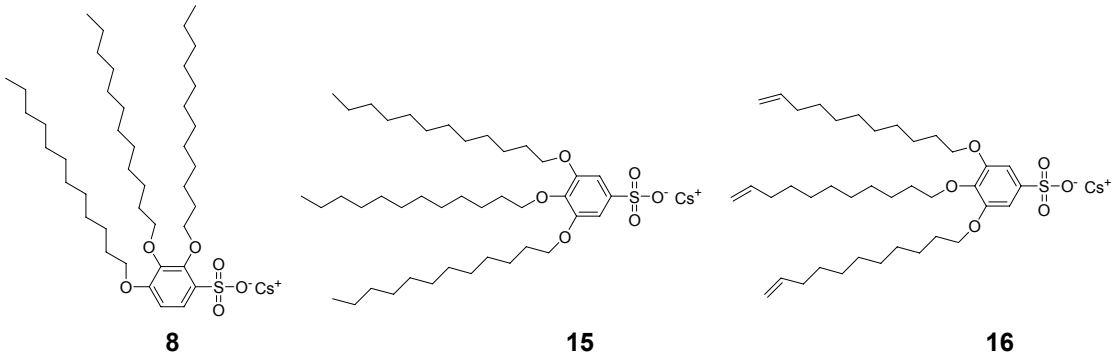

Figure 4.9 Chemical structures of **8, 15** and **16**.

Figure 4.10 shows the DSC thermograms of compound **15**. Similar to compound **7**, two endothermic transitions were observed in the DSC heating curves. At around 54 °C a shape large endothermic transition occurred, while a broad endothermic transition was observed at around 99 °C. The observation by optical microscopy indicated the gel melting temperature was about 98 °C. The gels of **16**/EHMA exhibited a simple thermal transition. One gel-sol phase transition occurred between 77 ~ 80 °C. The position of transition sifted to a little bit higher temperature with increasing concentration of the gels.

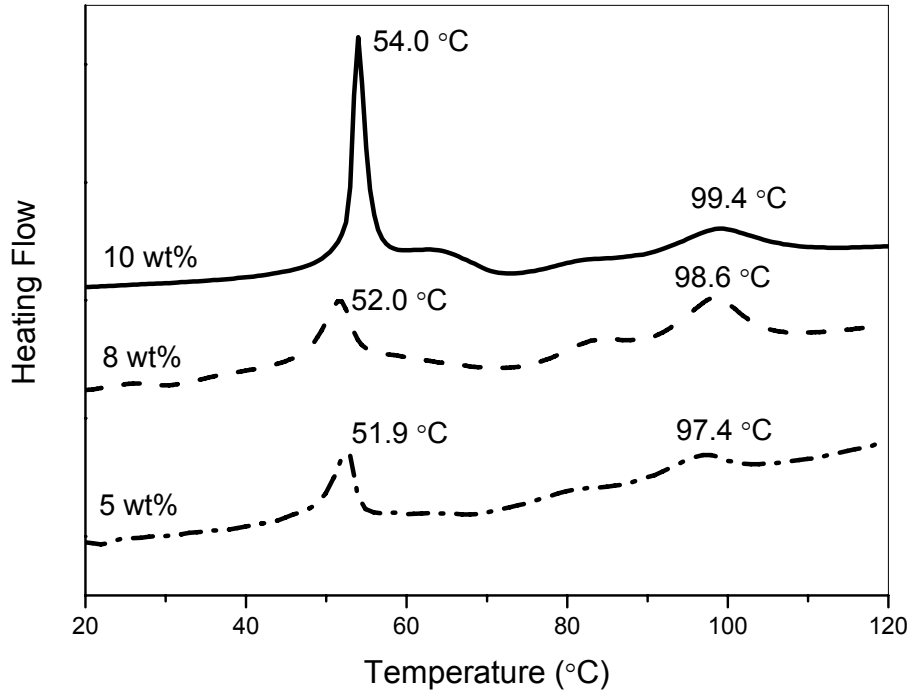

Figure 4.10 DSC thermogram of the caesium salt **15**/EHMA at different concentration.

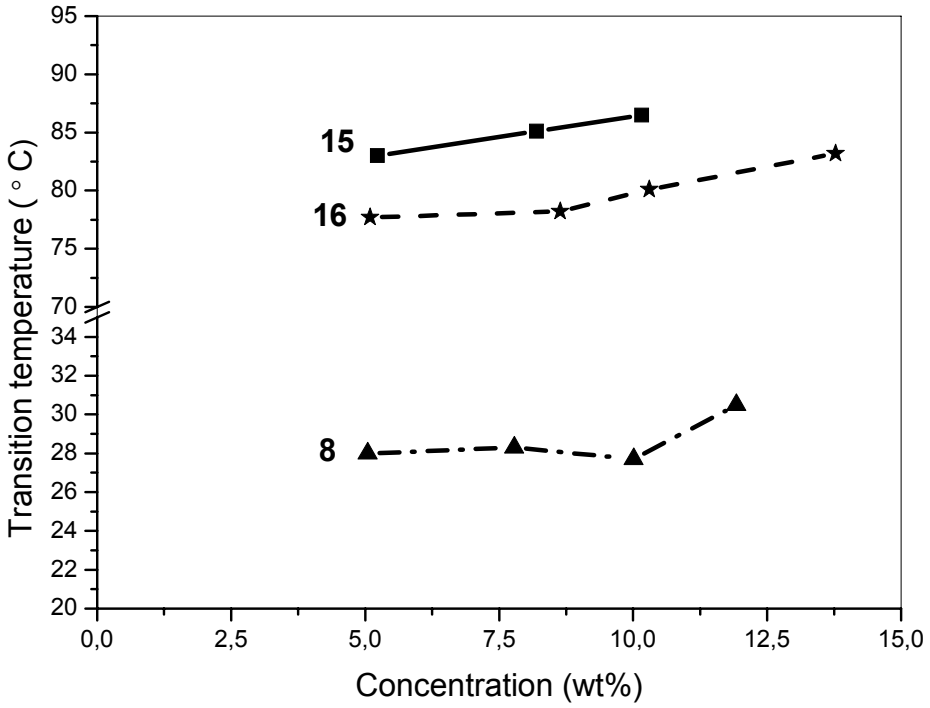

Figure 4.11 Concentration dependence of the gels melting temperature of **8, 15** and **16** in EHMA.

Figure 4.11 depicts the concentration dependence of the gels from **8**, **15** and **16** with EHMA in the concentration range from 5wt% to 15wt%. The symmetric compound **15**

exhibited the highest gel melting temperature (83 ~ 87 °C), followed closely by **16** (77 ~ 83 °C), while the gel melting temperature of asymmetric compound **8** was only around 28 ~ 30 °C. Obviously the symmetric compounds **15** and **16** exhibited much higher gelling temperatures than asymmetric **8**. The vinyl-end groups of compound **16** seem to increase the solubility and simultaneously to reduce the transition temperatures as compared to molecules with saturated chains. This is a common behaviour, frequently reported in the literature [7]. It can be concluded that the geometrically symmetric structure is in favour of self-assembly into ordered arrangements (like fibers). Meanwhile, besides the hydrophilic headgroup (cations), the alkyl chains of the hydrophobic bulk also determine the gelling temperatures.

Morphologies of the gels investigated by TEM

The morphology of gels in various solvents was investigated by transmission electron microscopy (TEM). Dried gels have been prepared by evaporation of the solvent in air. The specimen was picked up on carbon-coated cupper grids and stained by RuO_4 from the gas phase. The details of sample preparation are described in the experiment section.

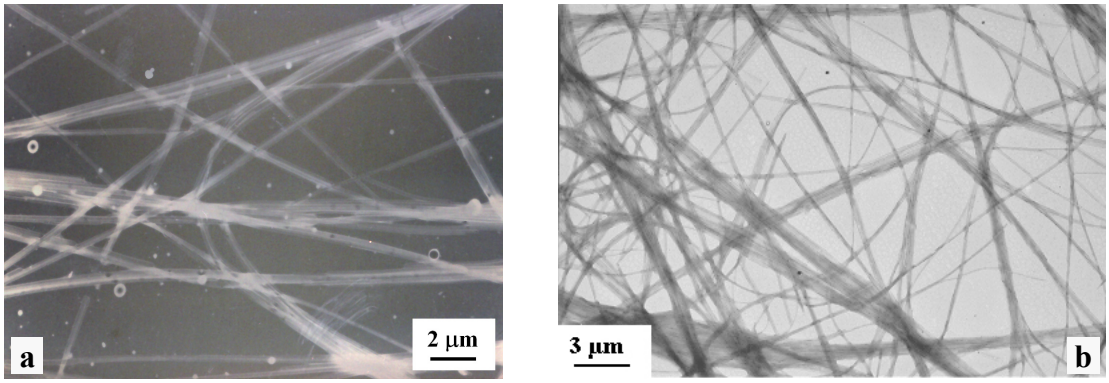

Figure 4.12 TEM micrograph from dried gel of sulfonamide **4** in (a) EHMA (0.5wt%); (b) styrene (2wt%), stained by RuO_4.

Figure 4.12 shows two electron micrographs of **4** (sulfonamide) in EHMA and styrene. In both cases long thin fibers, which form an entangled network, were observed. In Figure 4.12a, the average diameter of fibers was about 300 nm, which was much higher than molecular dimension. The observed smallest diameter of the elemental fiber in gel formed in styrene (cf. Figure 4.12b) was only 6 nm, which was very close to the

molecular or aggregation dimension. The bundles of single fibers were observed as well. The regular shape and the extreme aspect ration of the fibers must arise from a strong anisotropic growth process, indicating that the fibers have well-ordered molecular packing. It was found that the solvents had little effect on the morphology of the fibers. The only observed difference was that more condensed fibbers were formed in the higher polar solvent (EHMA) (cf. Figure 4.12a). It has been reported that the different morphologies should originate from differences in interfacial free energy or attachment energies in the various solvents [23]. However, no clear correlation between the fiber morphology and solvent properties like polarity, or hydrogen-bonding capability was observed.

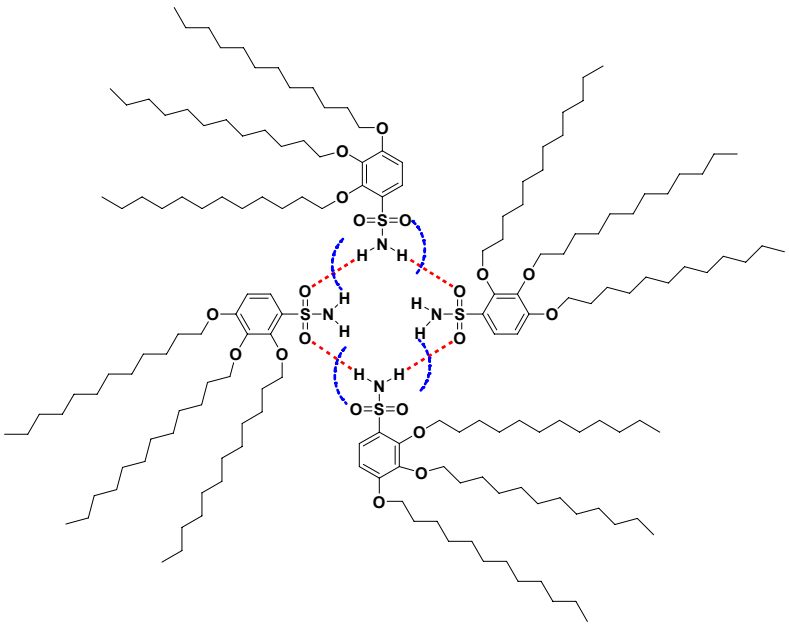

Figure 4.13 Illustration of the hydrogen-bonded self-organization of **4** in styrene gel.

As we discussed above, **4** is a hydrogen-bonding gelling agent. Therefore, hydrogen-bonding acts as a strong driving force to self organize the molecules into extremely elongate fibers. We proposed a model of self-assembly of molecules into fibers by hydrogen bonding. As illustrated in Figure 4.13, four molecules first form a tetramer by hydrogen bonds between S=O and -NH_2 groups. Subsequently, the tetramers stack together through intra-tetramers hydrogen bonds forming the molecular pack. Finally it results in an elongated fiber. By means of the force field molecular modelling calculation, a molecular packing model for 24mer of compound **4** was simulated. After

the optimization with respect to the force field energy, the resulting organizations of structure are showed in Figure 4.14. The formation of the planar tetramers was obviously found from Figure 4.14a. Such planar tetramer units stacked together to build up a column containing a channel in the center. Figure 4.14b depicts the side view of the 24mer. The hydrophilic sulfonamide head group were completely surrounded by the hydrophobic alkyl chains. The diameter of the column after calculation is about 5 nm, which is identical to the value (ca. 6 nm) that we observed in the TEM micrographs.

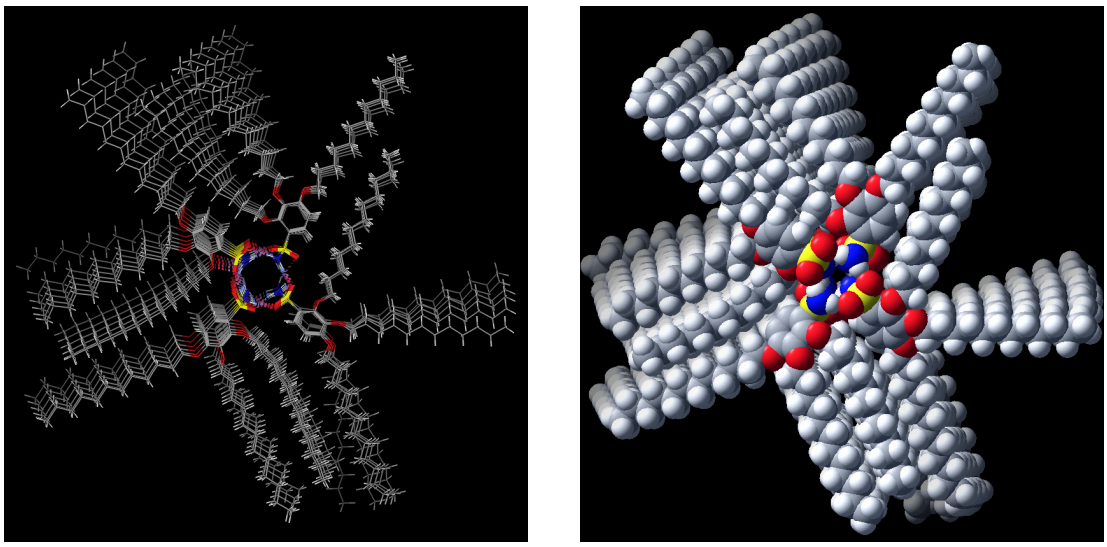

Figure 4.14 Illustration of the self-organization of sulfonamide **4** calculated by Force Field Molecular Models, (a) top view of a 24mer.

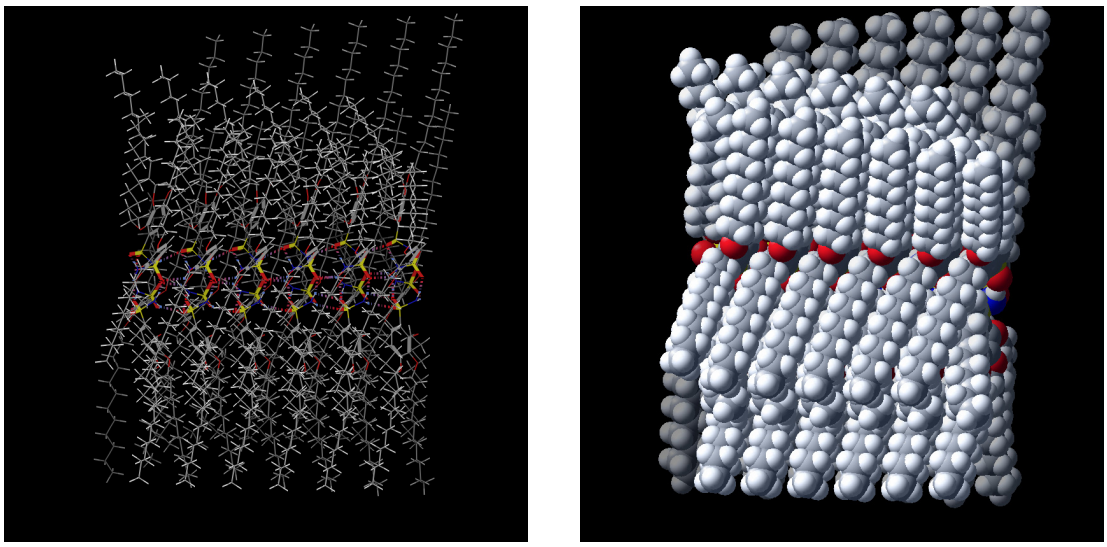

Figure 4.14 Illustration of the self-organization of sulfonamide **4** calculated by Force Field Molecular Models, (b) side view of a 24mer.

On the other hand, the rest of the compounds are non-hydrogen-bond-based gelators. Their gels were also investigated by TEM. Figure 4.15 shows the morphology of a translucent gel from 1wt% **5** (Li^+) in EHMA. Again long thin fibers with about 10 nm diameter of the smallest fiber were observed. The average diameter of the fibers was about 60 nm and the bundles were formed as well with much larger dimension (more than 0.5 μm).

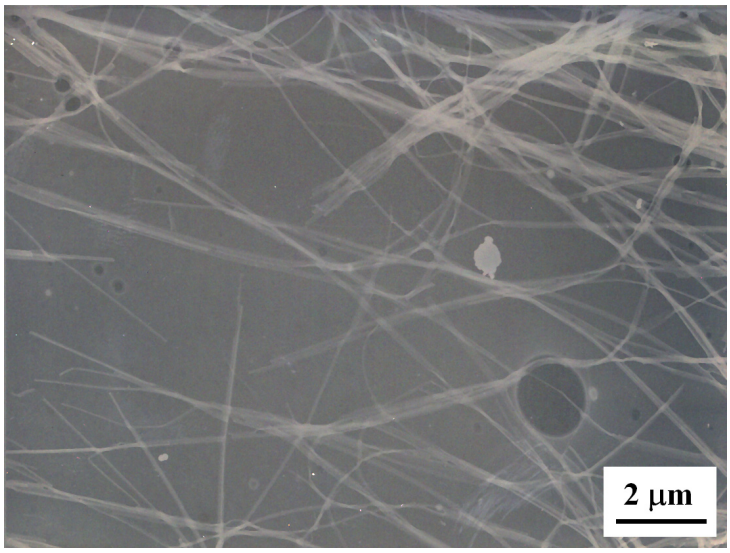

Figure 4.15 TEM micrograph from dried gel of **5** (Li^+) in EHMA (1wt%), stained by RuO_4.

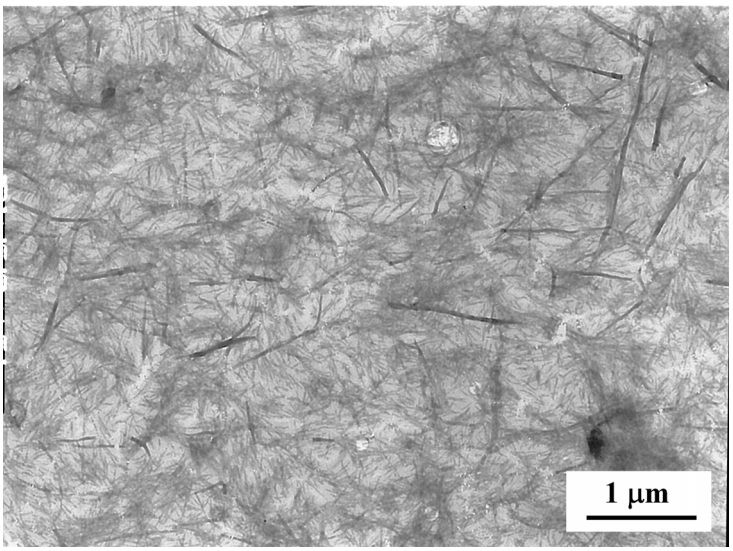

Figure 4.16 TEM micrograph from dried gel of **6** (Na^+) in EHMA (1wt%), stained by RuO_4.

The micrograph of the gel from **6** (Na^+) with EHMA is shown in Figure 4.16. Numerous fine but short fibers were observed. The diameter of the fine fibers was only about 6 nm and the aspect ratio was about 40–60. The gel of potassium sulfonate (**7**)

was found to consist of small crystalline aggregates (cf. Figure 4.17). That looked like that many small spheres arranged to linear structures. The diameter of the spheres was about 120 nm. The array of the spheres extended nearly infinitely.

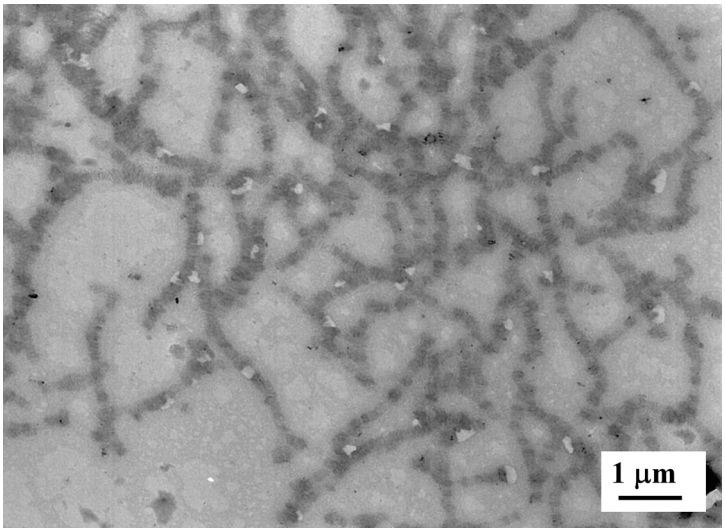

Figure 4.17 TEM micrograph from dried gel of **7** (K^+) in EHMA (1wt%), stained by RuO_4.

Caesium sulfonate (**8**) also formed short fiber-like structures, but they had a different appearance. Figure 4.18 showed the TEM micrographs of the gels from **8** with HEMA and EHMA. In both cases plenty of short fibrous microstructures, which looked like platelets (more flat structure), were observed. The diameter of the fibers in the gel of HEMA was about 30 nm. And the length of the fibers was 3 ~ 5 μm (aspect ration is around 50). The diameter of the fibers in the gel of EHMA was larger (around 200 nm) with aspect ratio of 30–50. The formation of the short fibers indicates that the driving force for molecular packing is relatively weak. Again, no obvious difference between the gels from two different solvents was found.

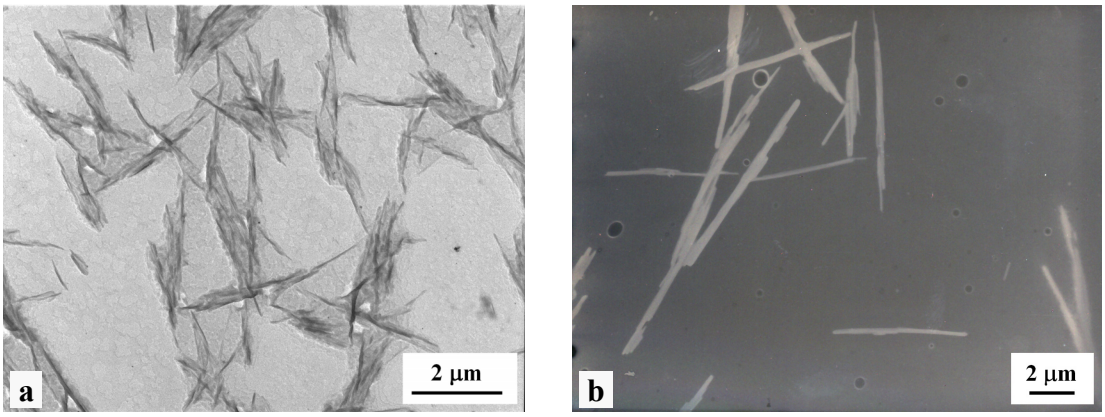

Figure 4.18 TEM micrograph from dried gel of **8** (Cs^+): (a) in HEMA (2wt%); (b) in EHMA (10wt%), stained by RuO_4.

The gels of pyridinium (**9**) and ammonium cations (**10a**–**10c**) sulfonates in EHMA were also investigated by TEM. However, only small crystal pieces instead of fibers network were observed (cf. Figure 4.19).

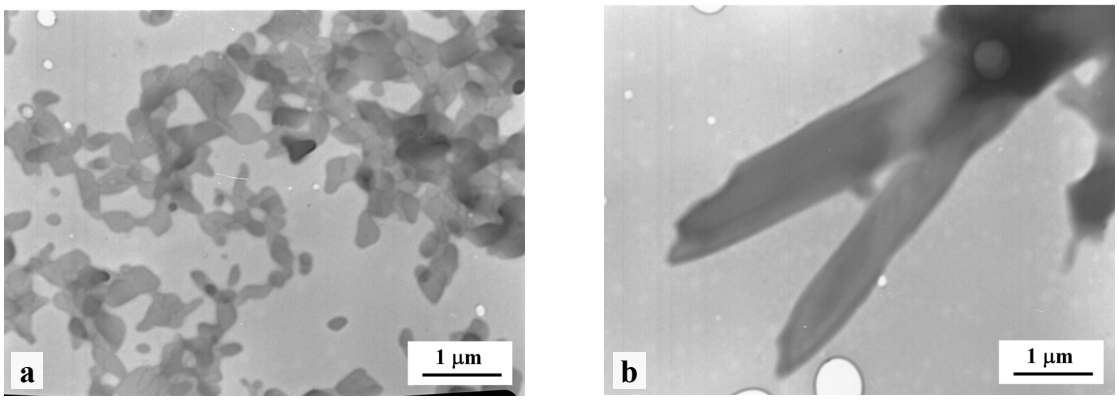

Figure 4.19 TEM micrograph from dried gel of (a) **9** (Py^+) in EGDMA (1wt%); (b) **10a** ($^+NMe_4$) in EGDMA (1wt%), stained by RuO_4.

Table 4.4 Relationships between amphiphile shape, water content and preferred aggregation structure, based on the Israelachvili Model [24].

Amphiphile "shape"	Amphiphile structure	$\rho = \frac{V}{a_0 l_c}$	Rel. H_2O content	Aggregate structure
hydrophobic tail(s), hydrophilic headgroup (conical)		< 1/3	high	
(truncated cone)		1/3–1/2	medium	
(cylindrical)		≈1	medium	
(conical)		> 1	low	
(tapered?)			low	
(cylindrical?)			medium	

Apparently, the geometrical shape of the amphiphiles plays a crucial role in determining geometry of the aggregation. Since the chain length of these compounds is identical, the size of the headgroup is the main factor of the molecular shape. The approach, which considers the system on the microscopic level in terms of the

molecular shape and packing preferences of the constituent amphiphiles to extrapolate the geometry of the preferred aggregation, has generally been rationalized [24]. The shape-based approach is presented mathematically by the "critical packing parameter", $q = v / a_0 l_c$, where v is the effective hydrocarbon chain volume, a_0 is the polar headgroup area and l_c is alkyl chain length of the amphiphile [24]. According to this model, relationships between amphiphile shape, water content and preferred aggregate structure are presented in Table 4.4. These very qualitative shape guidelines were originally developed to explain the formation of micelles, reverse micelles, and the hexagonal and lamellar phases, but did not extend to the lesser known inverted hexagonal phase (H_{II}) or bicontinuous cubic phases (Q_{II}) at that time. The reversed phases have not been systematically rationalized yet.

Figure 4.20 illustrates the different aggregation of **5** (Li^+), **6** (Na^+), **7** (K^+) and **8** (Cs^+). The amphiphile with smallest cation (Li^+) formed almost infinite long cylindrical structure, while for the amphiphile with sodium cation (Na^+), only short rods were formed. When the cation grows larger, i.e. K^+, spherical structure with linear array was found. With caesium cation, the flat aggregation, platelets, was formed. The amphiphiles with larger cations like pyridinium sulfonate (**9**) only formed flat crystals.

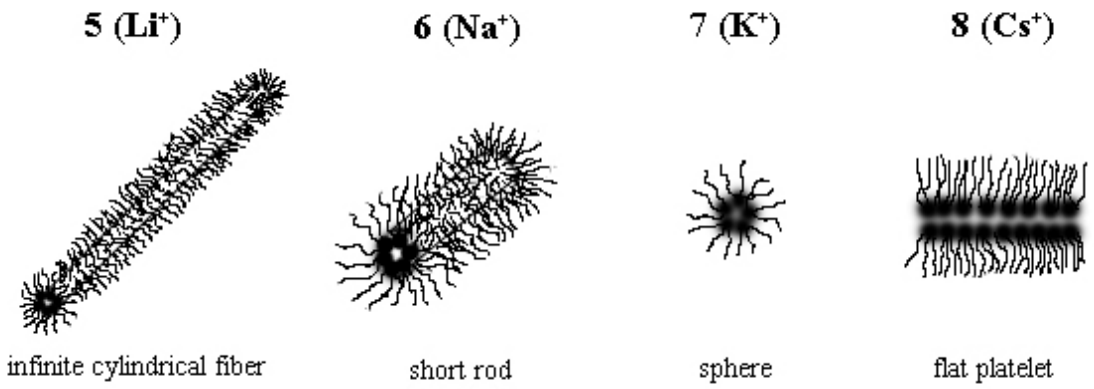

Figure 4.20 Illustration of the proposed aggregation of **5**–**8** in EHMA.

It has been concluded that the symmetric molecules were more powerful gelators than asymmetric molecules. Similarly, the structural differences have a large effect on the morphology of gels. The regular shape and the highly thin and elongate fibers were observed on the gels from **15** and **16** (cf. Figure 4.21 and 4.22).

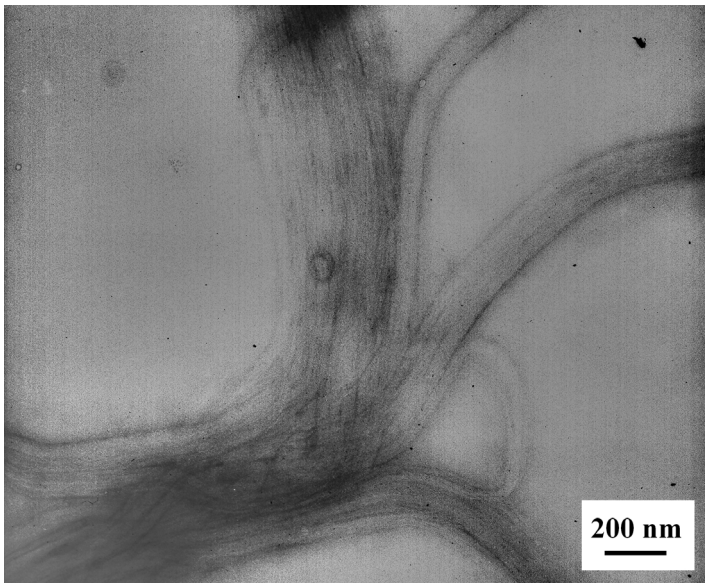

Figure 4.21 TEM micrograph from dried gel of **15** in toluene (2wt%), stained by RuO_4.

Many thin and fine elemental fibers can be distinguished on the micrographs, with diameter as small as 3 ~ 5 nm, which are comparable to the molecular dimension of **15** and **16**. In addition, the elementary fibers favoured to form the bundles, e.g. a bundle as large as 150 nm containing more than 10 elemental fibers (cf. Figure 4.22). From the micrograph, the arrangement of the fibers was found to be quite uniform. The TEM investigation confirms that besides hydrogen bonding, the appropriate molecular structure with Coulomb interaction is also favourable to self-assembly into supramolecular fibers.

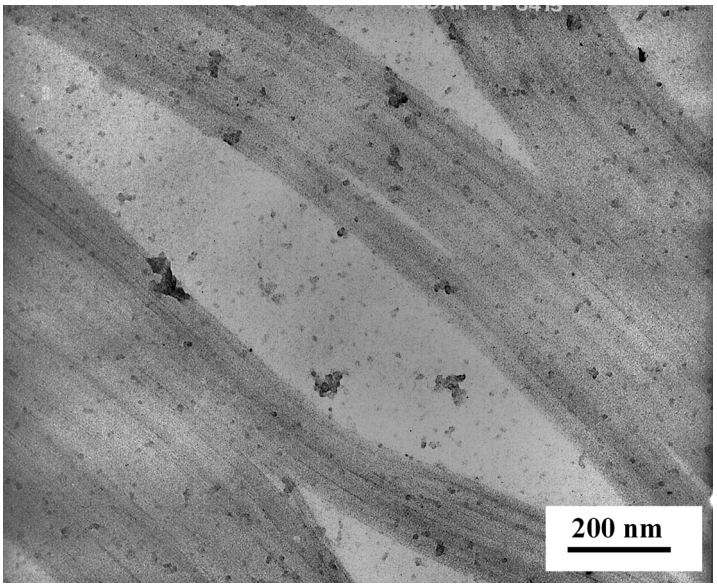

Figure 4.22 TEM micrograph from dried gel of **16** in EHMA (2wt%), stained by RuO_4.

The infinite cylindrical superstructure can be further applied to develop the functional materials with nanometer-scale architectures. The sulfonated moiety in the center of the cylinder provides the functions of the ions selectivity and transport.

Conclusion

In this chapter, the gelation capability of the series of sulfonated amphiphiles has been reported. Most of compounds are versatile organogelators, which are able to gel various solvents from non-polar to polar upon either the self-aggregation or the crystallization. It was found that compound **4** with hydrogen bond as driving force and the symmetric alkali sulfonate (e.g. **15** and **16**) driven by the Coulomb interaction, are most potent gelators for a wide range of organic solvents. The morphologies of gels were studied by TEM as well. Various morphologies of aggregation have been observed, e.g. infinite cylinders, short rods, array of spheres and flat platelets corresponding to the sequence of growing sizes of alkali cations. The structural differences between the compounds, which include the headgroup (size of cations), the alkyl chains and the geometry of the building blocks, have a large effect on the gelling capability and the morphology of gels. The infinite cylindrical aggregations that formed in the gels with sulfonated moiety in the center provide a route to construct the ion-selective transporting channels.

References

[1] T. Kato, *Science*, **2002**, 295, 2414.

[2] D. J. Abdallah and R. G. Weiss, *Adv. Mater.*, **2000**, 12, 1237.

[3] P. Terech and R. G. Weiss, *Chem. Rev.*, **1997**, 97, 3133.

[4] A. Ajayaghosh and Subi J. George, *J. Am. Chem. Soc.,* **2001**, 123, 5148.

[5] A. Aggeli, M. Bell, N. Boden, J. N. Keen, P. F. Knowles, T. C. B. McLeish, M. Pitkeathly, S. E. Radford, *Nature*, **1997**, 386, 259.

[6] D. Philip, J. F. Stoddart, *Angew. Chem. Int. Ed. Engl.*, **1996**, 35, 1154-1196.

[7] U. Beginn, *Prog. Polym. Sci.,* **2003**, 28, 7, 1049-1105.

[8] S. I. Stupp, S. Son, H. C. Lin, L. S. Li, *Science*, **1993**, 259, 59-63.

[9] G. M. Whitesides, J. P. Mathias, C. T. Seto, *Science*, **1991**, 254, 1312-1319.

[10] K. Hanabusa, M. Yamada, M. Kimura, H. Shirai, *Angew. Chem. Int. Ed. Engl.*, **1996**, 35, 1949-1951.

[11] Y. Yasuda, E. Iishi, H. Inada, Y. Shirota, *Chem. Lett.*, **1996**, 575-576.

[12] C. M. Paleos, D. Tsiourvar, *Angew. Chem.*, **1995**, 107, 1839.

[13] J.-H. Furhop, W. Helfrich, *Chem. Rev.*, **1993**, 93, 1565.

[14] H. Gankema, M. A. Hempenius, M. Möller, G. Johansson, V. Percec, *Macromol. Symp.*, **1996**, 102, 381.

[15] V. Percec, G. Johansson, G. Zipp,, U. Beginn, M. Möller, *Macromol. Chem. Phys.*, **1997**, 198, 265.

[16] U. Beginn, B. Tartsch, *Chem. Comm.,* **2001**, 19, 1924-1925.

[17] *a)* G. Kanig, *Coll. Pol. Sci.*, **1977**, 255, 1005; *b)* J. S. Trent, J. J. Scheinbeim, P. R. Couchman, *Polym. Sci. Technol.*, **1983**, 22, 205; *c)* D. Mantezinos, G. B. Wells, J. L. Burns, *J. Polym. Sci., Polym. Lett.*, **1985**, 23, 1220.

[18] U. Beginn, S. Keinath, M. Möller, *Macromol. Chem. Phys.,* **1998**, 199(11), 2379-2384.

[19] U. Beginn, S. Sheiko, M. Möller, *Macromol. Chem. Phys.,* **2000**, 201(10), 1008-1015.

[20] A. F. M. Barton, *Chem. Rev.*, **1975**, 75, 731-753.

[21] M. Mammen, E. E. Simanek, G. M. Whitesides, *J. Am. Chem. Soc.*, **1996**, 118, 12614-12623

[22] Jan H. van Esch, F. Schoonbeek, M. de Loos, H. Kooijman, A. L. Spek, R. M. Kellogg, Ben L. Feringa, *Chem. Eur. J.*, **1999**, 5, 937-950.

[23] P. Hartman, P. Bennema, *J. Cryst. Growth*, **1980**, 49, 145-156.

[24] J. N. Israelachvili, *Intermolecular and Surface Forces with Applications to Colloidal and Biological Systems*; Academic: London, **1985**; 249-257.

Chapter 5

Polymerized Lyotropic Liquid Crystal Assemblies for Functional Membranes

Introduction

Synthetic functional membranes, capable of selective transport of ions or molecules, represent a challenging target for preparative membrane science. Nowadays, the most frequently used functional membrane in application is Nafion®, a perfluorocarbon-based polymer carrying sulfonic acid residues. But Nafion® does not possess geometrically defined pores. On the other hand, numbers of membranes prepared with well-defined pores are not functionalized. Therefore, a membrane containing both spatially ordered, structurally defined pores and ion-selective transporting functions, presents great potential in industrial application, such as separation processes.

Our concept proposed an incorporating of functional superstructure (such as channels) into 'thick' films based on the self-assembly of amphiphiles into long, solid cylindrical aggregates. In previous work, it has been reported that wedge-shaped amphiphiles exhibited great tendency of self-assembly into hexagonal columnar mesophases [1]. Meanwhile, to enable supramolecular transport through the cylinders they should contain functional receptor units in their center. In the former work of our group, amphiphiles with crown ether (MCE) as the functional receptor were prepared for channel-like membranes, which performed selective ion-transport by hopping mechanism [2]. The chemical structure is shown in Figure 5.1. Since the selecting principle of the crown ether is based on the spatial size of ions, the intrinsic ion selectivity is large, however, the membranes selectivity was limited because of the specific channel structure [3]. Thus a different type of functional receptor is desired. In our case caesium sulfonate is investigated as receptor, because of the sulfonate group's inherent high polarity and super-selectivity [4].

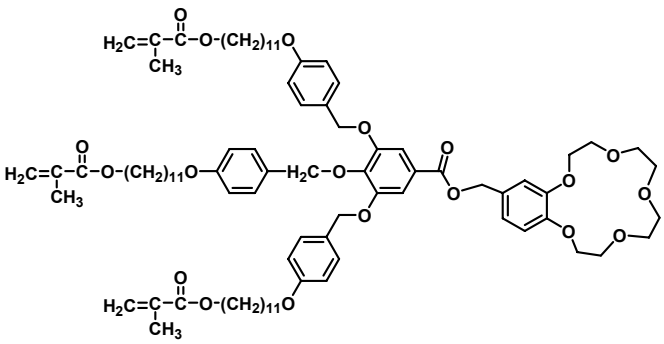

Figure 5.1 Chemical structure of MCE**:** (2-hydroxymethyl-[1,4,7,10,13-pentaoxacyclopentadecane]-3,4,5-tris[4-(11-methacryloylundecyl-1-oxy)benzyloxy] benzoate.

It was a successful approach to incorporate self-assembled networks of polymerizable cylinders into an apolar cross-linked methacrylate resin [5]. Hence, it is necessary to introduce polymerizable olefin groups on the outer rim of the cylinder in order to fix the channels permanently to the membrane matrix.

Based on the knowledge of the membranes formed by tri-methacrylated crown ether (MCE) [3], which exhibited only low absolute ion-transport rates, two improvements were suggested. One main improvement is to increase the volume fraction of the channel-building molecules in the membranes. The other improvement, which is probably most important, is to orient the supramolecular channels uniformly and perpendicular to the membrane surface. If the channels are arranged in isotropic orientation, transport distances are enlarged and their average length is unlikely to bridge the width of the membranes. Thus the ions have to transit from the end of one column into another one by moving through the strongly cross-linked, non-polar polymer matrix. Therefore, highly oriented anisotropic materials, for example lyotropic liquid crystals, are required. According to the above discussion, caesium 3,4,5-tris(undec-10-enyloxy)benzene sulfonate (**16**) was designed as the target molecule to fit for all requirements (cf. Figure 5.2).

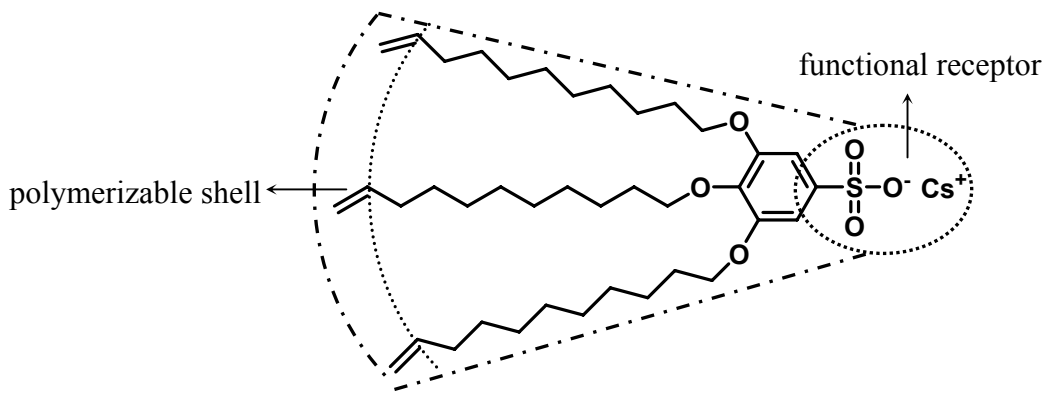

Figure 5.2 Chemical structure of wedge-shaped sulfonated amphiphile: **16**.

In Chapter 3 the synthesis of caesium 3,4,5-tris(undec-10-enyloxy)benzene sulfonate (**16**), which possesses caesium sulfonate as functional receptor and co-polymerizable olefin groups at the end of alkyl chain, has been described in detail. The compound was obtained by direct alkylation of 3,4,5-trihydroxy-benzene sulfonic acid with 11-bromo-undecene using caesium carbonate as a base, while 3,4,5-trihydroxy-benzene sulfonic

acid was synthesized by sulfonation of 3,4,5-trihydroxy-benzene and subsequent purification via the barium salt and liberation of the acid with a cation exchange resin (cf. Figure 5.3). The final product was at least 99% pure as revealed by TLC and elemental analysis.

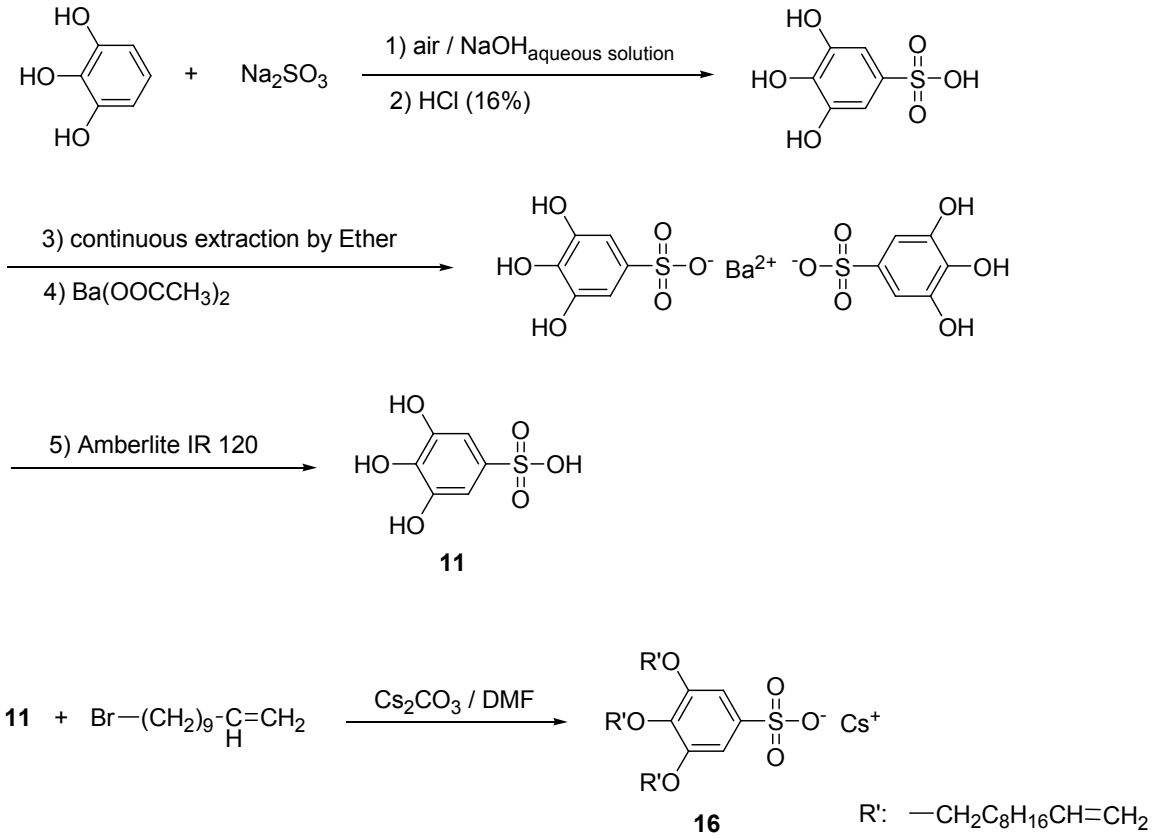

Figure 5.3 Synthesis scheme of caesium 3,4,5-tris(undec-10-enyloxy)benzene sulfonate (**16**).

The phase behaviour of compound **16** has been investigated in Chapter 3 as well. The vinyl-terminated caesium salt melts at 112 °C into a hexagonal columnar disordered mesophase (C_{hd}) and becomes isotropic at 222.5 °C. Figure 5.4 depicts the texture of **16** at 201 °C between crossed polarizer to be of the typical fan-shape / spherolithic type. Note that the visible texture requires the columnar superstructures to be aligned parallel to the surface of the glass slides.

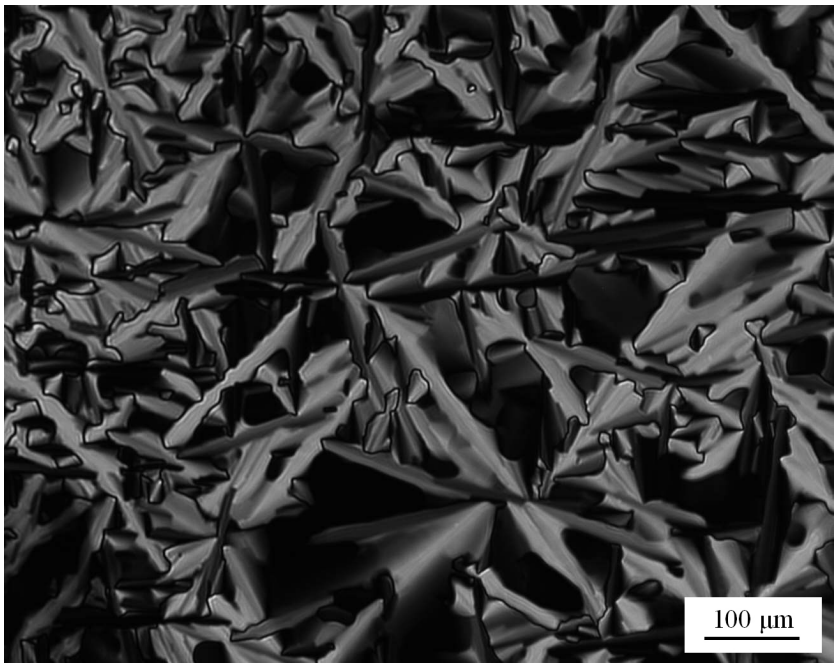

Figure 5.4 Polarized micrograph of the hexagonal columnar disordered mesophase of **16** at 201 °C.

Figure 5.5 illustrates the molecular arrangement of **16** in its hexagonal columnar mesophase. The wedge-shaped molecular geometry is of the mesogen illustrated in Figure 5.5 (left). The molecules spontaneously self-assemble into the flat disc, subsequently pack to the cylindrical stacks of well defined diameter and virtually infinite length. Since the aggregation is mainly driven by the microphase segregation between the bulk non-polar alkyl region and the small, but highly polar sulfonate-tip, the outer shell of the cylinders is covered with the non-polar terminal vinyl groups of compound **16** while the center of the cylinders confines the ions.

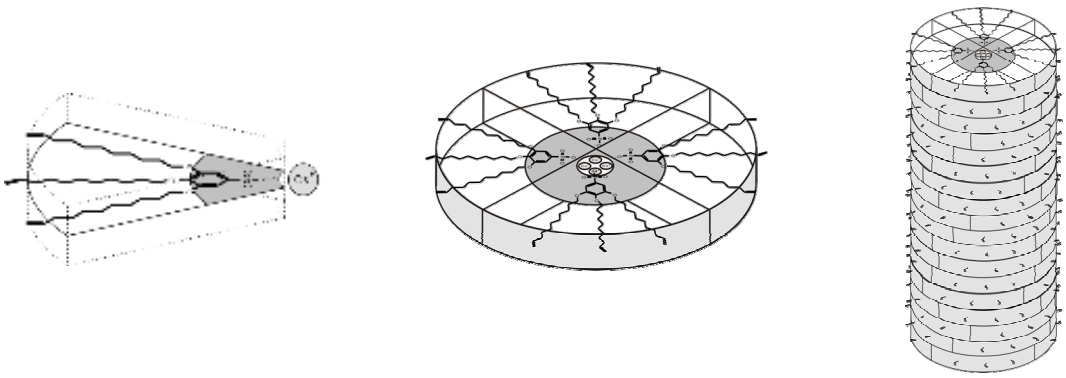

Figure 5.5 Illustration of the self-assembly of wedge-shaped amphiphiles (left) into flat disc-like aggregates (middle), which subsequently stack to form a column (right) containing well-defined channel in the center.

Hence, the described cylinder structure is highly suitable for the construction of an ion-transport channel containing material, since the molecular units of the superstructure can be covalently connected to a macro-molecular matrix, while the mobile cations may allow for ion transport along the axis of the cylindrical organization.

At ambient temperature the existence of individual, solid fiber structures can be demonstrated, since **16** forms organogels from diluted solutions with a variety of organic liquids. Figure 5.6 shows a TEM micrograph of the gel morphology of **16** (1wt%) in EGDMA containing long, thin and regular fibers that form an entangled network. The minimum diameter of the elemental fiber was found to be around 6 nm, which is comparable to twice the length of a **16** molecule.

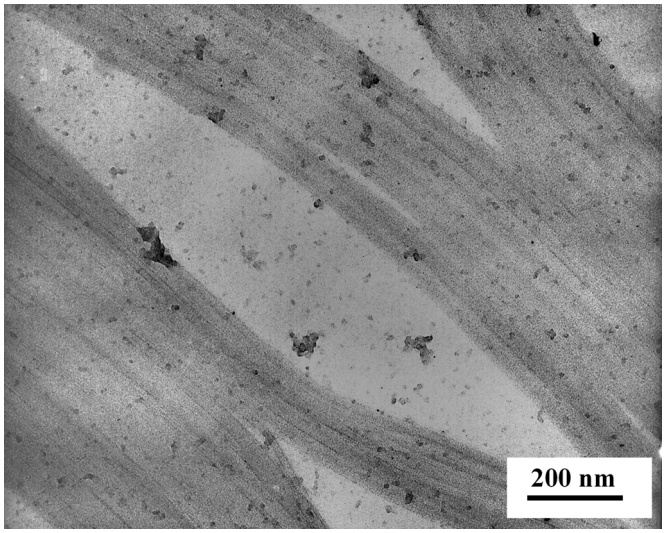

Figure 5.6 TEM micrograph of the dried gel from **16** with EGDMA (1wt%), stained by RuO_4.

In this chapter, the binary system of compound **16** with some crosslinker (types of methacrylates) will be investigated. The phase behaviors and morphologies will be reported. Furthermore, the preparation of channel-like membranes will be introduced from **16** / crosslinker systems. And the ion-transport experiments through the prepared membranes will be discussed as well.

Experimental Section

Materials

tert-Butyl acetate (≥99.0%, Fluka), 2-hydroxyethyl methacrylate (HEMA) (≥99%, Fluka), triethylene glycol dimethacrylate (TEGDMA) (≥95%, Fluka), ethylene glycol dimethacrylate (EGDMA) (≥97%, Fluka), 2- ethylhexyl methacrylate (EHMA) (≥98%, Fluka), *n*-hexyl methacrylate (HMA) (≥97%, Lancaster), styrene (≥99.5%, Fluka), acetone, *n*-hexane, toluene, ethanol, methanol, ethyl acetate (A.C.S. Reagents).

Techniques

^{1}H NMR (300MHz) and ^{13}C NMR (75MHz) were recorded on a Bruker DPX-300 spectrometer with tetramethylsilane (TMS) internal standard.

DSC (Differential Scanning Calorimetry) measurements were made with samples of about 5mg to 10mg. Thermal transitions were determined on a Netzsch DSC 204 'Phoenix' differential scanning calorimeter. In all cases, the heating and cooling rates were 10 °C/min. First-order transitions were reported as the maxima or minima of the endothermic and exothermic peaks during the second heating and cooling scans. Indium and cyclohexane were used as calibration standards.

Thermal Optical Polarized Microscope (Zeiss AXIOPLAN polarizing microscope) equipped with a METTLER FP 90 hot stage and the digital AxioCam MRc4 Zeiss camera with a resolution of 4 Megapixels was used to verify thermal transitions and to characterize the anisotropic textures.

Transmission Electron Micrographs were recorded with a Philips EM 10 microscope operating at 100 kV in the bright field mode. Samples were prepared by microtoming thin sections of the polymerized membrane embedded in epoxy resin (thickness ~ 100 nm as indicated by interference colour) at ambient temperature with a diamond knife (Leitz) on a Reichert ultra-microtome. The components of the epoxy resin for embedding include 63.4wt% (2-nonen-1-yl)succinic anhydride, 24.4wt% 4-vinyl cyclohexene dioxide, 2.4wt% 2-dimethyl amino ethanol and 9.8wt% epoxy resin. The sections were transferred on copper grids and stained in the gas phase with ruthenium

tetroxide freshly developed from trichloride hydrate in a 10wt% sodium hypochloride solution [6]. For a favourable contrast the sections were stained for 10–20 minutes.

Ion transport measurements

The transport properties of membranes were evaluated using a thermostated permeation-cell consisting of two identical cylindrical compartments ($V_{half\text{-}cell}$ = 50 ml, membrane area = 3.14 cm^2) as shown in Figure 5.7. Membranes with an effective area of 3.14 cm^2 were positioned between the cylindrical compartments containing the aqueous phases. The source phase (SP) and the receiving phase (RP) were stirred by two magnetically driven propellers (200 rpm).

(a)

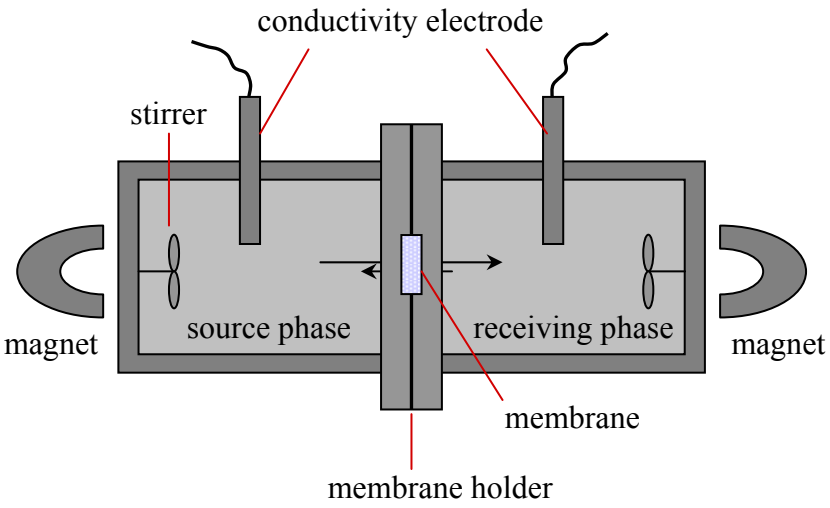

(b)

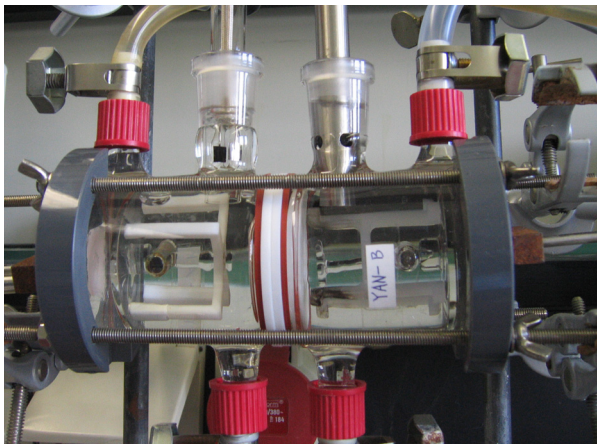

Figure 5.7 Schematically drawing (a) and the image (b) of the ion-transport measurement cell.

Generally, the receiving phase (RP) cell was filled with bidestilled water while the source phase (SP) contained a salt solution (e.g. LiCl) of a particular concentration. Both half-cells were stirred and the conductivity in the RP was continuously monitored (cf. Figure 5.1). Under this condition there is no concentration gradient within a half-cell and the salt concentration in the RP can be described by the diffusion equation according to eq. 5.1 [7].

$$C_{Salt}^{RP} = \frac{1}{2} C_{0t}^{SP} \left(1 - e^{-k \cdot t}\right) \qquad \textbf{e.q. 5.1}$$

Initially ($k \cdot t << 1$) the variation is linear in time, and the flux through the membrane can be described by:

$$\lim_{t \to 0} \left(\frac{dc_{Salt}^{RP}}{dt} \right) \to \frac{k}{2} \cdot C_0^{SP} \qquad \textbf{e.q. 5.2}$$

At low salt concentration, the conductivity of the solution obeys Ostwalds law ($\kappa_{solution} = \Lambda_\infty \cdot c_{salt}$) and the salt transport rate Φ is simply obtained from the measured conductivity:

$$\Phi = \frac{V}{A} \cdot \left(\frac{dc_{Salt}}{dt} \right) = \frac{V}{A} \cdot \frac{1}{\Lambda_\infty} \cdot \frac{d\kappa}{dt} \qquad \textbf{e.q. 5.3}$$

where V denoting the volume of the receiving phase, A being the effective membrane area and Λ_∞ being the equivalent ionic conductivity at infinite dilution. Table 5.1 lists equivalent ionic conductivity of salts employed for ion flux experiments [7].

Table 5.1 Equivalent ionic conductivity at 25 °C [7].

salt	Λ_∞ [cm^2 / S·mol] NO_3^-	Λ_∞ [cm^2 / S·mol] Cl^-	Λ_∞ [cm^2 / S·mol] ClO_4^-
Li^+	111.0	115.0	105.9
Na^+	123.0	128.1	110.0
K^+	144.9	149.9	140.9

Results and Discussion

Crosslinker

In the introduction of this chapter, it has been discussed the importance of fixing the ion channel permanently to the membrane matrix. Since the olefin groups are not able to homopolymerize, a crosslinker with the initiator is required. Three crosslinkers, neamely triethylene-glycol-dimethacrylate (TEGDMA), 1,6-hexanediol-methacrylate (HDMA) and ethylene-glycol-dimethacrylate (EGDMA) were tested. Their thermal stabilities as measured by DSC are shown in Figure 5.9. HDMA exhibited an exothermic reaction at 196 °C, followed by EGDMA at 185 °C, while TEGDMA started the reaction at 178 °C. Obviously, the thermal stabilities between these three crosslinker are not much different. Furthermore, considering that the supposed improvement of ion transport rate is due to increasing the volume fraction of the channel-building molecules in the membranes, obviously the molecular weight of the crosslinker should be as small as possible.

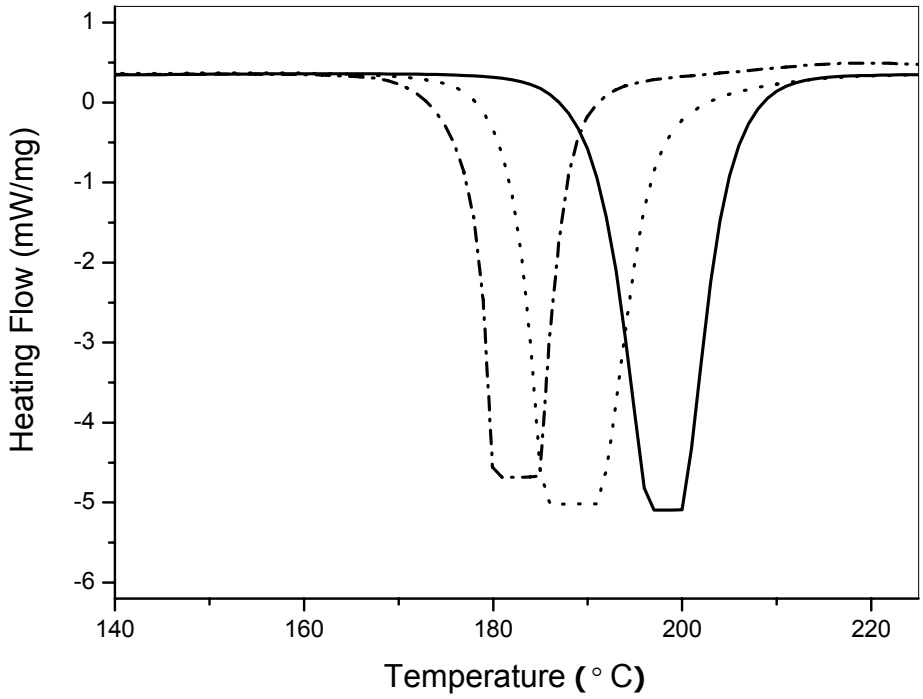

Figure 5.9 Thermal stabilities of the three crosslinkers 1,6-hexanediol-methacrylate (HDMA), ethylene-glycol-dimethacrylate (EGDMA) and triethylene-glycol-dimethacrylate (TEGDMA) (dT/dt = 10 °C/min). (—— HDMA, T_{onset} = 191 °C, ····· EGDMA, T_{onset} = 182 °C, –·–·– TEGDMA, T_{onset} = 178 °C)

Based on the molecular weight boundary condition, EGDMA was selected (M = 198.22 g/mol) and the minimum concentration for efficient cross-linking with **16** was estimated to be about 12wt%. Besides EGDMA, the methacrylates mixture HMT10 (72.45wt% ethylmethacrylate, 17.55wt% hexylmethyacrylate and 10wt% triethylene glycol dimethacrylate) was also used as solvents. The preparation of the mixture HMT10 was based on Lowicryl HM20, which is highly cross-linked methacrylate resin developed as embedding media for TEM specimen preparation and used over a wide range of embedding conditions. Note that for HM20, the crosslinker (TEGDMA) concentration may be varied from 5 to 17wt%. Higher crosslinker concentration made the membranes harder and more brittle. Hence in HMT10 10wt% TEGDMA was added.

Initiators

To initiate a radical polymerization, free radicals must be generated by decomposition of a radical initiator. One has to distinguish between thermal initiator that decompose upon heating and photoinitiators that disintegrate on irradiation with light of a certain wavelength.

The azocompound thermal initiators (AIBN and V-601, Wako) were tried in our systems. However, the membrane preparation required heating the system into isotropic phase, where the temperature is usually much higher than the activation temperature of the initiators. Hence, a rapid decomposition was initiated so that it was impossible to form the columnar mesophase prior to network formation. Therefore, the photoinitiator (benzoin mono methyl ether) was used for preparation of membranes. Photoinitiators are compounds that break down into free radicals upon exposure to ultraviolet radiation. Benzoin ethers undergo a unimolecular bond cleavage upon irradiation ($\lambda \approx 330$ nm) to yield free radicals. The main advantages of polymerization started by photoinitiators are low temperature-dependence of the rate of polymerization and easy to be controlled. It can be conducted at high or low temperatures and can be stopped simply by removing the light source. During the process of membrane preparation, the system can be heated for a certain time without decomposition of the initiator, subsequently the polymerization is started 'on the spot' when the orientation of the columns in the mesophase finishes.

Phase diagram of 16 / HMT10

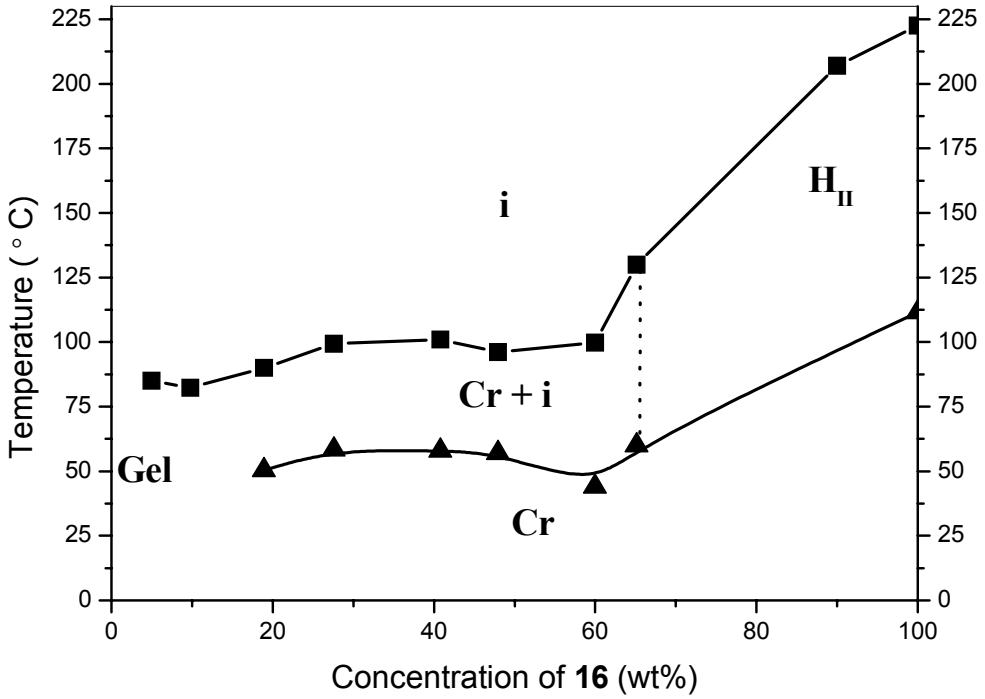

Figure 5.10 Phase diagram of **16** / HMT10 (72.45wt% ethylmethacrylate, 17.55wt% hexylmethyacrylate, 10wt% triethylene-glycol-dimethacrylate); i: isotropic phase; Cr: crystal phase; H_{II}: reversed hexagonal phase.

Mixtures of compound **16** and HMT10 were investigated with different composition by differential scanning calorimetry (DSC) and polarizing microscopy. Figure 5.10 depicts the phase diagram of the binary system **16 /** HMT10. The transition temperatures were determined by DSC measurements at the heating rate of 10 °C/min, taking the peak temperatures of the endotherms. In addition, the textures of the each mixture were studied by polarizing microscopy.

At very low concentration (C_{16} < 5wt%) of **16** in HMT10, a transparent or translucent gel was formed. By TEM infinite long and thin fibers could be observed, similar to the structures shown in Figure 5.5. The aggregation of fibers (bundles) could be observed as well by polarizing microcopy (cf. Figure 5.11). On exceeding 5wt% the gels became opaque (white). This indicated crystalline micro-domains to be formed by parallel alignment of the fibers. The transition at lower temperature was observed in some cases by the textures as well. For example, in the gel containing 5wt% **16** in HMT10, when the temperature was lower than 50 °C the Maltese crosses was observed (see the

marked area in Figure 5.11). Maltese crosses are known as a typical texture for spherulites, which are normally formed in crystalline, columnar or lamellar phases. The fiber structure was found in the gel state. Therefore, the observed spherulites were formed by the aggregation of the fibrous bundles, i.e. crystalline spherulites. When the concentration of **16** exceeded 10wt%, only the Maltese crosses were found instead of the fibrous bundles (cf. Figure 5.12).

The Maltese crosses arising from growing crystals could be observed below the first transition temperature (C_{16} < 65wt%) (cf. Figure 5.13). Meanwhile, the system was still in a mobile state. All these observations indicate a phase segregation to exist in the phase between the isotropic solution and crystalline phase. Another phenomenon was also observed that in the higher concentration of **16** in HMT10 the size of the spherulites became much smaller, as shown in Figure 5.14.

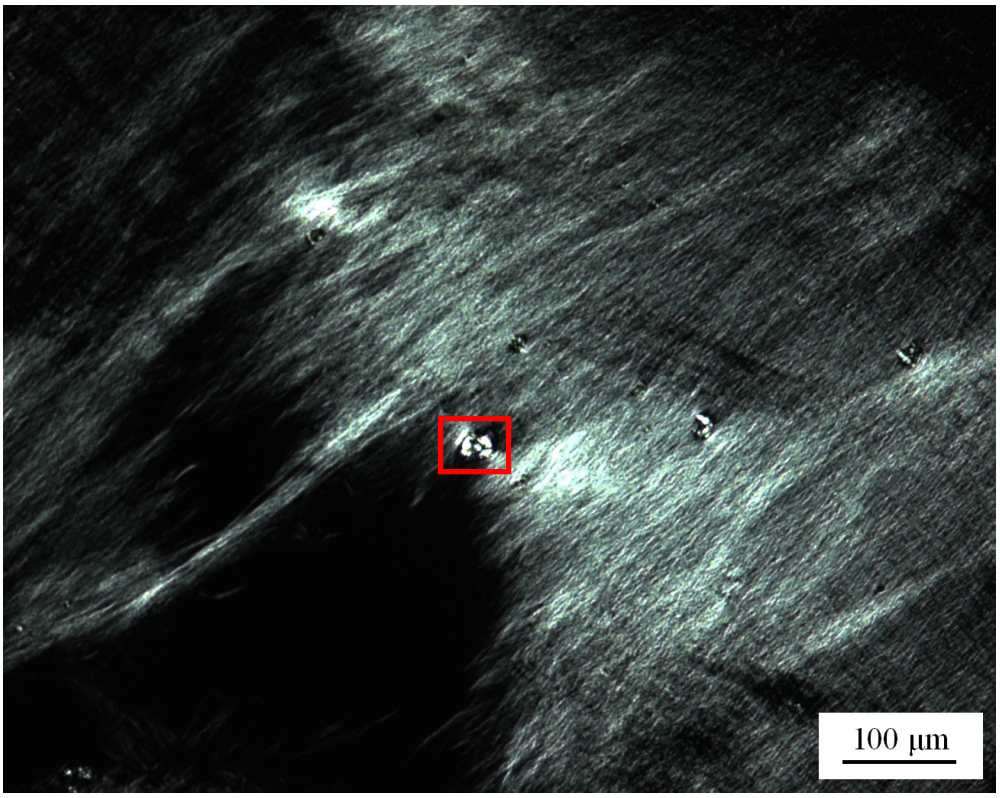

Figure 5.11 Polarized micrograph of a gel of **16** / HMT10 (5/95wt%) at 25 °C.

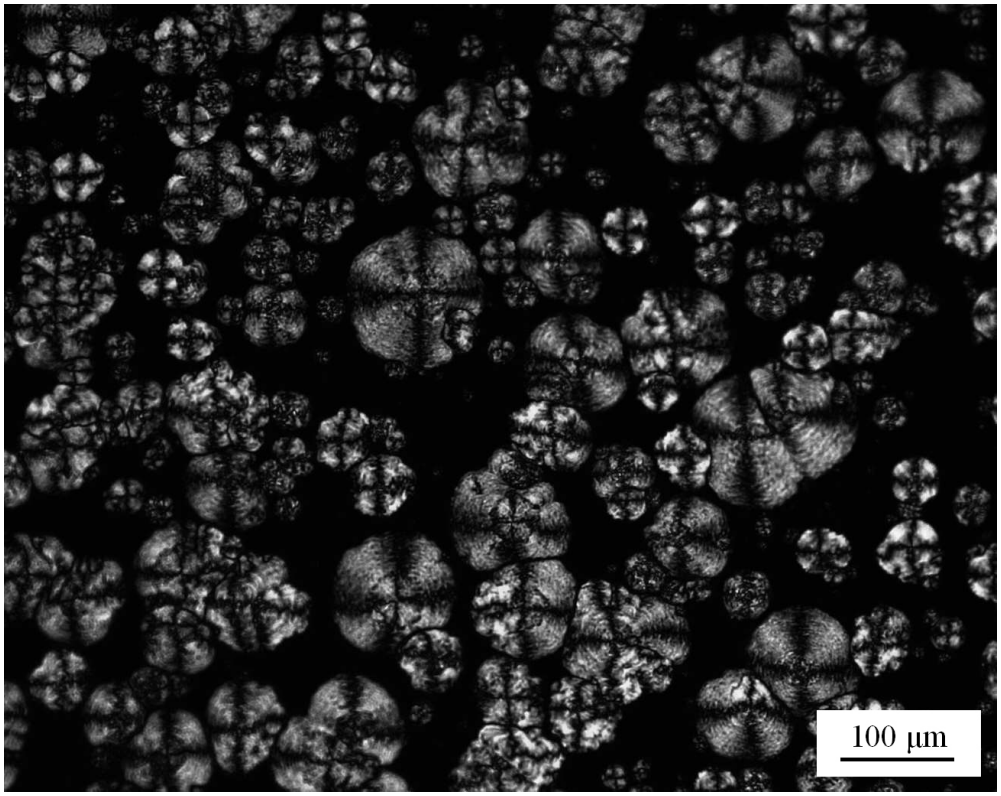

Figure 5.12 Polarized micrograph of a gel of **16** / HMT10 (30/60wt%) at 45 °C.

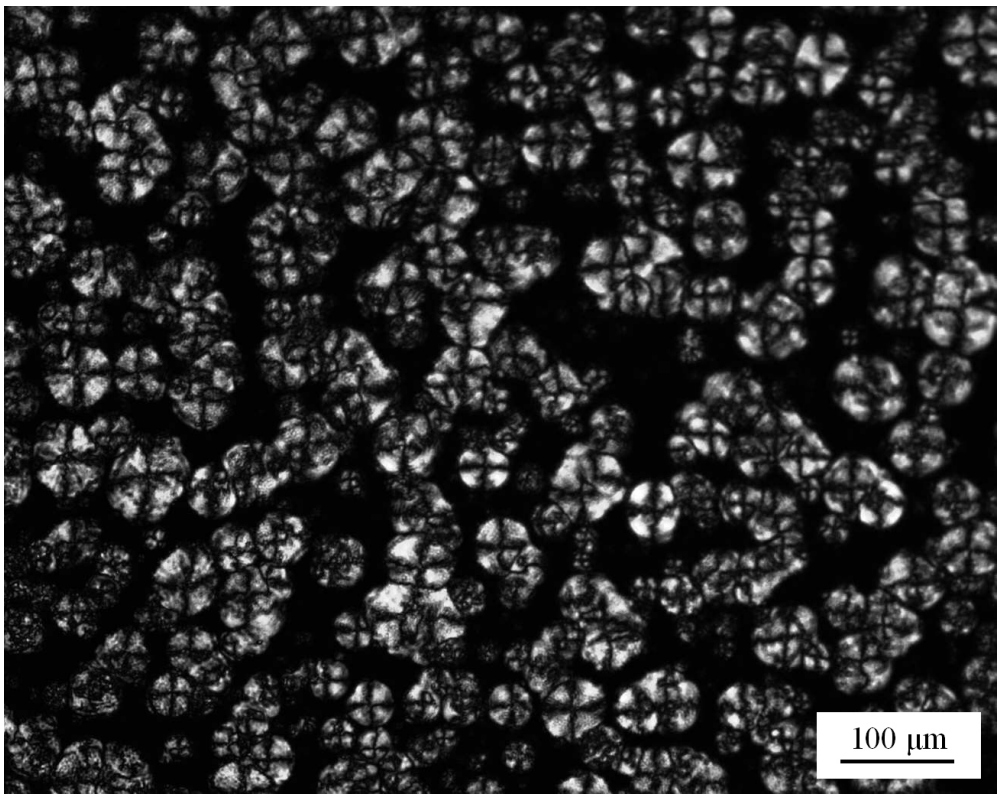

Figure 5.13 Polarized micrograph of a gel of **16** / HMT10 (30/60wt%) at 60 °C.

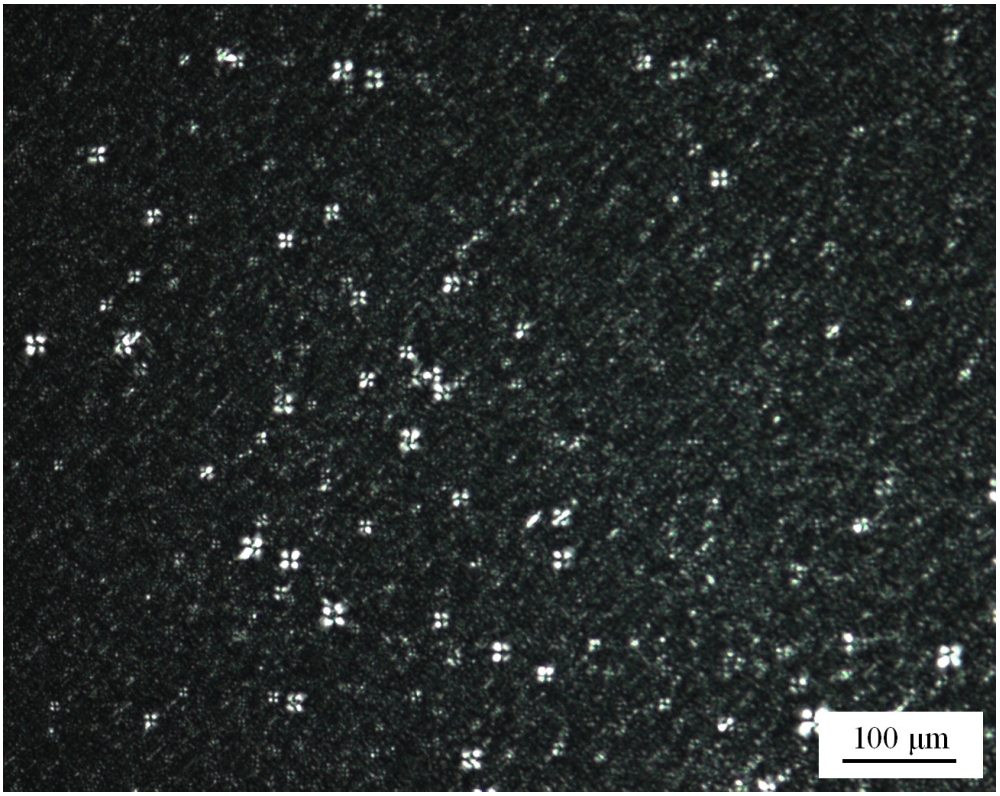

Figure 5.14 Polarized micrograph of a concentrated gel of **16** / HMT10 (53/47wt%) at 70 °C.

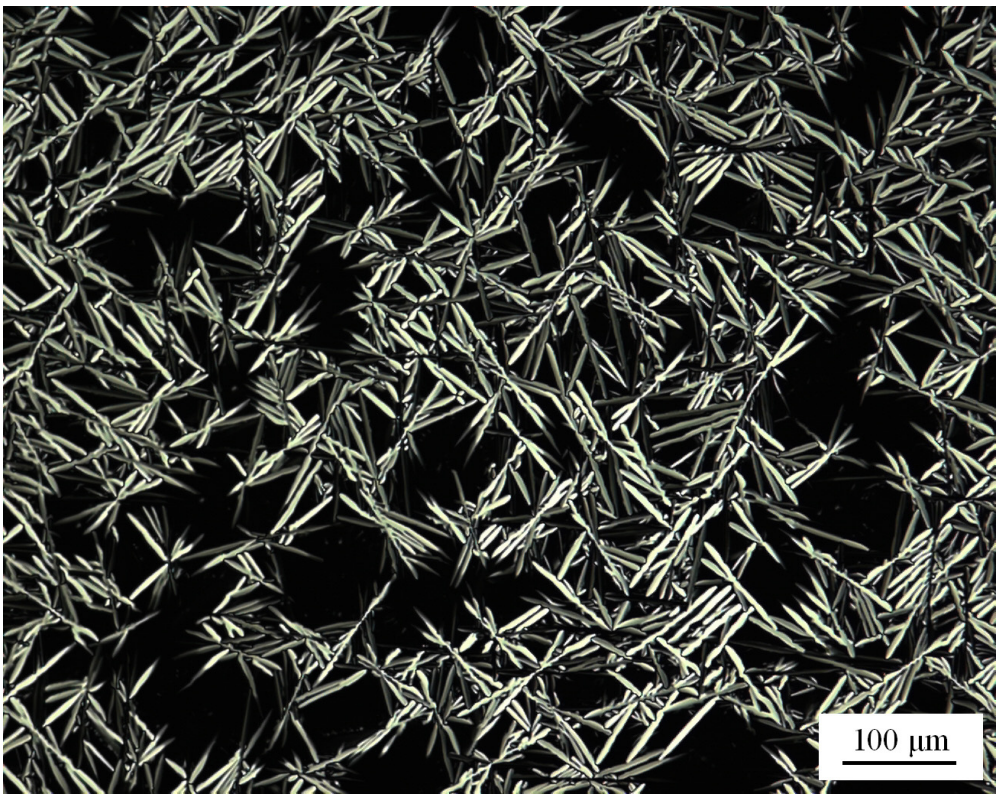

Figure 5.15 Polarized micrograph of **16** / HMT10 (65/35wt%) at 120 °C.

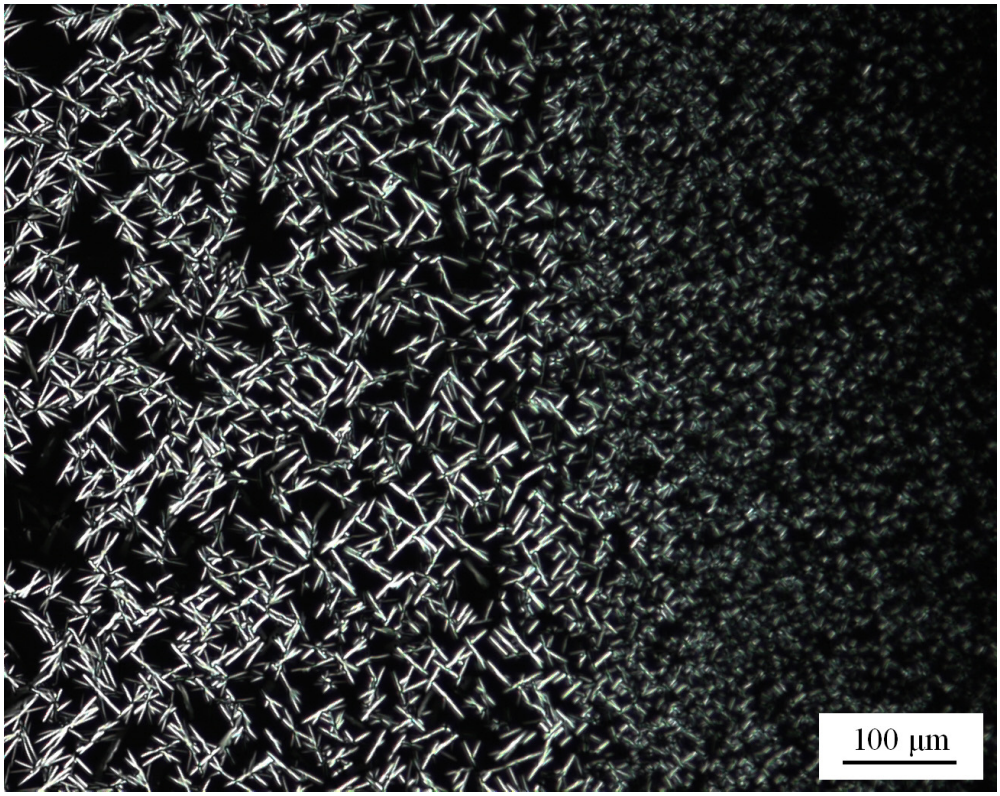

Figure 5.16 Polarized micrograph of **16** / HMT10 (65/35wt%) at 90 °C.

When the concentration of **16** exceeded 65wt%, a columnar lyotropic liquid crystal phase (H_{II}) was found. Figure 5.15 depicts the texture of **16** / HMT10 (65/35wt%) at 120 °C after cooling from the isotropic phase. A narrow banded texture was observed, which indicated the columnar mesophase as well. Since a smooth and gradually growing of the texture was observed as shown in Figure 5.16, the binary system **16** / HMT10 (concentration exceeds 65wt%) formed a lyotropic liquid crystal phase without phase segregation.

From the above observation, it can be concluded that the binary system **16** / HMT10 exhibited a columnar lyotropic liquid crystal phase on exceeding a mesogen content of 65wt%, making the system suitable for constructing a channel-containing membrane.

Preparation of membranes from 16 / HMT10

The process of the membrane preparation is illustrated in Figure 5.17. The gels of **16** / HMT10 (1 ~ 10wt%) containing 5wt% photoinitiator (benzoin mono methyl ether),

were transferred on pre-treated glass substrates and covered carefully by another glass slide. Prior to the preparation of membranes, the glass slides were pre-treated with a fluorinated copolymer: P[FOMA $_{0.52}$-co-MMA $_{0.48}$]$_{300}$. The treating procedure is described as followed: the glass slides were immersed for less than 1 min in a solution of P[FOMA $_{0.52}$-co-MMA $_{0.48}$]$_{300}$ in Freon : $CHCl_3$ (1 : 1 by volume), slowly pulled vertically out of the coating bath and dried in air at ambient temperature. The structure of fluorinated copolymer is shown in Figure 5.18. The purpose of this pre-treatment is to decrease the surface energy of the glass slides. On the low surface energy substrates the adhesion of the polymerized membrane film is low, allowing for simple lift off subsequent to polymerization. The mesogen / methacrylates mixture was molten to the isotropic phase and air bubbles were removed by pressing the glasses slightly. Afterward, the temperature was lowered to 60 °C where the lyotropic liquid crystal phase was formed between the two glass substrates.

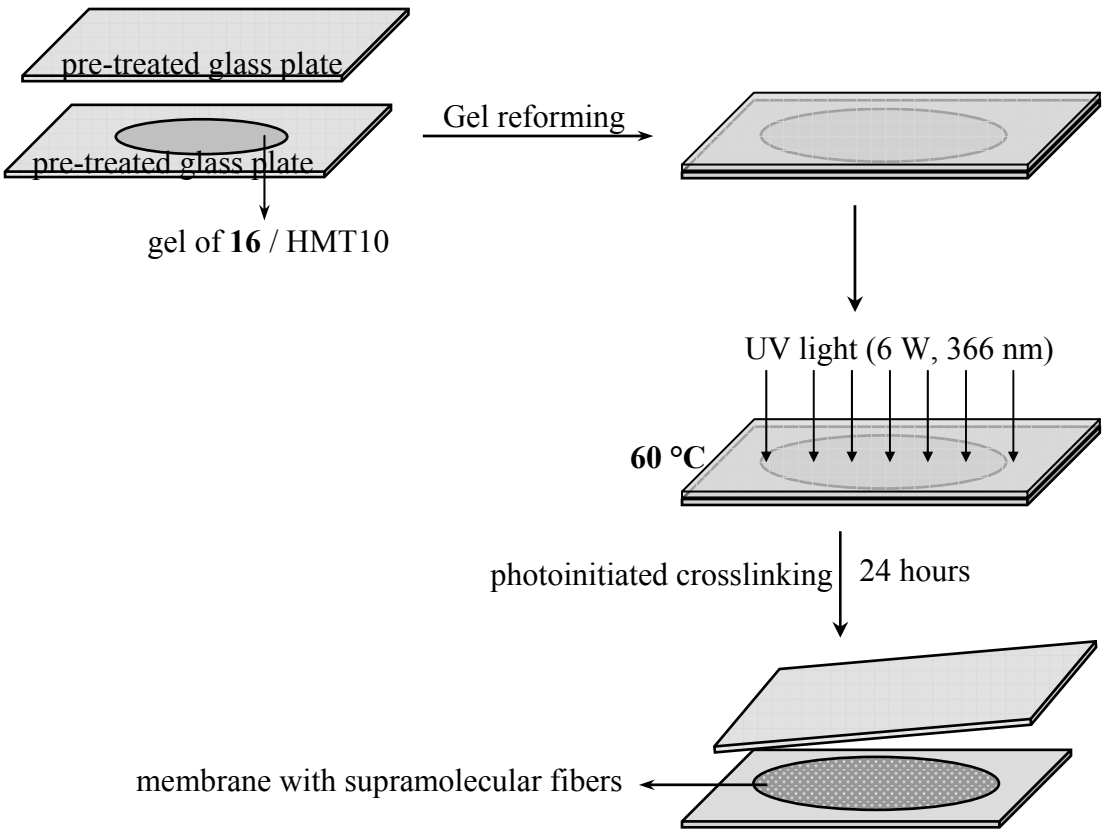

Figure 5.17 Illustration of the membrane preparation from gel of **16** / HMT10.

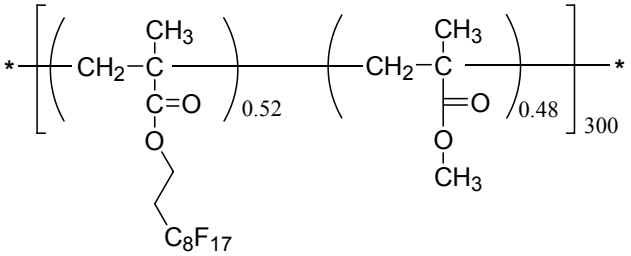

P [FOMA$_{0.52}$ - co - MMA$_{0.48}$]$_{300}$

Figure 5.18 Structure formula of the fluorinated copolymer P[FOMA$_{0.52}$-co-MMA$_{0.48}$]$_{300}$.

At 60 °C this glass sandwich containing the columnar mesophase was exposed to UV light (6 W, 366 nm) for at least 24 hours. During this time the photoinitiated cross-linking proceeded in the mesophase and the columnar aggregates were covalently fixed inside the membrane. The last step was to remove the membrane film from two glass substrates by immersing the glass sandwich in water until the cover-slide swam off. Figure 5.19 shows an image of a membrane that was prepared by this process. The obtained film was about 30~50 µm thick, exhibited good flexibility, toughness and could be handled without difficulties.

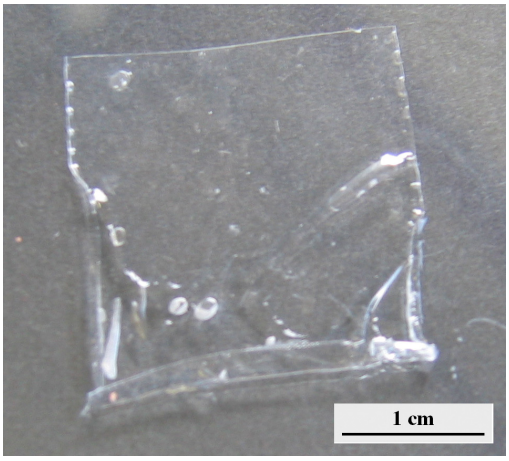

Figure 5.19 Membrane made from **16** / HMT10 (1wt%/99wt%).

The ion transport experiments were made with the obtained membranes using a conductivity measurement set up as described in the experimental part. Figure 5.20 depicts the conductivity vs. time curve of a 0.1 mol/L LiCl solution through a membrane made from **16** / HMT10 (1/99wt%). From equation 2.3 the Li^+ transport rate

was calculated to be 3.47×10^{-6} mol/cm^2 h, which is a very small value. That can be explained by the low concentration of the columnar channels in the membranes. Therefore, higher gel concentrations were used to prepare membranes. However, when the gel concentration exceeded 5wt%, the mechanic properties of the obtained membranes become too poor, i.e. the films became so fragile and brittle that they could not be inserted in the measurement system without destruction.

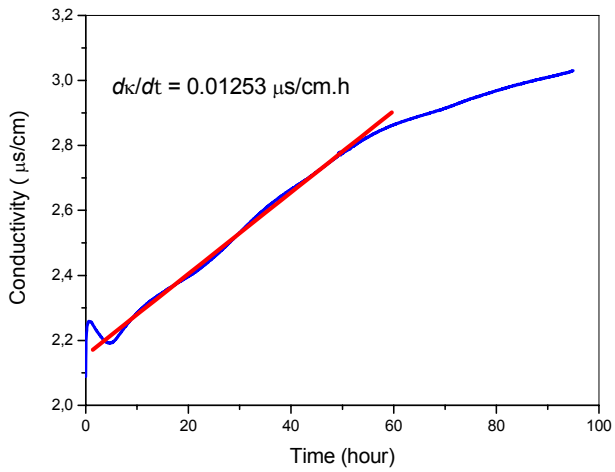

Figure 5.20 Conductivity vs. time curve of a 0.1 mol/L aqueous LiCl solution through a membrane made from 1wt% **16** in 99wt% HMT10.

In order to improve the mechanic property of the membranes, Anodisc porous aluminium oxide membrane filters (Whatman, pore size: 20 or 10 μm) were used as support membranes. As shown in Figure 5.21, pre-heated clear solutions were cast onto Anodisc membranes at 80 °C. On cooling down to room temperature, the white gel was formed in the pores of the support membrane.

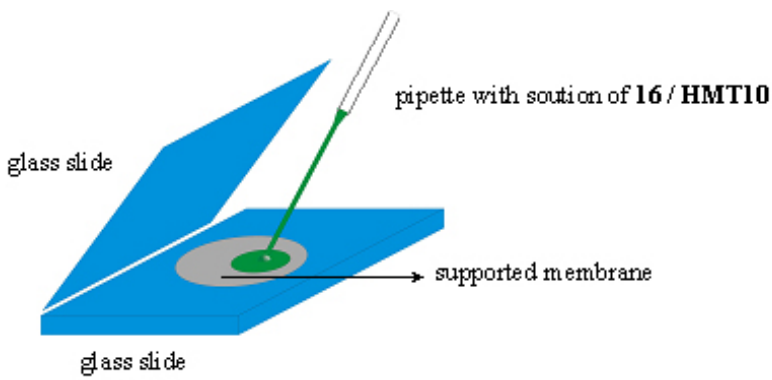

Figure 5.21 Illustration of the preparation of supported membranes from **16** / HMT10 in Anodisc membrane filters.

Photoinitiated cross-linking was performed by means of 6 W, 366 nm UV lamp for 24 hours. To remove the cross-linked supported membrane from the glass slide, the samples were immersed in distilled water until the glass slides were separated (within 24 hours). The obtained membrane is shown in Figure 5.22.

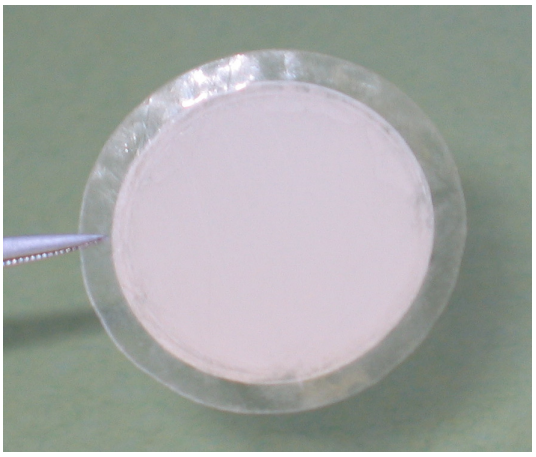

Figure 5.22 Cross-linked **16** / HMT10 (15/85wt%) on Anodisc membrane filters.

The ion transport rates were determined in LiCl (0.1 mol/L) and KCl (0.1 mol/L) solutions through the membranes containing **16** / HMT10 of two different weight ratios: 5/95wt% and 15/85wt% respectively.

Based on equation 2.3, for the membranes containing **16** / HMT10 (5/95wt%), the Li^+ transport rate was calculated to be 3.21×10^{-2} mol / cm^2 h and the K^+ transport rate was 5.59×10^{-2} mol / cm^2 h, while for 15/85wt%, the Li^+ transport rate was 1.73×10^{-2} mol / cm^2 h and the K^+ transport rate was 1.33×10^{-2} mol / cm^2 h. Compared to the reference experiments, the Li^+ transport rate through the untreated Anodisc support membrane in 0.1 mol/L LiCl was about 3.79×10^{-2} mol / cm^2 h. These two nearly identical values give the conclusion that the pores in the support membranes were not completely filled by the gelator systems.

Since the columnar lyotropic mesophase was found in the range of high concentration of **16**, it was attempted to use polymerized mesophases as membrane, hence only a crosslinker was used as matrix resin. As discussed above in the section of crosslinker, the difference of thermal properties between three crosslinker: TEGDMA, EGDMA and HDMA, were found to be very small. Meanwhile due to the requirement of a

maximum content of gelator **16**, the molecular weight of the crosslinker should be as small as possible. Hence EGDMA was chosen because of its relative low molecular weight (198.22 g/mol) and minimum concentration for efficient cross-linking of **16** requires about 12wt%.

Phase diagram of 16 / EGDMA

The phase diagram of **16** in ethylene glycol dimethacrylate (EGDMA)) is depicted in Figure 5.23 The transition temperatures were determined by DSC measurements at the heating rate of 10 °C/min. Furthermore the textures of the each composition were studied by polarizing microscopy. Depending on the composition of the system, the aggregates formed by the **16** / EGDMA can be either relatively simple individual structures such as micelles, or more complex such as fibers, gels or lyotropic columnar mesophases.

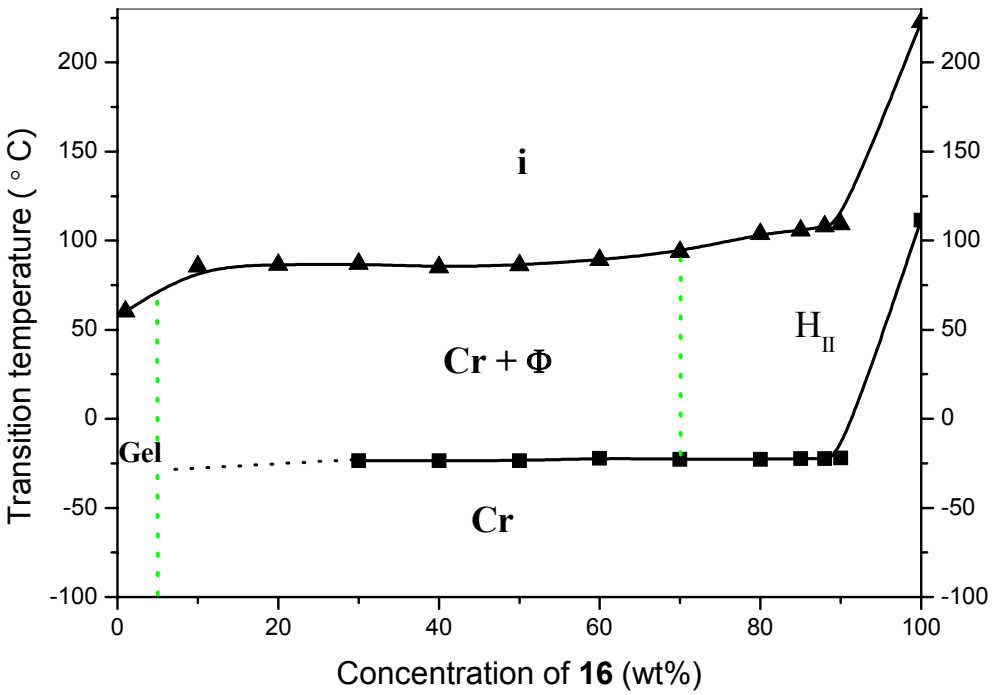

Figure 5.23 Phase diagram of **16** / EGDMA (ethylene glycol dimethacrylate); i: isotropic; Cr: crystal; H_{II}: reversed hexagonal phase; Φ: undetermined lyotropic mesophase.

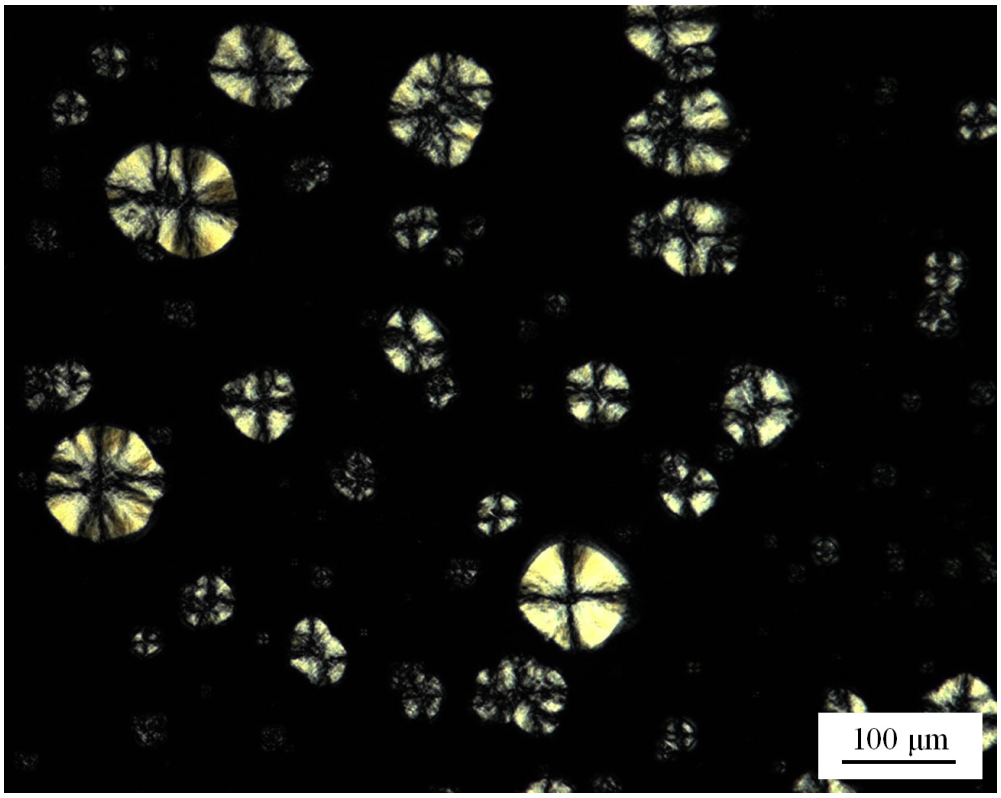

Figure 5.24 Polarized micrograph of the crystalline spherulites of **16** / EGDMA (5/95wt%) at 50 °C.

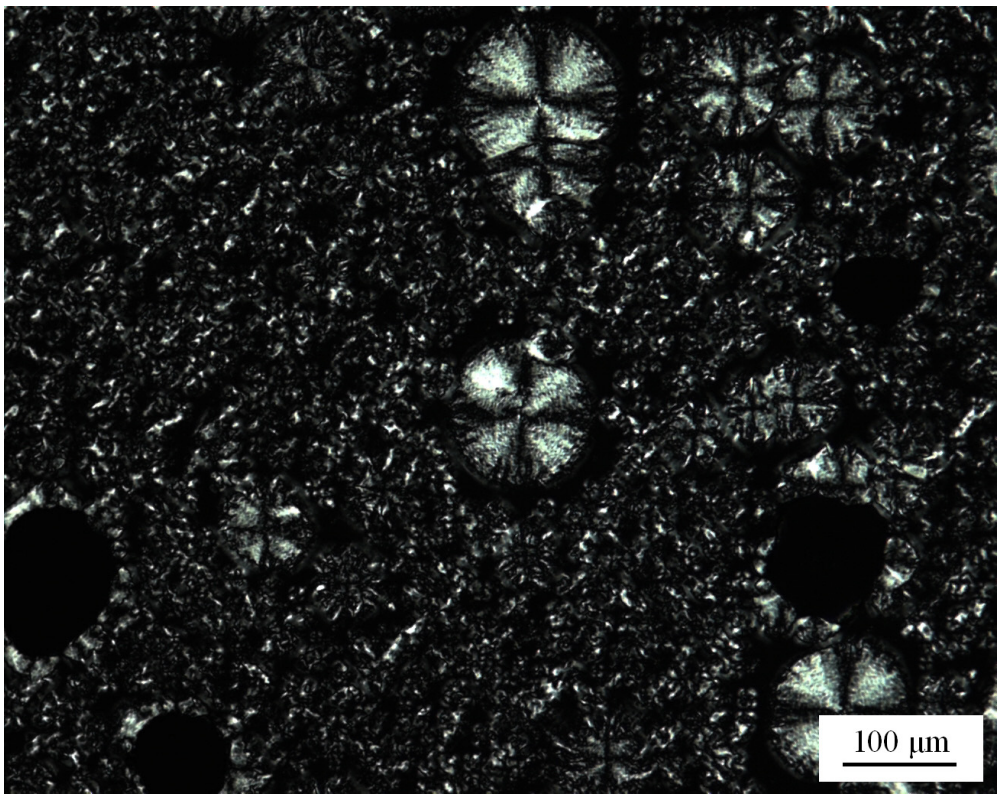

Figure 5.25 Polarized micrograph of **16** / EGDMA (20/80wt%) at 65 °C.

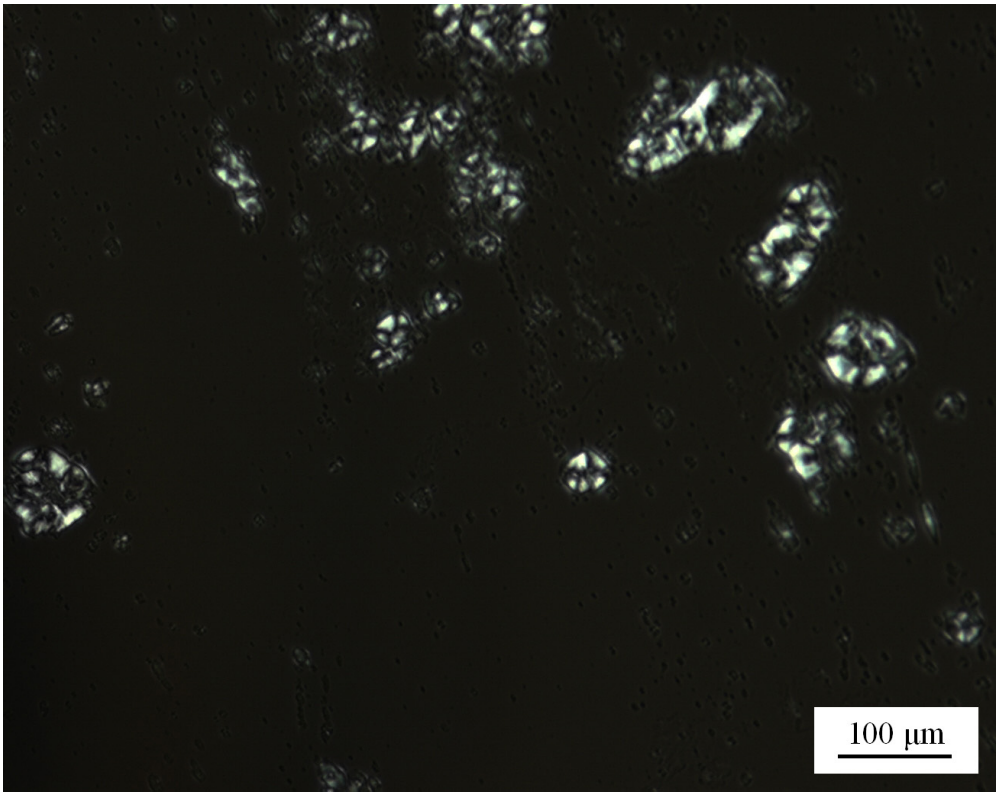

Figure 5.26 Polarized micrograph of **16** / EGDMA (60/40wt%) at 65 °C.

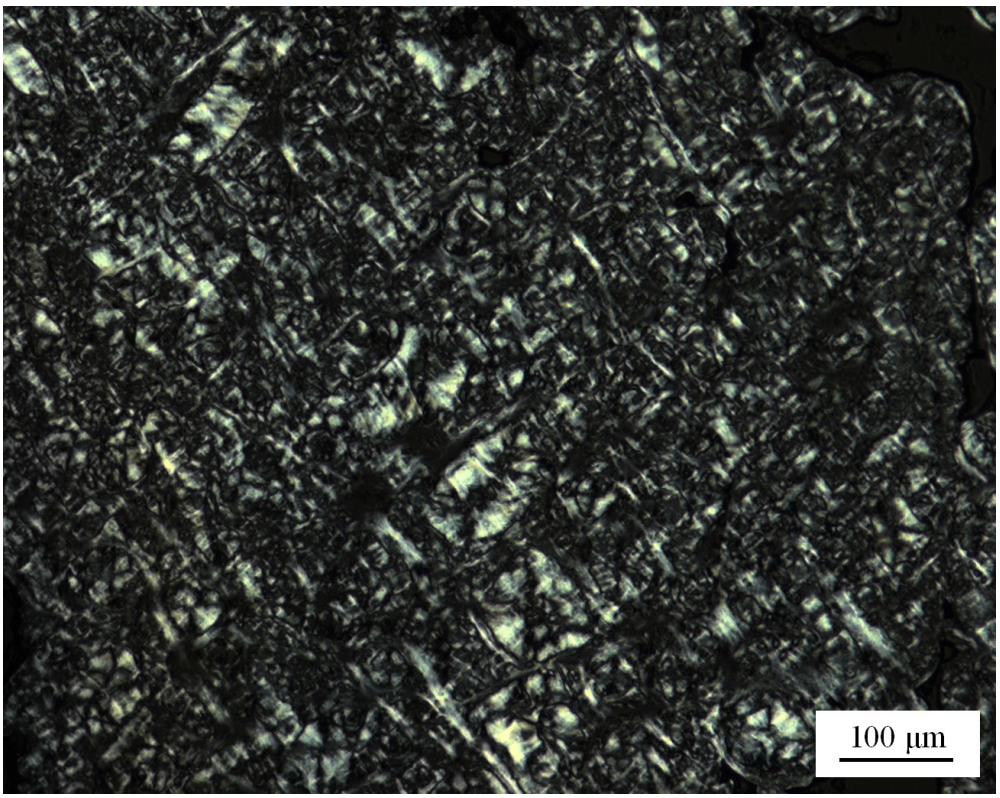

Figure 5.27 Polarized micrograph of **16** / EGDMA (60/40wt%) at 65 °C, after sheared.

At the relative low concentration of **16** (C_{16} < 5wt%) in EGDMA, a transparent or translucent gel was formed. The minimum concentration of **16** forming a gel at 25 °C was below 1wt%. TEM micrograph showed infinite long and thin fibers forming the network of the gel (cf. Figure 5.6). However, such fibrous aggregates were dispersed randomly without any ordering.

With increasing concentration the clear gels turned translucent and became opaque / white on exceeding 5wt%. Under the polarizing microscopy the Maltese crosses of spherulites were observed for 5wt% **16** in EGDMA (cf. Figure 5.24).

On the higher concentration of **16** in EGDMA, the Maltese crosses for crystalline spherulites were still observed until 60wt% of **16** (cf. Figure 5.25 and 5.26). Meanwhile, if the system between two glass slides of samples were sheared, the textures of the lyotropic mesophase were found either (cf. Figure 5.27). These observations indicate that the phase segregation of crystalline and mesophase occurs in range of the phase that exists between isotropic and crystalline phases.

When the concentration of **16** reached 70wt%, a homogeneous lyotropic liquid crystal phase was found. Figure 5.28 depicts the texture of **16** / EGDMA (80/20wt%) at 100 °C after cooling from the isotropic liquid. A few pieces of broken fans were observed. If the sample was sheared in one direction, numerous broken fan-shaped domains were observed over the whole area (cf. Figure 5.29). Hence, the dark areas are caused by a homeotropic orientation of the mesophase. In homeotropically oriented mesophases, the optical axis of the liquid crystal is oriented parallel to the observation direction, i.e. perpendicular to the glass slide surfaces. Since in columnar mesophases the director is parallel to the long axis of the columns, one must conclude that the black area in Figure 5.28 refers to a large monodomain, where the columns exhibit the orientation that is required for the preparation of a ion-channel membrane. Only after shearing, which changed the orientation of the aggregates by external shear forces the texture became visual by polarizing microscopy. From the broken fan-shaped texture, which is characteristic of columnar mesophases, the binary system **16** / EGDMA (**16** higher than 70wt%) was considered to exhibit a columnar phase. As common with mesophases, always a few defects were found where abrupt changes of the directors orientation around disclination of columns occurred. That is the reason that still a few pieces of texture were observed in Figure 5.28.

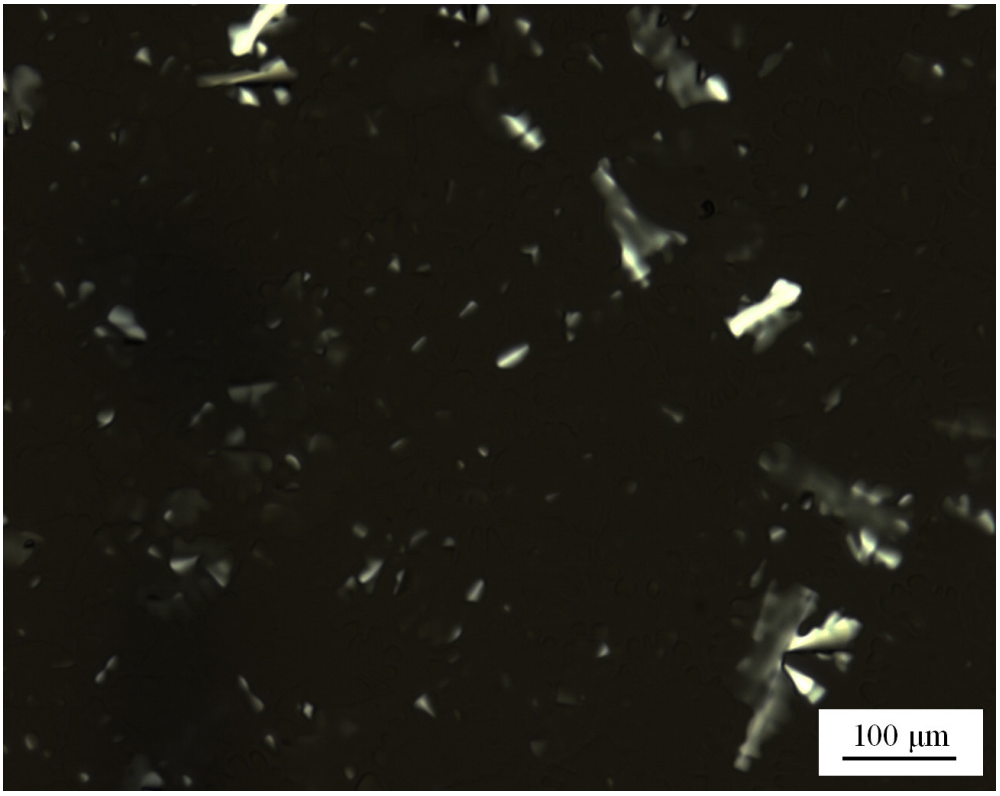

Figure 5.28 Polarized micrograph of the columnar mesophase of **16** / EGDMA (80/20wt%) at 100 °C.

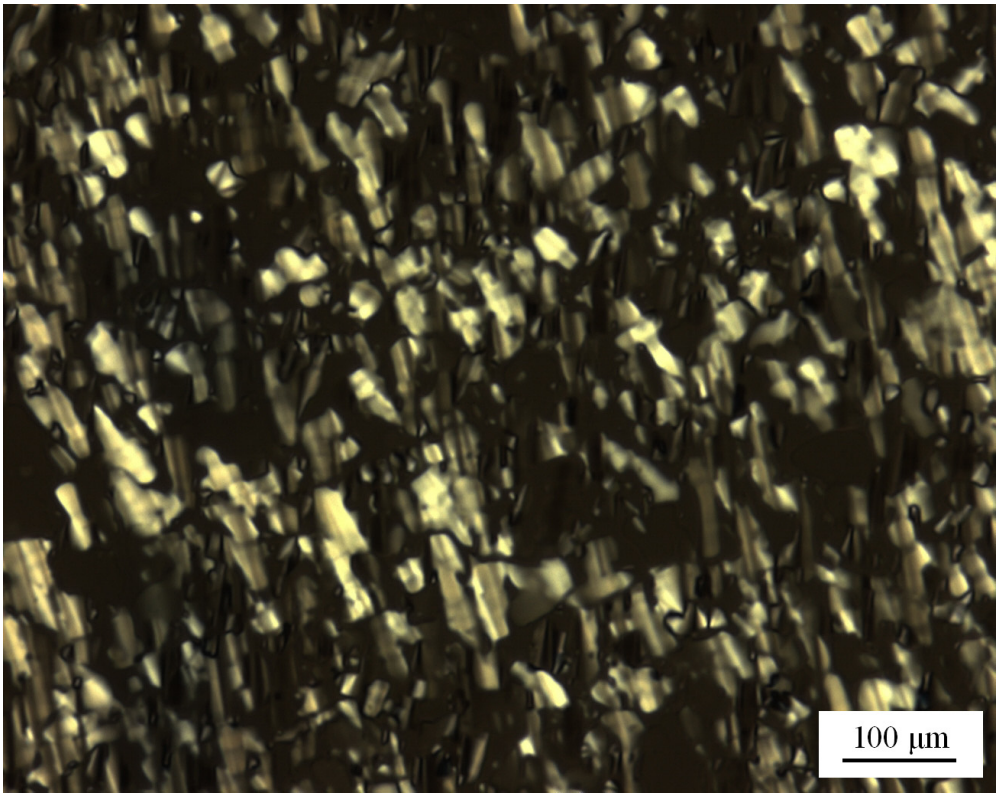

Figure 5.29 Polarized micrograph of the columnar mesophase of **16** / EGDMA (80/20wt%) at 100 °C, after sheared.

Preparation of membranes from 16 / EGDMA

The process of the membrane preparation from **16** / EGDMA mixtures is illustrated in Figure 5.30. A solution of 75–85wt% **16** and 5wt% photoinitiator (benzoin mono methyl ether) in EGDMA was transferred on the preheated glass substrate at 120 °C. The mixture was immediately melted in the isotropic phase. Another glass slide was covered slowly and carefully on the liquid and the air bubbles were removed by pressing the glasses slightly. Afterward, the temperature was lowered to 80 °C, where the lyotropic liquid crystal phase was formed between the two glass substrates.

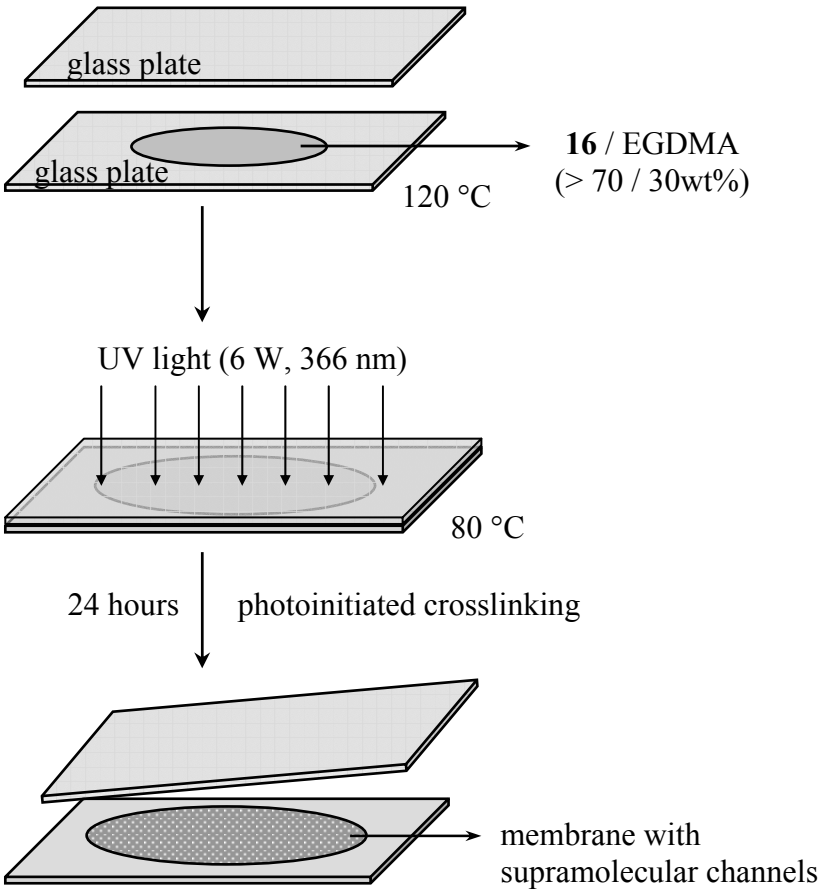

Figure 5.30 Illustration of the membrane preparation from lyotropic mesophase of **16** / EGDMA.

At 80 °C, this glass sandwich containing the columnar mesophase was exposed to the UV light (6 W, 366 nm) for at least 24 hours. During this time, the photoinitiated cross-linking proceeded in the mesophase and the columnar aggregates were fixed covalently inside the membrane. The last step was to remove the membrane film from two glass

substrates by immersing the glass sandwich in water until the cover-slide swam off. This procedure took around one week since the glass substrates were not pre-treated by fluorinated copolymer solution. By polarizing microscopy the texture of the columnar mesophase was still observed, the same as that before cross-linking (cf. Figure 5.31). However, the homeotropic orientation was not obtained in this experiment.

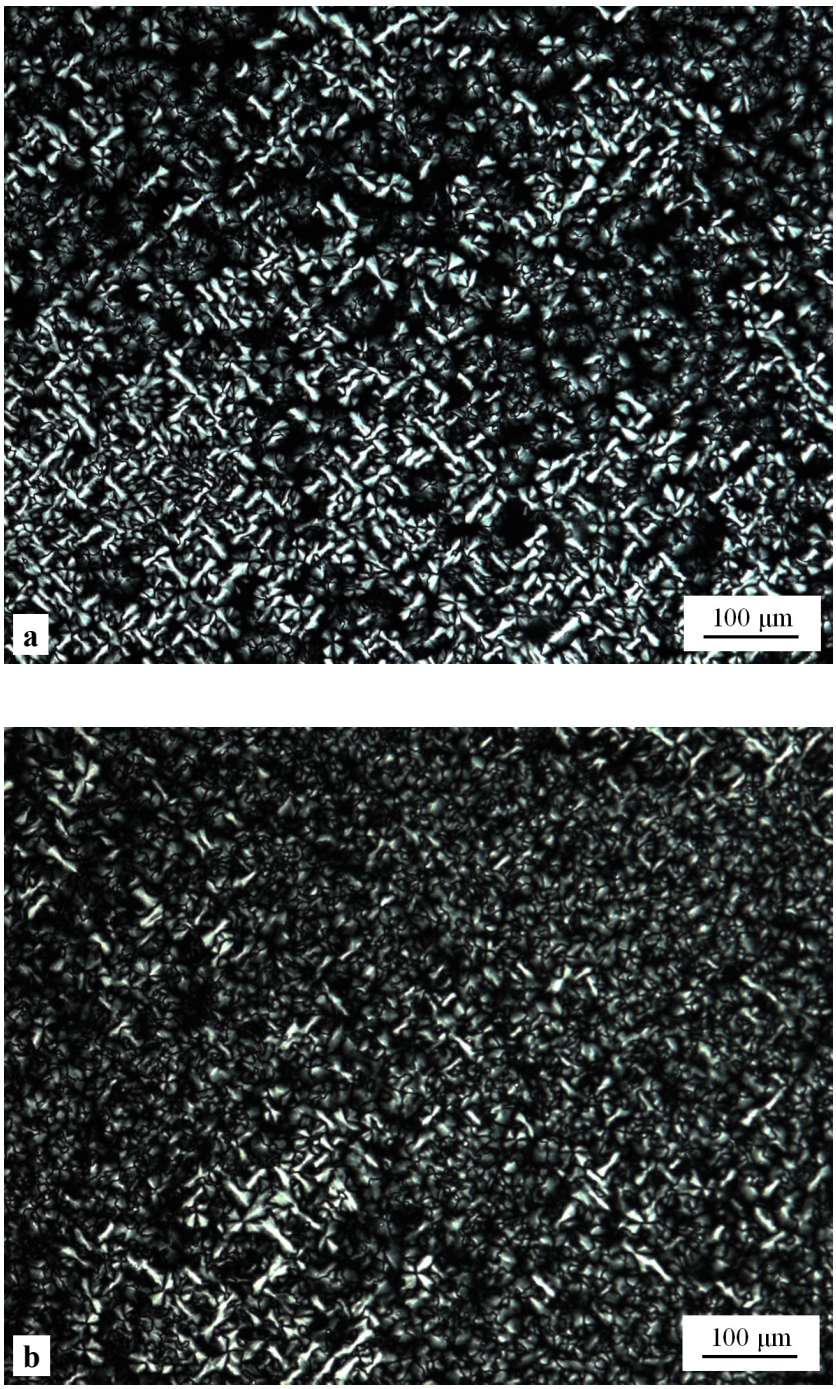

Figure 5.31 Polarized micrograph of the membrane prepared from **16** / EGDMA (85/15wt%), (a) before cross-linking; (b) after cross-linking.

Figure 5.32 shows the image of a membrane that was prepared by this method. The thickness of the obtained film was about 30~50 μm.

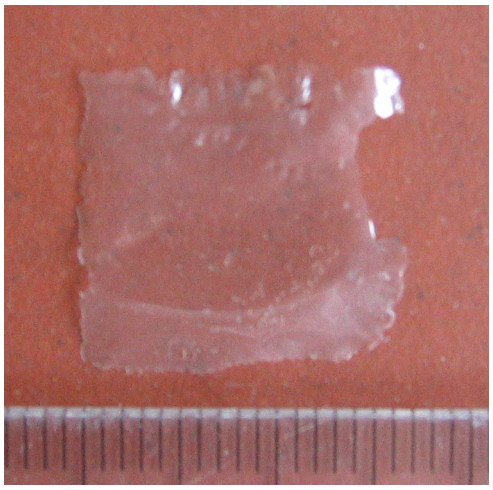

Figure 5.32 Picture of the membrane prepared from **16** / EGDMA (85/15wt%).

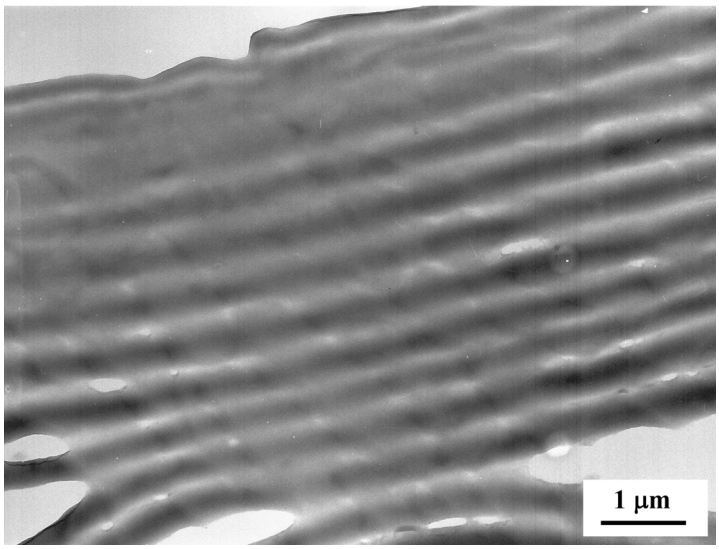

Figure 5.33 TEM micrograph of the membrane prepared from **16** / EGDMA (75/25wt%).

The obtained membrane was investigated by transmission electron microscopy (TEM). The preparation of TEM sample is descried in experimental section. Numerous cylinders were observed on the transverse section of the membrane. Figure 5.33 shows the TEM micrograph of membrane prepared from **16** / EGDMA (75/25wt%). The sample contained a dense and regular alignment of linear features. The observed units were of virtually infinite length ($l > 20$ μm) and exhibited a lateral periodicity of 300 nm. The diameter of the structures was much larger than molecular dimension (about 10 nm). That is probably due to the high aggregation of elemental cylinders. The

other disadvantage is that the orientation of the cylinders is very uniform but parallel to the membranes surface. This result confirmed the optical observation that the homeotropic orientation of columnar mesophase had not been obtained.

The ions transport experiments were also tried on the obtained membranes made from of **16** / HMT10 (75/25wt%) based on the conductivity measurements described previously. From equation 2.3, for the concentration of 0.1 mol/L, the Li^+, Na^+, and K^+ transport rate were calculated to be 6.21×10^{-4} mol/cm^2 h, 5.23×10^{-4} mol/cm^2 h and 4.56×10^{-4} mol/cm^2 h respectively. The absolute ion transport rates were improved for two orders of magnitudes as compared to the transport measurements that were made with the membranes from the low concentration gel system (3.47×10^{-6} mol/cm^2 h).

The ion transport rates exhibited a decreasing tendency in the sequence $Li^+ > Na^+ > K^+$. The $Li^+ : K^+$ ion transport rate ratio was 1.36. Since in a free solution Li^+ diffuses slower than Na^+ that diffuses slower than K^+, this opposite result is indicative of the transport in supramolecular channels. It is proposed that the diffusion became controlled by cation-sulfonate interactions during the transport through the supramolecular channels.

The absolute ion transport rates and the ion selectivity were relatively low since the orientation of the supramolecular channels was not achieved optimally. The further improvement is to use the carbon-coated glass substrate, on which the homeotropical orientation of the columns is more favorable.

Conclusion

The phase diagrams of the co-polymerizable sulfonated amphiphile **16** were presented in HMT10 and EGDMA. In both cases gels were found in the low concentration region, while lyotropic columnar mesophases exist at elevated concentrations ($C_{\mathbf{16}} > \sim 70$wt%) of the mesogen. A homeotropically orientated columnar mesophase was found in the **16** / EGDMA (ethylene-glycol-dimethacrylate) system. Synthetic membranes were prepared by cross-linking polymerization of either the **16** / HMT10 organogels or the **16** / EGDMA columnar phase.

References

[1] V. Percec, G. Johansson, J. Heck, G. Ungar, S. V. Batty, *J. Chem. Soc. Perkin Trans. 1*, **1993**, 1441.

[2] U. Beginn, G. Zipp, M. Möller, *Adv. Mater.*, **2000**, 12, 510.

[3] U. Beginn, G. Zipp, M. Möller, *Adv. Mater.*, **2000**, 12, 513.

[4] C. W. Martin, P. J. Nanapurkar, S. S. Katti, *Encylcopedia of Polymeric Material*, CRC Press, Boca Raton, Vol. 5, **1996**, p. 3427; A. Eisenberg, J. S. Kim, p. 3435.

[5] U. Beginn, S. Keinath, M. Möller, *Macromol. Chem. Phys.*, **1998**, 199, 2379-2384.

[6] *a)* G. Kanig, *Coll. Pol. Sci.*, **1977**, 255, 1005; *b)* J. S. Trent, J. J. Scheinbeim, P. R. Couchman, *Polym. Sci. Technol.*, **1983**, 22, 205; *c)* D. Mantezinos, G. B. Wells, J. L. Burns, *J. Polym. Sci., Polym. Lett.*, **1985**, 23, 1220.

[7] Landolt-Börnstein, *"Zahlenwerte und Funktionen aus Physik, Chemie, Astronomie, Geophysik und Technik"*, 6th ed., Springer Verlag Berlin, Vol. II, Part 7, **1960**.

Summary

Self-Assembly of Sulfonated Amphiphiles for Channel-like Synthetic Membranes

Functional synthetic membranes capable of selective transport of ions or small molecules could save large quantities of time and energy, which are now required for thermal separation techniques (e.g. distillation, crystallization) in industry and laboratory. There still exists no technical membrane that employs other than size selective separation principles except cation / anion selective membranes. The most prominent synthetic ion selective polymer membranes is Nafion®, which is made from poly(tetrafluorethylene) containing side-chain perfluoroethyl-sulfonic acid groups [1]. However, its ion transport mechanism is not fully understood and improvement of membrane performance in terms of selectivity and permeability has not considerably taken place during the last 20 years. Inspired from Nafion® our synthetic approach presents a new strategy to generate cylindrical nanostructures containing dense stacks of sulfonate ions in their interior along the cylinder axis that can be incorporated in macromolecular matrix and mimic sulfonate transport channels [2]. The key point is the design of the wedge-shaped sulfonated amphiphiles, which can self-assemble to cylindrical structures of molecular defined diameters, bearing the polar units (sulfonates) in their interior, while non-polar functional (e.g. polymerizable) groups

cover the outer surface of the superstructure (cf. Figure 1). Due to the head-to-head arrangement, sulfonate moieties are stacked along the axis of the cylinder forming a potential transport path for metal cations. By introducing the polymerizable group the columns can be covalently cross-linked in the columnar liquid crystalline state, i.e. the self-assembled sulfonate channels can be fixed in the polymer matrix. In such a way, a novel type of ion selective channel-like membrane is formed.

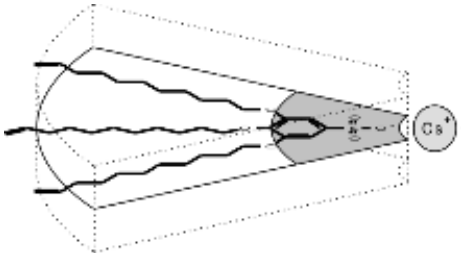

Figure 1 Scheme of wedge-shaped sulfonated amphiphiles.

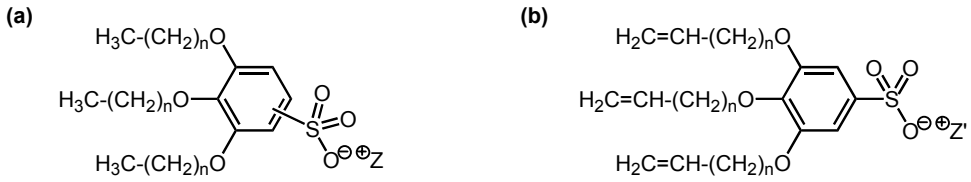

I: 2,3,4-substituted; II: 3,4,5-substituted **III**

Figure 2 Structure formula of **(a)** amphiphilic sulfonic acid derivatives **I** and **II** ($Z^{\oplus} = H^{\oplus}$, $Li^{\oplus}$, $Na^{\oplus}$, $K^{\oplus}$, $Cs^{\oplus}$, $Me_4N^{\oplus}$, $Et_4N^{\oplus}$, $Bu_4N^{\oplus}$) and **(b)** polymerizable sulfonated mesogens **III** ($Z'^{\oplus} = Cs^{\oplus}$).

In this work, a series of amphiphilic sulfonic acid derivatives **I** and **II** (cf. Figure 2a) differing in substitution pattern and molecular symmetry as well as the size of the cationic countions, were synthesized and characterized to give a better understanding of the self-assembly process. From the dependence of transition temperatures and enthalpies on the cation diameter it is conclusive that the occurrence of mesophases with these compounds is more ruled by the geometric shape of the mesogen than by the ionic interactions between cation and sulfonate anion. Depending on the radius of the cation the asymmetrically substituted compounds **I** ($Z^{\oplus} = Li^{\oplus}$, $Na^{\oplus}$, $K^{\oplus}$, $Cs^{\oplus}$, $Me_4N^{\oplus}$) exhibit cubic and columnar mesophases; the cubic symmetries are limited to the cations of small sizes. Compounds with larger radius exhibit columnar mesophases as long as the cation radius is below 0.35 nm, on exceeding this value only crystalline materials

are obtained. The symmetrical substituted alkali metal sulfonates **II** ($Z^{\oplus}$ = $Li^{\oplus}$, $Na^{\oplus}$, $K^{\oplus}$, $Cs^{\oplus}$) all exhibit columnar mesophases either on melting from the crystalline phase or on annealing at the proper temperature. The target molecule with polymerizable groups **III** (cf. Figure. 2b) was also found to exhibit a hexagonal columnar mesophase between 115 °C and 233 °C, as well as in semi-polar methacrylate solvents as the concentration of **III** exceeded 70wt%. Figure 3 shows the broken fan-shaped texture of the columnar mesophase of 80wt% **III** in EGDMA under crossed polarizers. Photo-curing this hexagonal columnar mesophase results in a cross-linked polymer film covalently embedded with the cylinders network.

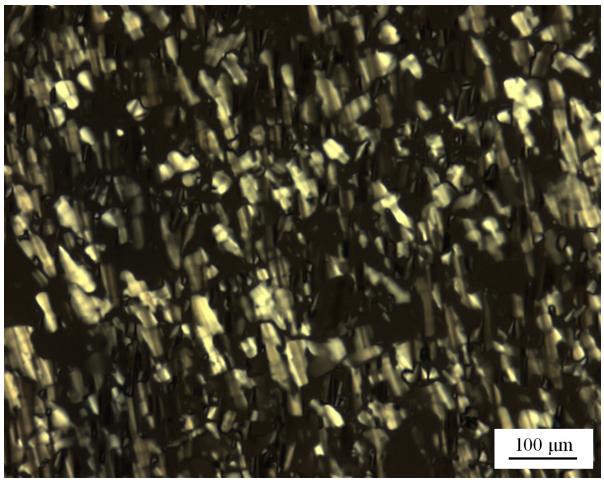

Figure 3 Polarized micrograph of the columnar mesophase of **16** / EGDMA (80/20wt%) at 100 °C, after sheared.

Based on the concept that was described above, the membranes with abundant sulfonate channels were obtained by photo-initiated polymerization in the state of lyotropic columnar mesophases without losing the ordered columnar arrangements. The ion-transport measurements showed their ability to transport small cations ($Li^{\oplus}$, $Na^{\oplus}$, $K^{\oplus}$) through the channels: the transport rate was about 4.5, 5.2 and 6.2 × 10^{-4} mol/cm^2 h respectively. The ion transport rates exhibited a decreasing tendency in the sequence $Li^{\oplus} > Na^{\oplus} > K^{\oplus}$. The $Li^{\oplus}$: $K^{\oplus}$ ion transport rate ratio was 1.36. Since in a free solution $Li^{\oplus}$ diffuses slower than $Na^{\oplus}$ that diffuses slower than $K^{\oplus}$, this opposite result is indicative of the transport through the supramolecular channels. It is confirmed that the diffusion became controlled by cation-sulfonate interactions during the transport through the supramolecular channels. Since the homeotropic orientation of columnar phase was not obtained during the preparation of the membranes, the low absolute ion

transport values and selectivity were reasonable. The further improvement is to optimise the homeotropical orientation of columnar channels by using the carbon-coated glass substrate.

In this dissertation, the sulfonated functional membranes with orientated columnar channels were achieved and used as a model system to investigate the mechanism of cation transport through the supramolecular sulfonate channels. Due to the possession of the geometrically defined superstructure, the presented strategy of constructing the channel-like functional membrane gives the potential to modify or tune the performance of the membranes for further application.

References

[1] C. W. Martin, P. J. Nanapurkar, S. S. Katti, "*Ionomeric Membranes, Perfluorinated*", in "*Encyclopedia of Polymeric Material*", CRC Press, Boca Raton, **1996**, Vol.5, p. 3427.

[2] (a) U. Beginn, G. Zipp, M. Möller, *Adv. Mater.*, **2000**, 12, 510; (b) U. Beginn, G. Zipp, A. Mourran, P. Welther, M. Möller, *Adv. Mater*, **2000**, 12, 513.

CURRICULUM VITAE

Linglong Yan （颜玲珑）
Chinese
11. Dec. 1975
Fuzhou, Fujian, China

2003-2005	PhD. Thesis on ″Self-assembly of sulfonated amphiphiles for channel-like synthetic membranes″. RWTH Aachen, Lehrstuhl für Textilchemie und Makromolekulare Chemie
2001-2002	& University of Ulm, Department of Organic Chemistry III
2000-2001	Scientific assistant on the project of ″The development of charge transporting materials″. Institute of Photographic Chemistry, Chinese Academy of Science
1997-2000	Degree: Master of Science. Thesis on ″The formation and the dynamic behavior of the complexes with phospholipid and protein″. Institute of Photographic Chemistry, Chinese Academy of Science
1993-1997	Degree: Bachelor of Science. Fuzhou University (China), Department of Chemistry (福州大学)
1990-1993	High school time Fuzhou The Second High School (福州第二中学)
1987-1990	Middle school time Fuzhou Yangqiao Middle School (福州杨桥中学)
1981-1987	Primary school time Fuzhou Hongshan Primary School (福州洪山小学)